ÉCOLE DOCTORALE SCIENCES ET MÉTIERS DE L'INGÉNIEUR

Développé du labo de recherche PIMM - Campus de PARIS

THÈSE

Présentée par **Luis IRASTORZA VALERA**
Soutenue le **28 janvier 2025**

pour obtenir le **Doctorat** délivré par

L'École Nationale Supérieure d'Arts et Métiers, Universidad Politécnica de Madrid

Spécialité **Matériaux (ENSAM), Génie Aérospatiale (UPM)**

Learning Techniques for Optimization in Engineering
Data-Driven Tools for Mechanical and Biomedical Settings

THÈSE dirigée par :
CHINESTA SORIA Francisco, Professeur des Universités (ENSAM)

SAUCEDO MORA Luis, Professeur des Universités (UPM)

et co-encadrée par :

DESTRADE Michel, Professeur des Universités (NUIG)

Jury

M. Pierre JOYOT	Professeur, Génie Mécanique, ESTIA	Président
Mme. Rena C. YU	Professeure, Génie Civil, UCLM	Rapporteure
M. Juan J. LÓPEZ CELA	Professeur, Génie Civil, UCLM	Rapporteur
M. Pierre JOYOT	Professeur, Génie Mécanique, ESTIA	Examinateur
M. Mohamed JEBAHI	Professeur, Génie Mécanique, ENSAM	Examinateur
M. Francisco CHINESTA	Professeur, Génie Mécanique, ENSAM	Directeur
M. Luis SAUCEDO MORA	Professeur, Génie Mécanique, UPM	Directeur
M. Francisco MONTÁNS	Professeur, Génie Mécanique, UPM	Invité

T H È S E

A mis padres, que me han dado todo y apenas empiezo a devolvérselo.

Somewhere, something incredible is waiting to be known.

Carl Sagan, Physicist (1934-1996)

Acknowledgments

I would like to thank, first and foremost, my parents, without whom I would not be presenting this work. All their patience, their encouragement, their help and dedication, has led me to this moment. After all that sowing, it is time to harvest the fruits of that shared effort, which I owe and dedicate to you. I can only try to ever repay you for all you have given me. I love you both, and I will always do.

To my Mom, which has accompanied me along this long vital experience, always supporting me throughout the numerous hardships coming with a PhD and life in general, giving valuable advice and lessons coming from years of wit and experience, for her infinite love and patience.

To my Dad, whom I have greatly missed all this time and, hopefully, has somehow seen me become a person worthy of his affection and teachings earlier in life, which I keep as my most precious treasure.

By extension, I would like to thank my family, whose support has kept me afloat all this time. A special mention goes to my cousin Itzi, who understands better than anyone the complications of pursuing a PhD, and whose valuable insight and support in key moments has helped me fight my way through.

I am especially grateful to my thesis supervisors, being lucky enough to have two of them. Both have greatly contributed with vast and complementary knowledge, research styles and perspectives, shaping an eager but naive Master's student into a (hopefully competent) researcher.

To Luis Saucedo, whose natural talent for teaching and research, to make the complicated simple and the unknown appealing; has no doubt had a deep impact in my approach to Science. Your optimistic and confident way to tackle new endeavors, your innovative ideas and your enthusiasm and generosity in sharing them are something I look up to, and I think everyone should.

To Paco Chinesta, for his experienced outlook on research, always attentive to new developments and trends while focused on practical goals and applications. Generous and jolly, while strict when needed. Thanks for trusting me for this task and all the valuable advice.

To all members of the jury (R.C. Yu, J.J. López Cela, M. Jebahi and P. Joyot), who generously offered their time and expertise to evaluate this work. I am grateful for your comments and suggestions so it can live up to the most demanding scientific standards.

To my secondment supervisors Michel Destrade (University of Galway) and Juan García (INTA), who taught me there is more to research than papers, for helping me see the forest for the trees and not letting me forget there is joy to be found in Science and the connections we share along the way.

I would also like to thank Paco Montáns, who introduced me to this project. His pragmatic outlook and dedication to research helped me make my mind on pursuing an academic career, and I will be forever thankful for the chance and trust to partake in such an adventure.

Many thanks to Ignacio Angulo and Francisco Cordovilla, my final Master's project supervisors, whose first introduction to research and encouragement were key in choosing this academic path.

To all my friends whom I have been continuously pestering with my many complaints and concerns when motivation was running low. Thanks for dealing with me at difficult times and keeping me focused and strong in such weak moments. I hope I was up to the task from your perspective, and please forgive me if I was ever oblivious to your own real everyday problems. Now it is time to share this work with you, and celebrate accordingly! I would like to mention Jose and Alex, whose constant support and understanding have made me arrive to this day more or less sane. To my friends from Colegio de España in Paris (Pablos, Iván, Irmina, Elena, Luis, Josep), thanks a lot for the encouragement and all shared unforgettable moments - and the ones to come! If I have arrived to this stage, it is thanks to you all. You, my friends, are by far the most precious gift the PhD has given me.

It would be unfair to forget my lab colleagues at ENSAM and UPM, with whom I have shared many valuable experiences - which I hope to continue! A particular mention goes to Sebastián and Paula, whose friendly advice and support has been key to not give up and continue pursuing the sometimes distant and seemingly unreachable goals of a PhD.

To all my fellow Early Stage Researchers in the XS-Meta project, with whom I had the pleasure to share this adventure, in its ups and downs but always with the solace of being in this together and counting on each other when the road ahead seemed too bumpy. I hope to keep this friendship in good shape for many more years to come, and wish you the very best - I know for a fact you are fighting it and do not deserve less than that.

Last but not least, I am thankful to everyone who has helped me with the sometimes cumbersome and frustrating paperwork, especially Victoria Lapuerta and Mª Jesús de Andrés in UPM and Claire Mandon in ENSAM. To everyone, from administrative stuff to cleaning and security personnel, that has made this possible in indirect yet decisive ways. To Angélica and Norma, the friendliest cafeteria workers there will ever be in ETSIAE UPM.

To Extremoduro and Electric Six, among many others, whose music has been motivation fuel to keep me awake while writing this manuscript.

I hope this acknowledgment list is long enough to encompass everybody that has somehow been involved in my PhD studies or other aspects of my life while immersed in this life-changing experience.

Abstract

In the automotive and aeronautical industries, structures must adapt to the most demanding needs. At the same time, mechanical and economic reasons favor lighter options. In some cases, the behavior of structural materials must be gradual, as in composites or architectural materials, the so-called metamaterials. The geometries of these designs in the micro scale offer macro properties not found in continuous media, within the smallest volume. Conversely, their versatility poses problems for modeling ("direct" problem) and designing ("inverse" problem).

The direct problem, i.e. describing the performance of an architectural material with a predefined geometry, becomes sometimes intractable by traditional structural calculation methods because of the general complexity and non-linearity of its behavior. Thus, the definition of a purely analytical model (such as Hooke's law for isotropic materials) is impractical because the necessary variables are too numerous and/or partially unknown (internal or non-observable).

Sometimes, the only solution is to create surrogate models that can capture key features of the structure's mechanical response, thus reducing computation cost of calculation, via Model Order Reduction (MOR) or Machine Learning (ML). The reduced model obtained through MOR has a slightly lower resolution, but it is faster. Methods such as Proper Orthogonal or General Decomposition (POD/PGD) are used. ML is based on statistical regressions from large, labeled databases, where the underlying behavior is adjusted during a training phase and validated with new data. This methodology uses neural networks inspired by the brain's. Different architectures are available: multilayer perceptron (MLP) for vectors and matrices, convolutional networks for images and text (CNN), recurrent (RNN) for time sequences - with extended short-term memory (LSTM) if necessary -, or graph-based (GNN). Physics-informed networks (PINN) allow the differential equation to be directly introduced, describing the behaviour to be predicted in the loss function.

ABSTRACT

The inverse problem deals with a much more difficult task, that of finding the structure (geometry, material, etc.) which gives the desired properties. This is a challenge since there is no unique solution and the mathematical formulation of the problem is ill-posed (non-convexity). Topology optimization methods are used, e.g. penalizing the isotropic solids (SIMP) by removing material to the minimum necessary to support the applied load with the least energy of deformation. This approach must consider the real properties of the material (anisotropy, fatigue) as well as the practical conditions of manufacture and use; introduced as further penalization, image filters or even new algorithms. All this allows to build a Machine Learning model to simplify and, thus, accelerate the optimization process.

As a mathematical object, graphs offer multiple possibilities for the compact representation of data with states as vertex and their relationships as segments. This analogy applies directly to the two main case studies that are relevant to this work, namely mechanical structures (centered on metamaterials) and biological neural networks, assimilating nodes/neurons as vertex and beams/axons as segments of a graph. This way, the methodologies developed are leveraged to create a basic Digital Twin of the human brain to improve medical diagnoses.

Keywords: Reduced Models, Machine Learning, Metamaterials, Neuroscience, Digital Twins.

Résumé

Dans les industries automotive et aéronautique, les structures doivent s'adapter aux besoins les plus exigeants. En même temps, des raisons mécaniques et économiques privilégient des options plus légères. Dans certains cas, le comportement des matériaux structurels doit être graduel, comme chez les composites ou les matériaux architecturés, dits métamatériaux. Les géométries de ces designs dans l'échelle micro offrent des propriétés macro introuvables dans les milieux continus, dans le moindre volume. En revanche, leur versatilité pose des problèmes pour les modéliser (problème direct) et concevoir (problème inverse).

Le problème direct, c'est-à-dire, décrire la performance d'un matériau architecturé de géométrie prédéfinie, devient parfois intraitable par les méthodes traditionnelles de calcul structurel à cause de la non-linéarité et complexité générale de son comportement. Ainsi, la définition d'un modèle purement analytique (comme la loi d'Hooke chez les matériaux isotropes) n'est pas pratique car les variables nécessaires sont trop nombreuses et/ou partiellement inconnues (dits internes ou non observables).

Pourtant, la seule solution est parfois de créer des modèles substitutifs qui puissent capturer les caractéristiques principales de la réponse mécanique de la structure en réduisant le coût de calcul, comme la réduction de l'ordre des modèles (MOR) et l'apprentissage automatique (ML). La MOR le modèle comme une version de résolution légèrement inférieure mais plus rapide, pour lequel on utilise des méthodes telles que la Décomposition Orthogonale ou Générale en valeurs propres (POD/PGD).

En revanche, le ML est basé sur des régressions statistiques issues de grandes bases de données étiquetées, où le comportement sous-jacent est ajusté dans une phase d'entraînement et validé après avec de nouvelles données. Cette méthodologie utilise des réseaux neuronaux inspirés par les cérébraux. Il y a différentes architectures disponibles : perceptron multicouches (MLP) pour vecteurs et matrices, réseaux convolutifs pour les images et le texte (CNN), récurrents (RNN) pour les séquences temporelles

- avec mémoire à court terme étendue (LSTM) si besoin -, ou basés sur des graphes (GNN). Les réseaux informés par la physique (PINN) permettent d'introduire directement l'équation différentielle qui décrit le comportement à prédire dans la fonction de perte.

Le problème inverse s'occupe d'une tâche beaucoup plus difficile, celle de trouver la structure (géométrie, matériau, etc.) qui donne les propriétés souhaitées. C'est un enjeu car il n'y a pas de solution unique et souvent la formulation mathématique du problème est mal conditionnée pour en trouver une (non-convexité). Des méthodes d'optimisation topologique sont employés, notamment en pénalisant les solides isotropes (SIMP) en enlevant du matériau jusqu'au minimum nécessaire pour supporter la charge appliquée avec la moindre énergie de déformation. Cette approche doit considérer les propriétés réelles du matériau (anisotropie, fatigue) ainsi que les conditions pratiques de fabrication et usage ; introduits comme des pénalisations, filtres d'image ou même nouvelles algorithmes. Tout cela permet de construire un modèle d'apprentissage automatique pour simplifier et, pourtant, accélérer le processus d'optimisation.

En tant qu'objet mathématique, les graphes offrent de multiples possibilités pour la représentation compacte de données avec des états comme vertex et leurs interrelations comme segments. Cette analogie s'applique directement aux deux principaux cas d'étude qui concernent ce travail, à savoir les structures mécaniques (centrées sur les métamatériaux) et les réseaux neuronaux biologiques, pouvant dans les deux cas assimiler des nœuds/neurones comme vertex et des poutres/axons comme segments d'un graphe. De cette façon, on profite des méthodologies développées pour créer un jumeau numérique basique du cerveau humain pour améliorer les diagnoses médicales.

Mots clés : Modèles réduits, Apprentissage automatique, Métamatériaux, Neuroscience, Jumeaux digitaux.

Resumen

En las industrias automovilística y aeronáutica, las estructuras deben adaptarse a las necesidades más exigentes. Al mismo tiempo, razones mecánicas y económicas favorecen las opciones más ligeras. En algunos casos, el comportamiento de los materiales estructurales debe ser gradual, como en los materiales compuestos o los llamados metamateriales. Las geometrías de estos diseños a escala micro ofrecen propiedades macro que no se encuentran en medios continuos, en un volumen más pequeño. En contrapartida, su versatilidad plantea problemas para su modelización (problema directo) y diseño (problema inverso).

El problema directo, es decir, la descripción de las prestaciones de un metamaterial de geometría predefinida, se vuelve a veces difícil de resolver por los métodos tradicionales de cálculo estructural debido a la complejidad general y la no linealidad de su comportamiento. Por ello, la definición de un modelo puramente analítico (como la ley de Hooke para los materiales isotrópicos) es impracticable, ya que las variables necesarias son demasiado numerosas y/o parcialmente desconocidas (internas o no observables).

En ocasiones, la única solución es crear modelos substitutivos (subrogados) que puedan capturar las características clave de la respuesta mecánica de la estructura, reduciendo así el costo del cálculo, mediante reducción de orden de modelos (MOR) o aprendizaje automático (ML). El modelo reducido obtenido mediante MOR tiene una resolución ligeramente inferior, pero es más rápido. Se utilizan métodos como la descomposición en valores propios ortogonal o la general (POD/PGD).

El ML se basa en regresiones estadísticas de grandes bases de datos etiquetadas, donde el comportamiento subyacente se ajusta durante una fase de entrenamiento y se valida con nuevos datos. Esta metodología utiliza redes neuronales inspiradas en el cerebro. Existen diferentes arquitecturas: perceptrón multicapa (MLP) para vectores y matrices, redes convolucionales para imágenes y texto (CNN), recurrente (RNN)

para secuencias temporales - con memoria a corto plazo extendida (LSTM), si es necesario -, o basado en grafos (GNN). Las redes de informadas por la física (PINN) permiten introducir directamente la ecuación diferencial que describe el comportamiento a predecir en la función de pérdida.

El problema inverso se ocupa de una tarea mucho más difícil: encontrar la estructura (geometría, material, etc.) que proporcione las propiedades deseadas. Esto es un desafío, al no haber una solución única y estar la formulación matemática del problema mal planteada (no convexidad). Se utilizan métodos de optimización topológica, p. ej., penalizando los sólidos isotrópicos (SIMP) mediante la eliminación del material al mínimo necesario para soportar la carga aplicada con la menor energía de deformación. Asimismo, deben considerarse las propiedades reales del material (anisotropía, fatiga) y las condiciones prácticas de fabricación y uso; introducidas como penalización adicional, filtros de imagen o incluso nuevos algoritmos. Todo ello permite construir un modelo de aprendizaje automático para simplificar y, por tanto, acelerar el proceso de optimización.

Como objeto matemático, los gráficos ofrecen múltiples posibilidades para la representación compacta de datos con estados como vértices y sus relaciones como segmentos. Esta analogía se aplica directamente a los dos principales estudios de campo en este trabajo, a saber, las estructuras mecánicas (centradas en metamateriales) y las redes neuronales biológicas, asimilando nodos/neuronas a vértices y barras/axones a los segmentos de un grafo. Así, se aprovechan las metodologías desarrolladas para crear un gemelo digital básico del cerebro humano para mejorar los diagnósticos médicos.

Palabras clave: Modelos reducidos, Aprendizaje automático, Metamateriales, Neurociencia, Gemelos digitales.

Résumé Étendu

INTRODUCTION

Dans la modélistation des phénomènes physiques, il y a plusieurs difficultés inhérentes à la méthodologie scientifique, voir des défauts ou imprécisions dans les appareils de mesure, des lacunes théoriques, l'indisponibilité de toutes les variables pour prendre la mesure ou même la méconnaissance de celles qui jouent un rôle dans le système à modéliser.

Tous ces facteurs provoquent des graves soucis à l'heure de concevoir ces modèles analytiques (soit, entièrement contenus dans des expressions mathématiques): gros nombre de variables considérées (haute dimensionalité), observabilité partielle, complexité numérique et inefficacité computationelle. C'est le cas pour beaucoup de systèmes mechaniques - notamment structures complexes dont l'obtention de proprétés générales n'est pas si évidente, comme les composites ou les métamatériaux - et aussi des diverses environnements biologiques, comme le cerveau humain.

C'est pourquoi il est parfois nécessaire de créer modèles plus simples mais suffisamment précis pour décrire ces phénomènes, enlevant la complexité du model "complet". Ces modèles, dits "substitutifs", permettent d'obtenir simulations et résultats au moindre coût numérique. Ils ne son construits qu'à base des données expérimentales, obtenus auparavant dans une phase plus coûteuse, dite "online"; créant une base assez grande pour pouvoir générer cettes réponses rapides dans la phase "offline".

ÉTAT DE LA TECHNIQUE

Ce chapitre décrit les méthodes bien établies dans ce moment pour développer ces modèles substitutifs, ainsi que leurs applications aux deux principaux domaines de recherche ciblés par ce travail de thèse: les structures complexes (métamatériaux) et les systèmes biologiques (cerveau humain).

Modèles substitutifs

Comme techniques préférées pour construir des modèles dirigés par les données, la réduction d'ordre et l'apprentissage automatique peuvent être cités. La première consiste à mesurer plusieurs états pendant l'evolution du système et réconstruire le comportement sous-jacent à partir de ses caractéristiques les plus importantes. Pour cela, la décomposition en valeurs propres (SVD/PCA), modes orthogonales (POD) et général (PGD) sont disponibles.

Le deuxième choix correspond plus particulièrement aux réseaux de neurones artificiels, basées sur ses équivalents biologiques dans le cerveau, où les valeurs initiales (entrées) experimentent une série de transformations algebraïques pour obtenir par regression statistique les valeurs objectives (sorties).

Il y a de divers architectures pour ces réseaux, en fonction du type de données d'entrée/sortie qui doivent être traitées: perceptron multi-couche (MLP) pour les vecteurs, convolutionnels (CNN) pour des images et du texte, récurrents (RNN) pour les séquences témporelles - avec une grande mémoire (LSTM) pour capturer des comportements persistants et oublier les effets transitoires - ou en graphes (GNN) pour exprimer valeurs et ses interactions, en les mettant à jour lorsque le système évolue.

Métamatériaux

En tant que structures complexes, les métamatériaux ou máteriaux architecturés ont des besoins spécifiques pour être modélisés. Contrairement aux milieux continus, où l'homogénéité, isotropie et linéarité sont hypothèses de travail communes; les caractéristiques géométriques et topologiques de ces máteriaux sont conçues précisement pour briser cettes hypothèses. L'anisotropie est assuré dès que le máteriau est composé de cellules non-pleines distribuées tout au long de l'espace disponible, avec ses creux et discontinuités.

Donc, même si cette cellule base est symmetrique et ses propriétés globales associées presque homogènes, l'isotropie du continu est effectivement disparue. Fréquemment, leur comportement est aussi non-linéaire, montrant parfois des réponses méchaniques inélastiques (plasticité, hyper-elasticité, flambage).

Comme résultat de tous cettes caractéristiques, les calculs nécessaires pour leur description (obtention de propriétés physiques équivalentes à partir des descriptions géométriques) et design/optimisation (création d'une topologie capable d'offrir les propriétés globales souhaitées) deviennent trop exigeants, d'où l'utilisation de techniques basées sur des données au lieu des expressions analytiques. La réduction d'ordre de modèles a été employée pour diminuer les degrés de liberté des modèles constitutifs

micro- (cellule) et macroscopiques (niveau prototype), ainsi que pour simplifier l'expression des propriétés globales micro et macro à partir de paramètres géometriques. D'autre part, l'apprentissage automatique peut accélérer l'optimisation topologique en prévoyant l'évolution de cette procédure itérative, notamment à travers les réseaux neuronaux convolutionnels (CNN).

Études biomédicales

Pour les modèles biomédicaux, des questions supplémentaires doivent être posées, comme l'incomplétude du cadre théorique, le cycle de vie des cellules biologiques (naissance, nutrition, croissance, reproduction et mort), et surtout la complexité des phenomènes y ayant lieu, qui rendent difficile la distinction épistémologique entre causes et conséquences. Obtenir des modèles substitutifs simples mais efficaces dans ces conditions est une tâche assez compliqué.

Même si les techniques déjà commentées (réduction d'ordre, apprentissage automatique) peuvent tout à fait simplifier les efforts, il est commun dans la recherche médicale de choisir des options plus heuristiques, comme la modélisation par agents: cellules avec propriétés individuelles qui sont capables d'interagir avec son entourage (autres cellules), en modifiant ces propriétés selon une série de régles établies préalablement.

Plus précisement, le tissu cérébral se comporte comme un réseau de néurones connectées physique- (structure: axons/dendrites) et conceptuellement (fonctions: synapses) qui conforment le connectome. En plus de l'approche (bio)mécanique, qui décrit ce tissu comme une structure très mou, hétérogène et hyper-élastique; il faut y ajouter les perspectives électrophysiologique (le connectome comme circuit électrique composé par neurones excitables), hémodynamique (l'ensemble de veins qui transportent le sang avec ses nutriments) et purement mathématique (le cerveau en tant que graphe dont les sommets sont les noyaux des neurones et les arêtes correspondent à leurs extensions: dendrites/axons). Ces aspects sont complémentaires et ils doivent pourtant être pris en compte pour créer des modèles cérébrales.

MÉTHODOLOGIE

Ce chapitre explique comment l'état de la technique a été employé, modifié et/ou élargi par rapport aux domaines d'intérêt de ce thèse doctoral, en les séparant en trois grands blocs thématiques: description de structures, design/optimisation de structures et jumeaux numériques pour applications biomédicales.

Description de structures

Dans la première section, la description des structures conçues auparavant est considérée. Des propriétés équivalentes d'une cellule base de métamatériau vont être prédites grâce à des techniques d'apprentissage automatique. Pour générer assez de variabilité, des cellules asymmetriques seront étudiées, dont leurs géometries cubiques contient toujours les 8 nœuds dans leurs sommets et un nombre aléatoire de nœuds intérieurs en positions assignées au hasard.

Tous ces nœuds sont unis par triangulation de Delaunay en 3 dimensions (c'est-à-dire, tétraédrisation). Ces cellules vont être soumises au même déplacement verticale quasi-statique dans les sommets supérieurs, étant les reste des dégrés de liberté des sommets restreints et les nodes intérieurs libres de se déplacer. Des differents modèles analytiques sont mis en œuvre pour calculer la réponse méchanique de ces cellules, notamment des poutres à treillis articulées ou fixées.

Il est théorisé que la rigidité des cellules en trois dimensions est équivalent à la somme de celles de ses tranches transversales en série, d'où l'expression analytique que les réseaux neuronaux vont essaier de reproduire à base des données obtenues. Deux types de réseau sont choisis pour prédire le module de Young équivalent dans la direction chargée.

Le premier est dense (DNN), c'est-à-dire, un perceptron multi-couche (MLP) dont chaque neurone est connecté avec tous ceux des couches précedante et suivante. Le deuxième est basé sur des graphes, où les nœuds de la structure correspondent évidemment aux sommets du graphe et les barres sont ses arêtes. L'information géometrique et mécanique est passée à travers le graphe deux fois et après filtrée par une couche dense pour donner le module de Young équivalent.

Comme cas particulier de prédiction de propriétés, un système dynamique est proposé pour évaluer la construction des modèles substitutifs en conditions d'observabilité partielle. Des élements Kelvin-Voigt (masse en série avec ressort et amortisseur en parallèle) son mis en série et soumis à une force dynamique dans le dernier élement observable, à partir de laquelle la réponse méchanique de l'ensemble du système va être reconstruite. Pour cette tâche, il y a plusieurs options.

Tout d'abord, les variables dynamiques observables (déplacement et moment linéaire de la dernière masse) peuvent être liées entre elles au moyen de la condensation statique. Si la réponse du système dépend du temps, la transformée de Fourier est apliquée à l'expression analytique pour obtenir les

fréquences caractéristiques sans rien connaître de partie intérieure du système. Pour opérer directement dans la domaine temporelle, une discrétisation en temps est requise.

En revanche, les réseaux neuronaux apportent à nouveau une façon agnostique de prédire l'évolution temporelle de l'ensemble du système en connaissant uniquement un nombre assez grand d'états méchaniques antérieurs (déplacements, moments linéaires) dans la bille la plus externe. En effet, l'architecture choisie dans ce cas est récurrente (RNN), dont les entrées sont la valeur actuelle de la force extérieure appliquée et le déplacement précédent tandis que la sortie contient le déplacement suivant.

Au cas où il y aurait présence de comportéments persistants, les blocs RNN seraient substitués par ses versions de longue mémoire (LSTM), en permettant conserver l'historique complet dans la réponse prédite ainsi qu'écarter les déviations transitories.

Design et optimization de structures

Cette deuxième section méthodologique contient tous les stratégies dévéloppées pour la conception des structures à partir de certaines propriétés souhaitées. Le plus commun en industrie (ponts, bâtiments, etc.) c'est construire la structure portante à partir des élements discrets dont leur géometrie est prédéfinie et. pourtant, aussi leur inertie et rigidité.

Une option évidente pour le faire c'est juste choisir les structures existantes le plus similaires parmi celles dans la base de données déjà générée pour entraîner les réseaux DNN/GNN auparavant. Pour affiner la recherche, le volume et le module de Young permettent de créer une limite d'óptimalité (front de Pareto) pour sélectionner les architectures plus résistantes (rigides) pour le moindre poids.

Si une réponse méchanique plus complexe (non-linéaire, adaptative, etc.) est préférée, des distributions de matériau flexibles seront cherchées au lieu d'une structure rigide prédétérminée. Par example, dans les cas des prothèses orthopédiques, il arrive souvent que les pièces au milieu des articulations (génou, hanche) sont exposées à deux distributions de charge méchanique différents de chaque côté (máteriaux et forces diverses).

Par conséquent, il serait très pratique de concevoir une structure capable de s'adapter à de diverses distributions de force. À cette fin, une stratégie heuristique de design est dévéloppée. Dans une domaine en 2D, une série de nœuds en positions aléatoires sont liés par triangulation de Delaunay, en créant des poutres.

En supposant que leur comportement méchanique correspond au modèle Euler-Bernoulli, un déplacement de traction est imposé dans deux des côtés du domaine carré, ce qui donne une réponse de la structure: des forces de réaction extérieures. Le but maintenant c'est d'arriver à changer la localisation initiale des nœuds et/ou la section transversale des poutres pour transformer ces réactions en les profils de forces souhaités.

Donc c'est plutôt un problème d'optimisation structurelle itérative à partir d'une suggestion initiale. Avec cet objectif, un indice de charge est défini pour chaque poutre, en considérant la différence entre les réactions et les forces objectives, l'orientation de la poutre et la fraction de la tension limite (élastique, rupture, flambage, etc.) qu'elle supporte. Des directions de recherche (descente de gradient avec moment) dirigent le mouvement des nœuds et l'élargissement des poutres. Ce processus termine dès que la différence entre réactions et forces cible est plus petite qu'une tolérance.

Par contre, si le domaine de design est infini, la distribution de matériau va être donnée par des élements dans une grille. Les designs vont être optimisés pour des conditions aux limites (supports, forces) prédéterminées, mais cette optimisation, en tant que non-convexe, permet améliorer certains aspects non-considérés par les procédures standard.

Pour inclure l'incertitude dans les forces appliquées (à cause des vibrations ou les mesures expérimentales elles-mêmes), quatre types de charges sont conçues, chacune avec une probabilité associée: constantes (si elles sont appliquées tout le temps), alternées (présentes un pourcentage fixe du temps total), statistiques (distributions de forces dont leurs modules et/ou positions changent dans chaque itération) et occasionnelles (fixées en position et module, apparaissent chaque n itérations). Ces forces sont combinées, en apportant chacune ses pénalisations (pour l'énérgie de déformation et le volume) dans le processus d'optimisation, à niveau des cycles, force et itération.

Ces de pénalisations peuvent provenir de différents origines en dehors des forces elles-mêmes. Par exemple, des effets de dégat du matériau dûs à la fatigue sont introduits par une fonction de dommage isotrope, ce qui entraîne une représentation plus réaliste de ses capacités pendant et après l'usage commun du prototype. Aussi, des différents matériaux ont des préférences méchaniques : tandis que l'acier et ses dérivés supportent très bien la traction, ils ont un comportement faible à compression (même avec flambage). Le contraire peut être observé pour le béton (non-armé) et les sols en général. Donc, la traction ou compression seront aussi pénalisées respectivement en renforçant les éléments dont leur déformation correspond à ces états.

Pour tenir compte de la direction principale portante chez les matériaux composites et architécturés, il est proposé de pénaliser le produit scalaire de la direction d'impression et la principale pour chaque élement. Enfin, la méthode SIMP ("Solid Isotropic Material Penalization") et tous les critères cités supposent l'isotropie et linearité du matériau de base, qui peut être perturbée par des effets de fracture et concentration de contraintes. Si chaque élément est pénalisé par sa contrainte équivalente de von Mises, ces soucis peuvent être soulagés.

Pour atténuer le coût de calcul des strategies communes de post-traitement, un filtre de densité est proposé, ce qui permet de mieux définir le contour de la topologie optimisée juste en effaçant les éléments qui sont vaguement définis (densité sous un seuil donné). Le filtre cherche ces éléments dans toutes les directions marquées par ses voisins (en 2D: gauche, droite, haut, bas et les quatre coins), mais il permet aussi faire des recherches limitées à quelques sens ou directions d'intérêt.

De plus, une formule volume-compliance est fournie, donc connectant les deux variables principales (l'une restreinte et l'autre comme cible à minimiser) pour créer des familles topologiques entre lesquelles l'interpolation est possible, ce qui retient certaines propriétés de toutes les familles (courbes) parcourues. Si le filtre est y ajouté, un espace d'interpolation avec trois dégrés de liberté est crée: compliance (voir rigidité), volume (voir masse/poids) et distance filtré (voir épaisseur minimale des branches générées) - ce qui rend les prototypes réalisables.

Jumeaux numériques pour applications médicales

Cette section contient les strategies développées pour créer un jumeau numérique du cerveau humain en tant que réseau de neurones biologiques (connectome), liés par leur structure et fonctions. Un domaine 3D est rempli par des points aléatoirement distribués et connectés par triangulation de Delaunay. Une partie de ces neurones sont assumées d'entrée et quelques autres de sortie, laissant le reste pour transition entre les deux. La métastabilité est introduite en coordinant les signaux d'entrée activés séquentiellement (en fractions successives).

La migration des neurones en tant qu'agents indépendants est réservée à un tout petit pourcentage d'entre elles pour prévenir la surcharge numérique, en changeant ses connectivités structurelles et fonctionnelles selon les besoins du système et sous la neuroplasticité imposée. Pour faciliter (chemin excitateur) ou entraver (chemin inhibiteur) l'activation des neurones, les seuils et connectivités présynaptiques sont modifiées, menant à l'apparition de neurones centrales qui dominent le traffic.

La propagation des signaux elle-même va être déclenchée si les poids donnés aux neurones présynaptiques dépassent un seuil d'activation. Le sens de propagation à travers les neurones de transition va être attribué au hasard, pour simuler l'orientation caotique des neurones biologiques face à l'aménagement par couches dans les réseaux artificiels. L'apprentissage supervisé est appliqué en corrigeant les poids et activations de neurones qui empêchent la propagation des signaux d'entrée vers les sorties. Cela est intensifié pour la migration et la neuroplasticité, en créant des portes logiques booléennes AND/OR/NOT dans les nœuds centrales.

RÉSULTATS

Ce chapitre présent les résultats de l'application de la méthdologie proposée aux cas qui concernent cette thèse: la description et optimisation de structures et les modèles biomédicales.

Description de structures

Le réseau neuronal dense (DNN) a réussi à prédire le module de Young de l'exemple en 1D de manière presque exacte, ce qui confirme l'hypothèse envisagée: un élément rigide est assimilable à une série de ressorts dont leur rigidité est donnée par le cadre théorique qui les modélise (Euler, Timoshenko, etc.). Le nombre de tranches suffissant pour bien décrire la structure avec un coût raisonnable est estimé.

Alors que le DNN peut caractériser correctement une architecture aux nœuds épinglés, des modèles méchaniques plus compliqués montrent un comportement difficile à apprendre, vue l'inclusion de plusieurs dégrés de liberté additionnels non considérés dans le cas antérieur: moments, rigidité en torsion, etc. À ce tournant, il faut utiliser des réseaux plus descriptifs de la géometrie des architectures étudiées pour capturer ces comportements plus complexes. En utilisant des réseaux neuronaux basés sur graphes (GNN), la prédiction est encore plus précise que le DNN pour le cas épinglé et similairement satisfaisant pour les poutres Euler-Bernoulli.

Dans le cas partielment observable, la condensation statique des parties inconnues dans les parties mesurables permet d'obtenir une expression analytique qui va être apprise pour l'approche Fourier et les réseaux neuronaux. La transformé de Fourier permet en effet d'obtenir les fréquences caractéristiques qui décrivent la réponse méchanique du système en ignorant les aspects internes. Toutefois, cette description des phenomènes, bien que précise, est assez limitée.

C'est pourquoi des techniques d'apprentissage automatique sont nécessaires, particulièrement celles qui peuvent répresenter des données séquentielles de forme facile, c'est le cas des réseaux récurrents (RNN). Considérer un système d'à peine deux billes suffit pour vérifier la bonne performance de ces RNNs en obtenant la réponse dynamique (déplacement externe) du système, sans besoin d'introduir de forme explicite aucun paramètre.

Même si la réponse est non-linéaire (croissante monotonique), la prédiction est presque exacte. Au cas où des comportements inélastiques (voir plasticité) ou la dépendance du chemin seraient présents, la version du RNN de grande mémoire (LSTM) est préférée, étant capable d'offrir des prédictions efficaces en échange d'un nombre plus grand d'époques d'entraînement.

Conception et optimization de structures

En ce qui concerne le design inverse de structures, le front de Pareto donne des options réalistiques (existantes) très proches du point souhaité (module de Young, volume). Pour la réponse méchanique complexe, par contre, les résultats sont moins spectaculaires. Si bien quelques nœuds extérieurs sont devenus plus proches à leurs forces cible, la conséquence est souvent la dégradation de l'état des autres, proches ou pas (effets allostériques), ou même une accumulation de charge méchanique dans des certains nœuds intérieurs, ce qui peut conduire à la fatigue et, par conséquent, à la fracture.

De maillages plus ordonnés et/ou raffinés n'offrent pas meilleurs résultats, et la prolongation des itérations montre convergence et divergence alternativement. Comme solutions possibles à ces limitations, des diverses choix son considérées (POD quasi-statique, désordre progressif en introduisant des dislocations, migration nodal, formulation variationnelle, coupe sélective de poutres, etc.).

Pour les milieux continus, la robustesse de l'approche statsique pour l'optimisation topologique est prouvée car elle offre des structures plus résistants et relativement bien définies dans situations ou l'alternative traditionnelle (deterministe) est clairement moins effective ou même n'arrive pas à converger. Plusieurs cas différents de conditions aux limites et charges (quatre types mentionnés: constantes, alternées, statistiques, occasionnelles) sont étudiés, dont la proposition probabilistique renforce des zones négligées par les méthodes traditionnelles.

Aussi, l'équivalence entre distributions statistiques de position et module des forces est démontrée, ainsi qu'une solution pratique est envisagé pour les zones de volume mal défini: interpreter ces densités intérmediaires comme des différentes épaisseurs à l'heure de fabriquer le prototype.

Les critères de pénalisation sont utilisés dans divers cas, toujours en offrant des architectures cohérentes avec leurs pénalités respectives, c'est-à-dire, renforcement isotropique, en angle d'impression, réponse méchanique (traction/compression) ou énergie de distortion (von Mises). Ces critères sont combinés pour intensifier ou atténuer ses effets, ce qui a des conséquences positives dans leur distribution de contrainte et déformation (plus homogène, en adoucissant les concentrations ponctuelles).

Le design le plus souhaitable sera déterminé par les besoins de l'ingénieur(e). Certaines conditions aux limites (hyperstatiques) sont trop restrictives pour que les critères puissent dévélopper leur véritable potentiel, ce qui doit être pris en compte à l'heure de concevoir la structure. En contrepartie, les critères proposés sont parfaitement juxtaposables avec l'approche probabiliste.

Enfin, le filtre conçu homogénéise aussi la déformation et la contrainte tout au long de la topologie, particulièrement dans les joints, qui constituent les points les plus critiques à fatigue et fracture. Les topologies obtenues au moyen du filtre sont plus simples: ellos ont moins barres mais mieux définies, à savoir une meilleure exploitation du volume limite imposé. Comme résultat de tout cela, les éléments structurels qui sont en effet lourdement chargés sont plus faciles à identifier et séparer des outres, ce qui rend leur potentielle amélioration plus simple (par ex., les élargir ou les remplacer localement).

Si ce filtre est appliqué de manière asymétrique, l'anisotropie obtenue peut être exploité pour la conception de métamatériaux. L'approximation logarithmique offre des topologies différentes qui sont, par contre, quasiment équivalents en termes de rigidité et volume. L'interpolation entre les courbes générées donne des structures intermédiaires qui retiennent notamment des particularités topologiques de toutes les courbes traversées, en fonction du nombre d'iterations parcourues dans chacune.

Si le filtrage est y inclus, un espace paramètrique de design avec trois dégrés de liberté est disponible pour concevoir des structures également rigides avec le même volume mais en présentant des différents épaisseurs minimes des barres. Toutes ces conclusions sont transposables à des structures en trois dimensions, comme il a été vérifié aux niveaux micro (cellule de métamatériau) et macro (prototype composé par des cellules). Des techniques ML peuvent accélerer l'optimisation.

Jumeaux numériques pour applications médicales

Le jumeau numérique créé est en fait capable de réproduire avec une fidélité suffisante (en considérant son faible coût de calcul) le fonctionnement d'un réseau de neurones biologiques dans une partie localisé du cerveau (en tant que connectome).

Il peut moduler le temps qui le signal prend pour traverser le système (latence entre entrées et sorties), ainsi que l'intensité et coordination des signaux d'arrivée (métastabilité). Â cet effet, la neuroplasticité et la migration neuronal localisée jouent des rôles principaux.

DISCUSSION

Ce chapitre commente le résultats obtenus auparavant par rapport à d'autres études similaires dans l'état de la technique, en valorisant leurs avantanges et limitations. En général, une bonne performance est observée au niveau de la fidélité des modèles (au moins comparable et des fois supérieur à l'état de la technique) ainsi que leur bas coût de calcul (gérable par un ordinateur personnel).

La généralisation des résultats doit par contre être jugée dans le context pertinent, car les domaines d'intérêt ont des différents échelles de mesure.

Description de structures

En considérant le faible coût de calcul, les résultats offerts sont comparables a des études similaires, en présentant une précision semblable mais dans des situations plus compliquées: structures non-périodiques ou lieu de périodiques, poutres au lieu de treillis épinglés, etc. et tout cela en utilisant des bases de données aussi grandes ou même un peu plus pétites.

Design et optimization de structures

Le design inverse de structures discrètes par front de Pareto est une réussite en comparaison avec des autres options plus élaborées (autoencoders, réseaux génératives), qui prennent beaucoup plus de puissance numérique. Par contre, les structures intelligents qui reproduisent une réponse méchanique doit être améliorée, vues les difficultés, ce qui représente un champ de recherche peu éxploré.

Les structures continues obtenues par optimisation topologique ont démontré à niveau simulation ses avantages par rapport à un design traditionnel (statique, deterministe, etc.). En fonction du but de ces architectures, les priorités seront différentes, les méthodologies introduites permettant beaucoup de choix avec un coût de calcul semblable ou inférieur à celui de l'état de la technique.

Ces techniques, unies au filtre et l'interpolation proposée, offrent une variabilité énorme, surtout envisageant la conception des métamáteriaux, qui profitent de l'anisotropie et les designs complexes pour offrir ces propriétés particulières.

Jumeaux numériques pour applications médicales

Le jumeau proposé caractérise bien la transmission des signaux à travers le cerveau au moyen des simulations abordables numériquement. Si bien l'échelle est limitée en nombre et types de neurones et régions du connectome, il est raisonnable de considérer ces études préliminaires pour la réproduction de phenomènes biologiques, y compris les maladies, en tant qu'elles dérangent la propagation normale de ces signaux.

Notamment, la combinaison des traits mathématiques (portes logiques, structure en graphes) et biologiques (neuroplasticité, migration) parvient à résoudre (au moins, partiellement) des problèmes complexes comme celui du chemin plus court ou plus long, en racourcissant les routes nécessaires pour s'adapter a la réponse désirée. Cela pourrait être encore renforcé en introduisant des règles et paramètres mathématiques plus explicites.

CONCLUSIONS

Ce chapitre contient une récapitulation des leçons tirées de ces travails qui conforment ce manuscrit de thèse, de façon générale et puis particularisées pour chaque bloc thématique. Aussi, des suggestions de recherche pour le futur sont présentées.

Globalement, il a été démontré que les modèles substitutifs sont arrivés au monde de l'ingénierie pour rester, dès qu'ils permettent d'obtenir des simulations plus rapides et moins chers sur des données déjà obtenues.

Plus précisement, les techniques d'apprentissage automatique accélèrent encore plus l'obtention de résultats en supprimant le besoin d'expressions analytiques. Les graphes, d'autre part, aident à exprimer de façon plus directe et intuitive l'évolution de l'état des parties d'un système et ses interrelations.

Description de structures

Des méthodologies efficaces ont été dévéloppées pour prédire le comportement méchanique d'une structure composée des éléments discrets (poutres, barres épinglés, cellules Kelvin-Voigt), soit des propriétés équivalents (module de Young) ou l'évolution de leur réponse dynamique, même en conditions d'observabilité partielle. Ces outils pourraient être appliqués aussi à des autres cas de non-linéarité communs en métamatériaux (plasticité, auxeticité, etc.) ainsi qu'aux milieux continues (par exemple, structures spinoïdales ou gyroïdes).

Design et optimization de structures

La conception des structures qui présentent des propriétés souhaitées a été profondément explorée dans cette section. Alors que l'obtention des structures discrètes - à poutres ou barres - est rapide en cherchant dans une base de données déjà générée (front de Pareto), la solution pour obtenir des réponses méchaniques plus complexes directement est difficile et, pourtant, des techniques plus élaborées doivent être appliquées.

Pour les milieux continus, l'optimisation topologique a été élargie pour inclure des aspects liés à la reponse méchanique du matériau de base (fabrication, limite élastique, etc.) et aussi à des états de force mal définis (incertitude statistique).

De plus, une interpolation topologique assisté par une stratégie de filtrage est proposée pour créer un espace de design à trois dégrés de liberté: volume, rigidité et épaisseur minimale. Il serait intéressant de profiter de ces dévéloppements pour concevoir des métamáteriaux en deux et trois dimensions dont leur caractéristiques méchaniques sont déjà incluses dans la stratégie d'optimisation, soit comme contraintes ou cibles.

Jumeaux numériques pour applications médicales

Vu le grand besoin de modèles rapides et pas chers dans la domaine de la santé humaine, le jumeau digital offre, bien que limité dans sa représentativité, est capable de réproduire, en gros, la transmission des signales synaptiques de manière suffisament efficace. Ceci est très utile en situations où l'absence des moyens nécessaires (appareils de résonnance magnétique, etc.) rend difficile l'évaluation des lesions cérébrales, qui doivent être rapidement détectées et résolues.

Afin de mieux profiter de cet outil, il faudrait y ajouter des autres composants qui jouent un rôle dans le fonctionnement normal et malade du cerveau: cellules gliales, biochimie, tumeurs et modèles constitutifs méchaniques.

Contents

List of Tables

List of Figures

INTRODUCTION

In this initial chapter, context for this thesis and its motivation will be provided, alongside a succinct recap on the concepts of metamaterial, model order reduction and artificial intelligence.

Contenu

0.1 Context and Motivation

This first introductory section provides context for the fields of research concerning this doctoral work.

0.1.1 Data-Driven Models: Analytical and Surrogates

Modeling systems from data has been the usual procedure for centuries in technical sciences. Physicists, chemists, engineers and other scientists have used data (which may need to be sifted before, in order to avoid outliers, noise, etc.) to find correlations between variables, and to build models based on analytical expressions. Such a method entails several challenges, among which the most relevant two are going to be discussed.

Firstly, the model maker must carefully choose the variables by which to describe the model and its evolution. They must, of course, be measurable (be it directly or indirectly), so one can obtain the data needed to construct and test the upcoming model. They should preferably be related to physical concepts and magnitudes, that is, they should "make sense" from the physical point of view (which may not be the case in some reduced models).

That does not mean they must be immediately identifiable with those of an analytical model, but they ought to be linked to the physical process somehow. The chosen variables should not be too many either, or else the resulting model will be convoluted, and thus, costly in a computational and practical - even economic - sense; hence falling into the "curse of dimensionality".

Secondly, the accessibility of data plays an important role in the design of a model. It could happen that only part of the targeted system is accessible to perform measurements, or even known at all. In most cases, that means the inaccessible (non-observable) part of the system has an influence on its global behavior, thus shaping its describing model. How to include that information is not a straight-forward issue, for often times there is not enough data to work with. Not only is the experimental validation missing, but the variables needed to capture that behavior are also unknown.

Even if one wanted to build a model without taking that undisclosed part into account, relying only on the chosen, observable variables and trying to ignore the unknown ones, it could still be incomplete or outright incorrect because the former could be affected by the latter. Fortunately, there are multiple workarounds to overcome these issues, many of them involving data-augmentation [5, 6] and model order reduction techniques [7, 8].

In simulation-based engineering (SBE), constant monitoring and quick responses are vital to increase their service lives (preventive maintenance). One increasingly popular solution for that is the so-called Digital Twin [9, 10, 11], aiming to (re)create a virtual (simulated) system yielding the same outputs as the real one if given the same inputs. Such simulations usually rely purely on data, but they can be enriched through Physics (Hybrid Twins) [12].

However, they can prove limited in real-time applications. Model order reduction can help in simplifying the model and making it more responsive [7, 13, 14]. One must also bear in mind that, even when using the most accurate and fast methods available, uncertainty (i.e. in measurements) and undetected defects can still steer the results away from our target data (ground truth), be it experimental or simulated.

Machine Learning (Artificial Intelligence allowing computers to learn from data without explicit programming) can help alleviate the aforementioned limitations, providing accurate regressions from data (either empirical or synthetic) and thus permitting output collection in quasi real-time. Depending on the nature of the target data, different flavours of neural network could be used: convolutional [15] for images and text, graph-based [16] for graphs or recurrent [17, 18] for time series, which can be reinforced by Long Short-Term Memory cells [19] to account for history-dependent phenomena.

Graphs are a particularly suitable framework to depict large amount of data values and their associated interactions. A graph $\mathcal{G}$ is a mathematical object - more precisely, a set - consisting of vertices $\mathcal{V}$ and edges $\mathcal{E}$, which are fit to represent data points and the relationships between them. This poses interesting applications to many fields, namely any problem involving circuits of any kind: electrical, organic (blood-flow), electronic (the Internet), etc.

Such potential is being explored by Geometric Deep Learning [20]. This thesis will study its implications in two different fields easily translatable into graphs: mechanical structures (focusing on architected materials) and biomedical circuits (with the human brain as a paradigmatic example).

0.1.2 Field of Study I: Architected Structures - Metamaterials

Architected materials or metamaterials (from "*meta*", Greek for "beyond") are tailored micro-structures whose layout is designed to display certain macroscopic properties unseen in continua, such as left-handedness (negative refracting index) [21] or auxeticity (zero/negative Poisson's coefficient) [22].

This is done by periodical repetition of a unit cell, whose geometry is parameterized – although disordered architectures are also being considered [23, 24] for their interesting applications (e.g. localizing material failure). Conceived decades ago, the quick development of additive manufacturing techniques (namely, precision-wise) has rendered their manufacturing feasible only in the last two decades [25, 26]. Instead of depending on a given bulk material's (or alloy's) constituents, each suffering from their own imperfections (present in the raw material or induced by manufacturing: porosity, inclusions, etc.); this yields a much more flexible design space with a myriad of possible properties.

There are four main types of metamaterials according to their properties: mechanical (e.g. auxetic), electromagnetic (e.g. cloaks), acoustic (e.g. absorbers) or thermal (e.g. flux controllers) [27]. Focusing on mechanical metamaterials, they offer a lightweight alternative to bulk materials, for which a similar stiffness can be obtained with a fraction of their volume (as predefined topology optimization [28, 29]).

Since their properties depend on the building cells' geometries, the latter can be adjusted to yield functionally graded performances depending on the needs of the prototype for each section or volume, unlike a continuous medium. While Functionally Graded Materials (FGMs) [30, 31] have existed since the advent of composites – mainly fulfilling anisotropic mechanical constraints –, the tuneability of metamaterials proves more adequate for multi-scale considerations [32].

However, this flexibility comes at a price: due to their discrete geometry, composed of truss/beam elements known as "struts", non-linear phenomena (hyperelasticity, buckling, etc.) are to be expected, even if the base material is assumed linear elastic. There are multiple well-known analytical models for each of these eventualities for continuous media (e.g. Ogden's hyperelastic model, Euler's buckling formula for columns, etc.), but this is often not the case for truss-like discrete architectures as a whole – metamaterials, in a nutshell –.

Homogenization techniques have proven useful when tackling composites and periodic structures in general [33, 34], although they pose other challenges, such as high sensibility to phase contrast (infinite when comparing material and void) and the practical application of scale separation on micro- and macro-models (the choice of characteristic lengths could prove problematic) [35].

For all these reasons, on top of the computational expenses associated with the mentioned approaches – great, considering all degrees of freedom –, there is a dire need for surrogate models capable of capturing such complex mechanical behavior while bypassing the need for explicit analytical expressions.

0.1.3 Field of Study II: Biomedical Applications - The Brain

The brain acts as an animal's central computer: it generates knowledge by gathering information obtained through the senses (as a result of stimuli) and associative processes allowing it to act upon the host's environment. Furthermore, it regulates biological constants essential for life, like breathing, body temperature and heartbeat, as well as some other complex processes such as emotions and conscience. It is the most energy-consuming organ in relation to its size (20% of total in a resting state), despite undergoing evolutionary optimization in different animal species [36].

According to the World Health organization (WHO), two out of ten principal causes of death globally in 2019 were directly related to brain malfunction: strokes (also called cerebrovascular accidents, CVA) and dementia (including Huntington's chorea, Parkinson's, Alzheimer's, and Lewy's bodies) [37]. Cancer is another prominent source of mortality worldwide.

In fact, brain tumors, despite not being the most common ones (around one in fifty diagnoses [38]), are among the most fatal (one in three patients have a five-year survival rate on average in the US, around 5% for the most aggressive types, such as glioblastoma [39]) and they are alarmingly prevalent in children under 14 (about one-sixth of total cases as of 2019, second only to leukaemia [40]).

Neurological illnesses (including tumor-driven) are the leading worldwide cause of crippling disability, whose incidence is increasing, especially affecting ever-aging populations in the developed world [41]. In Psychiatry, the freshly emerged field of Pathoconnectomics explores the links between brain wiring degeneration [42] and disorders like depression [43], schizophrenia or autism [44]; e.g. the relation between cerebral small vessel disease (CSVD) [45] and cognitive impairment causing Alzheimer's [46].

Neurological disorders are very costly not only at a personal level (suffering by the patient and their relatives) but also on an economical one, dealing in billions of euros per year in developed countries where diagnoses are more prevalent [47, 48, 49, 50]. Poor health systems in developing countries make diagnoses and treatment more challenging [51, 52, 41] - which poses an inequality issue.

Although data is relatively abundant, it might not be representative enough [53, 54, 55]. In order to paint a broader picture of the current situation, new data managing approaches have become widespread, such as Data Mining [56, 57, 58] and Machine Learning [59, 60] in general - especially Graph Neural Networks [61, 62, 63, 64, 65, 66, 67].

Overall, it is self-evident that the study and characterization of the brain is a dire need not only for scientific purposes but also, and most importantly, for health reasons, such as the study and treatment of related pathologies for an early and accurate diagnosis and thus a effective treatment. Computational Neuroscience, i.e. modeling the brain's function via computers, could bridge the gap between the plethora of unconnected partial data available on the brain by providing a comprehensive *in silico* mock-up (Digital Twin [10]). However, that goal requires multiple challenges to be overcome [68].

Some of these problems come from "traditional" experimental neuroscience (availability of representative data, multi-field, multi-scalar aspects, general complexity, accurate diagnosis), while others have become apparent when trying to manage the obtained data (computational costs, compiling and memory, organization and classification, limiting mathematical approaches, lack of unified theoretical framework to analyze and compare, brain-environment interactions). Should these issues be successfully addressed, a powerful simulation tool for simulating healthy and ill brains would be available.

Thus, the diagnosis and treatment of any condition would be at the doctor's disposal, minimizing difficult, dangerous, and costly *in vivo* interventions. Additionally, as Neuroscience develops as a scientific field, its findings can be incorporated into computational tools (both hardware and software), which may in turn further ease the problem, since the brain remains the most powerful and efficient computer known to man [69].

0.2 Objectives

The objectives of the present thesis are dictated by the **XS-Meta project** "*Cross-scale concurrent material-structure design using functionally-graded 3D-printed metamaterials*" (H2020 MSCA 956401). The author's shared tasks as ERS6 within the global project objectives consist in providing assistance in the development of:

- Models to accurately predict experimental behavior of additively manufactured metamaterials.
- Efficient frameworks for metamaterial inverse design on a micro (cell) and macro level (prototype).
- Algorithms for progressive tuning of the matematerial's geometrical (and thus, mechanical) properties.
- Surrogate, continuous macro-models capturing mechanical behavior of a given set of metamaterial families from experimental and/or simulated data.

- Machine Learning procedures to identify internal and/or fictitious variables from experimental data at a cell level (micro).
- Model Order Reduction algorithms for the dimensionally efficient parametrization of the produced constitutive models.
- Manufactured proofs of concept (prototypes) to be tested experimentally.

These objectives, although ambitious, have been met to satisfying degrees, considering the relatively short contract time (3 years) and the total duration of the project (4 years). Despite the heavy material focus of such objectives, some conceptual similarities between metamaterial lattices and biological neural networks have lead to multi-function approaches and codes serving both industrial and biomedical purposes.

0.3 Content

Obeying UPM's new thesis writing rules, this manuscript has been structured in the fashion of a full, global research article, featuring the following sections:

1. **Introduction**. Short context for the presented work, including motivation, objectives, organization of contents and scientific contributions.
2. **State of the art**. A collection of previous techniques and advancements regarding structural description and design and biomedical modeling.
3. **Methodology**. Presentation and justification of the chosen methods to tackle the aforementioned objectives, highlighting the new perspectives and approaches in utilizing them, as well as fully novel proposals.
4. **Results**. Compilation of case studies applying the methodology to the main topics of this work: structural description and design for metamaterials and biomedical mock-ups.
5. **Discussion**. Assessment of the obtained results with respect to the main objectives and in comparison with similar state-of-the-art studies, weighing their improvements and shortcomings and proposing alternatives to overcome the latter.
6. **Conclussions**. A collection of global learned lessons and future research opportunities is disclosed, with particular comment for each topic: structural description and design and biomedical models.

On top of this main structure, the usual additional non-thematic sections can be found in this manuscript, namely:

- **Résumé** in French, **Abstract** in English and **Resumen** in Spanish, providing a short summary of the works contained in this manuscript.
- **Résumé Étendu** in French, containing a substantial synopsis of the presented doctoral thesis, comprising about 10% of the text written in English - as required by the SMI Doctoral School.
- **Bibliography** in citation order.

0.4 Scientific Contributions

This section contains a list of events of outreach and dissemination of scientific results during the PhD thesis, including articles (published in journal and archives), conferences, workshops, congress proceedings and talks.

0.4.1 Publications in Peer-Reviewed Journals

1. V. Champaney, V. J. Amores, S. Garois, **L. Irastorza-Valera**, C. Ghnatios, F. J. Montáns, E. Cueto, F. Chinesta. *Modeling systems from partial observations*. Frontiers in Materials (JCR Q2), vol. 9, 2022. Published 17^{th} October 2022, DOI: 10.3389/fmats.2022.970970
2. **L. Irastorza-Valera**, J. M. Benítez, F. J. Montáns, L. Saucedo-Mora. *An Agent-Based Model to Reproduce the Boolean Logic behavior of Neuronal Self-organized Communities through Pulse Delay Modulation and Generation of Logic Gates*. Biomimetics (JCR Q2), vol. 9, no. 2, p. 101, 2024. Published 9^{th} February 2024, DOI: 10.3390/biomimetics9020101
3. I. Ben-Yelun, **L. Irastorza-Valera**, L. Saucedo-Mora, F. J. Montáns, F. Chinesta. *On the data-driven description of lattice materials mechanics*. Results in Engineering (JCR Q1), vol. 22, p. 102235. Published 9^{th} May 2024, DOI: 10.1016/j.rineng.2024.102235
4. **L. Irastorza-Valera**, J. M. Benítez, F. J. Montáns, L. Saucedo-Mora. *Review of the Brain's behavior after Injury and Disease for Its Application in an Agent-Based Model (ABM)*. Biomimetics (JCR Q2), vol. 9, no. 6, p. 362, 2024. Published 14^{th} June 2024, DOI: 10.3390/biomimetics9060362

0.4.2 Congress Proceedings

1. **L. Irastorza-Valera**, L. Saucedo-Mora, F. Chinesta, F.J. Montans Leal, *Damage-Based Criteria for the Combination of Offset Probabilistic Temporal Loads in Topological Optimization Designs*, in P. Iványi, J. Kruis, B.H.V. Topping, (Editors), Proceedings of the Fifteenth International Conference on Computational Structures Technology, Civil-Comp Press, Edinburgh, UK, Online volume: CCC 9, Paper 2.2, 2024. Online since 9^{th} September 2024, DOI: 10.4203/ccc.9.2.2

0.4.3 International Congresses

1. *Forecasting Heat Diffusion on Lattices through Graph Neural Networks*. Seminar on Hybrid Twins in Advanced Engineering, 6-7 October 2022, CNRS@CREATE, Singapore
2. *Modeling Systems from Partial Observations*. IUTAM International Congress on Data-Driven Mechanics and Surrogate Modeling, 25-28 October 2022, ENSAM, Paris, France
3. *Topological Classification and Optimization of Randomized Metamaterial Architectures*. COMPLAS23 (IACM): XVII International Conference on Computational Plasticity, 5-7 September 2023, UPC, Barcelona, Spain
4. *An Agent-based Model (ABM) to Reproduce the Boolean Logic behavior of Neuronal Self-organized Communities through Pulse Delay Modulation and Generation of Logic Gates*. ECCOMAS24 (IACM): 9th European Congress on Computational Methods in Applied Sciences and Engineering, 3-7 June 2024, Palácio de Congressos, Lisbon, Portugal
5. *Damage-Based Criteria for the Combination of Offset Probabilistic Temporal Loads in Topological Optimization Designs*. CST24: 15th International Conference on Computational Structures Technology, 4-6 September 2024, CTU, Prague, Czech Republic

0.4.4 Other Certified Talks

1. *Metamateriales: de lo pequeño, algo grande* (in Spanish), 29^{th} January 2024, Colegio de España, Paris, France. ANECA certificate available.

0.4.5 Articles Pending Publication

1. **L. Irastorza-Valera**, J.M. Benítez, F.J. Montáns, L. Saucedo-Mora. *Numerical reproduction of the Sherrington-Adrian observations through a community of McCulloch-Pitts neurons with plastic remodeling*. bioRxiv, online since 7^{th} December 2023, DOI: 10.1101/2023.12.05.570084
2. **L. Irastorza-Valera**, L. Saucedo-Mora. *Probabilistic combination of loads in topology optimization designs via cumulative damage criteria*. arXiv, online since 25^{th} March 2025, DOI: 10.48550/arXiv.2503.19807
3. **L. Irastorza-Valera**, J. Montoya Adarraga, L. Saucedo-Mora. *Mechanostat-type effective density correction for the Carter-Hayes growth applied to topology optimization and its efficient interpolation*. ArXiv, online since 27^{th} March 2025, DOI: 10.48550/arXiv.2503.21456
4. L. Saucedo-Mora, **L. Irastorza-Valera**. *General form of the Gauss-Seidel method to linearly approximate the Moore-Penrose pseudo-inverse in random non-square systems and high-order tensors*. ArXiv, online since 28^{th} March 2025, DOI: 10.48550/arXiv.2503.22273
5. Krishnaraj Vilasraj Bhat, Ignacio Martínez Teres, Juan García-Martínez, Sergio Ulargui de Diego, Juan Carlos Catalinas Berlinches, María García-Martínez, Helena Sanz González, **Luis Irastorza-Valera**, Luis Saucedo-Mora. *New experimental design for local Mode I toughness measurement in 3D-printed samples.* Preprints

Chapter 1

STATE OF THE ART

This chapter compiles a short summary on the current trends and methods used in surrogate modeling and the two main research lines followed in this manuscript: architected materials and biomedical modeling.

Contenu

1.1 Surrogate modeling

Traditionally, modeling any physical system has yielded a subjacent theoretical framework to explain the phenomena showcased in such system. Following the scientific method, the beholder would make empirical observations to either prove previous hypotheses, reformulate them or discard them. The scientist would take annotations of qualitative and mainly quantitative measures, conveyed by variables yielding values within user-defined scales for any relevant system property. This methodology was useful for centuries and many vital scientific discoveries have been made this way. However, it poses several challenges and suffers from important epistemological flaws.

Firstly, experimental testing is an important source of uncertainty for the model. Drom the nature of the observed phenomena themselves (e.g. a defective prototype) to the accuracy of the instrumentation or the observer's interaction with the testing environment, many unforeseen alterations may affect the results. Hence the need for a big dataset and multiple experiments, to account for enough variability and try to mitigate such effects. Of course, this data is costly to produce (*offline phase*), and it does not even guarantee trustworthy results, thus the craving for accurate simulations and system mock-ups (*online phase*).

Secondly, the modeler's point of view influences the model since variables describing the theoretical framework are defined by them. On the one hand, if they choose too few, the system's complexity may not be fully captured by the model, and so it would yield wrong results. On the other hand, should the modelers designate too many variables, the model could become too cumbersome to be practically used or even totally unfeasible (e.g. unmeasurable variables), falling into the so-called "curse of dimensionality". Either way, the modelers could be missing important factors not represented by any defined variable (internal/hidden variables). The theoretical framework used to tackle the system could be too complex and/or induce bias on the observations.

These complications deepen when considering some commonly found traits in metamaterials, such as multi-scalar (local instabilities) and non-linear behaviors (e.g. plasticity). The resulting model's complexity is often unmanageable, both in practical (complicated testing) and in computational terms (long, demanding simulations). Regarding metamaterial design, it is very likely that more than one architecture yields the same desired property (surjection), so fully analytical models are limited.

When creating substitution models – surrogates – on partial observations, especial attention must be paid to their size (needed data), accuracy (closeness to "reality") and computational complexity (determining computing time) [70]. Some remarkable applications of such surrogates are system monitoring – often requiring (quasi) real-time responses – and optimization problems – needing many results – which heavy numerical simulations (e.g. Finite Elements) cannot efficiently (cheaply) provide [71]. The proposed solutions for such issues involve mathematical techniques (Algebra, Statistics, Information Theory, Graph Theory), perhaps inspired by biological aspects (Agent-Based modeling, Genetic Algorithms).

1.1.1 Model Order Reduction

Model order reduction (MOR) approaches strive for a reconstruction of a given original "full complexity" model, otherwise practically and computationally intractable, into a "reduced" version of it defined by a smaller set of variables representative enough to convey the overall behavior of the system within reasonable computational needs, while retaining an acceptable resolution (precision). Some of the most common techniques will be succinctly described in the present section.

1.1.1.1 Proper Orthogonal Decomposition

The POD (Proper Orthogonal Decomposition) [72, 71] rebuilds a lower-resolution version – and thus, easier to solve – of the original model on basis vectors extracted from a chosen set of snapshots representative of the system's dynamics. Given a full system model of the form

$$E(\mu)\frac{d\mathbf{u}}{dt} + A(\mu)\mathbf{u} = f(\mu, \mathbf{u}) \tag{1.1}$$

where $\mathbf{u} \in \mathcal{R}^n$ is a state vector, $\mu \in \mathcal{R}^p$ a parameter vector and $E(\mu), A(\mu) \in \mathcal{R}^{nxn}$ and $f(\mu, \mathbf{u})$ its operators; a vector $y \in \mathcal{R}^q$ is defined to map quantities of interest through an operator $h(\mu, \mathbf{u})$.

A matrix $\mathbf{U} \in \mathcal{R}^{nxn_s}$ containing n_s snapshots (state solutions for carefully chosen time instants and/or parameter combinations) as its columns can be processed through Singular Value Decomposition (SVD) to yield

$$\mathbf{U} = \mathbf{L}\mathbf{\Sigma}\mathbf{R}^T \tag{1.2}$$

in which $\mathbf{L}, \mathbf{R} \in \mathcal{R}^{nxn_s}$ are $\mathbf{U}$'s left and right singular vectors, respectively; and $\mathbf{\Sigma} \in \mathcal{R}^{n_s xn_s}$ is $\mathbf{U}$'s diagonal matrix containing its singular values in descending order.

The POD basis $\mathbf{V} \in \mathcal{R}^{n_s xr}$ is defined by the first r columns of $\mathbf{U}$ corresponding to the greatest singular values, thus generating an orthonormal basis (POD modes), which may take the form of deterministic spatial functions [73] - see Equation 1.4. $\mathbf{V}$ is guaranteed to minimize the least-squares error of snapshot reconstruction

$$\min_{\mathbf{V}\in\mathcal{R}^{n_s xr}} ||\mathbf{U} - \mathbf{V}\mathbf{V}^T\mathbf{U}||_F^2 = \min_{\mathbf{V}\in\mathcal{R}^{n_s xr}} \sum_{i=1}^{n_s} ||\mathbf{u_i} - \mathbf{V}\mathbf{V}^T\mathbf{U}||_2^2 = \sum_{i=r+1}^{n_s} \sigma_i^2 \tag{1.3}$$

i.e. the sum of the squares of all discarded singular values. After a computationally expensive snapshot generation with the original full model (*offline phase*), the latter can be projected onto the reduced POD basis: $\mathbf{u} \approx \mathbf{V}\mathbf{u_r}$, where $\mathbf{u_r} \in \mathcal{R}^r$ is the reduced state vector constituted by the resulting modal coefficients. Since this is still an approximation, the former expression yields a residual, whose orthogonality with respect to the basis can be enforced via Galerkin projection. The last step (*online phase*) would be to efficiently capture parametric dependence or non-linearity (e.g. through interpolation) [71].

Importantly, the POD basis makes no assumptions about the full model, since it is entirely built on some of its sampled state solutions, making this method suitable for both linear and non-linear applications. For transient problems, the approximated POD solution takes the form

$$\mathbf{u}(x,t) = \sum_{i=1}^{R} b_i(t)\Phi_i(x) \tag{1.4}$$

which is clearly separated into time-dependent $b_i(t)$ and space-dependent coefficients $\Phi_i(x)$ up to a certain level of complexity, determined by the basis's size [71, 73]. On top of that, the choice of such basis entails an inconvenient trial-and-error iteration if the appropriate basis is not found at once, which can only be checked *a posteriori*.

1.1.1.2 Proper Generalized Decomposition

In order to alleviate POD's shortcomings, Proper Generalized Decomposition (PGD) [7, 8] enables the construction of the approximation basis as the problem is being solved, so that each problem's solution is expressed in its own associated basis. The modeler decides how many approximation terms to consider according to the desired accuracy.

Unlike POD, PGD is not restricted to a predefined reduced basis, considering a general space-time separation through space $\mathbf{X_i}(x)$ and time functions $\mathbf{T_i}(t)$ instead:

$$\mathbf{u}(x,t) \approx \sum_{i=1}^{N} \mathbf{X_i}(x) \cdot \mathbf{T_i}(t) \tag{1.5}$$

similarly to the typical basis of shape functions $\mathbf{N_i}(x)$ in the Finite Elements Method (FEM). By doing this, PGD allows to express a solution as a finite sum of lower dimensional functions. For any given parametric problem $\mathbf{u}(x,t,p_1,..,p_M)$, Equation 1.5 takes the general form

$$\mathbf{u}(\mathbf{x},t,p_1,..,p_M) \approx \sum_{i=1}^{N} \mathbf{X_i}(\mathbf{x}) \cdot \mathbf{T_i}(t) \cdot \prod_{k=1}^{M} \mathcal{P}_i^k(p_k) \tag{1.6}$$

where $\mathcal{P}_i$ represents the parametric functions with parameters $p_k, 1 < k < M$.

Starting from an initial temporal guess $\mathbf{T}_n^0(t)$, spatial functions $\mathbf{X}_n^p(t)$ in Equation 1.5 are obtained from the preceding temporal ones $\mathbf{T}_n^{p-1}(t)$ until the change between iterations meets a user-defined tolerance ε. For step n:

$$\mathbf{u}_n^p(x,t) = \sum_{i=1}^{n-1} \mathbf{X_i}(x) \cdot \mathbf{T_i}(t) + \mathbf{X}_n^p(x) \cdot \mathbf{T}_n^p(t) \tag{1.7}$$

$$||\mathbf{X}_n^p(x) \cdot \mathbf{T}_n^p(t) - \mathbf{X}_n^{p-1}(x) \cdot \mathbf{T}_n^{p-1}(t)|| < \varepsilon \tag{1.8}$$

so that the enrichment process is finished when the global error is sufficiently low, $\epsilon(n) < \tilde{\varepsilon}$.

Remarkably, PGD admits spatial separation. Being Ω the problem's spatial (3-dimensional) domain and assuming it can be redefined as Ω_x x Ω_y x Ω_z (hexahedral elements) or Ω_{xy} x Ω_z (plates), Equation 1.5 can be rewritten as

$$\mathbf{u}(x,y,z,t) \approx \sum_{i=1}^{N} \mathbf{X_i}(x) \cdot \mathbf{Y_i}(y) \cdot \mathbf{Z_i}(z) \cdot \mathbf{T_i}(t) \tag{1.9}$$

or

$$\mathbf{u}(\mathbf{x},t) \approx \sum_{i=1}^{N} \mathbf{X_i}(\mathbf{x}) \cdot \mathbf{Z_i}(z) \cdot \mathbf{T_i}(t) \tag{1.10}$$

alternatively, where $\mathbf{x} = (x,y)$. This way, each spatial function can be obtained by solving its equivalent 1D (or 2D, for $\mathbf{x}$) boundary value problem (BVP) for their spatial domains and another 1D initial value problem (IVP) in Ω_t for . Full spatial separation implies notable computational savings since the problem's complexity now depends on the selected 1D meshes for each direction [71].

1.1.1.3 Manifold Learning

Manifold learning, i.e. non-linear dimensionality reduction, projects multidimensional data onto lower dimension latent manifolds in the hopes of rendering them more easily interpretable to the modeler, while retaining their most defining features.

Principal Component Analysis (PCA) [74, 75] reduces the dataset's dimension by finding uncorrelated linear functions (principal components, PC) which repeatedly maximize variance to keep statistical variability, by solving the following eigenvalue problem

$$\mathbf{Sa} = \lambda \mathbf{a} \tag{1.11}$$

where $\mathbf{S} \in \mathcal{R}^{pxp}$ is the covariance matrix of $\mathbf{X} \in \mathcal{R}^{nxp}$ containing p n-dimensional data vectors, $\mathbf{a} \in \mathcal{R}^{p}$ is each of its eigenvectors (PC loadings) and λ their corresponding eigenvalues – that is, the variance of the principal components $\mathbf{Xa}$, made of PC scores for each eigenvector $\mathbf{a_k}$. The modeler's focus is on the first (i.e. biggest) eigenvalues conveying the greatest possible variance. A standard quality measurement for a PC is the proportion of total variance it accounts for, given by [76]

$$\pi_j = \frac{\lambda_j}{\sum_{j=1}^{p} \lambda_j} = \frac{\lambda_j}{tr(\mathbf{S})} \tag{1.12}$$

Usually, PCA is performed on the column-centered data matrix X*, so that $x^*_{ij} = x_{ij} - \hat{x_j}$. This way,

$$(n-1)\mathbf{S} = \mathbf{X^*}^T \mathbf{X^*} \tag{1.13}$$

holds true. Applying SVD (Equation 1.2) to $\mathbf{X^*}$ and assuming $\mathbf{L}, \mathbf{R}$ are orthonormal, Equation 1.13 turns into

$$(n-1)\mathbf{S} = (\mathbf{L\Sigma R}^T)^T \mathbf{L\Sigma R}^T = \mathbf{R\Sigma L}^T \mathbf{L\Sigma R}^T = \mathbf{R\Sigma}^2 \mathbf{R}^T \tag{1.14}$$

yielding the spectral (eigen-) decomposition of $(n-1)\mathbf{S}$ whose eigenvalues are contained in Σ^2. A variant called kPCA involves the use of integral operator kernel functions (e.g. Gaussian) to account for non-linear mappings [77, 78].

Locally Linear Embeddings (LLE) [79] transform high-dimensional non-linear inputs into low-dimensional, neighborhood-preserving embeddings for linear approximations along a single global coordinate system through locally linear fits, unlike PCA or multidimensional scaling (MDS) linking faraway points.

To this aim, each data point x_i is assigned a set of neighbors (e.g. via the k-NN algorithm [80]). The weights w_{ij} which reconstruct x_i best are computed through a common linear least-squares scheme

$$\varepsilon(\mathbf{w}) = \sum_{i=1}^{n} |x_i - \sum_{j=1}^{k} w_{ij} x_j| \tag{1.15}$$

Minimizing error $\varepsilon(\mathbf{w})$, the low-dimensional embedding vectors y_i minimize in turn the cost function

$$\mathbf{\Phi}(\mathbf{y}) = \sum_{i=1}^{n} |y_i - \sum_{j=1}^{k} w_{ij} y_j| \tag{1.16}$$

where weights w_{ij} have been obtained in the previous step. This simple method relies exclusively on geometric intuition and basic algorithms, without computing local minima. A broader collection of manifold learning techniques is unfolded in [81]. Notably, they allow for computational modeling of inelastic behaviors [82], commonly found in metamaterials.

1.1.2 Machine Learning

Model order reduction techniques are especially useful to diminish such complexity. Even so, computation of such reduced models can remain costly and so, the last resort is to get rid of any analytical model altogether and rely only on fully data-driven predictions (e.g. Machine Learning), leveraging the abundance of data nowadays [83].

Machine Learning (ML) is a subset of Artificial Intelligence (AI) focused on how to make a programmable machine "learn" the behavior of a system only through data, bypassing the need for – and limitations of – any analytical assumption about the model. It can be supervised if predicting upon labeled data (e.g. linear regression and classification), unsupervised if data is unlabeled (e.g. autoencoders) or reinforced if it "rewards" the machine when it predicts correctly (e.g. robots). A common goal is extracting the model relating measured inputs to their corresponding outputs [84, 85]. In general, the measured outputs depend on the whole internal state.

In physics-based structural mechanics, the system's internal response is obtained by discretization of the continuum mechanics model. From this internal state, the output of interest is directly extracted at each time instant. Alternatively, Machine Learning looks for the direct relation between observables, the input action and the measured response that can depend on the present and past values of a series of non observed internal variables [86].

1.1.2.1 Multilayer Perceptron

Often times, ML comes in the form of artificial neural networks (ANN), based upon the McCulloch-Pitts neuron model, i.e. the "perceptron" [87]. It was the first mathematical model of signal processing in a biological neuron [87], capable of a similar behavior. The output neuron is connected to a number of pre-synaptic (input) neurons, each with a different activation potential. If the average summed potential received from those neurons is higher than a given threshold, the next neuronal layer will fire too. Alas, this only produces binary outputs (fire or not-fire), so most ANNs include variable synaptic weights and more elaborate firing rules.

With the rise of Deep Learning (DL) [88], this idea evolved into MultiLayer Perceptrons (MLP) after the incorporation of hidden layers h_i between inputs $\mathbf{x_i}$ and outputs $\mathbf{y_i}$, transforming them:

$$\mathbf{y}_i^n = \mathbf{z}^n(\mathbf{h}_i^n) = \mathbf{z}^n(\sum_{j=1}^{k_n} w_{ij}^n \mathbf{y}_j^{n-1} + b_j^n), ... \mathbf{y}_i^1 = \mathbf{z}^1(\sum_{j=1}^{k_0} w_{ij}^0 \mathbf{x}_j^0 + b_j^0) \tag{1.17}$$

where superscripts indicate layer number, subscripts neuron number within that layer (out of k_n in total), w_{ij}, b_j synaptic weights and biases respectively and $\mathbf{z}^n(h)$ an activation function for that layer (tanh, sigmoid, etc.) assigning a normalized interval to the hidden output h_i. After an initial forward-propagation of inputs to outputs (with predefined w_{ij}, b_j), a loss (or cost) function $\mathbf{E}(\mathbf{y_{pred}}, \mathbf{y_{real}})$ (e.g. mean-squared error (MSE)) is computed to evaluate the prediction's accuracy. If layers are multiple and fully connected, MLPs can also be called Dense Neural Networks (DNN).

In subsequent steps, backpropagation schemes [89] – based on the chain derivative rule and gradient descent – are performed to iteratively correct weights and biases until the desired tolerance between targets and outputs is reached. After training with known labels comes testing with unseen ones. The universal approximation theorem [90] proves that any sufficiently complex multilayer feed-forward ANN can replicate any Borel-measurable functions to any sought accuracy. Cost minimization is perform through various forms of gradient descent (e.g. stochastic - SGD [91]), some of them incorporating momentum into their own tailored optimizers, such as adam ©[92].

This methodology may seem computationally costly, especially in the *offline phase* (generation of ground truth data) for a large amount of user-defined inputs. However, the fast increase in processing power during the last decades has greatly eased the analysis of very extensive datasets, and so various ANN architectures have been designed for specific applications.

1.1.2.2 Recurrent Neural Networks and Long Short-Term Memory

Recurrent Neural Networks (RNN) incorporate self-feedback loop connections, so the current iteration is computed on top of previous values, thus keeping the history. Let $\mathbf{s}(t)$ be a signal vector designing state and $\mathbf{x}(t)$ an input vector. RNNs perform the following recursive update operations inside their "cells" [18]:

$$\mathbf{s}^n = \mathbf{W_s}\mathbf{s}^{n-1} + \mathbf{W_r}\mathbf{r}^{n-1} + \mathbf{W_x}\mathbf{x}^n + \mathbf{\Theta}_s \tag{1.18}$$

$$\mathbf{r}^n = \mathbf{G}(\mathbf{s}^n) \tag{1.19}$$

where $\mathbf{r}(t-\tau_r)$ is the readout signal vector, a warped version of $\mathbf{s}(t)$ transformed by an activation function $\mathbf{G}$ (e.g. tanh) where τ_r is the synaptic delay, $\mathbf{W_s}, \mathbf{W_r}, \mathbf{W_x}$ are weight matrices and $\mathbf{\Theta}_s$ is a bias vector. The most common RNN formulation considers the contribution of $\mathbf{W_s}\mathbf{s}^{n-1}$ negligible and thus excludes it from practical implementation. RNNs are said to be "unrolled/unfolded" if initial conditions are specified for $\mathbf{s}^n$ and Equation 1.18 is evaluated for finite discrete steps.

If $\mathbf{W}$ represents a dense matrix to be constructed (learned) from the available data and $\sigma(\cdot)$ its activation function, then a practical RNN implementation (see Figure 1.1) is described by:

$$\begin{cases} \mathbf{h}_t = \sigma^h(\mathbf{W}^h\mathbf{h}_{t-1} + \mathbf{W}^x\mathbf{x}_t) \\ \mathbf{y}_t = \sigma^y(\mathbf{W}^y\mathbf{h}_t) \end{cases} \tag{1.20}$$

RNNs can process sequential data and its temporal or path dependencies efficiently, which is relevant for mechanical metamaterials experimenting plastic, inelastic or hyperelastic phenomena. However, it suffers from common issues in ML, such as vanishing/exploding gradients, and costly computations if the time dependence to be captured comes from very ancient steps. Certain techniques such as backpropagation through time (BPTT) [93] seek to overcome this problem.

Long Short-Term Memory cells [19] are a subtype of RNN introduced as a response to the aforementioned issues, in the hopes of capturing long-term dependencies while reducing the influence of irrelevant data at every time-step, all of that while keeping a "constant error cascade" and minimum computational complexity, $\mathcal{O}(1)$. In the fashion of control devices, this is accomplished via several interconnected gates, working as filters. The operations performed in an archetypal LSTM layout (see Figure 1.2) are:

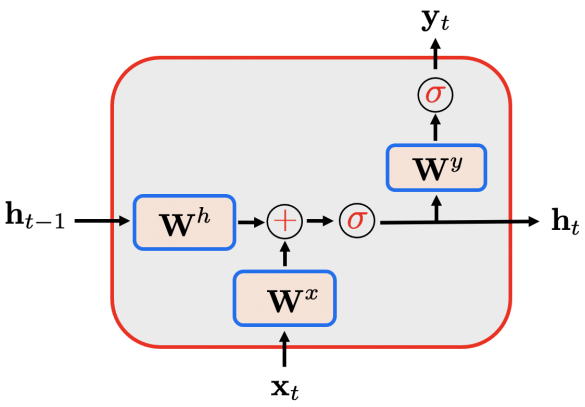

Figure 1.1: Practical implementation of a Recurrent Neural Network - RNN.

$$\mathbf{f}_t = \sigma(\mathbf{W}_f \cdot [\mathbf{h}_{t-1}, \mathbf{x}_t] + \mathbf{b}_f) \tag{1.21}$$

$$\mathbf{i}_t = \sigma(\mathbf{W}_i \cdot [\mathbf{h}_{t-1}, \mathbf{x}_t] + \mathbf{b}_i) \tag{1.22}$$

$$\tilde{\mathbf{c}}_t = \mathbf{tanh}(\mathbf{W}_c \cdot [\mathbf{h}_{t-1}, \mathbf{x}_t] + \mathbf{b}_c) \tag{1.23}$$

$$\mathbf{c}_t = \mathbf{f}_t * \mathbf{c}_{t-1} + \mathbf{i}_t * \tilde{\mathbf{c}}_t \tag{1.24}$$

$$\mathbf{o}_t = \sigma(\mathbf{W}_o \cdot [\mathbf{h}_{t-1}, \mathbf{x}_t] + \mathbf{b}_o) \tag{1.25}$$

$$\mathbf{y}_t = \mathbf{h}_t = \mathbf{o}_t * \mathbf{tanh}(\mathbf{c}_t) \tag{1.26}$$

With a slight change of notation with respect to the RNN formulation in Equations 1.18 and 1.19: time-step t substitutes iteration n, x for s to define the signal state, b for Θ to denote bias. Operator $\mathbf{G}$ in Equation 1.19 is now an activation function: sigmoid in Equations 1.21, 1.22 and 1.25; and hyperbolic tangent in Equations 1.23 and 1.26. The internal cell state and its output at time-step t are given by $\mathbf{c}_t$ and $\mathbf{h}_t$, respectively. $\mathbf{W}$ stands for weights.

LSTM cells contain three mutually interacting layers or "gates" (Equations 1.21, 1.22, 1.23 and 1.25) in their (internal) cell state $\mathbf{c}_t$, acting as "memory". Each gate has a specific function:

- The forget gate $\mathbf{f}$ filters concatenated former outputs (history) $\mathbf{h}_{t-1}$ and current inputs (signal) $\mathbf{x}_t$ through a sigmoid activation function (Equation 1.21), multiplying the result $\mathbf{f}_t \in (0,1)$ by the former cell state $\mathbf{c}_{t-1}$ (Equation 1.24). This conveys the degree to which memory is to be kept, i.e. whether former inputs will be "remembered" or "forgotten".

- The input gate $\mathbf{i}$ performs the same operation on $[\mathbf{h}_{t-1}, \mathbf{x}t]$ (Equation 1.22) and an analogous one (Equation 1.23, choosing *tanh* instead) yields the new candidate values $\tilde{\mathbf{c}}_t \in (-1, 1)$ for the cell state $\mathbf{c}_t$, each with their respective weights and biases. The obtained values $\mathbf{i}_t \in (0, 1)$ and $\tilde{\mathbf{c}}_t$ are multiplied and fed (added) to the current cell state $\mathbf{c}_t$, along with the former history (Equation 1.24). Thus, new information is stored in the cell with a relative importance given by $\mathbf{i}_t$.
- The output gate $\mathbf{o}$ performs the same operation on $[\mathbf{h}_{t-1}, \mathbf{x}t]$ (Equation 1.25), deciding which parts $\mathbf{o}_t \in (0, 1)$ of the cell state $\mathbf{c}_t$ will be considered. Finally, $\mathbf{o}_t$ is multiplied by a filtered (*tanh*) $\mathbf{c}_t$ to obtain the output $\mathbf{h}_t$ (Equation 1.25).

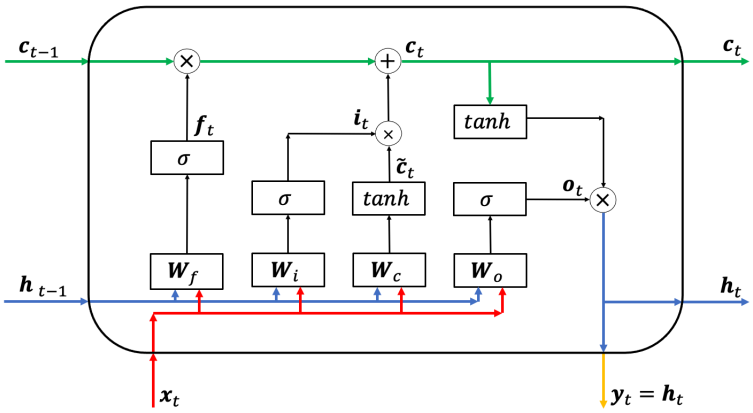

Figure 1.2: Standard LSTM architecture used in [1].

The green line in Figure 1.2 represents the long time memory path, the blue line designates short memory, whereas red and yellow lines represent the input and the global output (prediction) paths, respectively. LSTM presents an evanescent memory for the long-time path in such a way that the combination of long and short leads to the short memory response, [94, 95, 96].The canonical, full formulation can be found in [18].

LSTM-based surrogates are quite efficient at predicting metamaterial dynamics [97], even from partial observations, i.e. ignoring internal, non-measurable influential variables [1]. RNN-LSTM can accurately capture (long) time dependencies. They model the internal state's evolution at the same time they construct the model relating the observable input and output (action and response). However, they do not provide any information on space dependencies, i.e. topology, which is needed for various applications, including metamaterials.

1.1.2.3 Graph Neural Networks

Graph Neural Networks (GNN) [16] were conceived to embed geometrical and topological considerations into Machine Learning, both in software and hardware. By taking input data in the form of graphs, i.e. topological spaces composed of nodes (or vertices, v) and edges e joining them, GNNs can map their nodal features into an high-dimensional space. Instead of processing data as tensors, devoid of any topological information, GNNs preserve such meaningful relationships by design, saving the great computational cost of learning such relationships *a posteriori*. This is quite convenient, since graph-based structures are ubiquitous in everyday life (social networks, chemistry, maps, etc.).

Such a goal had already been attempted by Recursive Neural Networks [98], alas limited to directed, acyclic graphs. Most importantly, GNNs can process dynamically changing databases as long as they are represented in a graph form $\mathcal{G} = (\mathcal{V}, \mathcal{E})$ – unlike fixed-size tensors, which, on top of that, need pre-processing. This permits the user to update the model not only with new data, but also new representative variables to be considered or discarded, thus smoothing the "curse of dimensionality" and some other problems that lie within, i.e. internal/fictional variables not considered by the model [1].

Training and feature update in GNNs are substantially different from that of MLPs, CNNs or RNNs. Instead of performing backpropagation through gradient descent, new nodal properties are updated via Message Passing [99]: a technique inspired by thermal diffusion by which the system's evolution is conveyed through edges to update their neighboring nodes iteratively until an equilibrium (solution) is reached. A general expression of such process is given by these sequential steps:

$$\mathbf{m}_v^t = \sum_{w \in \mathcal{N}(v)} \mathbf{M}^{t-1}(\mathbf{h}_v^{t-1}, \mathbf{h}_w^{t-1}, \mathbf{e}_{vw}) \tag{1.27}$$

$$\mathbf{h}_v^T = \mathbf{U}^{t-1}(\mathbf{h}_v^{t-1}, \mathbf{m}_w^t) \tag{1.28}$$

$$\hat{\mathbf{y}}_t = \mathbf{R}(\mathbf{h}_v^T | v \in \mathcal{G}) \tag{1.29}$$

where Equation 1.27 represents Message Passing itself: for each node v and time-step t, its neighbors' (hidden) nodal values are updated by a message function $\mathbf{M}$ taking their preceding nodal $\mathbf{h}$ and edge $\mathbf{e}$ values. Later on, hidden states are updated through their former instances and current messages processed by an update function $\mathbf{U}$ (Equation 1.28). These two steps are repeated until the solution is obtained through a graph-level readout function $\mathbf{R}$ (Equation 1.29).

All three functions **M**, **U** and **R** is permutation invariant, that is, their output is independent of arbitrarily assigned node indices as a result of pooling operations such as averages or sums. In this fashion, these operations can be compared to those of two mutually feeding MLPs [100]:

- The "edge MLP" passes information through the edges ($\mathbf{e}_{vw}$), thus learning the diffusion law behind the modelled phenomenon, i.e. learning the Partial Differential Equations (PDEs) describing the underlying Physics.
- The "node MLP" ensures equilibrium conditions on the nodes. This is equivalent to learning the corresponding conservation laws, e.g. Kirchoff's for electric circuits.

Updates can happen via convolutional ($\mathbf{e}_{vw}$ is a multiplicative constant as in GCNs [101]) or attentional means ($\mathbf{e}_{vw}$ is implicitly computed through attention mechanisms [102]). Either way, GNN's embedded graph architecture provides topological (global) and relative (local) properties neglected by other ML approaches. This allows for data-driven description (and design) of lattices, relevant for metamaterial characterization [103]. Some AI experts advocate for a paradigm shift in ML's mathematical framework, adopting a more topologically consistent classification giving birth to Geometric Deep Learning [20].

GNNs have proven useful to convey graph-like structures, both from a conceptual - knowledge graphs [104] describing relationships between nodes e.g. social networks [105] - and practical point of view - intertwining nodal and edge behavior as in molecular behavior [99], neural interaction [106] or structural mechanics [107]. These features can help process what regular DNNs cannot, such as non-Euclidean data presented in a graph form [108] or tree dependencies not captured in an identically layered network [109]. Diffusion phenomena constitute a clear example of an easily implementable model tailored for graph layouts [110] with varied applications, e.g. heat transfer.

1.1.2.4 Other Neural Network Architectures

Convolutional Neural Networks (CNN) [15] can process large inputs in matrix forms, e.g. images. Physics-Informed Neural Networks (PINNs) [111, 112] include PDE-derived terms in the loss function, thus explicitly introducing Physics. Thermodynamic-informed GNNs [100], Structure-Preserving Neural Networks [113]and Hybrid Twins [10, 12] also want to alleviate the ignorance of the physical model through data. There are many other tools and techniques available (autoencoders [114], transformers [115], Support Vector Machines [116], Spiking Neural Networks [117], Generative Adversarial Networks [118], etc.). Some even consider human-machine interaction (e.g. Active Learning) [119, 6].

1.1.3 Heuristic Approaches

In highly dimensional and/or quickly changing scenarios, obtaining optimized solutions can be rather computationally expensive, even infeasible. In such cases, heuristic approaches might be useful alternatives. Although perhaps suboptimal – considering they are not subjected to any strict optimization rule nor constraint –, they do provide "fast" solutions with acceptable accuracy trade-offs; notably to NP-hard problems (e.g. traveling salesman). Convergence, however, is usually ill-defined, limited to local equilibrium criteria (e.g. conservation of mass).

A paradigmatic example of such techniques is Agent-Based Modeling (ABM), in which a discernible control unit – an "agent" – interacts with its environment and/or other agents according to a given set of behavioral rules. Agents possess attributes updated by their interactions, resources they can interchange with their environment and memory able to keep track of former exchanges [120]. ABM is extensively used in dynamic settings such as Economics [121], Biology [122] and Chemistry [123]. ABM is especially suitable to replicate diffusion between agents (as GNNs do between nodes). Should the modeler consider agents as nodes/neurons and their interactions as edges, it can create dynamic (structure-changing) surrogates for GNNs, with important hardware and software implications [124], potentially applicable to lattices or comparable bio-mechanical networks [125].

Other tools draw inspiration from biological aspects, e.g. evolution (genetic algorithms – survival of the fittest [126, 127]), competition (Generative Adversarial Networks - GAN [118]) or "greed" (greedy algorithms choosing local optima at each step). Heuristics has important applications for metamaterials, such as crash topology [128] or multi-scale optimization [129].

1.2 Metamaterials

This section contemplates current trends in metamaterial property description and the tools used for their design and optimization. This is a new but rapidly growing research field, so many fundamentals are still being defined and explored, leaving room for new developments.

1.2.1 Characterization

Most metamaterial lattices are periodic and symmetric - via repetition of a parametric unit cell, significantly easing their design and manufacturing. Metamaterials' versatility [130] makes them a perfect candidate for structural optimization problems, which poses multi-scale challenges [131, 132].

The application of lattice-like frameworks in engineering fields demands real-time calculations, which require the fast evaluation of models, e.g. the mentioned structural optimization [133] or health monitoring (SHM) [134, 135, 136].

Nevertheless, periodic lattices are also vulnerable to the propagation of mechanical issues such as buckling, fatigue, or creep. Having identical struts orderly distributed throughout space means that, should any of them reach critical conditions, the rest will contribute to transform a local failure into a global one. In extremely aperiodic lattices, no two struts would be identical, and thus, never share the exact same critical requirements.

Such lattices also present advantageous applications in fracture, e.g. toughness improvement [137] and vibration suppression via enhanced damping [138]. While aperiodic configurations are being designed and tested [139, 140], a unified framework or methodology relating their architecture to their final properties remains elusive, let alone inverse analysis - obtaining a tailored architecture from the desired performance - although some promising ML-based techniques have been developed [141].

In periodic metamaterials, the geometry and topology of the unit cell are tightly defined beforehand. However, more rigorous classifications have been proposed [142] and optimized [143]. Their properties can usually be obtained - at least, partially - from their geometry via experimental testing [144], the Finite Element Method (FEM) [145] and NNs [146]. This is different for randomly-generated architectures, so the first step would be to find a robust way to classify them i.e. telling them apart from each other so their relative advantages and inconveniences can be evaluated.

Some statistical descriptors are already used for heterogeneous media like alloys or composites [147, 148]. Topological Data Analysis (TDA) [149, 150] has been successfully used to classify composites [151]. Nonetheless, some studies suggest a topological perspective may not suffice to capture nor predict the metamaterial's mechanical behavior [144] and call to incorporate homogenization [152], affinity deformation considerations between different "phases" (unit cells) [153] or even ML to capture non-linear responses [154]. In multi-scale optimization problems, different techniques are used for computing the homogenized or equivalent behavior [155]. When lattice structures span different length scales, numerical techniques address the full-resolution of the structure, such as FE^2 [156], although at a high computational cost.

Homogenization is sometimes key in sizable lattices as a method for accurate, simplified behavior portrayal [157, 158, 159], either in a purely analytical form [160, 161] or inverse design [162], via FEM [163] or graph-assisted [164, 165, 166, 167]. Homogenization methods [168], e.g. FFT-based [169, 170] (Fast Fourier Transform) overcome this expensive problem. Alas, this method presents issues when applied to two phases with different stiffness, very pronounced in the case of lattice materials since one of the phases is void, i.e. null stiffness - the so-called infinite stiffness contrast [35].

Data-driven techniques bypass this expensive step, hence allowing for fast evaluations by building less complex surrogate and/or reduced order models [7, 171] learning the (potentially) complex underlying physical phenomena, e.g. using Machine Learning (ML) algorithms. Once the surrogates have been trained in an *offline* stage, they offer benefits for *online* metamaterial characterization and optimization, such as accelerating computations in multi-scale optimization or fast prediction in real-time scenarios. These approaches are widely applied in other engineering fields, like solving complex numerical problems as parameterized partial differential equations (PDEs) [172, 173, 174].

ML-based tools such as Convolutional Neural Networks (CNNs), Genetic Algorithms, or DL have been applied in metamaterial design [175]. In particular, GNNs [16] and Message-Passing [99] have proven very useful for capturing - and optimizing [176] - the topology while learning both the underlying physics and the respective conservation laws. As surrogate models [177], they can characterize mechanical behaviors such as buckling [178], fracture [179, 180], fatigue [181] and non-linear stress/strain relationships [182], which are crucial needs in SHM and metamaterial design.

GNN's hardware approach can convey the physical layout of the predicted model more accurately than any other ML architecture. They can be further enriched by introducing the PDEs describing the physical phenomenon to be replicated in a similar fashion to the aforementioned PINNs [111, 112] - and enriched by graph theory concepts [183]. Some such variants have tackled unstructured meshes [184] and soft-tissue mechanics [185].

PINNs allow for the solution of forward and inverse problems [184, 186] - noting the ill-posedness of the latter [187, 188]. Althoung DNNs can yield good accuracy in this task [189], they typically require many trainable parameters and a fixed input vector. Graph Neural Networks (GNNs) [190] overcome this step by dealing with variable-size input data (graphs themselves), even learning complex non-linear problems [191] with a much smaller parameter set.

All these tools can be viewed as surrogate models since they bypass the need for accurate analytical expressions to describe or predict the material's behavior. In non-deterministic problems, the outcome is not known in advance, so models - such as neural networks - cannot be "trained" as easily, since data is scarce and/or costly. Some non-deterministic/stochastic surrogate examples can be found [192, 193, 194], even for the prediction of material properties [195, 196]; namely fatigue [197], fracture [198] and corrosion [199].

1.2.2 Design and Optimization

Traditionally, structural design in industry has sought a trade-off between mechanical (e.g. maximum stiffness) and economic goals (e.g. minimum material). Frames [200], flexural meshes [201, 28] and the continuum [29, 202] have been successfully tackled in that regard by Topology Optimization (TO), in which the aim is changing the prototype's genus (i.e. number of holes) to fit the designer's purposes.

SIMP is no doubt the most widespread TO method for its simplicity [203], which makes it easy to implement on code in 2D [204, 205] and 3D [206]. It redistributes material throughout the dominion Ω to fit a target volume fraction $v_f \in (0, 1]$ with the minimum possible compliance (twice the elastic deformation work: $\mathbf{c} = \mathbf{u^T K u}$). This is enforced through a (non-physical) density parameter ρ spanning from 0 (void) to 1 (material), penalizing stiffness by a real constant $p > 2$ iteration after iteration until a material-void distribution is obtained, given by the updated Young's modulus $E^t = E_0 \rho^p$.

Other available methods involve sequential element elimination (Evolutionary Structural Optimization, ESO) [207, 208] - simple yet heuristic - and/or homogenization techniques (Near-Optimal Microstructure, NOM [29]; Optimal Microstructures with Penalization, OMP [209]) - thus, computationally costly [203]. Level set methods [210] allow for a great geometrical flexibility at the cost of higher conceptual and computational complexity [211].

1.2.2.1 Uncertain Boundary Conditions

The TO framework was conceived for static settings, that is, time-invariant boundary conditions and loading. However, stationary conditions seem quite reductionist when considering real loading conditions entail naturally occurring uncertainties (load misplacement by vibrations, faulty measurements, slight variations in modulus and direction due to impacts, etc.) and wear/tear (the material's resistance decays with its use, perhaps leading to fracture).

Loading uncertainty has been analyzed by several authors using different mathematical tools (statistics, model order reduction, etc.) [212, 213, 214]. This lead to reliability/performance-based topology optimization (RBTO/PBTO) and inverse optimum safety factors (IOSF) [215, 216], which strive for a more robust, probabilistic approach, compatible with multi-objective optimization (e.g. multi-axial) and more suitable for additive manufacturing [217]. Unfortunately, this industrial fail-safe approach often results in oversized prototypes, coming from their load envelope over-estimating real service loads.

Structural design applies the superposition principle to loading: the individual loads are added on top of each other so that the resulting topology endures their combined effects, often linearly, as a truss-like approximation of the continuum [218, 219, 220]; or perhaps by integrating force fields (pressure) [221]. In TO, this is tantamount to summing up the compliance contributions of each individual load [204, 205, 206]. A "load envelope" is usually the sole design criterion, so the whole conceived structure can withstand the worst loading scenario applied to any of its parts.

1.2.2.2 Post-Processing: Filtering

The output of TO is a binary material (black, $\rho = 1$) and void (white, $\rho = 0$) distribution. Intermediate states (gray, $0 < \rho < 1$) frequently need finer profiling strategies [222]. To tackle these problems, many filters address sensitivities or material density [223, 224, 225, 205]. They alleviate some numerical issues like checkerboard patterns and mesh-dependence and practical ones like resolution (namely, contour definition) and continuity, with various penalization schemes [226]. Techniques such as remeshing, subdivision and fitting are often used [224]. Some of them revolve around erosion phenomena, i.e. scratching material off the structure's contour to get a clear void-material frontier, as in nature [227]. Such effects are global, targeting all the contour simultaneously instead of specific areas of interest.

Many post-processing tools have been suggested with manufacturability in mind, particularly after the rise of additive manufacturing. They entail multiple challenges regarding multi-scale scenarios [228] and printing restrictions (length, connectivity, self-support) as well as opportunities (e.g. tailored anisotropy for functionally-graded metamaterials [229]). They solve issues like visibility of inner/void regions (occluded holes in 3D prototypes) to avoid complicated printing paths [230] and create self-supporting structures [231] with minimum spending of support material while immune to gravity-driven deformation. Level-set [210, 211] and spline-based methods [232, 233] suit those needs by default.

These post-processing techniques are, however, computationally costly and put the quasi-optimality of the given solution at risk [228]. Hence, many topology/shape optimization proposals embed manufacturing constraints into the iterative process [234]. Despite some drawbacks regarding reduced design space and generality [235], the possibilities are plentiful, e.g. auxetic metamaterial design [236].

1.2.2.3 Constrained Optimization under Effective Material Properties

Since TO is a non-convex minimization problem [237], the result obtained through this process is not necessarily the global optimum (e.g. minimum compliance in SIMP). This can be dealt with via several methods [238], such as filtering and relaxation [239] and model order reduction (MOR) [214, 240]. Nevertheless, this non-convexity "flaw" can also be seen as an opportunity to match a set of particular requirements not directly related to the TO process.

For instance, these extra criteria could cover aspects commonly neglected by plain TO, such as material properties besides the Young's modulus (maximum stress [241, 242, 243], fatigue [244, 245, 246]), manufacturability [247], load uncertainty [248] and/or general maintenance concerns - giving raise to the so-called reliability-based topology optimization (RBTO) [215, 216].

Implementation of such criteria should be straightforward and not excessively demanding, computationally speaking. Fatigue damage, mechanical response (traction/compression), manufacturing (printing direction) and distortion (von Mises equivalent stress) are some suggestions to be considered. This way, the design would not only be optimized topologically (material), but also more robust when facing service conditions.

As an inverse design tool for a given canonical static loading, TO rarely considers damage or maintenance concerns. Damage should be taken into account, since it can alter the material's effective mechanical properties and even its quantity or distribution (creep, fatigue and fracture). For the usual static case, simple stress-based formulations (e.g. Tresca) can be implemented, whereas fatigue damage induced by dynamic loads requires more elaborate stress (Wöller's diagram), strain (e.g. Smith-Watson-Topper's model [249]) and/or energy criteria (e.g. fracture mechanics) integrated over time.

The latter is directly related to TO's objective (SIMP) - minimizing compliance, i.e. elastic strain energy. Some realistic material stress constraints can be considered [250], as well as efficient FE2 approaches [251] and accurately separated multi-phase solutions [252]. The first point is two-fold: optimization must yield feasible, realistic material solutions while avoiding oversized designs.

By accounting for fatigue damage, the structure can be reinforced to withstand wear and tear and thus enhance its service life. Some approaches include both cyclic attrition and a material-dependent stress threshold for fatigue effects [253, 254], while others just consider the latter [248]. Fatigue constraints are linked to fracture, challenging due to the non-linear implications coming from plasticity [255] - although some linear energy-based approximations exist [256, 257, 258]. Total strain energy (elastic and plastic) can be used as an index for cumulative fatigue damage in itself - including explicit fracture considerations (e.g. crack growth) [253, 254] - proven useful for damage prediction [259].

Their physical behavior (e.g. mechanical response) can be included in the optimization scheme as well, be it directly as a target variable - like the Updated Properties Model (UPM) [260] does - or as a penalization on the target variable to be minimized (compliance). For instance, concrete-based materials work great under compression but poorly under traction, whereas the opposite is true for steel and many other commonly-used metals, due to buckling when the struts are slender enough.

While anisotropy can be interesting for functionally graded materials (composites, metamaterials) and multi-scale tailored structures [261, 262], it does disrupt SIMP's axioms, and so the method must be adapted accordingly to stay valid. When relatively predictable (within confidence intervals), taking it into account or even leveraging it is much easier, as in composites and additively manufactured prototypes - more robust along their fibers and layers, respectively. This leaves room for tailored functional grading [263, 264].

Yield limit is yet another important material property to be considered, determining the boundaries for SIMP's assumed linear elasticity. Stress-based thresholds like von Mises yield criterion [265] can determine whether this linear approach is accurate enough or non-linearity (viscoelasticity, plasticity, hyperelasticity [266, 267]) needs to be enforced via more complex formulations, or perhaps stress-based constrained optimization [241, 244, 246, 248, 268, 269, 270, 271]. The multi-scale implications of non-linear frameworks often require homogenization steps [272].

1.3 Biomedical Models: the Brain Paradigm

Studying the brain's structure is a difficult task for multiple reasons [273]. There is no univocal model or chart of the brain due to individual variability, which makes the overall description of the brain and its standardization on the micro- and nano-scales challenging.

Seemingly related tasks may be performed by different areas within a brain region; such is the case of facial recognition and evaluation [274]. Activity patterns for the same task differ [275] and even change with age [276] or illness. Although there is a certain consensus on a "default" network configuration in resting states [277, 278, 279], it is still subjected to individual variations and pathological conditions [280]. Additionally, structural and functional pathways in the brain influence each other. Most brain mappings show a correlation between tasks and activations, rather than causation [281].

Brain cartography [282] has grown to be popular in recent decades, yielding notable examples [283, 284] as a result of a coordinated effort in the sharing and management of huge amounts of data. Such data has been traditionally obtained via physical means, namely haemodynamics [285] (blood oxygen level-dependency, BOLD): computerised tomography (CT), (functional) magnetic resonance imaging (f)(MRI), positron emission tomography (PET), etc. Obtaining measurements through microscopy has its own difficulties: tissue handling, contrast, stain density, dissection, lighting, etc. [286] These techniques are costly and subject to instrumental mishandling and/or failure, increasing uncertainty.

Zooming into the nano-scale, the brain's most basic individual parts are neurons: electrically excitable cells allowing for the transmission of information through the nervous system. Neurons come in various shapes and specific functions, but they do usually share a basic structure. Generally speaking, they are composed of a nucleus (soma) and an extension covered by myelin (axon) ending in appendices (dendrites) responsible for communication between them (synapse). In mathematical terms, these two main elements could be seen as vertices $\mathbf{v}$ (soma) and edges $\mathbf{e}$ (axon/dendrite) in a graph $\mathbf{G}(\mathbf{v}, \mathbf{e})$.

These electrically excitable cells are connected structurally - physical links between neurons, i.e. "highways" - and functionally - the links actually used during synaptic activity, i.e., "traffic" - forming the connectome [287]. Structural and functional connectivities can be mutually affected due to injury and/or disease and/or biological aging.

Such connections are subjected to neuroplasticity: rewiring (structural [288]) and alternative paths (functional [289]) on a life-long basis [290], especially during growth [291], aging [292, 293], injury [294, 295] and disease [296]. Diaschisis is a functional perturbation by which a damaged area can deteriorate another distant zone's performance [297]. Beyond the structural requirements described above, brain cells use chemical signals (neurotransmitters) to communicate. They can be excitatory (e.g. glutamate), inhibitory (e.g. GABA), and modulatory (e.g. endocannabinoids [298]).

Neurons also interact with hormones allowing communication with other organs in the body. These chemical signals could play a key role in neuroplasticity and pathological conditions. For example, Parkinson's disease is characterized by a deficit in dopaminergic transmission. Likewise, changes in acetylcholine could be associated to Alzheimer's. On top of that, neurons migrate between brain regions [299], especially - but not solely [300] - in early growth [301].

Connectomics relies on quantitative graph parameters such as local network efficiency, clustering coefficients, and global communication path lengths to assess damage [302]. For an extensive overview of the most common brain illnesses and injuries from a connectomic perspective, the interested reader can refer to the author's review article on the topic "**Review of the Brain's behavior after Injury and Disease for Its Application in an Agent-Based Model (ABM)**" [**125**].

1.3.1 Biological vs. Artificial Neural Networks

Although artificial neural networks (ANNs) are in fact inspired by the signal processing of their biological counterparts in the brain [87], several authors [303, 304, 305] have pointed out major differences between them: non-univocal backpropagation, unlayered neural networks, neural plasticity and migration. Thus, any modeling approach must combine both mathematical and biological aspects, introducing Graph Theory and Machine Learning concepts while accounting for biomedical brain phenomena.

1.3.1.1 Metastability

Different wave bands in the brain (alpha, beta, mu, etc.) can be positively or negatively correlated among themselves [306], although they need to undergo processing since they are out of phase. Metastability explains how the brain coordinates diverse input signals from multiple receptors in time (neural oscillations, i.e. generated by sensory neurons after receiving stimuli) into a coherent, unison response, locked in frequency (like the movement order sent to a muscle from a motor neuron).

This way, the brain makes sense of all the unsorted information it receives to produce meaningful data that will decide on a given outcome [307]. These brain waves synchronize, travel in sequence and experience nonlinear instabilities [308]. This coordination affects spatial and temporal intervals, generating perception, emotion, and ultimately, cognition itself [309].

1.3.1.2 Neural Migration

Migration is common in some types of cells, including neurons, mainly during brain development [301] and abnormally as a result of disease [300]. It follows two main mechanisms:

- radial, including somal translocation - resettlement of the neuron's nucleus - and glia-guided locomotion - e.g. from the ventricles to the developing cortical area.
- tangential, e.g. cortical interneurons migrating from the ventral telencephalon to the cortex [300].

The migration process entails two aspects: leading - determining migration direction - and trailing — a wake along which new axonal connections are conformed [299].

1.3.1.3 Neuroplasticity

Neuroplasticity is the brain's ability to modify its connections and/or paths so that the information can get across despite severed, non-existing (during growth) or malfunctioning connections, avoiding them and finding alternatives. It is ultimately responsible for the adaptation of the brain's structural and/or functional connections to external - senses - and intrinsic stimuli - learning. This lifelong [290] adaptation occurs during growth and after injuries [310], regaining lost functionalities [311] to astonishing extents in some cases [312]. Neuroplasticity can be:

- structural, by regeneration or collateral sprouting (including reactive synaptogenesis, rerouting and axon retraction [288])
- functional, by task relocation within an already existing neural infrastructure (homologous area adaptation, cross-modal reassignment, map expansion, and compensatory masquerade [289])

In biological neural networks, Hebb's learning rule applies: "neurons that fire together, wire together", implying functional connectivity determines the structural connectivity, and so structural plasticity caters to functional needs. Such a restriction poses a problem for a realistic implementation of ANNs, since neural connections must be strong enough to ease memory recalls but not too strong to create numerical overcharge. Some solutions to this problem imply transient non-linear analysis [108].

Synapses between neurons are also subjected to plasticity: their intensity and distribution change according to the task [275], electrical stimulation [313], age [314, 315] and brain damage [288, 316]. In essence, synapses are also trainable [292] - which can be replicated through a simple given rule [317, 318, 319, 320, 304, 321, 322].

1.3.1.4 Backpropagation

Neural backpropagation happens in reverse to the habitual soma-axon sense, i.e. from the axon hillock to the dendrites aiming for the dendritic voltage-gated calcium [323] or sodium channels [324] when the soma undergoes depolarization. There is empirical evidence that pyramidal neurons (with separated apical and basal dendrites) perform backpropagation [321], and modeling attempts of this phenomenon are abundant [325, 326, 327]. Nonetheless, this neurological concept differs greatly from its more widely known mathematical counterpart in Machine Learning.

In ANNs, the signal propagates forward first. By repeatedly applying the chain rule of derivatives, one can define the rate of change (gradient) of the output prediction $\hat{y}$ or any layer's immediate outputs z_i in relation to a given input x_i, being $z_i = W_i x_i + b_i$. After evaluation of a given loss function $E = f(y, \hat{y})$, backpropagation in ANNs is the process by which signals travel backwards (from outputs towards inputs) to correct previous steps and so approach a target output y, recomputing the weights W_i and biases b_i of each neuron layer to "learn" (approximately) the combination yielding the target outcome. Using Automatic Differentation (AD) [328], that gradient derivation is carried out by most Artificial Intelligence packages such as Pytorch© [329, 330] or Tensorflow© [331].

In MultiLayer Perceptrons (MLP), Convolutional (CNN) and Recurrent Neural Networks (RNN), layers are usually fully connected, i.e. all neurons in layer i are connected to all their inputs in the previous layer $i-1$ and all their outputs in the next one, $i+1$. The relevance of such connections is typically left to the weights W_i and biases b_i, even though in some deep ANNs "weak" connections may be eliminated. In Graph Neural Networks (GNN), partially-connected graphs can update their nodal and edge features via tailored functions without computing the gradient ("Message Passing" [16, 99]).

A monotonic (ever-growing) activation function (ReLu, tanh, sigmoid, etc.) is enforced to cast the layer's output $a_i = f(z_i)$ into a [0,1] interval. Biological membrane activation (responsible for neurons and muscle cells) does have a threshold (an electrical activation potential around -55 mV), like activation functions in ANNs. Membrane activation is non-monotonic, instead going through four separate steps:

1. depolarization (Na^+ ions enter, potential rising to the maximum, +40 mV)
2. repolarization (K^+ ions exit, potential decreasing to the minimum)
3. refractory period (hyperpolarization)
4. resting (potential stabilized at -70 mV)

Synapses themselves are regulated by very convoluted biochemical (neurotransmitters, proteins) and electrical processes usually not considered in an ANN model at all. A single synapse takes milliseconds [303], a somewhat slow rate when compared to some high-performance multi-layered ANNs after training - which does require longer times [332].

The biological brain's neural networks are undirected. Inhibitory and excitatory paths for backpropagation are distinct, since neurons produce either inhibitory or excitatory synapses. Inhibition/excitation paths are diffuse since biological neurons are not fully connected, let alone layer-structured, and thus they receive no information other than their preceding neighbors' outputs [303].

This is a direct obstacle for ANN-like backpropagation where all weights are needed, known as the "synaptic assignment problem" [320]. Moreover, neurons in primates tend to activate on the basis of attention mechanisms rather than error backpropagation when reacting to visual stimuli [333], e.g. when learning to recognize and classify physical shapes [334]. Some ANNs feature this behavior [335].

1.3.2 Medical Modeling Approaches

Obtaining an accurate model of the brain's pathologies is challenging due to its inherent complexity. Individual variation, evolution over time, induced damage and many other aspects must be considered. Attempting to reproduce the connectome's structure and function requires a flexible, cohesive and data-rich model, imperatively multiscalar in space (from synaptic level to the whole brain) and time (from signal processing to complex reasoning and memory).

The microscale concerns cell-level phenomena (synapses, neurotransmitter releases, etc.), the mesoscale involves neural networks and their interactions, and the macroscale implies brain structure and activity as a whole; in synergy with its environment - yielding whole-brain models (WBM) [336, 337].

The large amount of neurons ($\mathcal{O}(10^{11})$) [338] and synapses ($\mathcal{O}(10^{15})$) [339] in the human brain makes it computationally unfeasible to transpose or extrapolate individual neuronal function directly onto the macroscale, there must be some compromise between accuracy and complexity. Regarding time scales, neuron spiking takes milliseconds [303].

Thus, fast computing is pivotal for any real-time simulation attempts, including non-linear transient events [108]. Measures obtained by common methods (CT scans, DTI, (f)MRI) are often too broad to cover the meso- and micro-scales. Studies about synaptic processes are (relatively) easily obtainable, but they are globally meaningless when devoid of their network context.

In general terms, two ways to tackle multi-scale modeling are applied to the brain and many other physical phenomena:

- bottom-up ("direct problem"): from cause to effect, growing in complexity when directly relating local phenomena to global responses
- top-down ("inverse problem"): tracing causes from effects, inverse local inference out of global observations

The latter is the most common in Medicine, since most measurement techniques (MRI, DTI, CT, etc.) have the whole brain (global scale) as the target, yielding virtual brain models [340]. Fortunately, there is a huge amount of available data, although representativity remains an issue. The challenge remains in the limited extent of many of these analyzes and the interpretation and generalization of their results to an archetypal "human brain". Although network hubs seem to be quite consistent and homogeneous in healthy individuals [341], this is not the case for ill patients [342, 343]. Besides, such generalizations do not provide the whole dynamical picture of functional connectivity [344, 345].

While *in vivo* data has grown in quality and availability, high-fidelity brain mock-ups could prove quite convenient for a more accurate, non-invasive (*in silico*) diagnosis and treatment. Prognosis and differential diagnosis remain two complicated questions that still rely mostly on statistical data, which could be biased and/or incomplete, as previously discussed.

Models must be sensitive to structural-functional decoupling [346, 347] as well, resulting from the brain's evolutionary adaptability to disturbances (injuries, disorders). As in many other phenomena, surjection can be an issue: if the model were given by a function $\mathbf{y} = \mathbf{f}(\mathbf{x})$, there would be many input possibilities x_i yielding the same global observation y. This is also known as neurodegeneracy, a direct consequence of brain redundancy and the nature of graph networks themselves - where many paths could join two different nodes through very different sets of edges [340].

In spite of the advantages of connectomics, the researcher must not reduce neuroscience to a mere topological study; hence, it is a dire necessity to incorporate biological [348] and chemical considerations [349]. Furthermore, modeling the brain as an isolated organ is a mistake, for it is constantly influenced by external stimuli and internal factors (e.g. peripheral hormones or metabolic signals), playing crucial roles in pathological states. To account for this, Medicine has three main tools at its disposal: Electrophysiology/Haemodynamics, Biomechanics and Mathematics - see Figure 1.3.

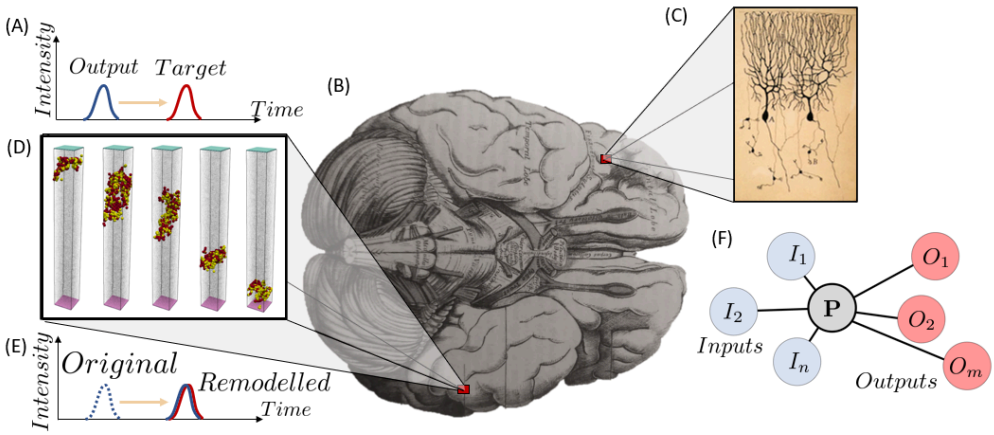

Figure 1.3: Multi-scalar brain modeling: signal transmission (**a** overview,**d** propagation,**e** neuroplasticity), global brain anatomy (**b** from [2]) and neurons (**c** by Ramón y Cajal - see [3]).

1.3.2.1 Electrophysiology/Haemodynamics

Electrophysiology studies the electrical behavior of biological tissue in an almost non-invasive manner (no need for surgery). Modeling the connectome as an electric circuit seems obvious, given that neurons act as membranes (electrically excitable cells). Electroencephalography (EEG) yielded some of the first attempts at brain modeling, mainly describing synapses [350] and their non-linear implications [351]. It provides useful information about many brain pathologies, e.g. intellectual disability [352].

Electrical excitation can be induced artificially, allowing for measures *in vitro* and *in vivo*, e.g. electrical brain stimulation (EBS) can alter neural activation thresholds and measured in many ways (evoked potentials) [353]. EBS provides direct information about functional connectivity across different scales, using varying methodologies [354], and structural connectivity can be inferred from functional observations or the lack thereof.

Electrophysiological and haemodynamical (blood flow) mappings are intertwined and often complementary. The available imaging techniques rely either on electrical excitation (EEG, MEG, TMS, NIRS) or tracking iron contained in blood's haemoglobin (haemodynamics: fMRI, CT, PET, SPECT) [285]. Electromagnetic theory links both phenomena (Maxwell's laws).

Whereas electrophysiology showcases an electrical neuronal circuit - membrane activity, i.e. synapses - haemodynamics provides the vascular structure feeding the brain, being correlated. Haemodynamic measures are especially useful to detect angiomas (abnormally overgrown blood vessels), which are themselves benign but perhaps they surround a malignant tumor.

Task-driven models focus on the activation patterns observed via functional MRI (Magnetic Resonance Imaging), EEG, or a combination of both [355] while subjects perform a given activity, usually obtained via electrophysiology. Their partial observations can be superposed to form a global - yet not fully integrated - functional connectivity chart. Signal analysis tools (e.g. spectral techniques [356] and Fourier transform [357, 358]) are used to extract useful information out of EEGs. Some authors even argue the brain performs simplified Fourier analysis on its own [359, 360].

1.3.2.2 Biomechanics

Bio-mechanical models explain the brain from a mechanical point of view - kinematics, dynamics, etc. - within biologically plausible parameters. Brain tissue features properties and behaviors unseen in inert materials (namely, physiological functions: birth, growth, nourishment, death) or affected by them in a different way than inorganic materials (biochemistry). While most of these effects outgrow the mechanical perspective in itself, they do have an influence over (bio)mechanical properties, so they must be taken into consideration. Brain growth, for instance, has been characterized as a morphological process during development [361].

Despite being protected by the thick, hard skull around it, brain tissue is a very soft material, mechanically speaking: 30 times less shear-resistant than silicone gel [362]. It is compliant (i.e., non-stiff) [363], presenting non-linear mechanic properties such as loading rate dependency [364, 365]. It is also fragile, heterogeneous [366], bi-phasic (80% water) and scarce as an asset [367]. Thus, brain matter can be modelled as a soft tissue, at least at the micro-scale [368, 369].

Alas, performing measurements on brain tissue samples is not easy: they are conditioned by (costly) conservation [370], preparation [371], and the testing environment [372]. Shear tests are common [364, 362], since extreme softness complicates uni-axial testing. Non-invasive techniques such as ultrasounds - namely, shear waves [373, 374] - can perform *in vivo* mechanical measurements.

Brain stiffness varies in time and space, globally increasing with age. Some brain regions are more robust than others [375], being positively correlated with collagen [376] and myelin content [377]; the latter being a marker for disease [378]. Deformations are not homogeneous either [379], except in unconfined compression tests, whose friction coefficient depends again on loading rate [380]. The brain's stress-strain curve is approximately exponential. For that reason and its strain rate dependency, viscoelastic [381, 382] or combined models [383] are preferred over purely hyperelastic ones [384, 385].

Brain damage does not require skull breakage: accelerations, swift turns, external impacts and medical conditions (infections, toxicity, cancer, etc.) can wreck havoc in the brain, both structurally and functionally - the latter most frequently being a consequence of the former.

Despite individual physiological variability, biological tissue presents two fundamental features:

- Tensional homeostasis. Under the Monro-Kellie principle (intracranial volume remains constant [386]), soft tissues (brain, arteries, etc.) have a preferred "homeostatic" loading state and trigger biological responses (segregation of certain biomolecules by the cell) to reach it. This is why, across several ages and species, intracranial pressure remains constant at around 2-4 N/m per lamellar unit [387], yielding a Cauchy stress of 150 to 300 kPa. This can be altered by unforeseen (Traumatic Brain Injury) or planned medical events (surgery) [363, 388]; or disease [389].
- Turnover. Cells grow, reproduce, interact with their ever-changing environment and die, resulting in a mass balance known as "turnover". This phenomenon is multi-scalar in time (minutes to months) and space (cellular or extracellular). It can be balanced (homeostatic, healthy individual) or skewed (adaptative or pathologic), positive (fibrosis) or negative (atrophy) [387].

Attempts to explain growth and remodeling in biological soft tissues in terms of mass-stress interactions yielded the so-called constrained mixture models [390, 391]. They can help evaluate physical brain trauma and set the mechanical limits to avoid, as well as providing a model for damage evaluation and treatment follow-up.

Whole-brain mechanical studies [365, 392, 393] are complex and costly, and they frequently neglect the angiome (blood vessel network) [376] and its mechanical (e.g. stiffness induced by anoxic necrosis) and organizational aspects (network connectivity). This causes dependence on haemodynamical models. Isochoric and (quasi-)incompressible mechanical models (e.g. Hencky's) pose a good approximation [394], providing insight unobtainable via medical imaging, like diffuse axonal injury [384, 366].

Biophysical models, especially those allowing for brain activity tracking, can greatly enhance diagnoses of neurodegenerative illnesses [395, 396]. However, different methodologies, datasets (sample size, patient age [397], environmental factors - namely, humidity [398] and temperature [372, 370]) and theoretical frameworks yield varying mechanical results, even spreading across orders of magnitude.

1.3.2.3 Mathematics

These models try to depict the brain through mathematical tools, i.e. calculus, algebra, statistics, information theory (IT), etc. This task proves challenging considering its multi-scalarity (space- and time-wise), complex biochemical processes and difficult sampling. Thus, obtaining purely analytical expressions for such complex biochemical phenomena is extremely difficult - if not impossible. Mathematical models attempting to convey this complexity often fall short, keeping to mere statistics.

Important assumptions about the model's work variables are made to tackle this variability, such as homoscedasticity, i.e. the homogeneity of variance, and normality, i.e. following the normal distribution. Along with non-linearity and outlier interpretation, these are the foremost problems in traditional statistical approaches, ending in false positives (Type I errors) and broader accuracy concerns [399]. Statistics can introduce size bias, variance and/or data collection techniques. Therefore, robust models rule out any statistical method exclusively based on mean and/or variances.

In the past, the brain's adaptive variability in neuronal morphology [400, 401, 402, 403] has perhaps been addressed with limited statistical tools, frequently from a static perspective [404]. More practical, data-driven interpretations - thus, free of theoretical assumptions and problematic coarse generalizations - have emerged to solve these problems, such as statistical learning, focused on data-inferred interpretations [405]. Stochastic/Heuristic approaches are available for this purpose, such as Boolean networks [406] - wherein logic junctions act as stochastic surrogates for brain activation dynamics - and agent-based models [407, 408]. These tools can be combined in a synergic way [124].

Agent-Based Models (ABM) provide a more flexible framework, where an agent (e.g. a migrating neuron) interacts with its environment, reaching equilibrium points (homeostasis) within complex dynamic settings. Allowing for quick decision making [409], this technique has been used to simulate different biological aspects: neural community interactions [410, 411, 124] and pathological contagion [412] and evolution (tumor-induced angiogenesis [413], glioblastoma multiforme [414]).

The biggest issue that biological models face - especially for the brain - is computing power. The amount of neurons and synapses in the real brain remain intractable even by the best-performing computers available today, given the best existing microprocessors contain around 10^{12} transistors and hundreds of kilometers of wire, whereas the human brain processes around 10^{14} synapses through $3{\cdot}10^{5}$ km of neural pathways (longer than the Earth-Moon distance) [415].

The advent of quantum computing may provide a feasible solution, given its similarities with the biological brain's functioning [416, 417]. Neuromorphic computing, also known as neuroinformatics, produces hardware and software [418] inspired by the brain's efficiency [419], using qu-bits aiming to replicate superposing signals (metastability) [420].

Such complex models often entail many variables, defined by the user and so subjected to representativity and generalization issues. Some proposals provide parameter-free statistical testing to alleviate such subjectivity [421]. In lieu thereof, two main tools are available: Model Order Reduction (MOR) and Machine Learning (ML) - see Section 1.1 for a full recap.

Convolutional neural networks (CNNs) can enhance MRI [422, 423], e.g. finding unnoticed patterns use to identify [424, 425] and classify [426] prodromal brain tumors or Alzheimer's [427].

Spiking neural networks (SNNs) [428, 429, 430] seem to capture the brain's behavior in a more biologically plausible manner, aiming at real-time functional connectivity [431]. Their performance can be boosted by synaptic plasticity functions, namely spike-timing-dependent (STDP) [432, 433, 434] instead of the regular gradient descent. Structural plasticity can be implemented as well [432]. SNNs can be combined with quantum neuromorphic architectures [435, 436] to enhance their versatility and information processing power.

Graph neural networks are also pertinent because of their ability to capture the network's topology - that is, structural connectivity [437] - and include it into the information flow, with the backbone of graph theory behind it [438, 439, 440, 441, 442], providing promising results [62, 66, 65]. GNNs can be further empowered by considering the fractal nature of dendrites, again a result of evolutionary structural and functional adaptability [443].

Chapter 2

METHODOLOGY

This chapter presents the proposed methodologies for all case studies within their respective fields of application, pondering how they can expand and improve the current state of the art. This existing tools will be combined in novel ways, leading to newly-developed techniques.

Contenu

2.1 Structural Description

This section encompasses all methodological contributions regarding structural characterization, i.e. the study of mechanical behavior for pre-conceived structures (lattices, metamaterials, dynamical systems) and the tools used for that purpose. This constitutes the "direct problem": extracting structural properties from a given topology/geometry.

2.1.1 Property Prediction

In trusses, parameterized periodic lattices and other similar structures, computing global properties is relatively straightforward, even if direct methods are computationally demanding due to a high number of elements and/or very fine meshing strategies. In such cases, homogenization techniques [33, 34] can accelerate computations, as previously explained. However, the methodology is not that clear when the structure to be modeled is aperiodic. In this subsection, a case study for the data-driven characterization of an aperiodic metamaterial cell is considered, as detailed in the author's research article "**On the data-driven description of lattice materials mechanics**" [103].

2.1.1.1 Database Generation

Several lattice structures are defined in a unit cube $\Omega \subset \mathbb{R}^3$ and is made of n_j nodes (or joints) and n_e members (or struts). Eight nodes of the lattice correspond to a vertex of the cube (clamps in which forces or displacements will be applied), thus the only ones with a fixed position - unlike [444] - whereas the remaining $n_j - 8$ user-prescribed joints are randomly distributed within the domain Ω.

Samples are generated with 1 to 50 non-fixed inner nodes, with coordinates sampled from three independent and identically distributed (iid) uniform distributions $\mathcal{U}(\delta, 1-\delta)$. The δ prevents the randomly located joints from joining the domain's boundary $\partial\Omega$, since that would disturb the lattice's external appearance and so thwart repeatability.

The elements are defined by a 3D generalization of Delaunay's triangulation (through Bowyer-Watson's algorithm [445, 446]), yielding a total n_e (not prescribed). This ensures both the absence of unforeseen - and undesired - intersections (nodes) and a short yet rich interval for strut length. In mechanical terms, it reduces buckling (strut slenderness is bounded) and prevents the generation of sliver triangles with acute angles potentially causing stress concentration and instabilities - mechanisms - if the truss is pin-jointed. See Figure 2.1 for an example of a cubic lattice with a single inner node ($n_j = 9$).

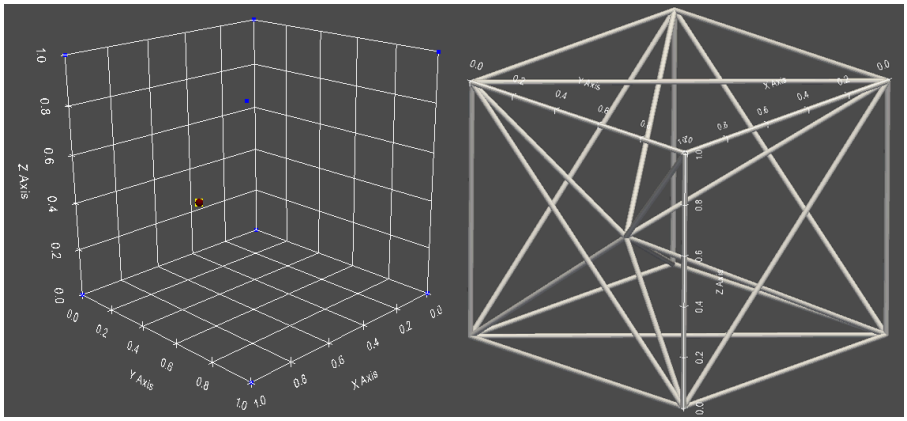

(a) Node location. (b) Generated lattice.

Figure 2.1: Example of lattice generation (right) from the initial set of nodes (left), differentiating between clamp (blue, along top and bottom XY planes) and inner ones (red, inside the cube).

2.1.1.2 Mechanical Behavior

The lattice is subjected to uniaxial testing, imposing a displacement u^* along the vertical direction ($z-$axis), as shown in Figure 2.2. Some degrees of freedom are restricted - denoted by r. Conversely, the sub-index f designates free degrees of freedom.

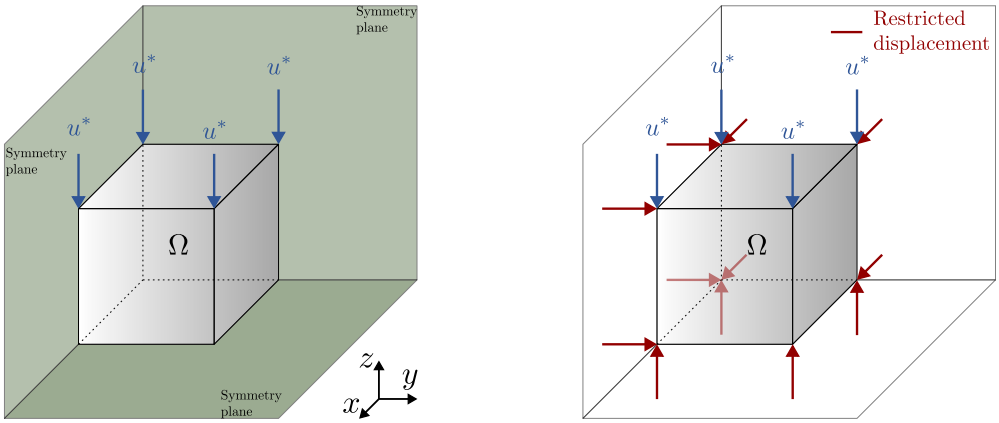

(a) Imposed displacement and symmetry planes. (b) Resulting boundary conditions.

Figure 2.2: Boundary conditions of the lattice structure, where u^* is the imposed displacement (blue). The restricted displacements in (b), depicted in red, are orthogonal to green symmetry planes in (a).

Each element is modeled either as a pin-jointed bar or an Euler-Bernoulli beam. The linear equilibrium equation for a lattice structure with n_d degrees of freedom - $3n_j$ for trusses, $6n_j$ for beams - reads

$$\mathbf{K}\mathbf{u} = \mathbf{f} \tag{2.1}$$

where $\mathbf{u} \in \mathbb{R}^{n_d}$ and $\mathbf{f} \in \mathbb{R}^{n_d}$ are respectively the nodal displacements and forces vectors, and $\mathbf{K} \in \mathbb{R}^{n_d \times n_d}$ is the structure's global stiffness matrix before imposing the boundary conditions. The local stiffness matrix $\mathbf{K_e}$ of a truss e is given by

$$\mathbf{K_e} = \frac{E_e A_e}{\ell_e} \begin{bmatrix} 1 & 0 & 0 & -1 & 0 & 0 \\ 0 & 0 & 0 & 0 & 0 & 0 \\ 0 & 0 & 0 & 0 & 0 & 0 \\ -1 & 0 & 0 & 1 & 0 & 0 \\ 0 & 0 & 0 & 0 & 0 & 0 \\ 0 & 0 & 0 & 0 & 0 & 0 \end{bmatrix} \tag{2.2}$$

where E_e, A_e and ℓ_e are the stiffness, cross-sectional area and length of member e, respectively. The 12 degrees-of-freedom Euler-Bernoulli beam local stiffness matrix can be found in Equation (5.116) of [447]. Note that the global stiffness matrix used in this work comes from the direct stiffness method (DSM), but it can be extended to other forms of deriving the stiffness matrix, e.g. with FE discretization.

The equilibrium equation in 2.1 can be split into free f and restricted r degrees of freedom, leaving

$$\left[\begin{array}{c|c} \mathbf{K_{ff}} & \mathbf{K_{fr}} \\ \hline \mathbf{K_{rf}} & \mathbf{K_{rr}} \end{array}\right] \left[\begin{array}{c} \mathbf{u_f} \\ \hline \mathbf{u_r} \end{array}\right] = \left[\begin{array}{c} \mathbf{0} \\ \hline \mathbf{f_r} \end{array}\right] \tag{2.3}$$

where the nodal forces vector on the free degrees of freedoms is null ($\mathbf{f_f} = \mathbf{0}$), since the loading is purely displacement imposition. Performing static condensation on the free degrees of freedom, the vector of nodal displacements $\mathbf{u_f}$ gives

$$\mathbf{u_f} = -\mathbf{K_{ff}}^{-1}\mathbf{K_{fr}}\mathbf{u_r} \tag{2.4}$$

and the nodal forces on the restricted nodes i.e. the reactions, are

$$\mathbf{f_r} = \left(\mathbf{K_{rr}} - \mathbf{K_{rf}}\mathbf{K_{ff}}^{-1}\mathbf{K_{fr}}\right)\mathbf{u_r} \tag{2.5}$$

The work done by external forces $\mathcal{W}_{\text{ext}}$ is now introduced into the lattice

$$\mathcal{W}_{\text{ext}} = \mathbf{f} \cdot \mathbf{u} = \mathbf{f_r} \cdot \mathbf{u_r} \tag{2.6}$$

An effective material with volume $|\Omega|$ is deemed energetically equivalent to the lattice structure. Uniaxial testing is performed and energies are equated to compute the equivalent stiffness of the lattice, specifically the Young's modulus along the $z-$axis direction - see Figure 2.2. The potential of the internal forces of the equivalent solid $\Pi_{\text{int}}^{\text{eq}}$ comes in the form

$$\Pi_{\text{int}}^{\text{eq}} = \int_{\Omega} \boldsymbol{\sigma}^{\text{eq}}\left(\boldsymbol{\varepsilon}^{\text{eq}}(\boldsymbol{x})\right) : \boldsymbol{\varepsilon}^{\text{eq}}(\boldsymbol{x}) \mathrm{d}V \tag{2.7}$$

where $\boldsymbol{\sigma}^{\text{eq}}$ and $\boldsymbol{\varepsilon}^{\text{eq}}$ are the equivalent body's Cauchy stress and infinitesimal strain second-order tensors, related through the constitutive law $\boldsymbol{\sigma}^{\text{eq}} = \mathbb{C}^{\text{eq}} : \boldsymbol{\varepsilon}^{\text{eq}}$, being $\mathbb{C}$ the fourth-order stiffness tensor. Note that any stress-strain work conjugate might be used since the material is working under its linear regime. Particularizing for uniaxial testing yields $\sigma_{zz}^{\text{eq}} = E_z^{\text{eq}} \varepsilon_{zz}^{\text{eq}}$, hence the integral in previous Equation 2.7 is straightforward to compute, namely

$$\Pi_{\text{int}}^{\text{eq}} = \sigma_{zz}^{\text{eq}} \varepsilon_{zz}^{\text{eq}} |\Omega| \tag{2.8}$$

The imposed displacement u^* is the same for both solids, so the (continuum-)equivalent strain $\varepsilon_{zz}^{\text{eq}}$ is

$$\varepsilon_{zz}^{\text{eq}} = \frac{u^*}{L_z} \tag{2.9}$$

where L_z is the longitudinal dimension along the studied direction z, i.e. the structure's vertical size. By energy balance, the potential of external forces and that of internal forces are equal in both lattice and equivalent solids, i.e. $\mathcal{W}_{\text{ext}} = \Pi_{\text{int}}^{\text{eq}}$, yielding

$$\mathbf{f_r} \cdot \mathbf{u_r} = E_z^{\text{eq}} \left(\frac{u^*}{L_z}\right)^2 |\Omega| \tag{2.10}$$

Taking into account that $|\Omega| = A_z L_z$, where A_z is the equivalent solid's cross-sectional perpendicular to the studied direction, the equivalent stiffness in $z-$direction E_z^{eq} is obtained:

$$E_z^{\text{eq}} = \frac{\mathbf{f_r} \cdot \mathbf{u_r}}{u^* A_z} \frac{L_z}{u^*} \tag{2.11}$$

Note that this is tantamount to computing the ratio of the resultant of the reaction forces $\mathbf{f_r}$ at the top face and the cross-sectional area perpendicular to the loading application A_z, i.e. dividing the equivalent stress σ_{zz} by the imposed strain ε_{zz}.

In the two other perpendicular directions, macro-scale responses in x and y are estimated by averaging displacements in the corresponding direction at the structure's external faces orthogonal to that direction. Then, the strains ε_{xx} and ε_{yy} are computed dividing the displacement magnitudes by their length. Then, the corresponding Poisson's ratios ν_{xz} and ν_{yz} can be computed

$$\nu_{xz} = -\frac{\varepsilon_{xx}}{\varepsilon_{zz}}, \quad \nu_{yz} = -\frac{\varepsilon_{yy}}{\varepsilon_{zz}} \tag{2.12}$$

2.1.1.3 Data Processing: Machine Learning

In this particular application, ML techniques have been chosen as surrogates to compute the lattice's global mechanical properties, in this case its equivalent Young's modulus E_z^{eq}. The motivation behind this choice boils down to computational efficiency.

2.1.1.3.1 Dense Neural Network Considering a toy example composed of linearly arranged springs, a plain Dense Neural Network (DNN) model is trained with the most meaningful variables. Pin-jointed truss lattices are sliced and weighted to predict the target property E_z^{eq}. Consider the 1D linear, elastic problem comprised of $e = 1, ..., n_s$ uniaxial elements with different axial stiffness $(EA)_e$ and equal length ℓ arranged in series, as in Figure 2.3.

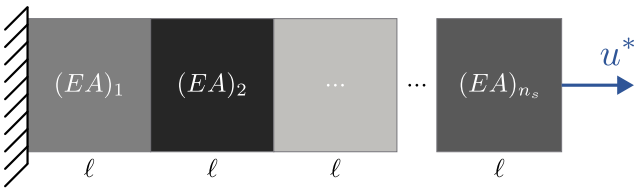

Figure 2.3: 1D linear, elastic problem composed of $e = 1, ..., n_s$ elements of same length ℓ and different axial stiffnesses $(EA)_e$, arranged in series.

The equivalent stiffness k_{eq} of n_s springs with constant k_e arranged in series is given by

$$k_{\text{eq}}^{-1} = \sum_{e=1}^{n_s} k_e^{-1} \tag{2.13}$$

Given the relation $k_e = (EA)_e/\ell_e$ between a spring e with constant k_e and a uniaxial element (i.e., bar) with stiffness $(EA)_e$ and length ℓ_e, the equivalent axial stiffness $(EA)_{\text{eq}}$ for Figure 2.3 is

$$(EA)_{\text{eq}} = \frac{n_s}{\sum_e (EA)_e^{-1}} \tag{2.14}$$

$(EA)_e$ being element e's axial stiffness. This is the equation to be learned when approaching this problem with ML. By means of the universal approximation theorem [448], this formula may be accurately represented by a sufficiently wide MLP/DNN architecture by feeding the member's axial stiffness $(EA)_e$ as inputs.

A DNN model is trained to this aim. Its input features are the elements' inverse axial stiffness $1/(EA)_e$, since this allows the DNN to better approximate the target $(EA)_{\text{eq}}$, i.e. Equation 2.14. The architecture is described in Table 2.1. From this point onward, 19 slices are considered ($n_s = 19$).

Layer	**Neurons**	**Activation**
Input	$n_s = 19$	selu [449]
Hidden #1	$5n_s = 95$	selu [449]
Output	1	linear

Table 2.1: Fully-connected DNN architecture for the toy example.

Parameter	**Choice**
Optimizer	nadam
Learning rate	0.001
Epochs	2000
Loss, $\mathcal{L}$	MSE
Validation split	15%

Table 2.2: Training hyper-parameters for the toy example.

Furthermore, a learning rate reduction on plateau by 0.5 and an early stopping criterion are applied on the loss function. Lastly, the dataset is generated by drawing $N = 20000 \times n_s$ samples from a uniform distribution $p(EA) \sim \mathcal{U}((EA)_{\text{min}}, (EA)_{\text{max}})$, where $(EA)_{\text{min}} = 10\,\text{N}$ and $(EA)_{\text{max}} = 100\,\text{N}$. This way, the set $\left\{ \{(EA)_e^{(i)}\}_{e=1}^{n_s}, (EA)_{\text{eq}}^{(i)} \right\}_{i=1}^{N}$ is generated.

A random train-test split of 85/15% is enforced, and both features and targets normalized with a standard scaler. Training hyper-parameters are shown in Table 2.2, with *nadam* as an optimizer [92].

Analogously, the randomly-generated lattice structures are now sliced into n_s parts, defining an "effective" area per slice (n_s in total), to train a DNN with inverse of their effective areas as inputs. A schematic drawing of a general slice s is depicted in Figure 2.4.

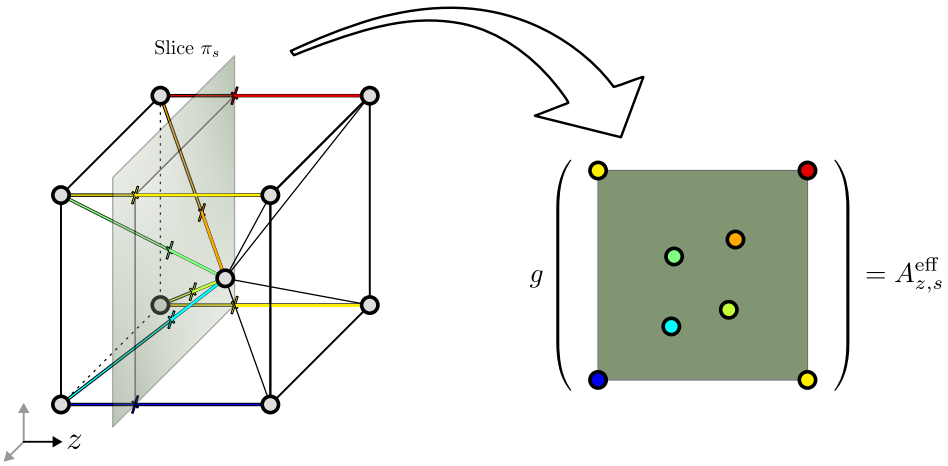

Figure 2.4: Lattice slicing perpendicular to $z-$axis for an arbitrary plane π_s. Joints are gray and intersected bars and their cross-section are colored. The slice's effective area $A^{\text{eff}}_{z,s}$ transverse to z is given by a yet unknown function g.

To define the effective area per slice, the function $g(\cdot)$ is applied to the areas and directions of the bars intersected by the slice. Given an element e with cross-sectional area A_e and unit vector $\boldsymbol{n}_e = [\cos\theta_{x,e}, \cos\theta_{y,e}, \cos\theta_{z,e}]^\intercal$, the effective area $A^{\text{eff}}_{z,s}$ of the slice s perpendicular to the z-axis is computed as the sum of all intersected bars' projected areas along z in the plane π_s, i.e.

$$A^{\text{eff}}_{z,s} = \sum_{e \in \pi_s} A_e \cos^2\theta_{z,e}. \tag{2.15}$$

The quadratic exponent in the cosine function in Equation 2.15 comes from the projection of both the forces and displacements onto the local bar axis, as displayed in Figure 2.5. By simple rotations, the equivalent stiffness K^{eq}_{xx} in the x direction is given by the actual bar stiffness, i.e. EA/ℓ, multiplied by the cosine square of the angle between the bar and the $x-$axis:

$$K^{\text{eq}}_{xx} = \frac{EA}{\ell}\cos^2\theta_x \tag{2.16}$$

The same definition applies to any other direction d, with its respective cosine $\cos\theta_d$ as input.

Lastly, the transverse effective areas have to be considered when generalizing the problem from 1D to 2D or 3D. Let I and II be two 2D lattice structures, with slightly different square unit cells of length ℓ, depicted in Figure 2.6. All bars are made of the same material with Young's modulus E and the same cross-sectional area A. Both lattices I and II have the same effective area perpendicular to x, i.e. $A^{\text{eff}}_{x,s} = 3A$ for every slice s contained in the structure, according to Equation 2.15.

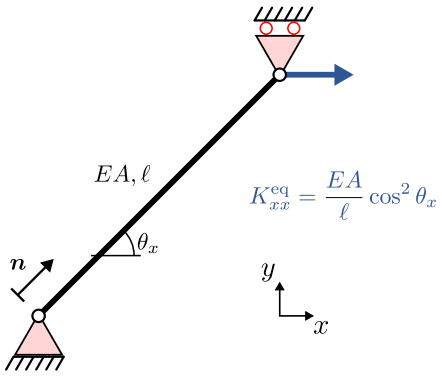

Figure 2.5: Equivalent stiffness K_{xx}^{eq} along direction x for a strut. The bar presents an arbitrary inclination with respect to x defined by the angle θ_x.

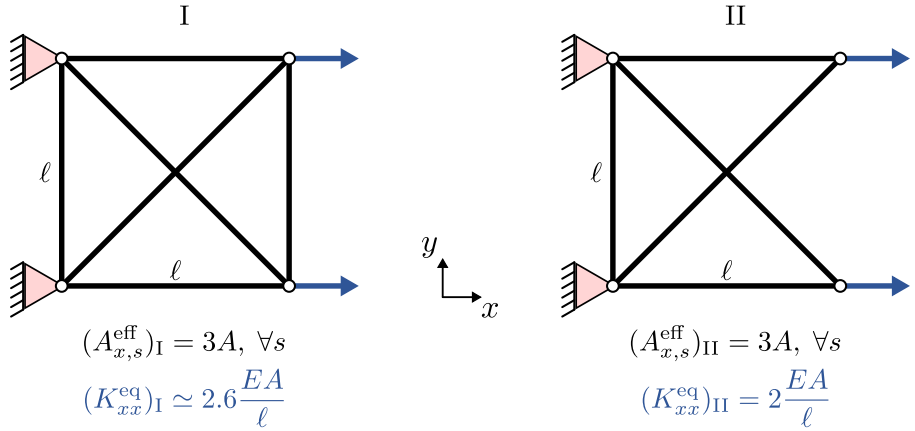

Figure 2.6: 2D lattice structures I and II made of different square unit cells of length ℓ. Whereas the effective area transverse to x is the same, $(A_{x,s}^{\text{eff}})_{\text{I}} = (A_{x,s}^{\text{eff}})_{\text{II}} = 3A$ (for every slice s), the equivalent stiffness differs, $(K_{xx}^{\text{eq}})_{\text{I}} \simeq 2.6EA/\ell$ and $(K_{xx}^{\text{eq}})_{\text{II}} = 2EA/\ell$.

However, the equivalent stiffnesses K_{xx}^{eq} following the previously derived procedure are different for cases I and II, i.e. $(K_{xx}^{\text{eq}})_{\text{I}} \neq (K_{xx}^{\text{eq}})_{\text{II}}$, due to transverse effects: lattice II is the same as lattice I with a (transverse) bar removed. Therefore, the effective areas $A_{y,s}^{\text{eff}}$ perpendicular to y have to be considered likewise in the surrogate model to yield accurate predictions for the general, multi-axial case. These effective areas for the lattices in Figure 2.6 are $(A_{y,s}^{\text{eff}})_{\text{I}} = 2A$ and $(A_{y,s}^{\text{eff}})_{\text{II}} = A$.

2.1.1.3.2 Graph Neural Network The lattice is now re-interpreted as a graph $\mathcal{G}(\mathcal{V}, \mathcal{E})$ with joints as vertices $\mathcal{V}$ and struts as edges $\mathcal{E}$. By defining nodal and edge features, the GNN model is built, being agnostic to input data size. Hence, a properly trained GNN should be able to make predictions for two lattices with different topologies, i.e. regardless of differences in the number of nodes and/or struts.

In this case, only geometrical features are given as inputs, depriving the GNN of any mechanical context to assess its ability to mimic the underlying equations, that is, the equilibrium laws and computation of the sought equivalent property. Joint j's three spatial coordinates (x_j, y_j, z_j) are fed as node features, whereas the edge features are given by the coordinates of both endpoints (0,1), i.e. $(x_{e0}, y_{e0}, z_{e0}), (x_{e1}, y_{e1}, z_{e1})$, and their bar/beam e's associated length ℓ_e: seven in total.

Thus, only structured geometrical graph information fuels the GNN model. Since the base material is the same as in the previous examples (316 Stainless Steel), no material information is provided nor needed. Otherwise, it could be defined as a feature at the edge level. Note that heterogeneous lattices (e.g. multi-material) are admitted in these architectures. The variable to be predicted is again the equivalent Young's modulus E_z^{eq} along $z-$axis. The dataset can be compactly represented as $\left\{\{(x_j^{(i)}, y_j^{(i)}, z_j^{(i)})\}_{j=1}^{n_j}, \{(x_{e0}^{(i)}, y_{e0}^{(i)}, z_{e0}^{(i)}), (x_{e1}^{(i)}, y_{e1}^{(i)}, z_{e1}^{(i)}), \ell_e^{(i)}\}_{e=1}^{n_e}, E_z^{\text{eq}(i)}\right\}_{i=1}^{N}$.

The model's architecture comprises the following parts and steps:

1. Initial dense or fully connected (FC) layers are applied separately for each node and edge.
2. Two graph updates (or hops) update the node embeddings.
3. A FC output layer performs pooling in a convolutional fashion.

Module	**Layer**	**Input shape**	**Output shape**	**Activation**
Node embedding	Dense	$(3,)$	$(5,)$	PReLU
Edge embedding	Dense	$(7,)$	$(5,)$	PReLU
Graph Update #1	Message passing	$(15,)$	$(10,)$	selu
	Convolution (mean)	$(10 \times n_m,)$	$(10,)$	–
	Dense	$(15,)$	$(10,)$	selu
Graph Update #2	Message passing	$(25,)$	$(10,)$	selu
	Convolution (mean)	$(10 \times n_m,)$	$(10,)$	–
	Dense	$(20,)$	$(10,)$	selu
Output	Pooling (mean)	$(10 \times n_j,)$	$(10,)$	–
	Dense	$(10,)$	$(1,)$	linear

Table 2.3: Pin-jointed truss lattice GNN model.

Further details are displayed in Table 2.3. Their hyper-parameters have been computed after running a shallow, brute-force hyper-tuning, varying the output shape of the different layers in a range within the order of magnitude of the nodes and edges features. Similar configurations are rather close.

Table 2.3 summarizes the architecture of the graph-level regression, where the second component of the shapes is the batch size the model is fed with. Note that n_m in the convolution layer stands for the number of messages (adjacencies) arriving to one node in the graph - different for each node - and n_j in the pooling layer is the number of joints (nodes) per graph - different for every graph.

The input and output shapes displayed in Table 2.3 operate as follows. There are 3 node features i.e. the coordinates, which are expanded into 5 through the node embedding (dense) model. Similarly, 7 edges features are compressed into 5 through the (dense) edge embedding. This way, both dense models present a balanced output shape - recall that the compression performed in the edge embedding does not lose critical information, since 6 out of 7 edge features are nodal coordinates, which have been already embedded in the nodes.

The proposed GNN architecture is sketched in Figure 2.7. Dense layers (depicted in yellow) are initially applied to each node and edge in the graph, outputting node and edge embeddings of size 5. Overall, this ANN layout performs the following steps:

1. In the first graph update, a message is passed through the edges through a dense layer which inputs the concatenation of the node embeddings for both endpoints (shapes: $5+5$) and their respective edge embedding (shape: 5), with a total of 15 features. The message passing (dense) layer has an output size of 10.
2. Later on, the n_m messages merging in all arrival nodes are averaged, performing n_j convolutions. Then, an extra dense layer, taking the old node state and the convoluted features (shape: $5+10$) as input, outputs the new node state, where each node has a feature size of 10.
3. The second graph update is performed analogously, yielding new node states of size 10.
4. Just after that, an element-wise pooling layer averages the features of all nodes in a graph, encapsulating the graph in a total of 10 features.
5. Then, a final dense layer is applied to compress these 10 features into a unique output, which is the effective property predicted (per graph).

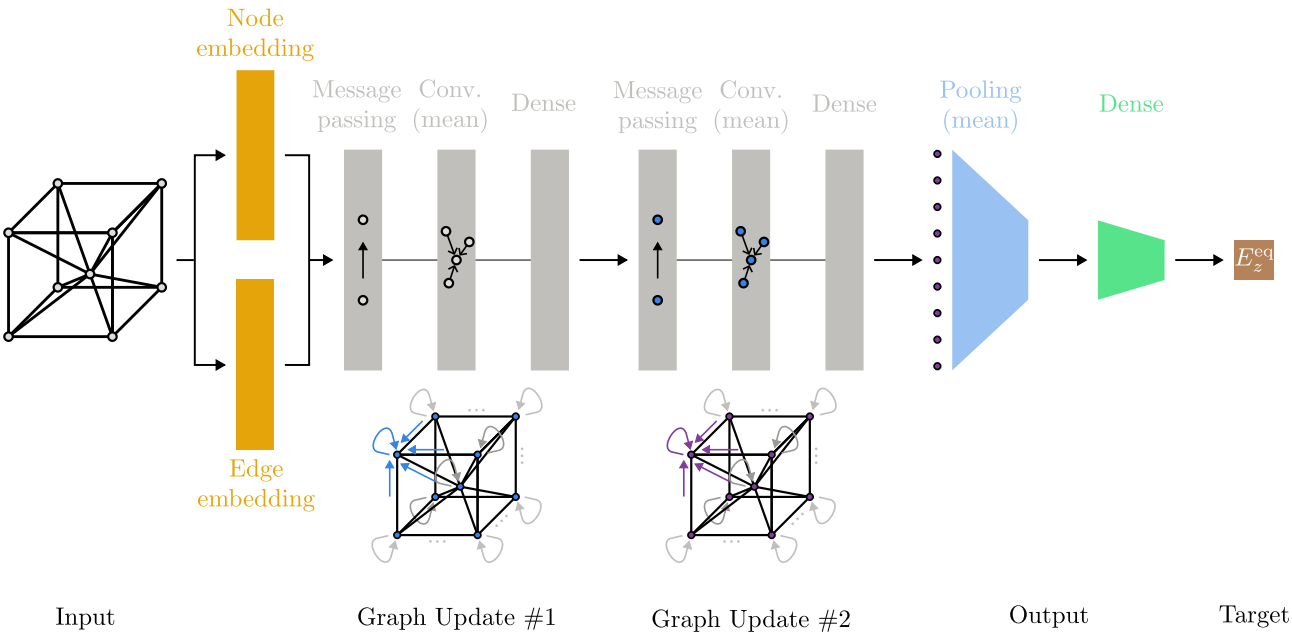

Figure 2.7: Schematic drawing of the GNN model's architecture for a pin-jointed truss.

2.1.2 Special Case: Partial Observability

Some hindrances in surrogate modeling have already been mentioned in the Introduction and State of the Art chapters. Issues related to variable definition and measurement have been emphasized most concerning, so a particular study has been dedicated to models built upon partially observable phenomena. This subsection is an extract of the author's research article "**Modeling systems from partial observations**" [1].

2.1.2.1 Models Relating Observable Features

Now, the problem of relating observable features to each other to bypass unknown (and unmeasurable) internal variables will be addressed. Consider a large system, whose behavior is described by a number of state variables, assumed well defined. The model governing the state or its time evolution is deemed unknown and the data describing the state is only observable and measurable on a part of the system, remaining unattainable otherwise. Previous analyses on the field can be found in [450] or [10].

In the two-mass oscillator in Figure 2.8, the state is perfectly defined by each bead's position and momentum, but only the second mass is accessible (and thus, measurable). The possibility of learning the model that governs the observable state (q_2, p_2) while ignoring the the first mass (q_1, p_1) is pondered.

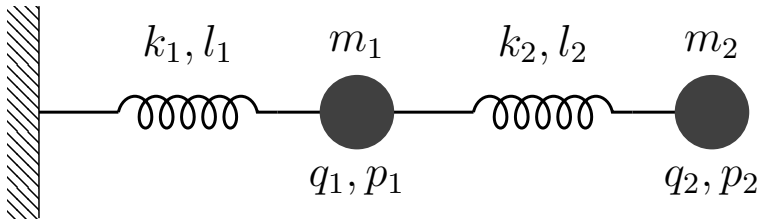

Figure 2.8: Oscillator composed of two masses, two linear springs of stiffness k_1 and k_2, reference lengths l_1 and l_2, whose state is defined by the position and momentum of each mass (q_1, p_1, q_2, p_2).

This question will be addressed using quite generic algebra in two situations: time-independent and a transient problems. The most generic setting is examined as a mass-oscillator system.

2.1.2.1.1 Time-Independent Problem A generic linear time-independent model is given by

$$\mathbf{K}\mathbf{U} = \mathbf{F} \tag{2.17}$$

which, considering the observable variables $\mathbf{U_o}$ and the internal ones $\mathbf{U_i}$, can be rewritten as

$$\begin{pmatrix} \mathbf{K_{oo}} & \mathbf{K_{oi}} \\ \mathbf{K_{io}} & \mathbf{K_{ii}} \end{pmatrix} \begin{pmatrix} \mathbf{U_o} \\ \mathbf{U_i} \end{pmatrix} = \begin{pmatrix} \mathbf{F_o} \\ \mathbf{F_i} \end{pmatrix} \tag{2.18}$$

Developing the last equation yields

$$\mathbf{K_{io}}\mathbf{U_o} + \mathbf{K_{ii}}\mathbf{U_i} = \mathbf{F_i} \rightarrow \mathbf{U_i} = \mathbf{K_{ii}^{-1}}\mathbf{F_i} - \mathbf{K_{ii}^{-1}}\mathbf{K_{io}}\mathbf{U_o} \tag{2.19}$$

and introducing the resulting expression of $\mathbf{U}_i$ into the first development, static condensation can be performed on observable o and internal i degrees of freedom:

$$(\mathbf{K_{oo}} - \mathbf{K_{oi}}\mathbf{K_{ii}^{-1}}\mathbf{K_{io}})\mathbf{U_o} = \mathbf{F_o} - \mathbf{K_{oi}}\mathbf{K_{ii}^{-1}}\mathbf{F_i} \tag{2.20}$$

which can be rewritten as

$$\tilde{\mathbf{K}}_{\mathbf{oo}}\mathbf{U_o} = \mathbf{F_o} - \tilde{\mathbf{F}}_{\mathbf{i}} \tag{2.21}$$

with

$$\begin{cases} \tilde{\mathbf{K}}_{\mathbf{oo}} = (\mathbf{K_{oo}} - \mathbf{K_{oi}}\mathbf{K_{ii}^{-1}}\mathbf{K_{io}}) \\ \tilde{\mathbf{F}}_{\mathbf{i}} = \mathbf{K_{oi}}\mathbf{K_{ii}^{-1}}\mathbf{F_i} \end{cases} \tag{2.22}$$

Several observations can be extracted from Equation 2.22:

- If $\mathbf{F_i} = \mathbf{0}$, a direct relation exists between $\mathbf{U_o}$ and $\mathbf{F_o}$.

- For a 1D system with accessible (observable) borders, $\mathbf{U_o}$ and $\mathbf{F_o}$ contain two components each. Applying $\mathbf{U_o}^T = (1,0)$, the resulting $\mathbf{F_o}$ represents $\tilde{\mathbf{K}}_{\mathbf{oo}}$'s first column and the solution $\mathbf{F_o}$ related to $\mathbf{U_o}^T = (0,1)$ will be $\tilde{\mathbf{K}}_{\mathbf{oo}}$'s second column.
- In the same one-dimensional system, when $\mathbf{F_i} \neq \mathbf{0}$, there are two effective internal variables, i.e. the components of $\tilde{\mathbf{F}}_\mathbf{i}$ convey all the richness of $\mathbf{F_i}$. This generates some sort of irreversibility: $\tilde{\mathbf{F}}_\mathbf{i}$ can be obtained from $\mathbf{F_i}$, but not the other way around.
- Computing these two internal variables needs additional steps, e.g. $\mathbf{F_o} = \tilde{\mathbf{F}}_\mathbf{i}$ when $\mathbf{U_o} = \mathbf{0}$.

Condensation of internal degrees of freedom into the observable ones increases entropy in an information theory sense: many micro-states $\mathbf{F_i}$ are linked to the macro-state $\tilde{\mathbf{F}}_\mathbf{i}$ (surjection).

2.1.2.1.2 Time-Dependent Problem Let a general linear second-order dynamical system be considered

$$\mathbf{M}\ddot{\mathbf{U}} + \mathbf{C}\dot{\mathbf{U}} + \mathbf{K}\mathbf{U} = \mathbf{F} \tag{2.23}$$

which, applying Fourier transform, becomes

$$-\omega^2\mathbf{M}\mathbb{U} + i\omega\mathbf{C}\mathbb{U} + \mathbf{K}\mathbb{U} = \mathbb{F} \tag{2.24}$$

with $i \equiv \sqrt{-1}$ (not to be confused with index i indicating internal variables or vector components) and $\mathbb{U}$ and $\mathbb{F}$ being the Fourier transforms of $\mathbf{U}$ and $\mathbf{F}$, respectively. Equation 2.24 can be rewritten as

$$\mathbf{K}^*\mathbb{U} = \mathbb{F} \tag{2.25}$$

in which $\mathbf{K}^* = -\omega^2\mathbf{M} + i\omega\mathbf{C} + \mathbf{K}$. Again, Equation 2.25 can be separated for each possible frequency (ω) involved in loading and operating in the complex domain, leading to

$$\tilde{\mathbf{K}}^*_{\mathbf{oo}}\mathbb{U}_\mathbf{o} = \mathbb{F}_\mathbf{o} - \tilde{\mathbb{F}}_\mathbf{i}, \tag{2.26}$$

thus verifying the same conclusions as the time-independent case, if the Fourier transform applies. This is true in the forced regime, i.e. far from the transient effects induced by the initial condition. For transient regimes, the Laplace transform could be used instead, although at a higher computational cost. The internal loading's Fourier transform should remain invariant in training to ensure the model's validity to relate observable variables in the time domain under certain constraints, e.g. dependence of $\tilde{\mathbb{F}}_i$ on the internal loading $\mathbb{F}_i$. This would imply considering history, implicit in the Fourier transform.

2.1.2.1.3 Time-Dependent Problems in the Time Domain Finally, to reinforce the previous conclusions, time-dependent problems modeling directly operating in the time domain will be studied. For the sake of simplicity, let the first order dynamical system

$$\mathbf{C}\dot{\mathbf{U}} + \mathbf{K}\mathbf{U} = \mathbf{F} \tag{2.27}$$

serve as an example, whose implicit time discretization reads

$$\mathbf{C}\mathbf{U}^n + \Delta t\mathbf{K}\mathbf{U}^n = \Delta t\mathbf{F}^n + \mathbf{C}\mathbf{U}^{n-1} \tag{2.28}$$

with Δt being the considered time-step. This equation can be reshaped into

$$\mathbf{K}^*\mathbf{U}^n = \mathbf{F}^{*,n} + \mathbf{C}\mathbf{U}^{n-1} \tag{2.29}$$

with $\mathbf{K}^* = \mathbf{C} + \Delta t\mathbf{K}$ and $\mathbf{F}^{*,n} = \Delta t\mathbf{F}^n$.

These equations can be sequenced in a matrix form, as in Dynamic Model Decomposition [451]:

$$\mathbf{K}^*\left[\mathbf{U}^n, ..., \mathbf{U}^1\right] = \left[\mathbf{F}^{*,n}, ..., \mathbf{F}^{*,1}\right] + \mathbf{C}\left[\mathbf{U}^{n-1}, ..., \mathbf{U}^0\right] \tag{2.30}$$

Defining the extended vectors $\mathcal{U}$ and $\mathcal{F}$:

$$\begin{cases} \mathcal{U}^T = [\mathbf{U}^{n^T}, \mathbf{U}^{n-1^T} ..., \mathbf{U}^{0^T}] \\ \mathcal{F}^T = [\mathbf{F}^{n^T}, \mathbf{F}^{n-1^T}, ..., \mathbf{F}^{1^T}] \end{cases} \tag{2.31}$$

and the extended matrix $\mathcal{K}$

$$\mathcal{K} = \begin{pmatrix} \mathbf{K}^* & -\mathbf{C} & \mathbf{0} & ... & ... \\ \mathbf{0} & \mathbf{K}^* & -\mathbf{C} & \mathbf{0} & ... \\ ... & ... & ... & ... & ... \end{pmatrix} \tag{2.32}$$

The previous system reads

$$\mathcal{K}\mathcal{U} = \mathcal{F} \tag{2.33}$$

where the solution $\mathcal{U}$ is, in general, computed from the $\mathcal{K}$ matrix pseudo-inverse.

This algebraic system can be addressed as before, although now the model explicitly involves the time evolution of input(s) and output(s), hence reinforcing the result obtained via Fourier transform.

An alternative formulation, more aligned with ML techniques, needs explicit integration:

$$\mathbf{C}\mathbf{U}^n = \Delta t\mathbf{F}^n - \Delta t\mathbf{K}\mathbf{U}^{n-1} + \mathbf{C}\mathbf{U}^{n-1} \tag{2.34}$$

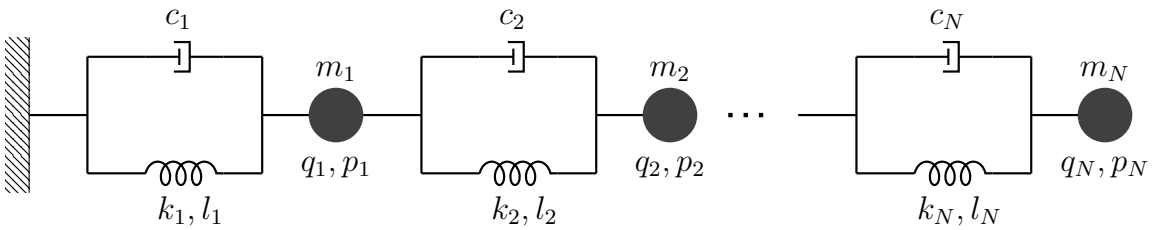

Figure 2.9: N-mass dynamical system composed of Kelvin-Voigt cells (mass-spring-damper).

that can be reformulated as

$$\mathbf{U}^n = \mathbf{A}\mathbf{F}^n + \mathbf{B}\mathbf{U}^{n-1} \tag{2.35}$$

which can be perfectly expressed by the RNN architecture in Figure 1.1. When the model concerns only the state's observable part, RNN and LSTM seem especially appealing to carry out the task.

2.1.2.2 Learning in the Fourier Space

Consider the linear N-mass dynamical system, including inertia, elastic and damping behaviors, illustrated in Figure 2.9. The state of each mass is represented by $\mathbf{z}_i = (q_i, p_i)$, q_i and p_i being the i-th mass position and momentum, respectively. The system's state is defined by the extended vector $\mathbf{Z}^T = (\mathbf{z}_1^T, ..., \mathbf{z}_N^T)$. Newton's equation leads to

$$\dot{\mathbf{Z}} = \mathbf{T}\mathbf{Z} + \mathbf{J} + \mathbf{F}, \tag{2.36}$$

where matrix $\mathbf{T}$ includes the system's mechanical properties: masses, spring stiffness and damper viscosity. On the other hand, $\mathbf{J}$ is a constant vector (in the linear case addressed below) and $\mathbf{F}$ contains external forces applied on masses at odd positions.

In the forced regime, the Fourier transform becomes a valuable route. The dynamical model in the Fourier domain reads

$$(-\mathbf{T} + i\omega\mathbf{I})\,\mathbb{Z} = \mathbb{J} + \mathbb{F}. \tag{2.37}$$

By defining the effective loading $\mathbb{S} = \mathbb{J} + \mathbb{F}$, and $\tilde{\mathbf{T}} = -\mathbf{T} + \mathbf{i}\omega\mathbf{I}$, the matrix form with separated degrees of freedom related to the measurable position (noted by q) and the derived momentum (p) comes as:

$$\begin{pmatrix} \tilde{\mathbf{T}}_{\mathbf{qq}}(\omega) & \mathbf{T}_{qp} \\ \mathbf{T}_{pq} & \tilde{\mathbf{T}}_{\mathbf{pp}}(\omega) \end{pmatrix} \begin{pmatrix} \mathbb{Z}_q(\omega) \\ \mathbb{Z}_p(\omega) \end{pmatrix} = \begin{pmatrix} \mathbb{S}_q(\omega) \\ \mathbb{S}_p(\omega) \end{pmatrix} = \begin{pmatrix} \mathbf{0} \\ \mathbb{S}_p(\omega) \end{pmatrix} \tag{2.38}$$

Since $\mathbb{S}_q(\omega) = \mathbf{0}$, $\mathbb{Z}_p(\omega)$ can be expressed in terms of $\mathbb{Z}_q(\omega)$:

$$\tilde{\mathbf{T}}_{\mathbf{qq}}(\omega)\mathbb{Z}_{\mathbf{q}}(\omega) + \mathbf{T}_{\mathbf{qp}}\mathbb{Z}_{\mathbf{p}}(\omega) = \mathbf{0} \rightarrow \mathbb{Z}_{\mathbf{p}}(\omega) = -\mathbf{T}_{\mathbf{qp}}^{-\mathbf{1}}\tilde{\mathbf{T}}_{\mathbf{qq}}(\omega)\mathbb{Z}_{\mathbf{q}}(\omega), \tag{2.39}$$

which, introduced into the second equation, leads to:

$$\left(\mathbf{T}_{pq} - \tilde{\mathbf{T}}_{pp}(\omega)\mathbf{T}_{qp}^{-1}\tilde{\mathbf{T}}_{qq}(\omega)\right)\mathbb{Z}_q(\omega) = \mathbb{S}_p(\omega), \tag{2.40}$$

or, in a more compact form:

$$\mathbf{A}(\omega)\mathbb{Q}(\omega) = \mathbb{R}(\omega), \tag{2.41}$$

with $\mathbf{A}(\omega) = \mathbf{T}_{pq} - \tilde{\mathbf{T}}_{pp}(\omega)\mathbf{T}_{qp}^{-1}\tilde{\mathbf{T}}_{qq}(\omega)$, $\mathbb{Q}(\omega) \equiv \mathbb{Z}_q(\omega)$ and $\mathbb{R}(\omega) \equiv \mathbb{S}_p(\omega)$.

Thus, momentum is removed from the state variables, since it derives directly from the measurable position. Now, internal and observable degrees of freedom can be separated:

$$\begin{pmatrix} \mathbf{A}_{\mathbf{oo}}(\omega) & \mathbf{A}_{\mathbf{oi}}(\omega) \\ \mathbf{A}_{\mathbf{io}}(\omega) & \mathbf{A}_{\mathbf{ii}}(\omega) \end{pmatrix} \begin{pmatrix} \mathbb{Q}_{\mathbf{o}}(\omega) \\ \mathbb{Q}_{\mathbf{i}}(\omega) \end{pmatrix} = \begin{pmatrix} \mathbb{R}_{\mathbf{o}}(\omega) \\ \mathbb{R}_{\mathbf{i}}(\omega) \end{pmatrix} \tag{2.42}$$

leading to

$$\tilde{\mathbf{A}}_{\mathbf{oo}}(\omega)\mathbb{Q}_{\mathbf{o}}(\omega) = \mathbb{R}_{\mathbf{o}}(\omega) - \tilde{\mathbb{R}}_{\mathbf{i}}(\omega), \tag{2.43}$$

with $\tilde{\mathbb{R}}_{\mathbf{i}}(\omega) = \mathbf{A}_{\mathbf{oi}}(\omega)\mathbf{A}_{\mathbf{ii}}^{-1}(\omega)\mathbb{R}_{\mathbf{i}}(\omega)$ and $\tilde{\mathbf{A}}_{\mathbf{oo}}(\omega) = \mathbf{A}_{\mathbf{oo}}(\omega) - \mathbf{A}_{\mathbf{oi}}(\omega)\mathbf{A}_{\mathbf{ii}}^{-\mathbf{1}}(\omega)\mathbf{A}_{\mathbf{io}}(\omega)$, where the same previously discussed remarks apply.

2.1.2.3 Neural Network Modeling

A simplified RNN architecture - see Figure 1.1 - models the system's dynamics at time step t. It predicts the present hidden state $\mathbf{h}_t$ and the output $\mathbf{y}_t$ on account of the incoming hidden state resulting from the previous time step $t-1$, $\mathbf{h}_{t-1}$ and the present value of the loading $\mathbf{x}_t$. The input data at time t could also contain some partial values of the latter. To simulate time evolution it suffices to re-inject the RNN output $\mathbf{h}_t$ as the input at the next time step (hence its name, "recurrent"), enabling the calculation of the model response (time series $\mathbf{y}_t$) from the input (time series $\mathbf{x}_t$).

The LSTM structure chosen for this study is displayed in Figure 1.2 for a unit cell, its functioning described in Section 1.1. This approach combines several RNN and LSTM units (accounting for the n previous states) within the so-called RNN or LSTM-block. Figure 2.10 describes the chaining n LSTM units.

The LSTM-block unit proceeds from an arbitrary choice of the initial state of both short and long memory states, $\mathbf{h}_0$ and $\mathbf{c}_0$ respectively. After transiting through n units, subjected to inputs $\mathbf{x}_t$, $\cdots$, $\mathbf{x}_{t-n-1}$, the output $\mathbf{y}_t$ has almost totally forgot the initial hidden states $\mathbf{h}_0$ and $\mathbf{c}_0$, its value being almost entirely dictated by the n most recent inputs. Thus, only the output of the last LSTM unit composing the LSTM-block is used. In this architecture, LSTM-blocks act as integrators.

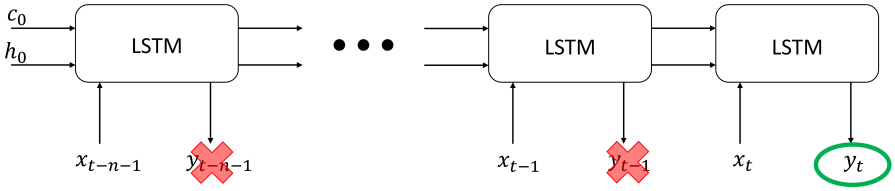

Figure 2.10: LSTM-block architecture.

2.2 Structural Design and Optimization

This section provides an overview of all techniques used, explored and/or developed to actively design the topology/geometry of a prototype from a desired global property or mechanical response, i.e. the "inverse problem", contemplating discrete (lattices, trusses) and continuous domains (bulk materials).

2.2.1 Discrete Structures: Trusses and Lattices

Firstly, discrete, strut-based design spaces (lattices and trusses) will be explored, due to the conceptual simplifications coming from a reduced domain, plus the clear analytical expressions relating structures to properties - now learned through an inverse surrogate model.

2.2.1.1 For a Target Global Property

The GNN surrogate models derived in Section 2.1 are now used to obtain the lattice structure given a user-prescribed Young's modulus $E_z^{\text{eq},*}$. As a non-bijective function, the inverse problem is ill-posed [187, 188]. Although a Newton-Raphson approach to obtain numerically the inputs for an output may be derived - computed via automatic differentiation [452] - unable to yield the number of nodes, struts and their adjacencies, i.e. the graph $\mathcal{G}$. Node and edge features and adjacencies are fed as inputs.

A database with 100 000 samples is rapidly generated through the surrogate to cover a wide range of Young's moduli E_z^{eq}. With a big enough sample size, several structural choices can yield the same effective property (surjection).

Hence, weight is introduced as second design parameter (or volume V as defined in Equation 3.3, for the same material), which could prove advantageous in structural optimization problems. The minimum-weight lattice will be sought among all structures. To study the maximum-stiffness-minimum-weight configurations, every pair $\{(V^{-1(i)}, E_z^{\mathrm{eq}(i)})\}_{i=1}^{N}$ is represented in a 2D scatter plot in Figure 3.14. Then, a Pareto front [453] is defined given the best stiffness-weight trade-offs, depicted in red.

2.2.1.2 For a Prescribed Mechanical Response

Metamaterial optimization is done mainly through two procedures: shape [28] and topological optimization [29]. However, these common methodologies are usually meant for static and deterministic loading, i.e. non time-dependent and fixed loads (position- and module-wise) determine the tailored optimal structure. This seems unfit for many metamaterial applications involving dynamic effects, such as vibration or impact attenuation.

To address the first issue (dynamic loading instead of static), which directly concerns Structural Health Monitoring (SHM) [454, 136, 135] as it deals with both static (buckling, creep) and non-static failure (fatigue), a biologically-inspired approach is proposed. Following the explained local-failure rationale, metamaterial architectures would greatly benefit from a disorganized, trabecular-like aperiodic architecture (like human bones) in which no two single struts behave identically under the same global loading conditions, as in [103].

Moreover, bones gradually adapt their tissue to the person's evolving mechanical needs. Trabecular (spongy) tissue is created according to a given loading state in just enough quantities to withstand it. Should the loading conditions change, the bone's "control cells" (osteocytes) will issue the creation (by osteoblasts) or destruction (by osteoclasts) of tissue to adjust its topology to its new needs. This includes static loading phenomena affecting artificial structures as well, like creep or relaxation. As opposed to topology optimization methods (e.g. SIMP [29]) with the full continuum as starting point, a discrete domain including a finite number of struts and predefined void areas is addressed here.

The 2D problem is considered as a starting point, from which latter 3D generalizations might stem. An aperiodic planar lattice is stretched a given amount u_0 from its top and bottom clamp nodes, in the vertical direction (y-axis). Considering Euler-Bernoulli 2D beams (implying reaction forces and momenta), their mechanical response is given by

$$\begin{Bmatrix} F_{1x} \\ F_{1y} \\ M_{1z} \\ F_{2x} \\ F_{2y} \\ M_{2z} \end{Bmatrix} = \begin{bmatrix} AE/\ell & 0 & 0 & -AE/\ell & 0 & 0 \\ 0 & 12EI/\ell^3 & 6EI/\ell^2 & 0 & -12EI/\ell^3 & 6EI/\ell^2 \\ 0 & 6EI/\ell^2 & 4EI/\ell & 0 & -6EI/\ell^2 & 2EI/\ell \\ -AE/\ell & 0 & 0 & AE/\ell & 0 & 0 \\ 0 & -12EI/\ell^3 & -6EI/\ell^2 & 0 & 12EI/\ell^3 & -6EI/\ell^2 \\ 0 & 6EI/\ell^2 & 2EI/\ell & 0 & -6EI/\ell^2 & 4EI/\ell \end{bmatrix} \begin{Bmatrix} u_{1x} \\ u_{1y} \\ \gamma_{1z} \\ u_{2x} \\ u_{2y} \\ \gamma_{2z} \end{Bmatrix} \tag{2.44}$$

Where I denotes inertial terms with respect to axis Z, orthogonal to the 2D plane XY in which the structure is contained. Condensating again restrained degrees of freedom into free ones (Equations 2.3-2.5), reaction forces $\mathbf{F_r}$ are easily obtainable. The goal is to rearrange the position of the structure's inner nodes (thus changing their lengths ℓ) and/or adjust the struts' radii r (and so, their cross-section A) to transform F_r into a prescribed target response F_p within reasonably similar ranges.

The nature of F_p must ensure a different force distribution from reactions along clamp nodes (top and bottom sides) while close enough to be achievable through optimization, e.g. an exponentially decreasing function from $F_{r,max}$ to $F_{r,min}$ (softening the force gradient) or perhaps $F_{r,mean}$ (averaging efforts across the clamps). This is done separately for top and bottom clamps, simulating a knee or hip prosthesis, for instance, where different materials can be found on either end. The other two sides in the 2D contour (left and right) can move freely, always within dominion limits - see Figure 3.17 left.

After the first loading process, reactions on clamp nodes and axial forces on struts are obtained via Equation 2.44. For each inner (not clamp-contained) strut b stemming from a clamp node i, a "load index" ind_b is assigned, succinctly describing its loading state:

$$ind_b = \gamma_b\{\alpha_b, \beta_b\}|\overrightarrow{\mathbf{n_{prop}}}| = (\bar{F_{p,i}} - \bar{F_{r,i}})\{\frac{\sigma_b}{\sigma_{crit}}, 1 - \frac{\sigma_b}{\sigma_{crit}}\}|\overrightarrow{\mathbf{n_{ref}}} \cdot \overrightarrow{\mathbf{n_b}}| \tag{2.45}$$

Each component in Equation 2.45 has a specific function:

- The "offset" term $\gamma_b = \bar{F_{p,i}} - \bar{F_{r,i}}$ is the (normalized) difference in external forces (clamp-stemming struts only, one of whose ends is assigned a target prescribed force $F_{p,i}$). It acts as a sort of implicit loss function, quantifying how far the obtained response F_r is from the target F_p. If $\gamma_b < 0$, the signal to be emitted is inhibitory (order: reduce load to target). If $\gamma_b > 0$, the command is excitatory: load must be increased to reach the target. In biological fashion, excitatory and inhibitory signals are sent from the clamp nodes through their neighboring struts.

- The conjugate "critical" terms $\alpha_b = 1 - \sigma_b/\sigma_{crit}$ and $\beta_b = 1 - \alpha_b$ are indicators for axial load criticality: how close the struts are to a critical tension σ_{crit}. This threshold depends on optimization priorities, e.g. the elastic limit σ_Y to prevent plasticity, σ_{Euler} to impede buckling or σ_L to thwart breakage altogether. Thus, it is a measure of structural integrity. For inhibitory signals ($\gamma_b < 0$), α_b is preferred, whereas β_b is chosen for excitatory ones ($\gamma_b < 0$).
- The "direction" term $|\overrightarrow{\mathbf{n_{ref}}} \cdot \overrightarrow{\mathbf{n_b}}|$ captures the fraction of the received signal projected onto the neighboring struts according to their orientation. This is computed as the absolute dot product (cosine vectors) of a reference input strut from which the "load signal" is coming, $\mathbf{n_{ref}}$, and the current strut's, $\mathbf{n_b}$. So, signals can propagate back in an opposite direction than expected.

After that first assignment to the clamp's neighboring struts, the "load signal" is propagated both ways (top to bottom, bottom to top) by superposition of all clamp nodes' signals, as long as they can find a viable path where $|\overrightarrow{\mathbf{n_{ref}}} \cdot \overrightarrow{\mathbf{n_b}}| \neq 0$. This operation yields a vector $\mathbf{v_{ind}}$ containing condensed information on the mechanical state of each strut b.

Then, optimization proper can begin. In $\mathbf{v_{ind}}$'s decreasing order, the k neighboring struts $v_k \in \mathcal{N}_b$ of each strut b are analyzed, and their endpoints i,j displaced in the direction and sense dictated by their respective local load maxima:

$$\overrightarrow{\mathbf{n^{t+1}_{(i,j)\in b}}} = \overrightarrow{\mathbf{n^{t}_{(i,j)\in b}}} \pm \omega^t_{i,j} \overrightarrow{\mathbf{n^{t}_{v|F_{max}\in\mathcal{N}_{i,j}}}} \tag{2.46}$$

$$\omega^t_{i,j} = \epsilon_n \frac{|v^t_{ind}(b)| \max_{\forall b} |(\overline{F^t_p(i)} - \overline{F^t_r(i)})\, \overrightarrow{\mathbf{n^t_{ref}}} \cdot \overrightarrow{\mathbf{n^t_b}}|}{\max_{\forall b} |\mathbf{v^t_{ind}}| + \delta_p} \tag{2.47}$$

where ω is a momentum modulated by $\epsilon \in [10^{-6}, 10^{-3}]$, a sort of learning rate or "softening" parameter for convergence; and other step-dependent attenuation factors.

Since $\omega = f(t)$, Equations 2.46 and 2.47 describe a sort of stochastic gradient descent (SGD).

Of course, any nodal displacement must be performed within dominion limits. The sign criterion is coherent with the loads': strut enlargement (+) for traction (+) – with high penalty $\delta_p = 10$ to hinder buckling – and shortening (-) for compression (-) – with low penalty $\delta_p = 1$ in case $\max_{\forall b} |\mathbf{v^t_{ind}}| = 0$–. For struts under traction, their radii r (or equivalent thickness e in 2D) is augmented to compensate

for their increased slenderness to further prevent eventual buckling, as in Equations 2.46 and 2.47:

$$r_b^{t+1} = r_b^t + \Delta r_b^t = r_b^t + \epsilon_b \frac{|v_{ind}^t(b)| V_b^t}{(\max_{\forall b} |\mathbf{v_{ind}^t}| + \delta_p) V_{total}^t} \tag{2.48}$$

which is now weighted by the relative volume of the strut V_b/V_{total} at each pseudo-time step t. The iterative scheme in Equations 2.46-2.48 is performed N_{iter} times, clamp node by clamp node, going through all struts each time. This way, any given inner (non-clamp) node can move and each strut can be widened up to N_{iter} x N_{clamps} x b times, hence the importance of keeping ϵ_n and ϵ_b low.

Node displacement and strut thickening are only possible under the linear elastic regime and small deformations to keep assumptions correct, so struts are pooled out as soon as they experience buckling. Note that the optimization routine affects exclusively the internal nodes and struts, excluding those along the clamps for the sake of simplicity and repeatability.

The expression in Equation 2.46 is not differentiable because the weight ω in Equation 2.47 is non-continuous due to the ever-changing optimization problem in each iteration. This may pose convergence issues if the inter-iteration changes are too significant, hence the need for a small softening factor ϵ_n. The same applies for the expression regulating strut thickening (Equation 2.48) and its respective smooth parameter ϵ_b. Ideally, changes between iterations should become less and less significant, progressively vanishing until convergence.

The process ends when the prescribed iterations N_{iter} or the tolerance $|\overline{F_p^t(i)} - \overline{F_r^t(i)})\, \overrightarrow{\mathbf{n_{ref}^t}} \cdot \overrightarrow{\mathbf{n_b^t}}| < \delta_t$ are reached for clamp node i. In a way, this procedure is akin to Message Passing along edges (struts) to nodes (vertices) – where loading, length and cross-section are the edge features (physical behavior) and node displacement and strut orientation the vertex features (conservation laws), both updating their status at each time-step.

2.2.2 Continuous Media: Bulk Materials

This subsection concerns inverse design as a topology optimization problem, i.e. distributing bulk material(s) throughout a continuous domain to withstand a given combination of boundary and loading conditions. With the famously straightforward 2D SIMP code "*top*88.*m*" in [205] (inspired by [204]) as a starting point, some slight changes will be introduced to fit several purposes, namely related to loading conditions, material constraints and manufacturability.

2.2.2.1 Loading Uncertainty

While safe, the load-envelope approach described in Section 1.2 is demonstrably sub-optimal (excessively conservative) in its material distribution, and perhaps counter-productive under certain loading conditions. Statistics can introduce the uncertainties derived from normal (vibrations) and "abnormal" eventualities (impacts) during a structure's life cycle in the TO process, providing realistic sizing based on their average frequency of appearance [212]. If each observed load is associated with a cumulative known damage contribution, the resulting optimized structure will be adequate in size, robust and reliable in predictive maintenance terms within a measurable confidence interval, as usual in industry.

Applying nominally invariant boundary conditions for each case study, uncertainty is to be induced via loading. Several types of loads i can be identified: constant, alternating, statistical and occasional, each of them with an associated probability p and cycles j:

- **Constant loads** are always applied and so, they just need one cycle per iteration to capture their ever-present contribution ($p_i = 1$). They represent static, invariant loads as in traditional TO.
- **Alternating loads** appear in alternative iterations (frequency) and/or positions, with $p_i = 1/(N_{f,i})$ for every load i. For instance, two loads switching between two alternative positions each iteration will have each a 50% probability ($p_i = 1/2$). They account for regularly-timed and predictable alternative loads, generating fatigue damage that will be introduced via specific penalization.
- **Statistical loads** capture the uncertainty (in position, direction and modulus) associated to the loading process, both inherent (e.g. the loading/unloading processes) and induced (vibrations). While they appear in every iteration, they have associated probabilities p_{ij} for each cycle j and load i, randomly drawn from statistical distributions whose means μ_p and μ_m represent their canonical position and modulus, respectively.

  On top of that, the direction of the load can be varied conveniently by changing the affected degree of freedom (e.g. from axis X to axis Y) and its sense can be decided randomly (e.g. alternating between iterations). However, load sense does not alter the process in any way but conceptually, since the minimized target variable (compliance, $\mathbf{c} = \mathbf{u^T K u}$) is a result of squared displacements u, which cancels out any sign. The statistical approach to loading entails a confidence interval for the results, as in industry (e.g. six-sigma). These loads convey variance in a statistically-predictable manner.

- **Occasional loads** appear every N iterations ($p_i = 1/N$). Their position and modulus are static, striving to capture the effects of unforeseen eventualities, such as impacts: significant in modulus, albeit non-frequent. They leave a noticeable mark in the TO process, which reinforces the structure to face such occasions.

By including all these loading types, the TO process is not only striving for a topologically optimized structure, but also learning how to adapt it to various scenarios, which renders the resulting topology more robust. Nevertheless, the increased computing time and the sometimes complex material layout can be cited as drawbacks, which will be dealt with in successive updates.

Instead of applying the same static loads in each iteration loop and computing a single global compliance c to update the volume distribution, as in the original SIMP approach [29], that global loop compliance comes from the superposed sum of all individual loads i applied simultaneously in that precise iteration - as in the cumulative fatigue damage in Miner's law. This is not wholly new, since the base "$top88.m$" code [204, 205] already ponders it for multi-load (including multi-axial) applications.

However, this proposal does not stop at the load level, still equivalent to a deterministic (and arguably oversizing) load envelope, by superposition of each load's action. Rather, a new sub-level is considered for each load i: that of loading cycles, j. By considering separate cyclic contributions, two additional non-deterministic dimensions are added to loading: variability and frequency.

On the one hand, individualizing cycles and loads separately allows for the selection of tailored cyclic strategies for each load, including slight variations in modulus to account for uncertainties (e.g. vibrations). On the other hand, cyclic contributions can be switched on and off on demand, effectively establishing different incidence frequencies for each load. This conveys the compliance-weighted influences of each load in the final optimized topology.

The algorithm "learns" which loads to expect and when and reinforces the optimizing topology accordingly, even if such loads are not constantly applied (i.e. deterministic TO). For instance, one big impact load applied every X iterations makes the topology more robust to withstand it, even if it does not appear in the meantime, so when it comes again; the structure is already prepared.

To account for damage, an isotropic energy function [253, 254] is considered, containing cyclic (N_f) and stress terms (σ_f). Its work $\gamma_{ij} = \Delta W_t$ penalizes compliance each iteration t: $c^{t+1} = c^t/\gamma^t$.

For each cycle j of a given load i in iteration t

$$\gamma_{ij} = \Delta W_t = \left[\frac{\kappa}{N_f}\right]^{\alpha} + \frac{1}{2E}\left[\sigma_f \frac{t}{N_f}\right]^2 \tag{2.49}$$

where κ and α are tuneable scalars, $N_{f,i}$ is the number of loading cycles j for each load i, E the base material's Young modulus and σ_f the tension damage threshold. Thus, Equation 2.49 encapsulates both material and loading effects.

This criterion is isotropic, i.e. it deems the material affected by cumulative wear and tear homogeneously in all its parts and along all directions. This highlights the effects of damage alone in the optimized topological distribution, but other options are also compatible (e.g. crack initiation around notches and stress concentration points). This penalization yields results close to the original vanilla configuration of *top*88.*m* [205], while adding reinforcement where needed (e.g. feeble struts and joints prone to stress concentration and thus plasticity and crack initiation).

Hence, the global damage contribution for each iteration t results of summing up the damage caused by all applied loads i, which in turn come from the addition of all cyclic instances j for each load, as in.

$$\gamma^t = \sum_{i=1}^{N_{l,t}} \gamma_i^t = \sum_{i=1}^{N_{l,t}} \sum_{j=1}^{N_{c,i}} \gamma_{ij}^t \tag{2.50}$$

$N_{l,t}$ being the number of different loads applied in that iteration t and $N_{c,i}$ the loading cycles for each of those loads i. Each damage contribution penalizes compliance at every level - taking into account the load's probability p_i - as seen in Figure 2.11 and Equation 2.51.

$$c^t = \frac{1}{\gamma^t} \sum_{i=1}^{N_{l,t}} c_i^t = \frac{1}{\gamma^t} \sum_{i=1}^{N_{l,t}} \sum_{j=1}^{N_{c,i}} (p_i c_{ij}^t \gamma_{ij}^t) = \frac{1}{\gamma^t} \sum_{i=1}^{N_{l,t}} \gamma_i^t \sum_{j=1}^{N_{c,i}} (p_i c_{ij}^t) \tag{2.51}$$

Volume fraction is updated analogously for each load i, not at cycle level j like compliance, since the changes in volume are not associated to a probability p_{ij} other than the algorithm's natural course:

$$v^t = \frac{1}{\gamma^t} \sum_{i=1}^{N_{l,t}} v_i^t \tag{2.52}$$

This volume update accounts for physical wear while avoiding numerical instabilities after embedded density filtering (e.g. null contributions from void elements). The procedure for each iteration is shown in Figure 2.11.

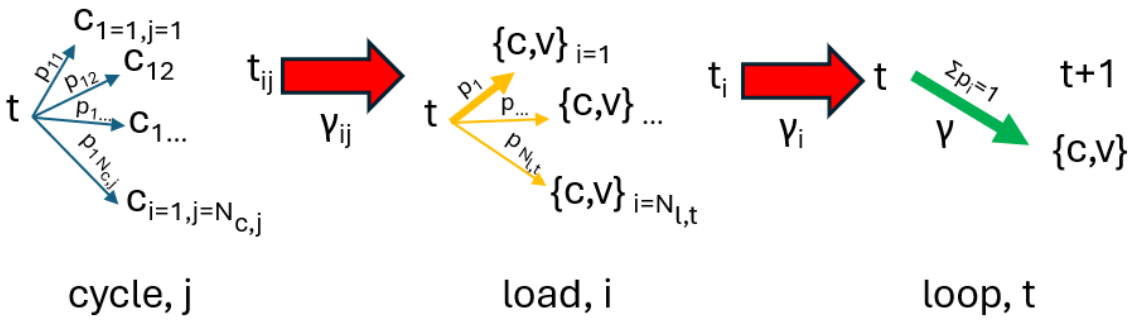

Figure 2.11: Diagram explaining damage contributions in a full iterative loop, from the load cycle level (blue arrows, sub-substep t_j) for each individual load type (yellow arrows, sub-step t_i) adding up to each iteration loop (green arrow, full step t).

The nature of cycles j and load probabilities p_i are both determined by the load's frequency. It must be noted that p_i are computed either directly (if constant or occasional) or by addition of cycle probabilities p_{ij} (when statistic): $p_i = \sum_{j=1}^{N_{c,i}} p_{ij}$. Hence, this framework is probabilistic, as opposed to the deterministic multi-load approach proposed in Section 5 of [205].

Obviously, for the same iteration t, all individual load probabilities add up to 1: $\sum_{i=1}^{N_{l,t}} p_i = 1$. In practical terms, this cyclic subdivisions only affect statistical loads under assumed distributions. For all three other loading types (constant, alternating and occasional), all cyclic probabilities are considered equal: $p_{ij} = p_i / N_{c,i}$.

In optimization terms, the gradient is now composed not only of the resulting sum of the searching directions for each load i, but also each of those loads is the combination of all the weighted gradients for each cycle j - see Equation 2.51 and Figure 2.11. This approach ensures the influence of statistically-measurable uncertainty, multi-axial and multi-load scenarios and fatigue damage considerations. In doing so, it reinforces the evolving topology on the go, as a part of the optimization process itself rather than computationally costly post-processing steps.

This proposal is but a first attempt with a very rudimentary finite element formulation (2D, linear elastic), but it can be extended more complex settings, even non-linear. Some practical examples of Figure 2.11's application can be found in Figure 3.27. Since the original code in [205] assigns unitary Young's modulus $E_0 = 1$ to avoid numerical issues (e.g. quasi-infinite density contrast [35]), all parameters in Equation 2.49 must be proportional as well.

2.2.2.2 Damage Criteria for Material Constraints

Many damage-based criteria can influence compliance (or whatever target variable to be minimized, e.g. stress [268]) within a constrained TO framework. These criteria are damage-based in the sense that the cumulative work γ at each iteration penalizes compliance directly: $c^{t+1} = c^t/\gamma^t$, as in Wöhler's diagram. Four non mutually exclusive proposals are considered, disrupting SIMP's assumed isotropy.

The first suggested criterion (energy-based fatigue) was already presented in Equation 2.49.

The second criterion concerns the topology's stress state, penalizing each cell's density with the highest principal strain ϵ_1 multiplied by a scalar factor P. For all cells undergoing the target strain state (traction/compression):

$$\gamma = P\Delta W_t \tag{2.53}$$

Therefore, the resulting structure will be reinforced against the mechanical behaviors the TO process is penalizing. Of course, such responses are strongly dependent on the material's properties, i.e. this criterion is tantamount to material choice, performance-wise: the stress/strain response that suits best the selected material(s) will constitute the designer's preferred choice.

For instance, compressive states are convenient for materials like plain concrete (with strong compressive properties but negligible traction resistance on its own), whereas traction should be promoted for steel-like materials (preventing buckling), cables (unable to withstand compression), or composites along their fibers (strength).

The third proposed criterion considers more practical constraints. If the material is printed via additive manufacturing (AM), the effects of the prototype's printing direction must be considered, since they have a noticeable impact in their global and local properties. Anisotropy is present along the printing layers and around defects (scale, porosity, burrs, etc.) [455, 456]. This distorts the optimized structure's assumed isotropy in the SIMP method, so ΔW_t is multiplied by the projection $proj$ of the chosen printing direction $r_{\vec{print}}$ onto the first principal direction $\vec{r_1}$ for each cell. For unitary vectors:

$$\gamma = \Delta W_t proj(r_{\vec{print}}, \vec{r_1}) = \Delta W_t(1 + \beta cos(\widehat{r_{\vec{print}}, \vec{r_1}})) \tag{2.54}$$

where β is a custom intensifying scalar parameter.

For Equation 2.54, the strain tensor must be computed beforehand. From the obtained displacements $\mathbf{u}$ and the strain matrix $\mathbf{B}$ for 2D square elements:

$$\begin{Bmatrix} \varepsilon_x \\ \varepsilon_y \\ \gamma_{xy} \end{Bmatrix} = \begin{bmatrix} \frac{\partial N_1}{\partial x} & 0 & \frac{\partial N_2}{\partial x} & 0 & \frac{\partial N_3}{\partial x} & 0 & \frac{\partial N_4}{\partial x} & 0 \\ 0 & \frac{\partial N_1}{\partial y} & 0 & \frac{\partial N_2}{\partial y} & 0 & \frac{\partial N_3}{\partial y} & 0 & \frac{\partial N_4}{\partial y} \\ \frac{\partial N_1}{\partial x} & \frac{\partial N_1}{\partial y} & \frac{\partial N_2}{\partial x} & \frac{\partial N_2}{\partial y} & \frac{\partial N_3}{\partial x} & \frac{\partial N_3}{\partial y} & \frac{\partial N_4}{\partial x} & \frac{\partial N_4}{\partial y} \end{bmatrix} \left\{ \mathbf{u}^{(\mathbf{e})} \right\} \tag{2.55}$$

which, assuming unit-side elements and node-centered integration points, becomes easy to compute if linear shape functions $N_i(x, y)$ are applied. Of course, more complex formulations can be contemplated.

Lastly, a fourth option for compliance penalty could be directly von Mises yield criterion, indicating the limits for linear elasticity and plasticity to occur, relevant for the linear approximations in all previous criteria. For that purpose, the stress tensor σ is computed from the Lamé-Hooke equations:

$$\sigma = \lambda tr(\varepsilon) + 2\mu\varepsilon \tag{2.56}$$

μ being the material's Poisson coefficient. When the stress-strain relationships ceases to be linear, Equations 2.55 and 2.56 must be reformulated accordingly, if possible, or rather substituted by approximate numerical methods, often path-dependent in metamaterials. With the stress tensor σ, the equivalent von Mises stress σ_{vM} can now be computed and used as a damage penalization γ:

$$\gamma = \sigma_{vM} = \sqrt{\sigma_{xx}^2 + \sigma_{yy}^2 - \sigma_{xx}\sigma_{yy} + 3\tau_{xy}^2} = \sqrt{\sigma_1^2 + \sigma_2^2 - \sigma_1\sigma_2} \tag{2.57}$$

This criterion provides a quantitative measure for the degree in which linear elasticity must be deemed an acceptable approximation or not, as well as giving valuable information on the material's internal distortion. The latter proves especially relevant when anisotropic properties arise, unexpectedly or not. Such is the case of functionally-graded materials (composites, metamaterials). Stress is homogenized and so, stress concentrations are softened and plasticity is less likely to occur, effectively shielding the optimized topology from complex non-linear effects. This can be interpreted as a rough compliance-stress TO compromise [268].

These criteria serve multiple purposes, not mutually exclusive for the most part (although that could be the case in some particular applications). That means they can be combined in different ways according to the designer's requirements for mechanical response, material, manufacturing, etc.

Depending on the boundary conditions of the TO problem, the enforcement of these schemes can become rater cumbersome, computationally speaking. For that reason, they will only be applied to elements (cells) already considered solid ($\rho = 1$) or likely to become so in upcoming iterations ($\rho > 0.8$), to avoid useless evaluation of void ($\rho = 0$) and vanishing elements ($\rho << 1$).

2.2.2.3 Filtering Strategies

Fine meshes and demanding or complex loading conditions (i.e. non-deterministic) in TO often raise mechanically "weak" topologies, featuring a wide range of different branch thicknesses creating artificial stress concentrations and so overall fragility. This volume distributions are sub-optimal, so filtering techniques (e.g. density-based) are used to smear out material, thus smoothing its curves [224]. Alas, this yields unclear material-void boundaries, inconvenient for modeling and manufacturing [457].

To alleviate the undesirable effects derived from feeble twigs in topology optimization (buckling, stress concentration, fracture, poor manufacturability), an additional filter was introduced on top of the sensitivity and density ones in [205]. This algorithm searches for neighboring elements whose densities are below a certain threshold within a given radius r and sets them to void, thus eliminating the unwanted twigs on a minimum-thickness basis.

Instead of costly and limited post-processing, such pruning takes place each X iterations, X being a user-defined interval: small enough to avoid unwanted regrowth but also sufficiently big not to thwart the SIMP TO process. In doing so, mesh-dependence is prevented [224] and volume adaptation is now part of the optimization process.

More precisely, the algorithm iterates through all non-void elements checking its neighbors at different distances horizontally, vertically and diagonally, as seen in Figure 2.12. Thus, if the advancement in opposite search directions exceeds the target diameter (for instance, $l_1 + l_5 \geq 2r$), the first adjacent elements encountered will be erased if their density is below the established threshold, that is, decreased to a negligible fraction around 0.001, non-zero to avoid singularities. Of course, the precision of this filter is that of the finite element meshing: 1 element.

Other common manufacturability-oriented variables like minimum hole size and sharp edge avoidance are left unrestricted in this first approach, since the evolution of the filtered topologies is deemed to diminish their effects anyway. This filter can be applied partially, choosing direction and sense, if the user requires so, which poses interesting implications for tailored anisotropy and functional grading.

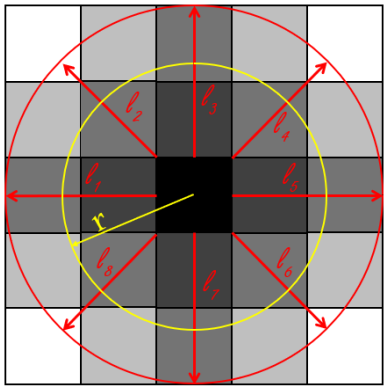

Figure 2.12: Filtering strategy with lengths $l_i, 1 < i < 8$ (in red) outside a radius r (yellow). Each element's color represents its physical density, x_{Phys}, from white (void) to black (full material).

After calling the new filter function, x_{Phys} is overwritten by its new filtered value $x_{Phys,filtered}$ containing the bi-phasic void/material distribution subject to the given threshold ($\rho > 0.8$). This enables local adaptation to manufacturing requirements.

2.2.2.4 Iterative Schemes

The proposed filtering strategy provokes sudden decreases in volume fraction, which might not be replenished in time to reach the prescribed target v_f unless the filter is applied timely and with the right scope (radius). There are many ways to solve this, e.g. leaving volume fraction unrestrained along the iterative process. To reconstruct a more robust topology after the filter is applied, volume fraction must grow quasi-monotonically, compensating the filter's momentary descent. Otherwise, the filtered structure would be even further restrained and the optimization process would be halted as the only possible change would be endless retraction of material till total annihilation (full void domain).

Interestingly, if volume fraction is left unconstrained, some other design parameters can come into play, e.g. compliance as an objective on its own [458, 459, 460, 461, 462]. By updating compliance to an evolving volume fraction, a design space is created for effective interpolation among actually existing topologies, offering an alternative to other more computationally expensive approaches [463, 464, 465].

If compliance is computed at each iteration as a function of the previously updated volume fraction (instead of a fixed one as in [204, 205]), the two most important parameters in SIMP (compliance c as the objective, volume fraction v as a restriction) are directly linked, simplifying the process as one unified expression updates both simultaneously where volume becomes a temporary constraint.

Carter-Hayes interpolation [466] - inspired by Ashby's law - Equation 2.58) relates initial E_0 and current E Young's moduli through their associated initial ρ_0 and current ρ densities:

$$\frac{E}{E_0} = \left(\frac{\rho}{\rho_0}\right)^{\xi} \tag{2.58}$$

where ξ is an adiabatic proportionality parameter. At the same time, Wolff-Frost's mechanostat theory [467, 468] - translated into mechanics by Huiskes [469, 470] and Weinans [471] - dictates a linear relationship betwixt mass growth over time (expressed via density $\rho = m/v_f$ for a fixed volume fraction) and strain energy $\Psi = Ku^2/2$:

$$\frac{d\rho}{dt} = B\,\Psi \tag{2.59}$$

through B as a mechanistic growth parameter (scalar). The optimized cell's effective density ρ_{eff} is defined as the logarithmic update of the real, physical density ρ_{Phys} using the mechanostat Equation 2.59:

$$ln[\rho_{eff}] = ln[\rho_{Phys}] + ln[d\rho_{Phys}] = Ln[\rho_{Phys}\,d\rho_{Phys}] \tag{2.60}$$

Replacing Equation 2.59 into the former yields:

$$\rho_{eff} = \rho_{Phys}\,B\,\Psi\,dt \tag{2.61}$$

Assuming strain energy Ψ independent of density on the grounds of discretization in steps of calculation, it leaves:

$$\frac{d\rho_{eff}}{d\rho_{Phys}} = \alpha\,\Psi \tag{2.62}$$

With $\alpha = B\,dt$.

Using the Carter-Hayes Equation 2.58 again, it holds:

$$\rho = \rho_0 \left(\frac{E}{E_0}\right)^{(1/\xi)} \tag{2.63}$$

Thus, deriving with respect to stiffness K:

$$\frac{d\rho}{dE} = \frac{\rho_0 \xi}{E_0} \left(\frac{E}{E_0} \right)^{(1/\xi - 1)} \tag{2.64}$$

If $\xi = 1$, the former expression verifies:

$$\frac{d\rho}{\rho_0} = \frac{dE}{E_0} \tag{2.65}$$

where $\rho = \rho_{eff}$ is the effective density and $\rho_0 = \rho_{Phys}$ is the physical reference. For each initial volume fraction, ρ_0 and E_0 will be variables, denoted as ρ and E.

The algorithm is now intended to optimize the strain energy density Ψ through variation of the local density related to the Young's moduli. This relationship is inverse, conveyed through a constant ζ as $\Psi = \zeta / E$. Hence, the derivative of the Young's modulus with respect to the strain energy density can be written as:

$$\frac{dE}{d\Psi} = -\frac{\zeta}{\Psi^2} = -\frac{E}{\Psi} \tag{2.66}$$

Substituting Equation 2.66 into Equation 2.65:

$$\frac{d\rho}{\rho} = -\frac{d\Psi}{\Psi} \tag{2.67}$$

Using $d\rho_{eff}$ instead of the real $d\rho = d\rho_{Phys}$ (Equation 2.62):

$$\alpha \frac{d\rho}{\rho} = -\frac{d\Psi}{\Psi^2} \tag{2.68}$$

Finally, by integration of both sides:

$$\alpha \, Ln[\rho] + \beta = \frac{1}{\Psi} \tag{2.69}$$

where β is the sum of the integration constants. Considering the equivalence $\Psi = 2c$ ($c = uKu$ being compliance) and $\rho = m/v$, the latter expression can be reshaped into:

$$\frac{1}{c} = a \ln(v) + b \tag{2.70}$$

where $a = 2\alpha m/\rho$ and $b = 2\beta$ are constants. More precisely, $b = 1/c_{min}$ corresponds to the lower compliance limit c_{min} for a maximum value of volume fraction, i.e. a full material domain: $v_{max} = 1$, with maximum stiffness. Such c_{min} can be computed from simple analogy to the continuum via analytical expressions or any surrogates (bisection method, AI).

Substituting b in Equation 2.70 yields a, a case-dependent constant defined by the initial volume fraction v_0 (assumed infinitely compliant) and the minimum compliance c_{min}: $a = -\frac{1}{c_{min} ln(v_0)}$. Reformulating Equation 2.70, the resulting history dependent iterative scheme for volume fraction update is given by:

$$v^{i+1} = \left(\frac{1}{c_{min}} - \frac{1}{c^i}\right) c_{min} \ln(v_0) \tag{2.71}$$

Equation 2.71 defines a given topology's evolution curve from the minimum v_{min} to the maximum volume fraction $v_f = 1$ while varying in compliance. Any data point along such curve represents an existing topology and thus allows for interpolation across different stages of the same evolving design. This can (and will) be easily implemented as the physical loss in a ML-driven scheme.

Such curves and the area below them constitute a constrained design dominion. This way, multiple volume fractions can provide different compliances and viceversa, on the designer's demand. Additionally, different filtering radii r can add an extra degree of freedom in such design space, amounting to a total of three: compliance, volume fraction and minimum branch thickness.

2.3 Digital Twins for Biomedical Applications

The human brain as a paradigmatic example of biomedical modeling is addressed, with the aim of creating a simple yet computationally efficient mock-up emulating its behavior regarding signal propagation throughout its biological neural networks (connectome). This work, including the aforementioned biological aspects (neuroplasticity, migration, etc.), can be interpreted as a rudimentary Digital Twin [10] which will eventually gain complexity, enriched by experimental data (Hybrid Twin).

More details can be found in the author's research article "**An Agent-Based Model to Reproduce the Boolean Logic behavior of Neuronal Self-organized Communities through Pulse Delay Modulation and Generation of Logic Gates**" [124].

A physical domain in $\mathbb{R}^3$ is created within a $4 \times 0.5 \times 0.5$mm prism (1mm^3) containing 40k neurons, thus matching the brain's neuronal density ($40{,}000 neurons/mm^3$ [472]).

In two of its boundaries (frontal and posterior faces of the prism), $n_1 = 1{,}000$ emitter/input and $n_2 = 1{,}000$ supervising/output neurons are placed. In between these two bounds, a much greater number of transition neurons ($n_0 = 20 \times (n_1 + n_2) = 40{,}000$) fills up the remaining space. The spatial coordinates of these neurons are given randomly within the domain in a sparse pattern. Mathematically, all the neurons are equal, but they have different roles assigned in the network. Their synapses determine the processing paths between them within a certain brain region (functional connectivity).

The initial random structural connections are deployed between the neighboring neurons via Delaunay's triangulation, generalized to N-dimensions through the Bowyer–Watson's algorithm [445, 446]. This approach is widely used to create unstructured meshes [473], yielding tetrahedra whose vertices are contained within their correspondent circumsphere. Its beneficial heterogenizing properties in joint angle and edge (axon) length were already discussed in Section 2.2: no edge intersection, moderate length variance, etc. In this particular case, it is useful to accurately represent a network composed of one specific type of neuron, presenting similar though not identical morphology - e.g. belonging to a volumetric sample within the same brain region.

Now the particular implementation of biological aspects into the neural network will be described.

2.3.1 Metastability

To emulate brain metastability, the density distribution of active supervising neurons must synchronize with a given desired target signal, e.g. an exponential curve centered at a certain propagation step. To train that synchronization, certain sets of input neurons (n_1) are sequentially lit by default during the initial time steps (25% in the first iteration, 50% in the second one and the remaining 25% in the third and last one). After the initial spiking cascade, neuron firing propagates forward, eventually reaching the supervising neurons and activating some of them. A practical example can be seen in Figure 3.60.

2.3.2 Neurons as Agents. Cell migration

Neurons are modeled as cells in an agent-based framework, so they display communitarian interactions and, as biological cells, they consume resources and may migrate. Their behavior influences their neighbors' - topology, structural and functional connectivity, small-worldness, neuron centrality (hubs), etc. This indicators are measurable through a certain set of parameters associated to each one of them - synaptic weights, activation, thresholds, neighborhood and sense of information flow.

As customary in agent-based models, neurons behave in an autonomous, unsupervised and proactive manner, as a sort of independent dynamical decision makers [474].

To replicate cell migration, new transition neurons randomly emerge throughout the connectome. Migrating neurons are limited to 0.05% of the total at each adaptation step to avoid numerical overcharge, but this fraction can be eventually increased. This humble changes could be interpreted as a specific functionally-driven migration rather than a full-scale one - as in developmental brain growth. For instance, should the modeler want to replicate GABAergic migration in early brain development, this would affect around 20% of neurons traveling from to ventral telencephalon to the cortex, inhibitory and excitatory in similar proportions [475]. Future model developments will include different cell migration criteria to enhance neuron adaptability.

2.3.3 Neuroplasticity

Plastic remodeling is also known as neuroplasticity, which can be structural [289] - rewiring neuronal infrastructure, i.e. "brain's highways"— and functional, changing the use patterns of said infrastructure, i.e. "neural traffic" [288].

In the proposed model, the structural remodeling process is addressed through changes in neuron connectivity: when a given neuron receives enough excitatory signaling, it modifies its pre-synaptic neurons. This is mandated when the neuron in charge of supervising the training process demands to receive a signal earlier than its current latency. Then, the remodeled neuron looks for new pre-synaptic neurons between the ones that have fired earlier than its current pre-synaptic cells. As in the migration case, an *ad hoc* function forces status changes for a selected group of neurons (again $< 0.05\%$ to avoid overcharge). Reactive synaptogenesis could also occur, relocating connections either in the damaged neuron's neighborhood (easiest, most straight-forward) or in unexpected far-away places (emulating axon rerouting and/or age-induced density loss, perhaps diaschisis).

One way of achieving that comes in response to backpropagation: negative-weighted neurons could reconnect along inhibitory paths and positive-weighted neurons could do likewise for excitatory ones, relieving or reinforcing them, respectively. That way, each possibly useful pathway is optimized while the rest perish if unneeded. If neural damage does not take place, axon retraction will be put into practice by progressively trimming (a fraction of) the least-used connections, striving for global connectome efficiency - a process commonly known as "pruning" in neuroscience [476].

Functional neuroplasticity is enforced by searching for the "hub" neurons (through which most signal paths go through) and exciting or inhibiting a small set of them accordingly. This excitation/inhibition is modelled by decreasing/increasing their activation potentials, respectively. Functional remodeling is dictated by inhibitory/excitatory paths, recreating variance in neurotransmitter receptors happening in synaptic plasticity [477]. In Graph Theory terms, these pivotal status-changing neurons (or nodes) are central, having the highest degrees (number of neighbors). This applies to the top 0.05% busiest.

2.3.4 Signal Propagation

Every neuron i is given an initial weight $w_i \in [-1, 1]$ and an activation threshold α_i (initially zero), so that if $\bar{w}_{\mathcal{I}_i} \geq \alpha_i$, it will be activated, being $\mathcal{I}_i$ the set of input neurons of i firing at the previous time-step, and $\bar{w}_{\mathcal{I}_i}$ their average value. Since neurons are not layered nor aligned in the real brain, neither sense-wise (soma to telodendria) nor path-wise (inputs to outputs), propagation sense is randomly decided for each of them. The only rule that applies is the non-connectivity of input or output neurons among themselves since they are deemed stimulated and supervising, respectively.

Following this reasoning, whichever inputs a given soma (nucleus) receives are considered its dendrites, and so its outputs would correspond to its axon terminals (telodendria), as in multipolar neurons all around the Central Nervous System. Then, edges in this model represent either dendrites or axon terminals, whereas nodes include every other part in the middle (nuclei, axon hillock, axon, myelin sheath, etc.). Of course, this is not the case in the real brain, where - as explained earlier - neurons are oriented in a given direction and sense: dendrites-soma-axon.

The purpose of this randomly assigned sense is to replicate the disorganized orientation of neurons, ignoring - by now - the different biological functions of dendrites and axons as this model focus exclusively on the flow of information throughout neural networks in the brain. Further biochemical implications will be included in later stages.

Due to the induced sense randomness, some signals are effectively lost, reaching a point where they cannot find a viable path matching the activation conditions and so, they disappear. This can indeed be interpreted as a biologically plausible consequence of network randomness, or perhaps signals traveling to other out-of-scope regions of the brain (far-away connectivity). This also accounts for neuroplasticity, allowing for new paths to be explored in different simulations.

To further enhance signal synchronization, a specific counter is set so that if the hop-distance (number of connections traversed) between two neurons is equal to the difference in time steps, the activation of the precedent one is promoted.

At each step, inhibitory and excitatory signals propagate backwards to neurons with incorrect status, inhibiting the neurons that should have been off but are on and exciting the inactive ones that should have been active. This is the supervised learning mechanism n_2 neurons apply to the connectome. After this first training iteration, newly corrected forward waves are sent to increase accuracy.

In every iteration, 0.05% of the neurons with a higher signaling threshold for inhibition or excitation will change their behavior in subsequent steps. Inhibition is modeled by assuming a higher firing threshold, which acts as a switch-off interrupter. Excitation is enhanced through plastic remodeling and/or by setting a lower firing threshold.

As a result of cascade spiking initiation, when the last fraction of n_1 neurons fires; the signal originated with the first stimulated ones will be 2 propagation steps ahead. Then, the signal propagates through transition neural networks n_0 until it reaches the supervising n_2 ones. The network is self-remodeled, and a new propagation cycle starts. A workflow visualization can be found in Figure 2.13. An example of Λ block including Boolean logic gates (next subsection) is used in Figure 3.61.

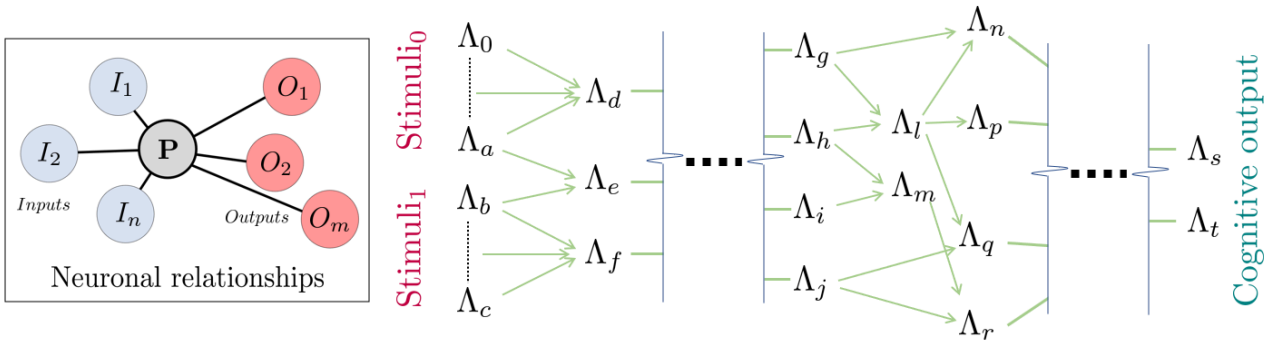

Figure 2.13: Overview of biological neuronal networks. **Left:** Relationship between inputs and outputs in a modeled neuron. **Right:** Concatenation of Λ neuronal blocks produces complex cognitive outputs.

2.3.5 Biologically-Plausible Boolean Logic Gates

This model aims to mimic biological neurons in their functioning by setting inputs – inhibitory or excitatory stimuli coming through the neuron's dendrites – which, after being processed by a user-defined aggregation function, yield a synaptic state (on/off) as its sole output.

This artificial connectome features 317,321 synaptic connections and 42 thousand neurons have been used to represent logic gates. For comparison, a modern CPU contains roughly 100 million. This is reminiscent of neuromorphic computing, both in hardware and software, as explained in Section 1.3.

The model shown in the previous subsection is showcased in the squares of Figure 2.14, as N_1 and N_2. Their role is that, given two stimuli I_1 and I_2, not necessarily coordinated, they will synchronize through the networks N_1 and N_2. Boolean configurations in Figure 2.14 can reproduce logic gates from asynchronous stimuli, namely "fire" (true) or "do not fire" (false).

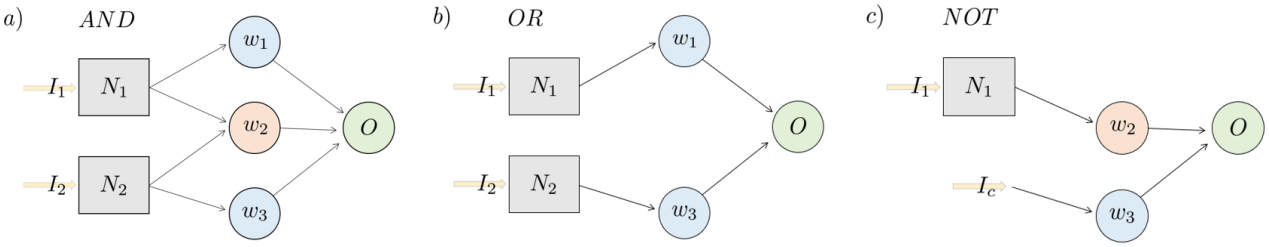

Figure 2.14: Diagrams of Boolean logic gates for asynchronous stimuli in the proposed methodology: AND (a), OR (b) and NOT (c).

2.3.5.1 AND Gate

In this case, $w_1 > 0$, $w_3 = w_1$, $w_2 < -w_1$ and $\alpha_O = 0$. If I_1 or I_2 are stimulated alone, the average weight sum $\bar{w}$ is lower than the threshold α, so the result will be negative (false: "do not fire"). Only if both fire simultaneously, $\bar{w} > \alpha$ holds true. Any other combination is valid as long as those proportions are fulfilled. In short, the Boolean output (O) can be defined as $O = I_1\ AND\ I_2$, if there is a stimulation in I_1 and I_2 the output in O is to fire, otherwise O will not fire.

2.3.5.2 OR Gate

For this gate, any stimulus I_1 or I_2 will make O fire, since the inhibitory intermediate neuron with w_2 is removed. The Boolean output (O) can now be defined as $O = I_1\ or\ I_2$.

2.3.5.3 NOT Gate

This gate switches between the I_1 and O states. Only one input is required, but a continuous fire I_c is needed to ensure that, when I_1 is not stimulated; O is. When I_1 is stimulated, the inhibitory neuron w_2 is activated and so O does not fire, since now $\bar{w} < \alpha$. The Boolean output reads $O = NOT\ I_1$.

Chapter 3

RESULTS

In this chapter, the results of applying the proposed methodologies are presented in a series of real case studies.

Contenu

3.1 Structural Description

Numerical examples for the methodologies developed in Section 2.1 are unfolded here.

3.1.1 Property Prediction

The surrogate conceived in [103] is employed to predict the equivalent stiffnesses and Young's moduli for the toy example (springs in series) and several cubic aperiodic lattices.

3.1.1.1 Dense Neural Network

Train and test metrics are computed for the toy example (Figure 2.3). Denoting the prediction with a hat $\hat{\cdot}$, the scaling with a tilde $\tilde{\cdot}$, and defining the error of a sample i as the squared residual r_i^2, namely

$$r_i^2 = \left(\tilde{E}_z^{\mathrm{eq}(i)} - \widehat{\tilde{E}_z^{\mathrm{eq}(i)}} \right)^2 , \tag{3.1}$$

the minimum, maximum and mean error - i.e. the loss function $\mathcal{L}$ (MSE) - are computed to assess every model shown. The DNN yields losses of $\mathcal{L}_{\mathrm{train}} = 3.94 \cdot 10^{-5}$ and $\mathcal{L}_{\mathrm{test}} = 4.89 \cdot 10^{-5}$, and coefficients of determination of $R^2_{\mathrm{train}} = 1.0000$ and $R^2_{\mathrm{test}} = 0.9999$. The maximum and minimum errors as defined in 3.1 are $(r^2_{\mathrm{min}}, r^2_{\mathrm{max}})_{\mathrm{train}} = (2.87 \cdot 10^{-14}, 6.64 \cdot 10^{-2})$ and $(r^2_{\mathrm{min}}, r^2_{\mathrm{max}})_{\mathrm{test}} = (1.34 \cdot 10^{-13}, 1.94 \cdot 10^{-2})$. The train and test predictions are shown in a scatter plot in Figure 3.1, where the ground truth is given by the line at 45°, noting a slight under-prediction close to the top limit.

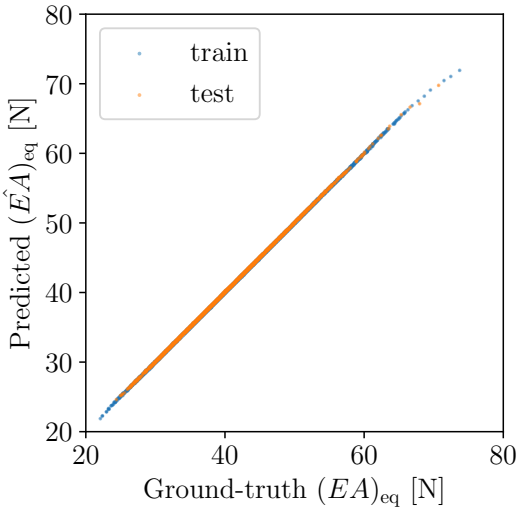

Figure 3.1: Toy example. Equivalent axial stiffness $(EA)_{\mathrm{eq}}$ prediction, representing train and test in blue and orange, respectively.

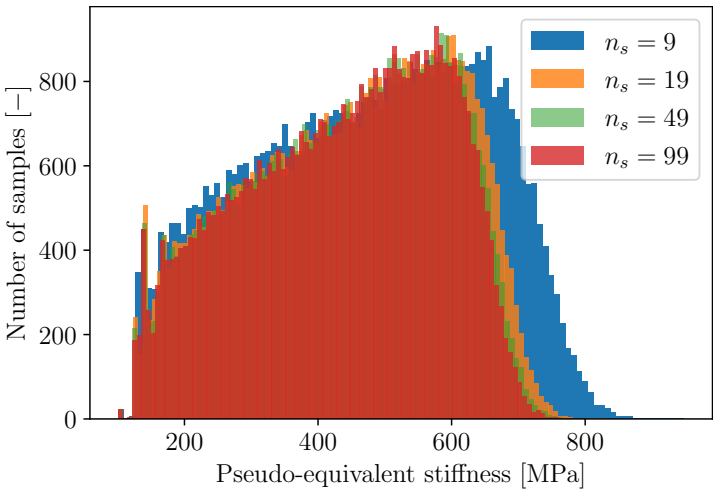

Figure 3.2: Pin-jointed truss lattice DNN model. Distribution of the pseudo-equivalent stiffness according to Equation 2.14 for different number of slices $n_s = \{9, 19, 49, 99\}$.

Of course, this is a simple problem solved with an explicit formula, which is almost perfectly approximated by the DNN model. Teachings from this method are leveraged to address the effective behavior with a similar DNN-based surrogate. Using the inverse of the effective transverse areas in the three spatial directions $A^{\text{eff}}_{x,s}$, $A^{\text{eff}}_{y,s}$ and $A^{\text{eff}}_{z,s}$ for n_s slices as inputs, a DNN model for 3D pin-jointed truss lattices is generated analogously to the toy example.

The dataset comprises 10 000 randomly-generated samples, i.e. lattices. The base material is AISI Type 316L Stainless Steel, annealed bar, with a Young's modulus of $E_{\text{base}} = 193\,\text{GPa}$, and the lattice members are circular bars with radius $r = 5\,\text{mm}$, leading to a cross-sectional area of $A = 78.54\,\text{mm}^2$.

In order to select a suitable number n_s of slices, the following limit analysis is performed on this number: a pseudo-equivalent lattice stiffness of the dataset is computed via Equation 2.14, using the effective area transverse to z per slice s, $A^{\text{eff}}_{z,s}$. This is not the actual equivalent stiffness to be predicted, but it serves as a global value for comparison purposes.

Then, these samples are sliced in different numbers of slices n_s. The histogram of pseudo-equivalent stiffnesses for the different n_s is depicted in Figure 3.2. Note that from $n_s = 19$ on, this global magnitude per lattice is similarly distributed. Therefore, two models with $n_s = 19$ and $n_s = 49$ slices are computed to show the performance balance between both.

Lastly, the actual equivalent stiffness, E^{eq}_z - Equation 2.11 - is divided by the lattice volume to facilitate the predictions of the model (a sort of normalization). Namely, for each sample

$$\overline{E_z^{\text{eq}}} = \frac{E_z^{\text{eq}}}{V}, \tag{3.2}$$

where V is the volume of the lattice i.e.

$$V = \sum_e A_e \ell_e, \tag{3.3}$$

leading to the following dataset

$$\left\{ \{(A_{x,s}^{\text{eff}})^{(i)}, (A_{y,s}^{\text{eff}})^{(i)}, (A_{z,s}^{\text{eff}})^{(i)}\}_{s=1}^{n_s}, \overline{E_z^{\text{eq}}}^{(i)} \right\}_{i=1}^{N}.$$

The architecture and optimization parameters displayed in Tables 2.1 and 2.2 are used. A validation set of 15% of the samples is separated, applying a train/test 85-15% split in the remaining dataset. Both features and targets are normalized with a standard scaler. Training and testing results can be found in Table 3.1.

DNN, truss	$\mathcal{L}_{\text{train}}$	R^2_{train}	$r^2_{\text{min,train}}$	$r^2_{\text{max,train}}$	$\mathcal{L}_{\text{test}}$	R^2_{test}	$r^2_{\text{min,test}}$	$r^2_{\text{max,test}}$
$n_s = 19$	$2.95 \cdot 10^{-2}$	0.971	$1.05 \cdot 10^{-10}$	0.784	$3.58 \cdot 10^{-2}$	0.965	$2.96 \cdot 10^{-10}$	0.730
$n_s = 49$	$2.64 \cdot 10^{-2}$	0.973	-	-	$3.21 \cdot 10^{-2}$	0.968	-	-

Table 3.1: Training and test parameters for the DNN surrogate model.

Since both models perform similarly, it is reasonably assumed that using $n_s = 19$ represents sufficiently the geometric information in this DNN model without incurring in a large set of features, hence errors are disregarded for $n_s = 49$. The model's predictions are depicted in a scatter plot in Figure 3.3. Although less precise than in the toy example, the non FE-based surrogate performs quite well.

The DNN proves unable to yield similarly accurate results for more intricate mechanical settings, e.g. beams. Thus, a GNN-based alternative is explored, hoping its ingrained topological features (vertex and edge embeddings) can effectively portrait more complex (e.g. rigid) lattices (nodes and struts).

3.1.1.2 Graph Neural Network

The GNN-based surrogate explained in Section 2.2 is put to the test with randomly-generated aperiodic lattices, under two different mechanical behaviors where struts act as either pin-jointed elements or Euler-Bernoulli beams.

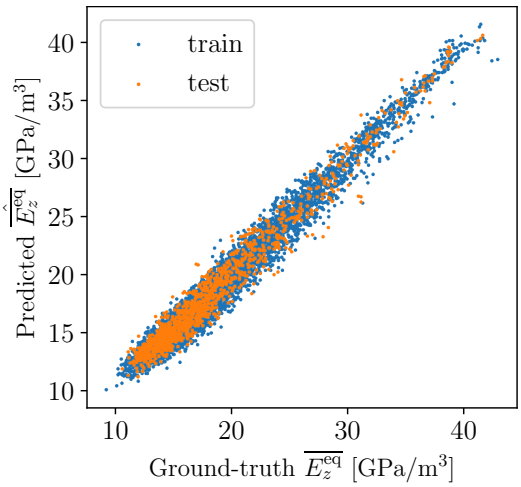

Figure 3.3: Pin-jointed truss lattice DNN model. Equivalent stiffness per unit volume $\overline{E_z^{eq}}$ prediction, where the train and test are represented by blue and orange points, respectively.

3.1.1.2.1 Pin-Jointed Truss The design of experiments (DoE) remains unchanged for this case: generating cylindrical strut lattices in 316L Stainless Steel. The training set results from varying the number of non-fixed (inner) nodes $n_j - 8$ from 1 to 50, sampling 400 lattices per each node, which leads to a total of $N = 400 \times 50 = 20\,000$ samples - where 15% of them are taken as a validation set i.e. 3 000 samples. The test set is generated similarly, sampling 40 lattices per node, i.e. 2 000 samples. In this regard, the training and test sets have the same (uniform) distribution of number of nodes, whereas the number of elements n_e varies according to Figure 3.4.

Figure 3.4 showed that the number of elements from the lattices in training and test sets are similarly distributed, indeed with slight differences due to the independent sampling processes.

All variables are scaled with standard normalization using the mean and standard deviation values of the training set. The optimization parameters and its results are displayed in Tables 3.2 and 3.3, respectively.

Parameter	Choice
Optimizer	nadam
Learning rate	0.01
Epochs	10 000
Loss, $\mathcal{L}$	MSE

Table 3.2: Pin-jointed truss lattice GNN model. Optimization parameters for training.

Judging by results in Tables 3.1 and 3.3 and Figures 3.3 and 3.5a, the GNN surrogate model visibly

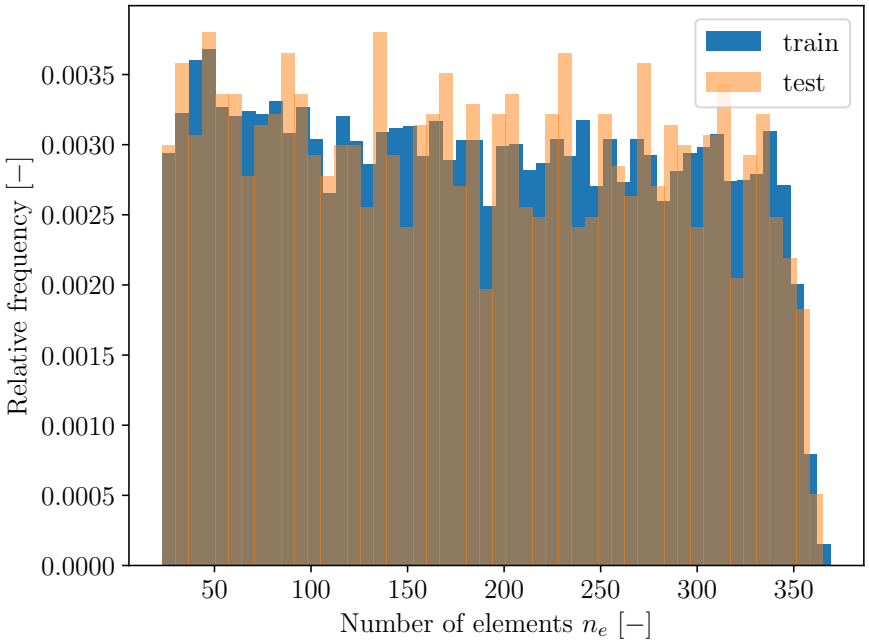

Figure 3.4: Pin-jointed truss lattices. Training and test set histograms of number of elements n_e distribution.

GNN, truss	$\mathcal{L}_{\text{train}}$	R^2_{train}	$r^2_{\text{min,train}}$	$r^2_{\text{max,train}}$	$\mathcal{L}_{\text{test}}$	R^2_{test}	$r^2_{\text{min,test}}$	$r^2_{\text{max,test}}$
$n_s = 19$	$1.02 \cdot 10^{-2}$	0.990	$3.20 \cdot 10^{-12}$	0.391	$1.23 \cdot 10^{-2}$	0.987	$2.39 \cdot 10^{-9}$	0.220

Table 3.3: Training and test parameters for the GNN surrogate model when tackling pin-jointed trusses.

and outperforms the DNN one for the same task.

Additionally, KFold cross-validation is computed to assess the model's learning capabilities, consisting of $k = 5$ folds performing a random split, i.e. dropping 20% of the information in five occasions. The results are displayed in Table 3.4. Note the similar performances of the 5 different training scenarios.

K-Fold	$k = 1$	$k = 2$	$k = 3$	$k = 4$	$k = 5$	Whole dataset
MSE_{test}	$1.47 \cdot 10^{-2}$	$1.48 \cdot 10^{-2}$	$9.66 \cdot 10^{-3}$	$1.91 \cdot 10^{-2}$	$1.51 \cdot 10^{-2}$	$1.23 \cdot 10^{-2}$
R^2_{test}	0.985	0.985	0.990	0.981	0.985	0.987

Table 3.4: K-Fold cross-validation (whole dataset) for a pin-jointed truss lattice under the GNN model.

3.1.1.2.2 Euler-Bernoulli Beams The same GNN surrogate will now analyze $N = 10\,000$ Euler-Bernoulli beam lattices, with the same material and geometrical properties than the pin-jointed truss lattice set counterpart, same node and edge features, and architecture - see Table 2.3 and Figure 2.7.

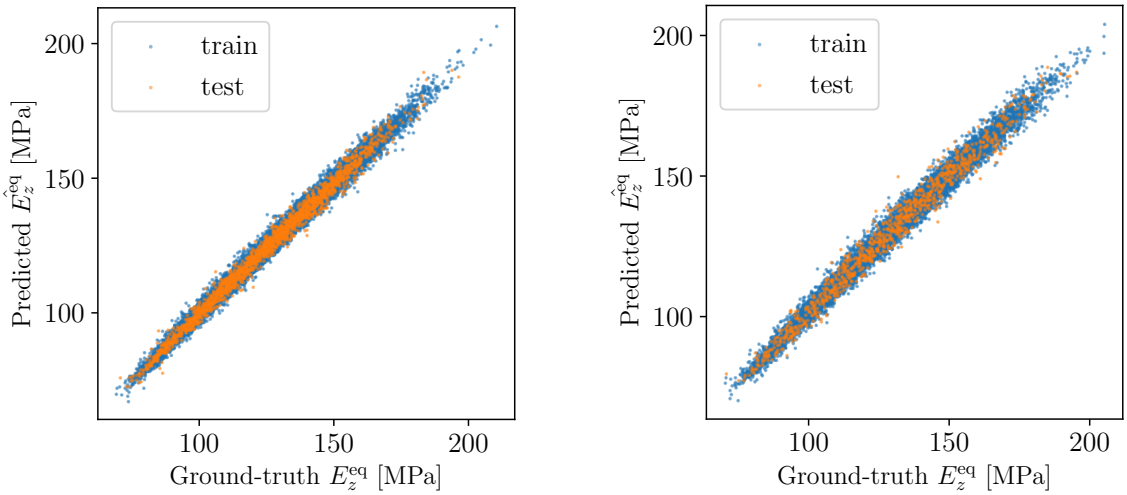

(a) Pin-jointed truss lattice GNN model.

(b) Euler-Bernoulli beam lattice GNN model.

Figure 3.5: Pin-jointed truss (a) and Euler-Bernoulli beam (b) lattice GNN models. Equivalent stiffness E_z^{eq} prediction (training in blue, testing in orange).

The validation set contains 15% of this dataset, whereas, for the test set, 1000 new samples (10%) are generated separately. Again, all features and targets are scaled with standard normalization, and training is performed using the parameters displayed in Table 3.2. Results can be seen in Figure 3.5b and Table 3.5.

GNN (b)	$\mathcal{L}_{\text{train}}$	R^2_{train}	$r^2_{\text{min,train}}$	$r^2_{\text{max,train}}$	$\mathcal{L}_{\text{test}}$	R^2_{test}	$r^2_{\text{min,test}}$	$r^2_{\text{max,test}}$
$n_s = 19$	$1.55 \cdot 10^{-2}$	0.985	$5.68 \cdot 10^{-10}$	0.336	$2.20 \cdot 10^{-2}$	0.978	$2.11 \cdot 10^{-9}$	0.514

Table 3.5: Training and test parameters for the GNN surrogate tackling Euler-Bernoulli beams.

Although prediction for this mechanical model becomes more challenging due to the appearance of shear forces and bending/twisting moments in the (now rigid) joints - leading to more equilibrium equations -, the GNN model is able to perform accurately on this dataset as well. The diagonal line at 45° in Figure 3.5 would be the perfect prediction, which results match almost perfectly.

3.1.2 Special Case: Partial Observability

A three-mass dynamical system is considered, only one of whom is observable. This short but epistemologically enlightening study demonstrates how models linking observable inputs (i.e. causes) and outputs (i.e. consequences) exist for time-dependent (Guyan reduction), transient (via Fourier analysis) and dynamical scenarios (sequential ANNs, e.g. RNN-LSTM).

3.1.2.1 Learning in the Fourier Space

As a particular example of Figure 2.9, let a system composed of 3 identical masses ($m_1 = m_2 = m_3 = m$), springs ($k_1 = k_2 = k_3 = k$) and dampers ($c_1 = c_2 = c_3 = c$) and spring length ($l_1 = l_2 = l_3 = l$) be proposed. Forces can be applied on both the internal masses (the first two) and/or on the third, observable one. The following values are considered: $m = 0.5\,\mathrm{Kg}$, $c = 0.8\,\mathrm{Ns/m}$, $k = 1\,\mathrm{N/m}$, $l = 1\,\mathrm{m}$.

The dynamical model reads:

$$\begin{pmatrix} \dot{q}_1 \\ \dot{p}_1 \\ \dot{q}_2 \\ \dot{p}_2 \\ \dot{q}_3 \\ \dot{p}_3 \end{pmatrix} = \begin{pmatrix} 0 & 1/m & 0 & 0 & 0 & 0 \\ -2k & -2c/m & k & c/m & 0 & 0 \\ 0 & 0 & 0 & 1/m & 0 & 0 \\ k & c/m & -2k & -2c/m & k & c/m \\ 0 & 0 & 0 & 0 & 0 & 1/m \\ 0 & 0 & k & c/m & -k & -c/m \end{pmatrix} \begin{pmatrix} q_1 \\ p_1 \\ q_2 \\ p_2 \\ q_3 \\ p_3 \end{pmatrix} + \begin{pmatrix} 0 \\ k_1 l_1 - k_2 l_2 \\ 0 \\ k_2 l_2 - k_3 l_3 \\ 0 \\ k_3 l_3 \end{pmatrix} + \begin{pmatrix} 0 \\ F_1(t) \\ 0 \\ F_2(t) \\ 0 \\ F_3(t) \end{pmatrix}, \tag{3.4}$$

which, in the linear case and taking into account that $k_1 = k_2 = k_3 = k$ and $l_1 = l_2 = l_3 = l$, undergoes the Fourier transform:

$$\begin{pmatrix} i\omega & -1/m & 0 & 0 & 0 & 0 \\ 2k & i\omega + 2c/m & -k & -c/m & 0 & 0 \\ 0 & 0 & i\omega & -1/m & 0 & 0 \\ -k & -c/m & 2k & i\omega + 2c/m & -k & -c/m \\ 0 & 0 & 0 & 0 & i\omega & -1/m \\ 0 & 0 & -k & -c/m & k & i\omega + c/m \end{pmatrix} \begin{pmatrix} \hat{q}_1 \\ \hat{p}_1 \\ \hat{q}_2 \\ \hat{p}_2 \\ \hat{q}_3 \\ \hat{p}_3 \end{pmatrix} = \begin{pmatrix} 0 \\ 0 \\ 0 \\ 0 \\ 0 \\ kl \end{pmatrix} \delta(\omega) + \begin{pmatrix} 0 \\ \hat{F}_1 \\ 0 \\ \hat{F}_2 \\ 0 \\ \hat{F}_3 \end{pmatrix} \tag{3.5}$$

where $\hat{\bullet}$ denotes Fourier transform of the masses' positions, momenta and applied forces.

By reordering the previous system, the position and momentum degrees of freedom can be grouped:

$$\begin{pmatrix} \tilde{\mathbf{T}}_{qq}(\omega) & \mathbf{T}_{qp} \\ \mathbf{T}_{pq} & \tilde{\mathbf{T}}_{pp}(\omega) \end{pmatrix} \left(\begin{array}{c} \hat{q}_1 \\ \hat{q}_2 \\ \hat{q}_3 \\ \hline \hat{p}_1 \\ \hat{p}_2 \\ \hat{p}_3 \end{array}\right) = \left(\begin{array}{c} 0 \\ 0 \\ 0 \\ \hline 0 \\ 0 \\ kl \end{array}\right) \delta(\omega) + \left(\begin{array}{c} 0 \\ 0 \\ 0 \\ \hline \hat{F}_1 \\ \hat{F}_2 \\ \hat{F}_3 \end{array}\right), \tag{3.6}$$

and then, the momentum degrees of freedom $\hat{p}_i$ condensed into the ones related to the masses positions $\hat{q}_i$, as previously discussed:

$$\left(\mathbf{T}_{pq} - \tilde{\mathbf{T}}_{pp}(\omega)\,\mathbf{T}_{qp}^{-1}\tilde{\mathbf{T}}_{qq}(\omega)\right)\mathbb{Z}_q(\omega) = \mathbb{S}_p(\omega). \tag{3.7}$$

Separating the internal and observable degrees of freedom in Equation 3.7:

$$\left(\begin{array}{cc|c} A_{11}(\omega) & A_{12}(\omega) & A_{13}(\omega) \\ A_{21}(\omega) & A_{22}(\omega) & A_{23}(\omega) \\ \hline A_{31}(\omega) & A_{32}(\omega) & A_{33}(\omega) \end{array}\right)\left(\begin{array}{c} \hat{q}_1 \\ \hat{q}_2 \\ \hline \hat{q}_3 \end{array}\right)=\left(\begin{array}{c} 0 \\ 0 \\ \hline kl \end{array}\right)\delta(\omega)+\left(\begin{array}{c} \hat{F}_1 \\ \hat{F}_2 \\ \hline \hat{F}_3 \end{array}\right) \tag{3.8}$$

allowing for explicit expression of model involving the observable degree of freedom, $\hat{q}_3$, as in:

$$\left\{A_{33}(\omega)-\begin{pmatrix} A_{31}(\omega) & A_{32}(\omega) \end{pmatrix}\begin{pmatrix} A_{11}(\omega) & A_{12}(\omega) \\ A_{21}(\omega) & A_{22}(\omega) \end{pmatrix}^{-1}\begin{pmatrix} A_{13}(\omega) \\ A_{23}(\omega) \end{pmatrix}\right\}\hat{q}_3(\omega)=$$

$$kl\delta(\omega)+\hat{F}_3+\begin{pmatrix} A_{31}(\omega) & A_{32}(\omega) \end{pmatrix}\begin{pmatrix} A_{11}(\omega) & A_{12}(\omega) \\ A_{21}(\omega) & A_{22}(\omega) \end{pmatrix}^{-1}\begin{pmatrix} \hat{F}_1(\omega) \\ \hat{F}_2(\omega) \end{pmatrix}, \tag{3.9}$$

that, arranged in a more compact manner, reads:

$$\tilde{A}_{33}(\omega)\,\hat{q}_3(\omega)=kl\delta(\omega)+\hat{F}_3(\omega)+\hat{F}_{i3}(\omega), \tag{3.10}$$

representing the system transfer function.

The final point concerns the data-driven model identification, that is, how to extract from the given data the different model components: $\tilde{A}_{33}$ and $\hat{F}_{i3}$, for each involved frequency ω. In the last equation, index i in $\hat{F}_{i3}$ conveys all the effects coming from the unresolved degrees of freedom (internal unobserved masses). The system identification proceeds as follows:

1. The free response associated to $F_3=0$ (only the loads on the internal masses apply), $q_3^f(t)$ ($\bullet^f$ for "loading-free"), is obtained (measured).
2. Then, for a non-null applied (and measurable) loading on the observable mass, $F_3\neq 0$, the system response $q_3(t)$ is recorded, now a consequence of all the loading terms involved in the right hand member of the previous equation.
3. The difference between the forced and free displacements can be obtained from $\Delta q_3(t)=q_3(t)-q_3^f(t)$, allowing for the computation of its Fourier transform $\widehat{\Delta q_3}(\omega)$.
4. Lastly, by means of $\widehat{\Delta q_3}$ and the measurable force's Fourier transform $\hat{F}_3(\omega)$, the model coefficient $\tilde{A}_{33}(\omega)$ is learned from

$$\tilde{A}_{33}(\omega)=\frac{\hat{F}_3(\omega)}{\widehat{\Delta q_3}(\omega)}. \tag{3.11}$$

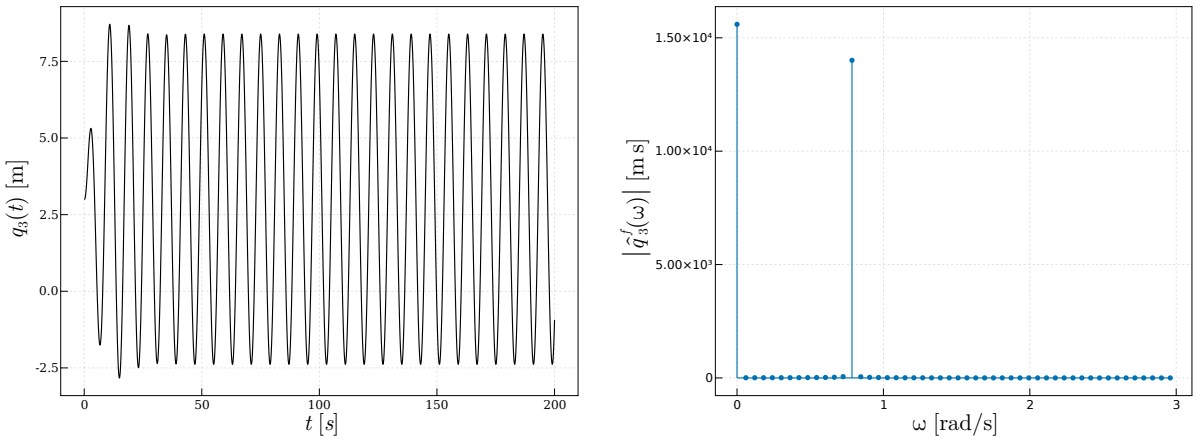

Figure 3.6: Free response ($F_3(t) = 0$): (left) $q_3^f(t)$; and (right) $\hat{q}_3^f(\omega)$

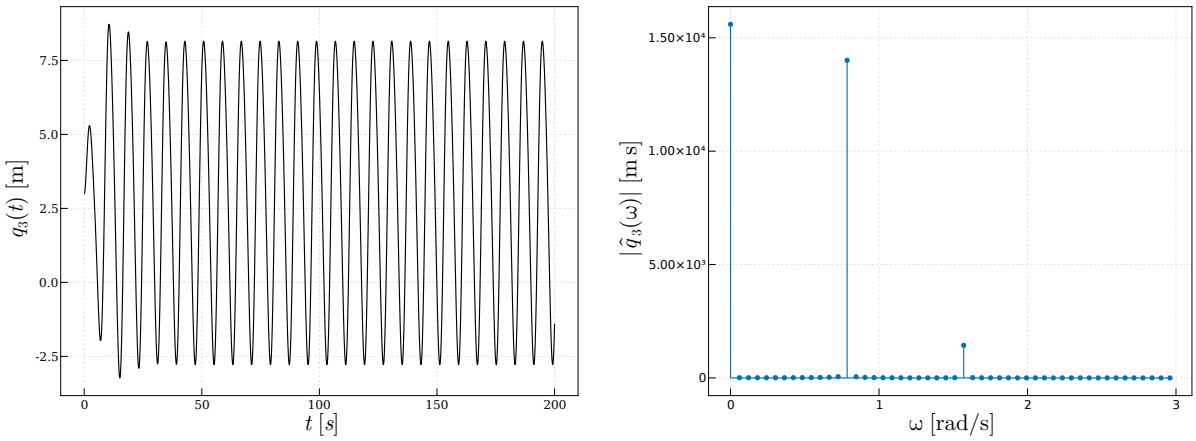

Figure 3.7: Forced response: (left) $q_3(t)$; and (right) $\hat{q}_3(\omega)$

For single-frequency loading:

$$\begin{cases} F_1(t) = 2\cos(2\pi t) \\ F_2(t) = 2\cos\left(\dfrac{\pi}{4}t\right) \\ F_3(t) = 2\cos\left(\dfrac{\pi}{2}t\right) \end{cases} \tag{3.12}$$

The free and forced responses, along with their Fourier transforms, are depicted in Figures 3.6 and 3.7, respectively. This loading is used to generate the synthetic data needed to identify the model's output $q_3(t)$ later on, i.e. as a function of the observed load $F_3(t)$. During the training process, $F_2(t)$ and $F_3(t)$ are fully ignored.

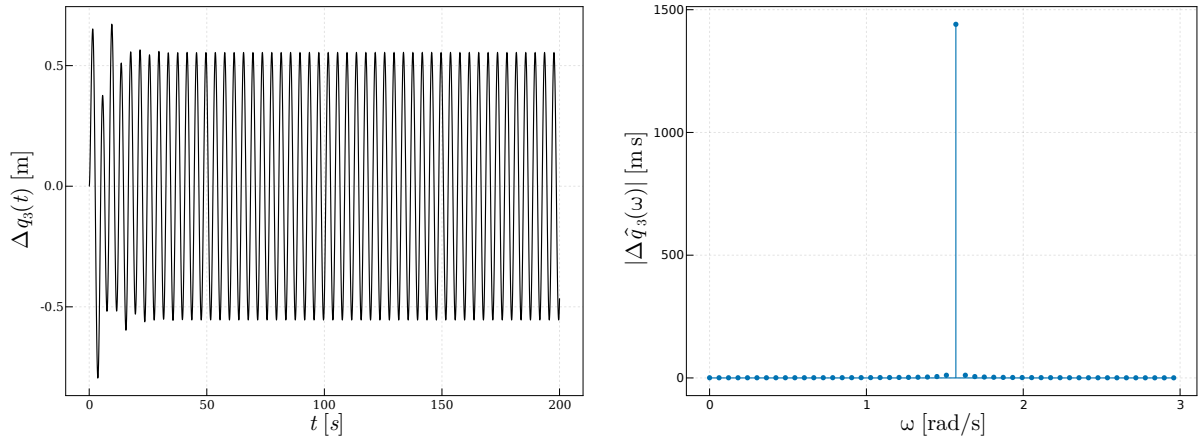

Figure 3.8: Response difference: (left) $\Delta q_3(t)$; and (right) $\widehat{\Delta q}_3(\omega)$

Figure 3.8 displays the response difference $\Delta q_3(t) = q_3(t) - q_3^f(t)$ and its Fourier transform $\widehat{\Delta q}_3(\omega)$ on the domain in which the difference $\Delta q_3(t)$ becomes almost stabilized, with a negligible transient component. When comparing the reference solution, obtained by the reference analytical model $\tilde{A}_{33} = -1.4848 + 1.0221i$, to the one obtained from the learned model $\tilde{A}_{33} = -1.5242 + 0.9823i$ (at principal frequency), great accuracy can be noticed.

3.1.2.2 Machine Learning as a Surrogate

The same 3-mass dynamical problem is integrated numerically to obtain the ground truth, that is, the reference solution to train the different neural network surrogates, i.e. RNN and LSTM.

In both cases, input data consists of the observable force F_3 and position q_3 in the previous time steps, defining surrogate $\mathcal{H}$:

$$\tilde{q}_3^i = \mathcal{H}\left(\begin{pmatrix} F_3^i \\ F_3^{i-1} \\ \vdots \\ F_3^{i-n+1} \end{pmatrix}, \begin{pmatrix} q_3^{i-1} \\ q_3^{i-2} \\ \vdots \\ q_3^{i-n} \end{pmatrix}\right), \tag{3.13}$$

where $\tilde{q}_3^i$ is the prediction of q_3 at time step i.

As Equation (3.13) reflects, different memory lengths from the use of positive integer $n \geq 0$ are taken into account. For $n \neq 0$, an initialization issue occurs. In this case, larger memory is the toll for ignoring the internal forces, whose consequences on the observed variables are learned from the time evolution of the latter.

Hence, initialization can follow two alternative strategies:

- In the forced regime, the long-time solution does not depend on the initialization.
- For the transient solution, one could consider a coarser model updating its current state from the preceding one for the first n values. Then, the LSTM can carry on with the task.

Due to memory storage concerns, the first n values are assumed known.

3.1.2.2.1 Recurrent Neural Network Firstly, a RNN surrogate model with $n = 2$ is built upon Equation (3.13). The database comprises 10,000 states of the observable variables coming from the integration of the dynamical system, split between testing (80%) and training sets (20%). The RNN's architecture features a single layer with one output $\tilde{q}_3^i$, its networks parameters and initialization choices reported in [478]. The algorithm is trained for 1,500 epochs, even though shorter training yields similar results. The linear problem considers, once more: $m_1 = m_2 = m_3 = 0.5Kg$, $c = 0.8Ns/m$, $k_1 = k_2 = k_3 = 1N/m$, and $l_1 = l_2 = l_3 = 1m$, expressing the applied loading as:

$$\begin{cases} F_1(t) = 2\cos(2\pi t) \\ F_2(t) = 2\cos\left(\frac{\pi}{4}t\right) \\ F_3(t) = \frac{t}{t_{max}} + \cos\left(\frac{\pi}{2}t\right) \end{cases}, \tag{3.14}$$

with $t_{max} = 500s$. This loading is used to generate the synthetic ground-truth data to identify the model $q_3(t)$ as a function of the observed load $F_3(t)$. During training, $F_2(t)$ and $F_3(t)$ are again completely neglected. The computed results from the trained network are given in Figure 3.9, being the mean absolute percentage errors (MAPE) 1.38% on the training set and 2.18% in the testing set.

The same RNN (now with $n = 3$ in Equation 3.13) was employed to tackle a non-linear dynamical system, with similar parameters to the ones considered in the linear case, except in what concerns the springs stiffnesses, given by:

$$\begin{cases} k_1 = k_{01}(1 + \alpha\Delta l_1) \\ k_2 = k_{02}(1 + \alpha\Delta l_2) \\ k_3 = k_{03}(1 + \alpha\Delta l_3) \end{cases}, \tag{3.15}$$

with $k_{01} = k_{02} = k_{03} = 10\ N/kg$, $\alpha = 10^{-4}\ m^{-1}$ (arbitrary, though carefully tuned to maintain the stability of the simulation) and where $\Delta l.$ is the elongation of the corresponding spring, i.e. $\Delta l_2 = q_2 - q_1 - f_2$, $\Delta l_3 = q_3 - q_2 - f_3$ and $\Delta l_1 = q_1 - l_1$. Importantly, this makes the three kl components in 3.5 non-zero.

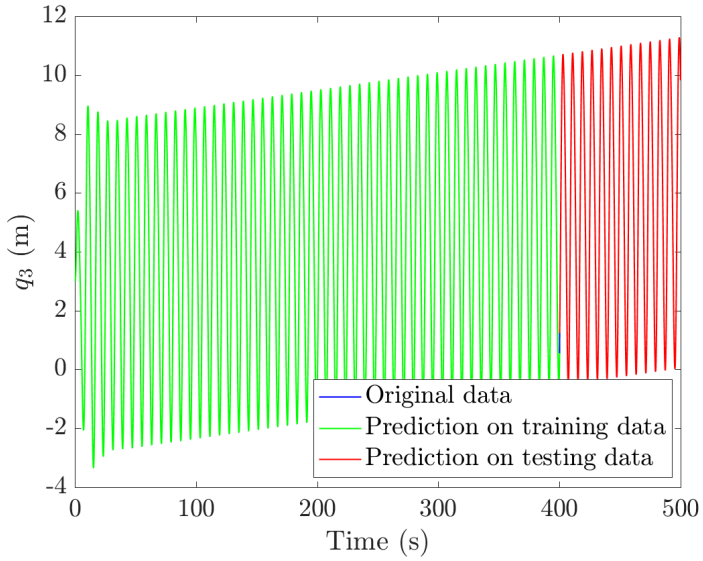

Figure 3.9: Prediction of the observable position $\tilde{q}_3(t)$ computed from a trained RNN with $n = 2$ (colors green and red mark the training and testing sets, respectively).

The considered loading, now without time slopes, reads

$$\begin{cases} F_1(t) = 2\cos(2\pi t) \\ F_2(t) = 2\cos\left(\frac{\pi}{4}t\right) \\ F_3(t) = \cos\left(\frac{\pi}{2}t\right) \end{cases} \tag{3.16}$$

The results concerning the non-linear dynamical system and its error are reported in Figure 3.10, yielding a mean absolute percentage error (MAPE) of 1.34% in training and 1.29% in testing. Training error being slightly larger is probably due to the larger transient phase presenting higher peaks.

3.1.2.2.2 Long Short-Term Memory The same linear and non-linear dynamical systems are now processed by LSTM cells, with the same network parameters and initialization used for the RNN surrogate. When addressing the linear case, the computed results are given in Figure 3.11, with a MAPE of 0.84% in the training set and 1.33% in the testing set.

The results and error in the non-linear case are reported in Figure 3.12, presenting a MAPE of 0.15% in the training set and 0.14% in the testing set. The error is again slightly larger in the training set for the same reasons given before. As expected, LSTM outperforms RNN for a large number of epochs. For a smaller amount of epochs, the opposite is true, since convergence is more easily achieved using a lower number of parameters.

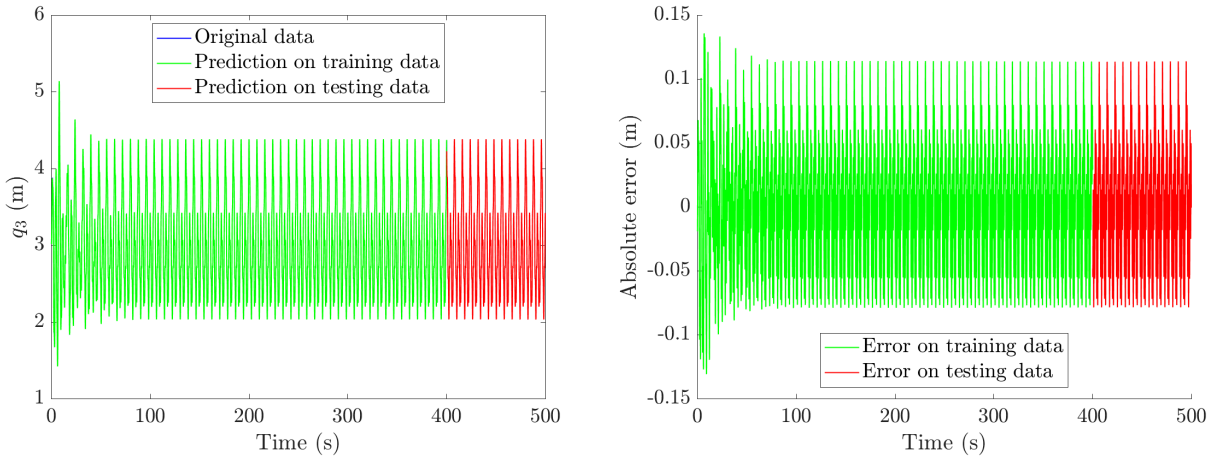

Figure 3.10: Prediction (left) and absolute MAPE error (right) of the observable position $\tilde{q}_3(t)$ in the non-linear case, computed by a trained RNN with $n = 3$ (again, colors refer to the training and testing sets).

The error in the linear case was larger, possibly due to the fact that it involves close to zero values which negatively impact error calculation. Several experiments with various number of elements, different dampening coefficients, stiffnesses, lengths and masses have been carried out with similarly satisfactory results (MSE error always below 0.07 for both training and testing).

To ponder the influence of internal unobserved variables, different loading scenarios are conceived for the 3-mass system:

- **Case 1.** All internal loads are applied ($F_1(t) \neq 0$, $F_2(t) \neq 0$), with no external load ($F_3(t) = 0$).
- **Case 2.** Only the external load is considered ($F_3(t) \neq 0$).
- **Case 1.** All loads are applied ($F_1(t) \neq 0$, $F_2(t) \neq 0$, $F_3(t) \neq 0$).

Lastly, an exploration of path-dependency and internal variables is carried out. To add complexity, non-linearity is also made path-dependent by updating stiffness upon their previous values instead of the initial ones, as in Equation 3.17.

$$k_i^{t+1} = k_i^t(1 + \alpha\Delta\ell_i^t) \tag{3.17}$$

Figure 3.13 proves the robustness of RNN-LSTM surrogates when providing approximate predictions of highly non-linear, path-dependent behaviors.

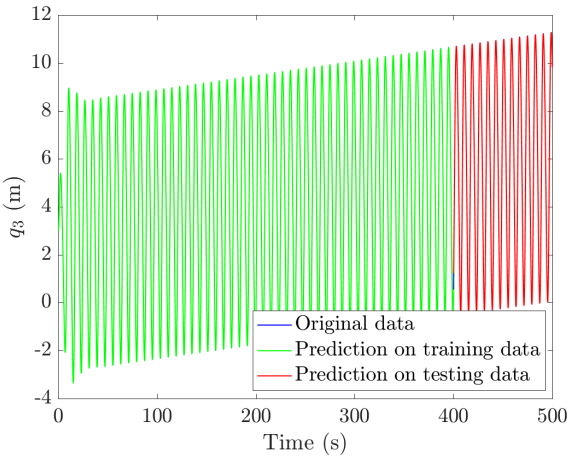

Figure 3.11: Prediction of the observable position $\tilde{q}_3(t)$ computed by a trained LSTM with $n = 2$ (the same color code is employed).

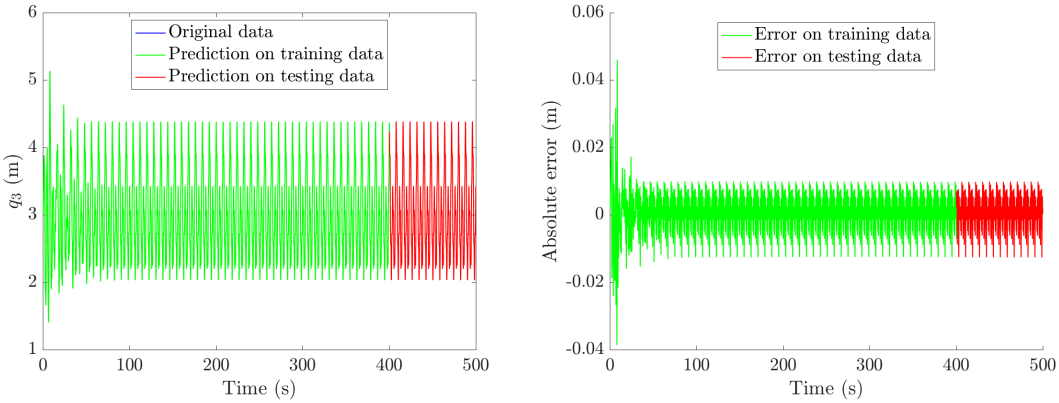

Figure 3.12: Prediction (left) and error (right) of the observable position $\tilde{q}_3(t)$ in the non-linear case, computed by a trained LSTM with $n = 3$ (same color code).

3.2 Structural Design and Optimization

This section covers all results related to inverse design and optimization strategies, i.e. obtaining the structure/topology yielding a given set of target properties. It aims to encompass various real-life examples, covering external mechanical responses an homogenized properties as targets applied to discrete (truss/beam) and continuous domains (bulk material). As inverse problems, they are ill-posed, so obtaining the global optimum will not always be possible, and many mathematical issues (non-linearity, surjection, etc.) are expected.

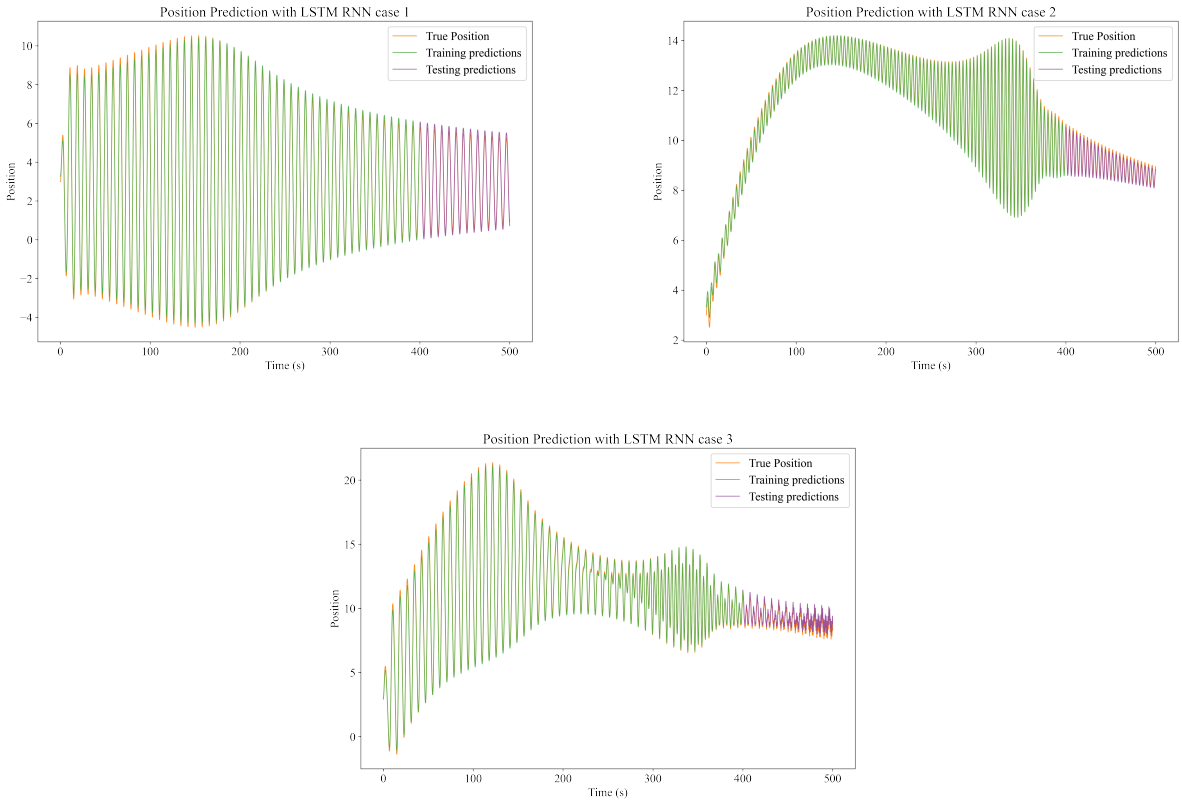

Figure 3.13: Displacement predictions via LSTM for load cases 1 (top left), 2 (top right) and 3 (bottom) when the path-dependent scheme is enforced.

3.2.1 Inverse Lattice Design

Firstly, discrete domains will be addressed, mainly truss lattices yielding either global mechanical properties (e.g. Young's modulus E) or external mechanical responses (e.g. external reaction force distribution under certain loading conditions of interest).

3.2.1.1 For a Target Global Property

This preliminary inverse strategy is the logical consequence of the direct problem (lattice -> property) developed in Section 2.1 and tested in Section 3.1. With all that ground data generated for the direct problem, a first approximation to the inverse problem consists of searching among the available, existing structures. This creates a finite domain whose boundaries can be defined by a Pareto front if another optimization variable (e.g. mass/volume) is considered.

A particular example follows. No direct length or force units will be given, since linear elastic conditions are ensured by choosing the yield stress as the critical threshold for axial stress, i.e. $\sigma_{crit} = \sigma_Y$. Hence, proportionality in mechanical responses is guaranteed, whatever the scale.

Setting a target Young's modulus e.g. $E_z^{\text{eq},*} = 170$ MPa, a local range $E_z^{\text{eq},*} \in [E_{\min}, E_{\max}]$ is defined. Then, a local Pareto front is depicted to look for the lightest solution within that range. In the case of Figure 3.14, $E_{\min} = 169$ MPa and $E_{\max} = 171$ MPa, thus the lightest solution corresponds to a lattice with $V = 7.66 \cdot 10^{-3} m^3$ and $\hat{E}_z^{\text{eq}} = 169.4$ MPa. The ground-truth effective behavior of that lattice given by the (direct) procedure yields $E_z^{\text{eq}} = 171.0\,\text{MPa}$. By defining the absolute value of the relative error ϵ with respect to the ground-truth property as

$$\epsilon = \frac{|E_z^{\text{eq}} - \hat{E}_z^{\text{eq}}|}{E_z^{\text{eq}}},$$

the relative error for this specific case is $\epsilon = 0.94\%$.

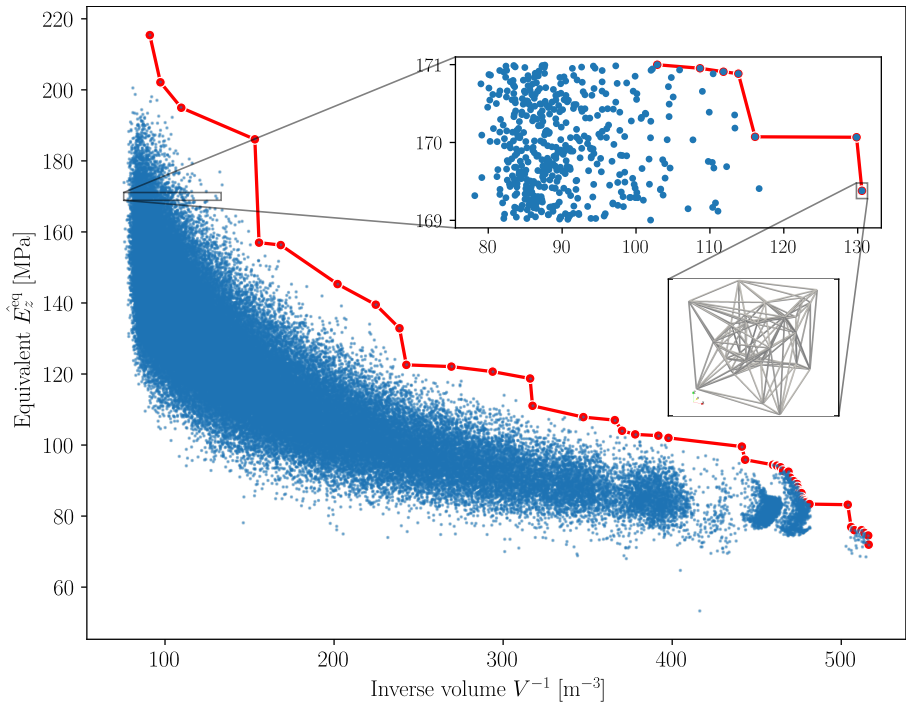

Figure 3.14: Distribution of inverse volume and equivalent predicted stiffness $(V^{-1}, \hat{E}_z^{\text{eq}})$ of 100,000 samples generated with the GNN surrogate model and its optimal Pareto front, in red.

3.2.1.2 For a Prescribed Mechanical Response

Employing the methodology developed in Section 2.2, consider an aperiodic lattice $\epsilon_n = 10^{-5}$, $\epsilon_n = 10^{-4}$, $N_{iter} = 1$, $N_{clamps} = 16$, $N_{inner} = 50$ (amount of non-clamp inner nodes) and $N_b = 173$ (number of struts) within a 7x7 square dominion - see Figure 3.15 left. The lattice generation strategy is the same followed in [103], only for 2D beams to ease the already ill-posed problem. The effects of 1-step optimization can be observed in Figure 3.15.

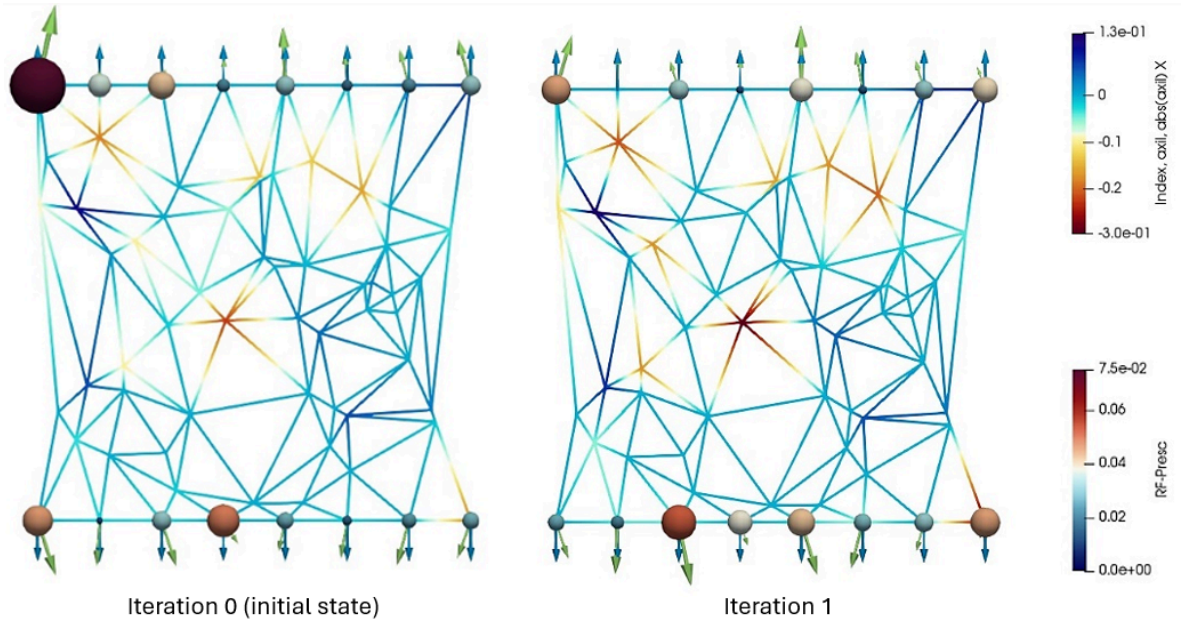

Figure 3.15: Initial state (left) and first iteration (right). Struts are colored with their respective load index ind_b (top right scale), while clamp nodes (bottom right scale) show the modulus difference between reactions (green arrows) and prescribed forces (blue arrows).

As seen in Figure 3.15, improving (balancing) the loading state of one node implies worsening others and/or the internal struts' states; such are the issues of multi-objective optimization. Due to the low ϵ_n and ϵ_b , the movement of the inner nodes is almost imperceptible. Regarding the outer reaction force profile, mending the reactive forces in some modes in modulus sometimes implies the appearance of forces in non-prescribed directions, or even momenta (which are not represented) and/or further offsets in other clamp nodes.

Regarding the internal nodes (N_{inner}), the slight movement of nodes and widening of inner bars updates the previous load equilibrium, thus altering the nodal stress concentration, represented by their respective load indices.

This changes can be derived from one of v_{ind}'s three components: offset in the outer clamp nodes (γ_b), axial stress on bars (α_b, β_b) and/or or the neighboring bars' relative orientation determining the propagation direction ($|\overrightarrow{\mathbf{n_{prop}}}|$). These multiple effects are superposed or opposed depending on the changing geometry.

For $N_{iter} = 10$, the top clamp is near the target, unlike the bottom one (Figure 3.16). Thus, convergence can be fast, but results are only partially satisfactory: the accuracy (less than 5% mean error) in the "output" (top side) clamp nodes comes at the sacrifice of the other clamp end ("input" nodes), with almost 100% error. On top of that, additional unforeseen (and undesired) forces appear in non-concerned degrees of freedom (e.g. horizontal forces in Figures 3.16).

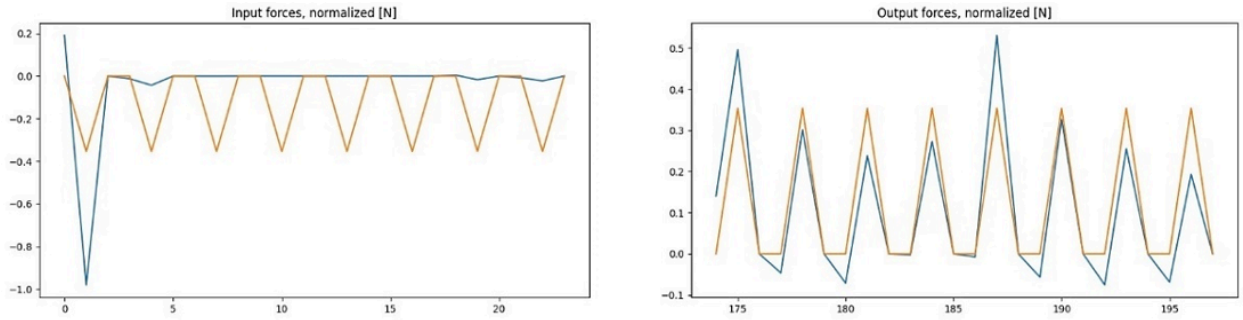

Figure 3.16: Normalized reactions (blue) versus normalized prescribed forces (orange) for Figure 3.15 left after 10 iterations. Degrees of freedom on horizontal axis (only vertical force is prescribed) and their relative offsets along the vertical one.

There are two possible solutions for that, both restraining the the problem's notable complexity: either keeping the nodes fixed in position and stick to cross-section updates (or in reverse) or set a periodic architecture as a starting point, introducing disorder as the nodes move. Considering the latter solution, disordered structures have been addressed on a first trial, considering the aforementioned beneficial features (localizing mechanical failure, organic continuum-like pseudo-isotropic behavior) [479, 103].

Alas, the already degenerate aperiodic lattices can prove challenging to adjust. Perhaps, a more promising approach would be to start with a (quasi-)periodic lattice and then progressively introduce disorder when searching for an appropriate inverse design.

Let the 7x7 planar lattice be considered again. This time, all possible integer node locations $(0,1),(1,0),(1,1),...(7,7)$ are explored, except for a few periodic inner holes created on purpose (e.g. on odd rows and even columns) to introduce some anisotropy.

Delaunay triangulation is applied to the remaining nodes, and thus an asymmetric yet periodic structure is obtained - see Figure 3.17a. To explore whether smoother target force profiles improve the algorithm's performance, the mean of the initial reactions will be prescribed separately for input (bottom clamp, *in*) and output (top clamp, *out*) nodes, i.e. $|F_p^{y,in,t}| = |\overline{F_r^{y,in,t=0}}|$ and $|F_p^{y,out,t}| = |\overline{F_r^{y,out,t=0}}|$.

This way, the objective is now to soften the reaction profile for the same prescribed initial vertical displacement $u_0 = 2 \cdot 10^{-2}$ by internally rearranging strut thickness and node positions (and thus, strut length). This could be of great interest in knee and hip prostheses, where the mechanical response in the joint material inter-phase must be smooth and homogeneous. With the same hyper-parameter set as the previous example (for comparison purposes), the algorithm is run for 100 iterations, obtaining the structure in Figure 3.17b. Iteration stops at $t = 100$ or $\delta_t = 10^{-3}$, whatever comes first.

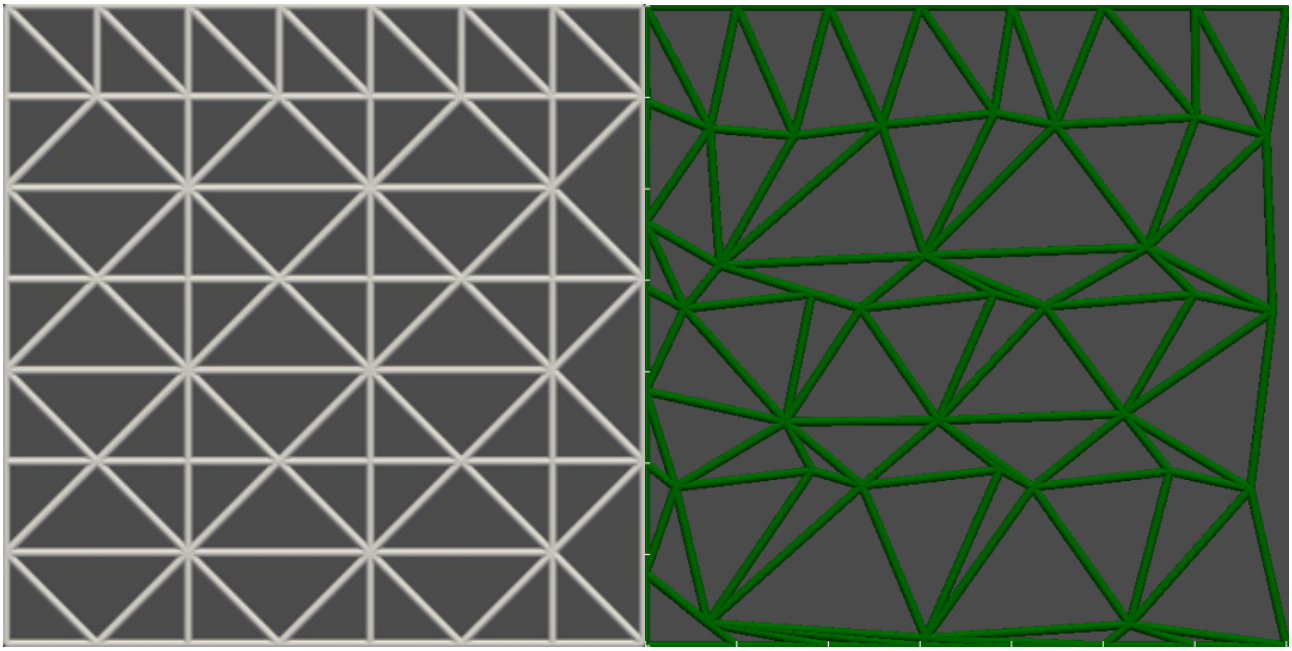

(a) Initial, ordered (b) Final, disordered

Figure 3.17: Results after application of 100 rearranging iterations to an "ordered" structure.

Figure 3.17 shows indeed a great difference between the ordered, semi-periodic lattice on the left and its disordered counterpart on the right. Note how some struts along the dominion's left, right and top side have kept some similarities while the original design, while the inner and bottom sides are much more distorted. It would seem the nodal displacements on the top inner side have piled up downwards, leaving close to no freedom for those bottom nodes to move.

Hence - although it is not reflected in the provided image for simplicity and better visualization -, the struts in the bottom side are much thicker than the top ones (about 5 times).

That means the two degrees of freedom in the inverse design process (nodal migration/strut length and strut thickness) alternatively cover for the other's shortcomings when overly restricted, i.e. longer struts tend to be thinner and shorter struts are usually thicker (in general terms). So, to prevent buckling, thickening is especially enhanced and lengthening is particularly penalized when the strut is under compression. Either way, convergence is still compromised: see Figures 3.17 and 3.18. When these issues are solved, discrete strut elimination can be enforced, as in [480, 481].

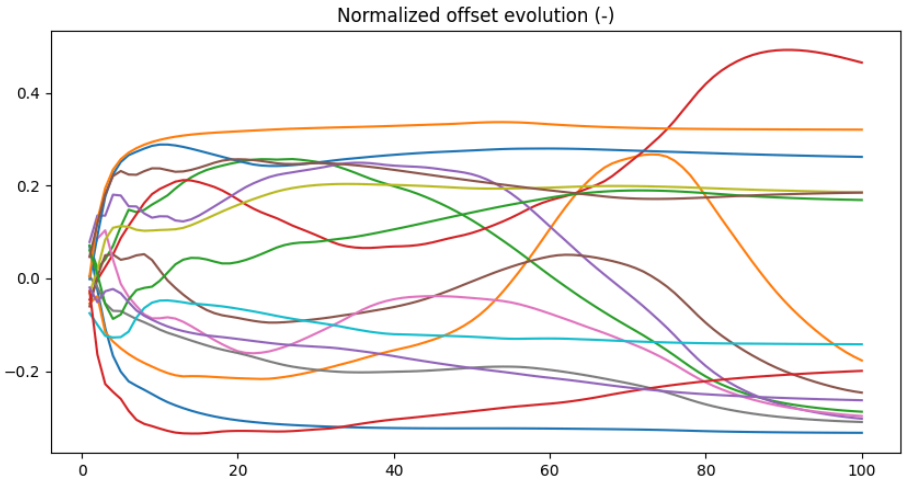

Figure 3.18: Response offset of structure in Figure 3.17 after 100 iterations. Each colored line stands for one clamp node.

Again, as seen in Figure 3.18, convergence is fast for some nodes (e.g. the dark green, pink and dark brown lines reach virtually zero offset - exact match - within the first 20 iterations), but many other diverge and so do the converged ones after a few iterations since the structure (and thus, the problem itself) has changed. That is, the gradient is generally not well adjusted for this kind of evolving setting.

This is tantamount to an ill-defined, non-convex problem and so many local minima in nodes are mistaken for global optima. Too many variables are being updated in each iteration, whose stress state iteratively changes – and so, the problem to be optimized also does.

Since fine-tuning of hyper-parameters proves difficult, several non mutually exclusive alternatives can be explored:

- Defining a global analytic expression for unison global displacement (hence with a global gradient, instead of a local strut-dependent one). However, coming up with such an expression is not trivial, so perhaps data-driven techniques (e.g. POD, GNN) can be employed as surrogates.
- Developing the "gradual disorder" approach, progressively introducing "dislocations" [479], holes and perhaps interstitial nodes with a clear methodology. Bending- or stretch-dominated lattices could be favoured according to the design requirements, which poses interesting mechanical implications.
- Introducing "nodal migration", similarly to biological cells [414, 124]. Note that this is an heuristic solution, and thus not guaranteed to be optimal, much less in an inverse problem framework like this; so more robust convergence criteria must be defined.
- Analytically extracting the dependence of strut enlargement ΔL and thickening ΔA to solve the resulting variational problem. For a discrete lattice with N_{clamp} external nodes, N_{inner} internal ones ($N_{total} = N_{inner} + N_{clamp}$) and $B < N_b$ inner struts (clamp nodes and struts are invariant), the problem is defined by

$$\min_{\forall dA_j, dL_j} || \sum_{n}^{N_{inner}} \sum_{j}^{B} F(A_j + \Delta A_j, L_j + \Delta L_j) + \lambda(\sum_{i}^{N_{clamp}} F_i^p - \sum_{i}^{N_{clamp}} F_i^r) ||_2 \tag{3.18}$$

  where λ is a Lagrange multiplier for external (clamp) force offsets, yielding the correspondent system of equations where axial strut at time-step t force takes the form:

$$F(A + \Delta A, L + \Delta L) = F(A, L) + \frac{\partial F}{\partial A}\Delta A + \frac{\partial F}{\partial L}\Delta L = AE\frac{\Delta L}{L} + E\frac{\Delta L}{L}dA - 2AE\frac{\Delta L}{L^2}dL \tag{3.19}$$

  in which A, L and their discrete changes $\Delta A, \Delta L$ come from the previous iteration $t-1$.

  This solution, although computationally costly (Equations 3.18 and 3.19 are computed for every iteration), is the most rigorous one in mathematical terms, defining a clear minimization strategy, although the problem is most likely non-convex, nevertheless.

  Despite focusing on offset ($\overrightarrow{F_p} - \overrightarrow{F_r}$) reduction, this proposal still does not solve the stress concentration problem in nodes and along struts, so constraints have to be added accordingly, thus yielding a multi-objective optimization problem.

- Selectively trimming struts and altering connectivity to create an allosteric effect [482] - that is, local actions having acting upon distant, not directly-connected regions in the domain, like proteins do. Isostatic "soft" regions with low nodal degree (around 3) can be alternated with more rigid, hyper-static areas (degree > 3) whose transition is defined by entropy thresholds (in a thermodynamic sense [483, 484]). Tailored convergence criteria are also imperative here.

Should the problem be successfully addressed, it would unfold interesting applications in several research fields: medical prostheses, structural maintenance (adaptation to stress relaxation, creep, etc. if the nodal "paths" are defined in a certain way), asymmetric properties (e.g. auxetic [485]), shape memory, etc. This can prove particularly useful in Structural Health Monitoring (SHM) if offsets between prescribed and reactive forces are defined as deviations from normal conditions [135, 136].

3.2.2 Inverse Design in Continuous Domains

Discrete solutions in the last subsection constrain further the infinite, non-bijective inverse design space, making them less difficult to encompass, i.e. approachable via relatively straightforward techniques like gradient descent and Pareto optimality. However, the inverse design space for continuous media (bulk material) is completely boundless, mesh-dependent and agnostic to any pre-conceived parametrizable shape or topology for load-supporting elements, i.e. discrete beams and trusses.

For this reason, more elaborate optimization frameworks must be employed to generate tailored load-bearing structures for a given set of boundary conditions. To this aim, topology optimization (TO) is employed, creating "holes" in an initially material-filled dominion until an appropriate structure is found. Please refer to Sections 1.2 and 2.2 for further explanations.

In the following examples, Solid Isotropic Material Penalization (SIMP) [29] will be used for its relative simplicity and popularity, mainly focusing on TO's aforementioned limitations: probabilistic loading, damage penalization, filtering and interpolation techniques. These results predominantly use 2D square elements for Finite Element Analysis (FEA), to ease computation and visualization of results. Nonetheless, these analyses can be extrapolated for 3D settings (some examples can be found at the end of this subsection) and more complex FEA, as well as other TO methodologies (e.g. stress-based).

3.2.2.1 Probabilistic Topological Optimization

Now, the uncertain TO settings derived from nondeterministic loading cases will be covered, applying the methodology explained in Section 2.2 and article **Probabilistic combination of loads in topology optimization designs via cumulative damage criteria** [486].

3.2.2.1.1 Conceptual Significance Firstly, the motivation must be understood. Let a cantilever beam be considered, with its left side fixed and two unitary outward-facing forces on each right corner, up and down (see Figure 3.19 top row). TO is then applied via the *top*88.*m* code [205].

If both forces are applied simultaneously (constant, present in each iteration), their compliance contribution is unique, thus easing convergence and obtaining a sharp result in few iterations (see Figure 3.19 middle column). However, should they be applied alternatively (one of them in each iteration), the result is much more topologically convoluted (Figure 3.19 left column): multiple fragile twigs, great asymmetry determined by the alternating load order (first introduced force is dominating), etc. All these issues can be tracked down to conflicting optimization directions with different, uncoordinated compliance contributions. More iterations do not help elucidate the converged topology in the second case: iteration 250 displays the same issues as iteration 50, even worse.

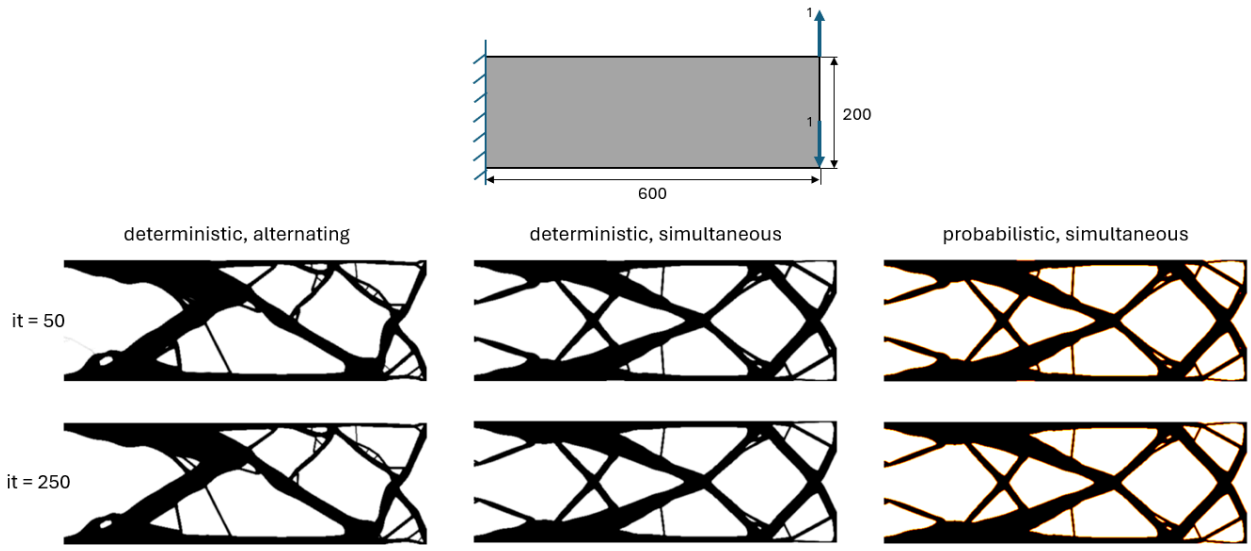

Figure 3.19: Cantilever beam with $v_f = 0.4$ (boundary conditions in top row) and its optimized topologies for the deterministic alternating (left column), deterministic simultaneous (middle column) and probabilistic simultaneous (right column) cases. Iterations 50 (middle row) and 250 (bottom row).

Should the proposed probabilistic framework (Equations 2.50 and 2.51) be introduced, with equal probability for each load ($p_{ij}^{up} = p_{ij}^{down} = 0.5$), the result is virtually equivalent to the deterministic case (Figure 3.19 right column), while retaining the same contributions as in the alternate case. This is expected, since the load share is equal for the top and bottom right corners.

Importantly, the amount of iterations does not visibly improve the deterministic (vanilla) topologies: no configuration shown along Figure 3.19's columns reaches noticeably simpler or less compliant solutions. However, one major advantage of this probabilistic framework is the fact that statistically-weighted loading results in lower overall compliances - about 1/2 of the deterministic equivalent when alternating and 1/4 when combined - see 5^{th} and 4^{th} columns in Table 3.6, respectively.

It.	**det., sim.**	**det., alt.**	**prob., sim.**	**prob.,alt.**
1	47602.41	12495.09	12494.83	24356.98
2	36143.52	67413.28	8080.67	18005.81
10	2878.20	1983.23	436.06	1029.41
25	1303.66	1287.22	281.30	673.12
50	1221.96	1221.09	270.58	642.89
100	1174.04	1177.86	264.38	625.97
150	1153.64	1161.40	261.85	617.87
200	1146.21	1152.52	260.35	612.26
250	1138.69	1145.43	259.03	607.87
300	1133.76	1140.06	257.98	604.97

Table 3.6: Compliances c_t for topologies (deterministic/proabilistic, simultaneous/alternating) shown in Figure 3.19. First 300 iterations.

Compliance values for the deterministic cases (1^{st} and 2^{nd} columns in Table 3.6) are quite similar. Note how minimization in the deterministic alternating case (2^{nd} column) is non-monotonic in the beginning, i.e. compliance grows instead of descending for some iterations (e.g. $it = 2$). This happens because, as seen in Figure 3.19, alternating loads in a deterministic manner ($p_i = 100\%$) implies influence of the loading order. The topology is first optimized for the firstly applied load, and so, when other unseen load comes into play, the layout fails to adapt to the newly loaded area.

Alas, Table 3.6 demonstrates how the optimization gradient is still heavily skewed towards the previous (dominating) load and so the available volume to be reallocated is limited, resulting in thin twigs that greatly increase compliance for a moment. As the gradient adjusts its minimization direction over iterations, this compliance unbalance wears out, although its topological effects are irreversible - see Figure 3.19 left column -, hence the need for probabilistically-weighted approaches.

By weighing compliance contributions according to the real share for each load, the minimization process is faster and always monotonic (ever-descending gradient), on top of a lower compliance, as already mentioned.

3.2.2.1.2 Asymmetric Loading Cases The solution is straight-forward when symmetric loading is in place, as in the previous example. However, the expectation is not so clear otherwise: if loading is skewed, the result will no longer by symmetric nor easily predictable. The proposed approach (Equations 2.50 and 2.51) can be used to optimize multi-load cases according to each load's share in frequency/modulus. If isotropic damage penalization (Equation 2.49) is also introduced, the resulting topology will be more robust and wear-resistant.

Consider the example cantilever beam in Figure 3.20 (same loading conditions as in Figure 3.19 top row, only the beam is now 1000 elements long). It is loaded symmetricly and asymmetricly in frequency, with damage configuration 1 ($\kappa_f = \sigma_f = 10^{-5}$ and $\alpha = 9 \cdot 10^{-2}$ in Equation 2.49). The percentages express the fraction of total iteration loops in which each load is applied (e.g. 50%/50% implies alternate loading, again with $p_{ij}^{up} = p_{ij}^{down} = 0.5$).

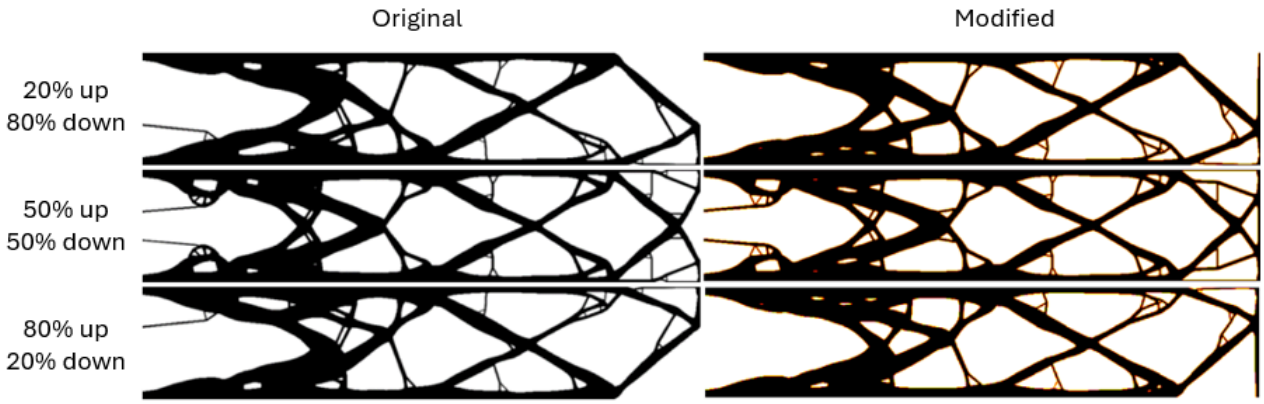

Figure 3.20: Cantilever beam (configuration 1, iteration 100, size 1000x200, $v_f = 0.4$) loaded as in Figure 3.19 top row with different frequency shares (up-down): 20%-80% (first row), 50%-50% (second row) and 80%-20% (third row). Deterministic (left) vs. probabilistic (right).

Several differences can be spotted between deterministic (Figure 3.20 left column) and probabilistic topologies (Figure 3.20 right column). Although their genus has not been significantly altered, the right ones showcase generally simpler and sturdier versions: absence of thin pins on the left for the asymmetric cases, reinforced struts near supports and loading, thickened and unified twigs, etc.

Most importantly, only the modified versions retain the whole vertical strut along the right wall, sustaining both loads - which makes them the only practically viable solutions in both skewed cases (20/80, 80/20). This proves how the proposed damage-based probabilistic approach is not only capable of a more efficient usage of the given target volume fraction (joint reinforcement, strategic thickening), but also as a guarantee to keep structurally relevant parts which would have been lost to the original SIMP process otherwise. Note how inverting loading fractions produces mirrored images with respect to the normal direction to loading - compare top and bottom rows in Figure 3.20.

For other frequency combinations in a 600x200 version, see Figure 3.21.

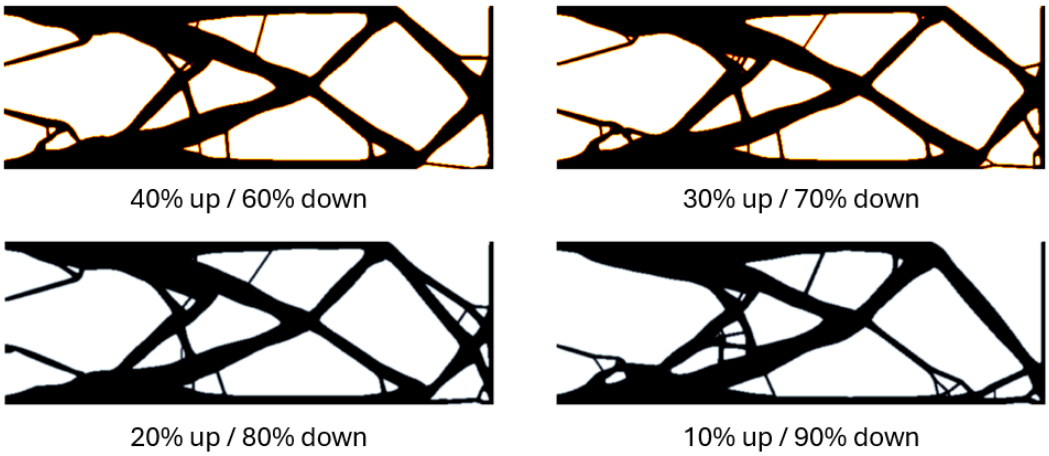

Figure 3.21: Asymmetric loading in frequency, applied to the cantilever beam in Figure 3.19 top row with different percentages (up / down): 40% / 60% (top left), 30% / 70% (top right), 20% / 80% (bottom left) and 10% / 90% (bottom right). Iteration 100, $v_f = 0.4$.

When compared to the 50% / 50% case (Figure 3.19 right column), asymmetricly loaded examples in Figures 3.20 and 3.21 display, as expected, equally asymmetric topologies with respect to the mid-horizontal axis. As loading share in Figure 3.21 is progressively shifted to the bottom half, more volume is diverted to the area to withstand it.

The least loaded end (top right corner) is still held by the vertical wall along the loading axis, whereas the most loaded point presents an horizontal strut as well, to transfer momentum to the rest of the structure. Note how the different beam lengths for the 20%/80 % case (1000 in Figure 3.20 bottom right and 600 in Figure 3.21 top left) yield slightly different topological features.

All previous cases have been optimized using the minimum density filtering radius in [205], $r_{min} = 2$, offering the sharpest possible contrast between material and void. However, these sharp designs come at a cost: they foster very thin twigs which induce fragility (especially in intersections), buckling, artificially increase compliance and pose manufacturing difficulties.

To alleviate that, the filtering radius can be increased (to $r_{min} = 10$, for instance), obtaining less crisp contours but simpler material layouts with fewer, thicker and structurally significant struts. See Figure 3.22 for a supported beam fixed on both walls or Figure 3.23 degrees of freedom on its bottom corners.

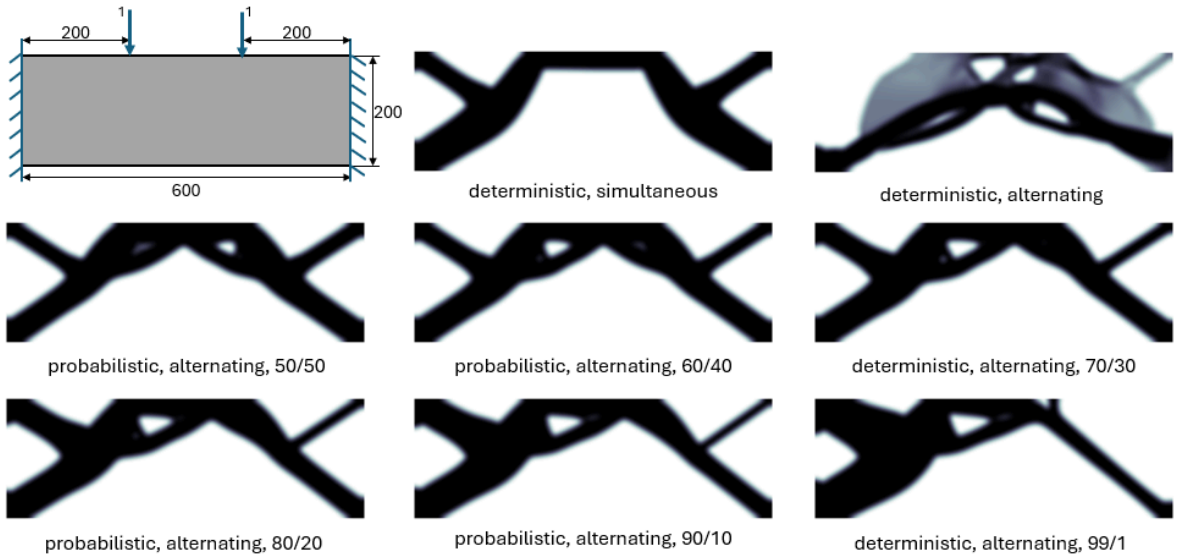

Figure 3.22: Several 600x200 beams (see top left corner for loading boundary conditions) with various frameworks (deterministic/probabilistic, simultaneous/alternating) and frequency shares (50/50, 60/40, 70/30, 80/20, 90/10, 99/1) expressed in percentages (%). Iteration 100, $v_f = 0.4$.

Figure 3.22 shows how volume is redistributed according to loading frequencies, albeit not in a strictly proportional way, since the final topology is also conditioned by the underlying fixed boundary conditions. In the cantilever examples (Figures 3.19 and 3.20), the structure was isostatic and so the right part was free to develop within the algorithm's prescriptions.

However, the boundary conditions in Figure 3.22 - both walls fixed on both degrees of freedom - make the resulting structure hyperstatic, and thus much more restricted. The deterministic simultaneous (middle, top row) and the probabilistic 50/50 cases (left, middle row) are both virtually symmetric (despite some right load dominance in the latter), but topologically different: extra holes and straighter struts can be seen in the probabilistic example.

As loading shifts progressively to the left side, so does the volume distribution in the optimized topologies (Figure 3.22 middle and bottom rows): material agglomerates on the left half (especially the pins joining the left wall to the loading points), gradually breaking symmetry to the point of erasing the top right pin in the most extreme case (99/1, bottom right corner).

Interestingly, almost all cases in Figure 3.22 converge by iteration 10 with very similar compliance values. The only exceptions are the alternating (top right corner) due to convergence issues and 99/1 examples (bottom right corner) because of important topological changes. A similar array of case studies for a centrally bi-supported beam with loads on both top corners is contained in Figure 3.23.

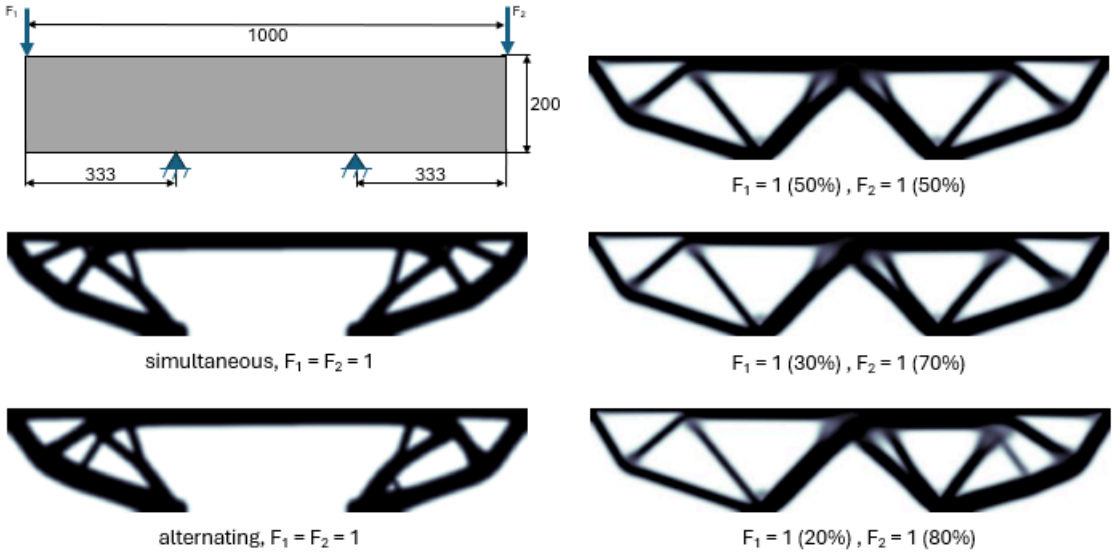

Figure 3.23: Supported 1000x200 beams (boundary conditions pictured top left) in various deterministic (simultaneous/alternating, left column) and probabilistic settings (alternating, right column). Iteration 100, $v_f = 0.4$.

Since the supported example (Figure 3.23) is less constrained than its fixed counterpart (Figure 3.22), the deterministic cases (left column) are quite similar. However, simultaneous loading (center left) yields axial symmetry with respect to the middle vertical axis, whereas alternating loads (bottom left) do not, allocating slightly more volume on the right side (first loaded).

For these particular boundary conditions, the probabilistic alternatives (Figure 3.23 right column) are quite different from the deterministic ones. By optimizing the resulting cumulative gradient of each frequency-weighted load instead of fully applied and constant, the probabilistic designs are topologically simpler, distributing volume more efficiently and protecting the central section between supports.

Up to this point, skewed loading has only involved different frequencies in load application, but skewed moduli have similar effects and can be used as an alternative or in a combined way. Consider Figure 3.24 displaying practically identical topologies row-wise. The top row proves yet again that deterministic and probabilistic approaches are equivalent when loading frequencies are symmetric - as in Figure 3.19, while the bottom row demonstrates how the proposed probabilistic loading framework can be interchangeably enforced via frequency or modulus variation, as long as their compliance contributions are identical.

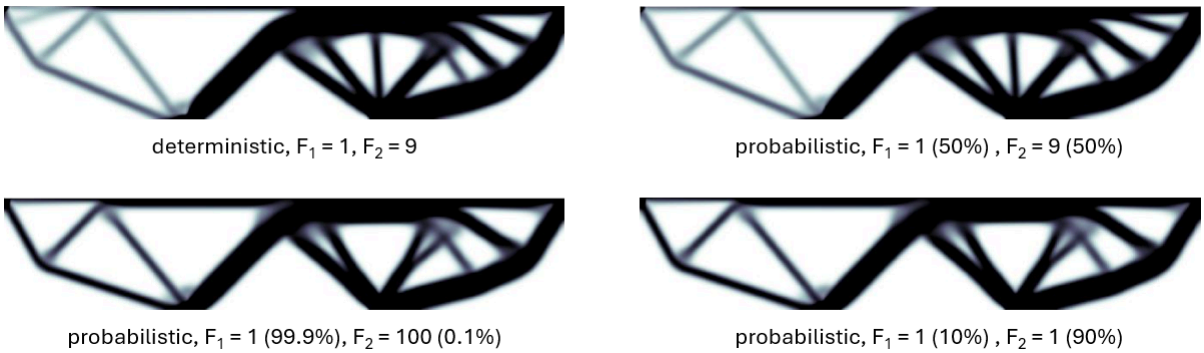

Figure 3.24: Bi-supported 1000x200 beams with different load frequencies and moduli. The overall boundary conditions are those of Figure 3.23 top left.

Conceptually, applying constant and simultaneous loading in each iteration (deterministic, Figure 3.24 top left) is tantamount to doing so alternatively with a 50% chance each. Since the same loading is applied just half of the time, the probabilistic case is half as compliant as the deterministic one - see Table 3.6. Interestingly, if this modulus imbalance is partially compensated by a countering frequency bias (Figure 3.24 top left), the resulting layout is equivalent to that obtained by assigning equal loading in modulus and adjusting the frequencies accordingly, as in Figure 3.24 top right.

3.2.2.1.3 Multi-axial Loading Multi-axial optimization with different loading types is also feasible under this framework, as shown in the next examples. See Figure 3.25 for comparison purposes, regarding the cantilever beam case. Very different topologies are given for the symmetricly loaded case, i.e. equal share in modulus and frequency (middle column). While simpler, the deterministic (top middle) design's load transmission is weaker and vulnerable to small variations, whereas the probabilistic alternative (bottom middle) is more robust as volume is better distributed -i.e. covering wider angle ranges.

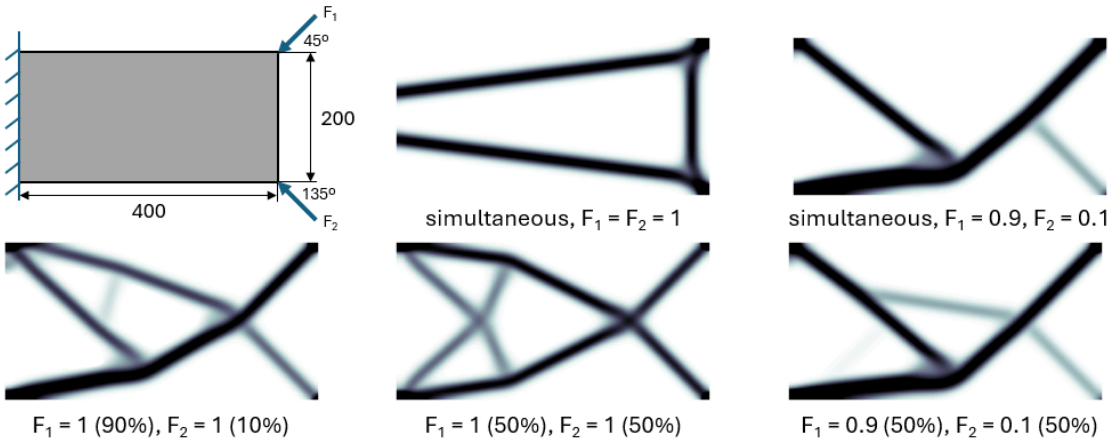

Figure 3.25: Tilted loads (loading conditions: top left) on a 400x200 cantilever beam with $v_f = 0.2$. Iteration 100. Deterministic simultaneous (top row) and vs. probabilistic cases (bottom row).

Such is the case for asymmetric loading as well (Figure 3.25 right column): the overall volume layout is similar, but the probabilistic case (bottom right) is yet again more robust (additional middle strut for better load transmission) than its deterministic twin (top right).

Up to this point, uncertainty has been expressed through the load's modulus and frequency, always with a fixed static application point. For a spatially-uncertain setting, consider a 600x200 cantilever beam fixed on its left side where downward loading is distributed around the bottom right corner. Such loads have a constant unitary modulus, whereas their position is randomly drawn from a normal distribution $\mathcal{N}(\mu, \sigma)$ for 25 cycles per iteration - μ being its mean and σ its standard deviation. Cases for spatial distributions $\mathcal{N}(500, 100)$, $\mathcal{N}(400, 200)$ and $\mathcal{N}(300, 300)$ are displayed in Figure 3.26.

These examples show how position-wise uncertainty in loading yields diffuse material layouts with sizable intermediate density pockets (blurry areas). The broader the load distribution is, the greater the share of intermediate volumes will be. Since these intermediate densities are, of course, stiffer than void, compliance is lower when the loading is more sparsely distributed. Figure 3.26 center is about 1.5 times stiffer than Figure 3.26 right, i.e. in the same proportion as their loading lengths. This eases compliance minimization, despite partially defeating the purpose of binary material-void results.

The same cantilever beam (size 600x200, $v_f = 0.4$) is loaded on the top right ($pos_x = 600$) and bottom middle ($pos_x = 300$) with two static leftward horizontal loads (5 N) applied every 20 loading cycles and two alternating vertical loads varying in modulus and position via two distinct normal distributions: $\mathcal{N}(1, 0.5)$ for modulus and $\mathcal{N}(pos_x, 50)$ for position - 10 cyclic samples are drawn per iteration.

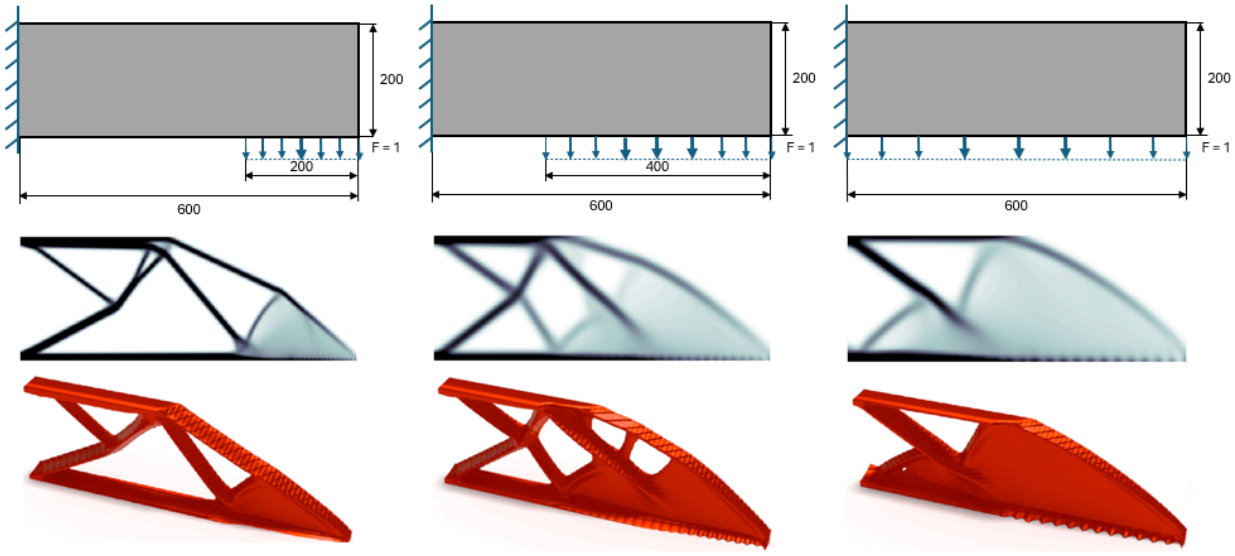

Figure 3.26: Cantilever beams (600x200, volume 0.4) loaded with constant unitary modulus and spatial distributions $\mathcal{N}(500, 100)$ (left column), $\mathcal{N}(400, 200)$ (middle column) and $\mathcal{N}(300, 300)$ (right column). Iteration 250. Suggested 3D representations can be found below, reinterpreting density as thickness.

See Figure 3.27 top left for the boundary conditions. Notably, using a standardized statistical distribution with known mean and deviation allows for reliable confidence intervals, widespread in industry (e.g. six-sigma). The regular approach (top middle) is unrealistic and feeble for distributed loading. Although the TO algorithm guarantees supporting the applied loads, the resulting topology is clearly sub-optimal: unadapted to the uncertainty induced by the distributed and impact loads, prone to buckling and quite oversized, yielding a poor volume distribution: excessive for the bottom middle and insufficient for the top right end.

Conversely, the modified versions using the proposed methodology (Figure 3.27 bottom row) offer more organically-shaped, intuitive designs where the topology actually reinforces struts linking loaded points between each other (e.g. bottom right curve) in a direct and smooth manner. The probabilistic alternatives harness loading by strengthening (left pins and overall right contour), adding (middle region) and/or bifurcating struts (right end) in several directions.

Loading diagrams in Figure 3.27's right side shed some light on the obtained topologies. In the deterministic case (top row), the contribution of constant loads is well accounted for (solid yellow arrows), whereas the distributions' (dashed yellow arrow) changes with every iteration (thick, dashed green arrow).

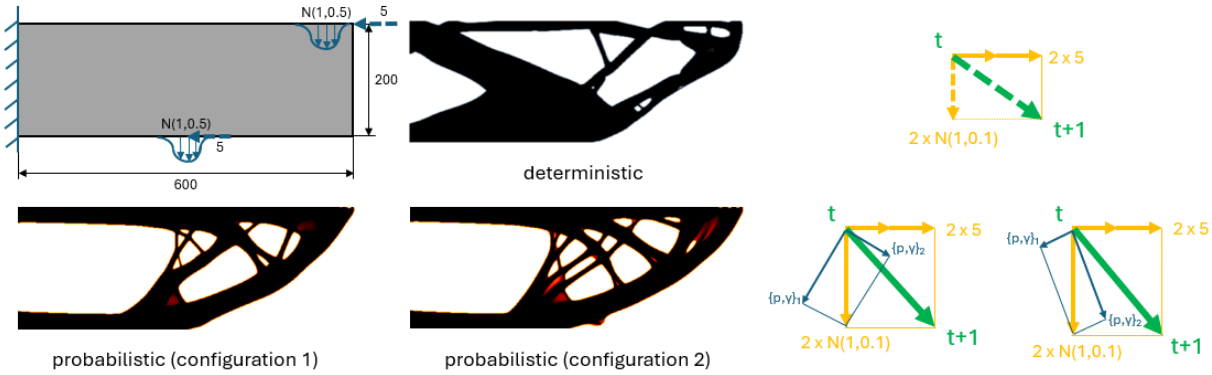

Figure 3.27: Multi-load cantilever topologies (iteration 100, penalization factor $p = 3$, filter radius $r_{min} = 2$) with load position and modulus uncertainty (top left): vanilla (top middle), configuration 1 with $\kappa_f = \sigma_f = 10^{-5}$ and $\alpha = 9 \cdot 10^{-2}$ (bottom left) and configuration 2 with $\kappa_f = 5 \cdot 10^{-5}$, $\sigma_f = 5 \cdot 10^{-2}$ and $\alpha = 9 \cdot 10^{-3}$ (bottom middle), along their respective load diagrams (right) at the cycle (blue), load (yellow) and loop level (green).

The latter provokes an ill-defined gradient that thwarts convergence and so yields impractical topologies (Figure 3.27 top middle). In the probabilistic examples, however, every iteration is well defined from the cyclic level j (thin, blue arrows) - with associated probabilities p_{ij} and damages γ_{ij}, through the load level i (yellow) and finally adding up to iteration t (green). Hence, although cyclic contributions remain randomized and unpredictable, each iteration has an univocal, well-defined gradient for each iteration loop, i.e. weighted gradient descent.

Alas, two main drawbacks are also patent in Figure 3.27: topologies are more convoluted (higher genus) - which could entail manufacturing issues - and several intermediate-density pockets arise inbetween struts. This can be erased via filtering [487] - with the consequent increase in computational time. Both inconveniences can be partially dealt with via clever choice of parameters in Equation 2.49.

Interestingly, if some of the loads in Figure 3.27 are modified (in modulus, frequency and/or position) or outright erased, the resulting probabilistic topologies remain somewhat similar (e.g. same overall contour), hinting at the existence of some "canonical" solution, perhaps globally optimal. Self-evidently, this is more visible for small loading variations. Consider Figure 3.28 for some examples.

For the same iteration (100), Figure 3.28's similarities with the solutions in Figure 3.27 are clearer when the loading conditions undergo slight changes. For instance, making horizontal impact loads follow the same distribution as the vertical ones - and adding an occasional impact load of 10 N at iteration 50 - (Figure 3.28 middle) barely alters the design seen in Figure 3.27 middle.

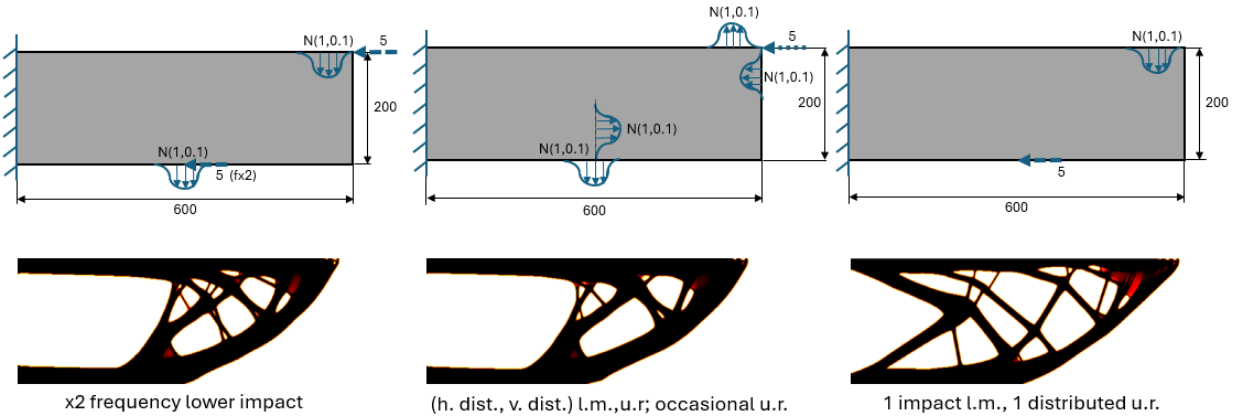

Figure 3.28: Variations on Figure 3.27 (with configuration 1): bottom impact gets doubled in frequency (left), loads distributed vertically and horizontally plus an occasional horizontal load on the top right corner (middle) and only one vertically distributed load and one horizontal impact (right).

In contrast, just doubling the frequency of one of the applied loads (horizontal impact in the bottom middle now happens each 10 iterations, Figure 3.28 left) creates a sort of "hybrid" topology with some features of Figure 3.27 bottom left and others from Figure 3.27 bottom right.

However, the topology in Figure 3.28 right does not clearly resemble any in Figure 3.27, since significant loading changes have occurred. Now the solution focuses on reassuring multiple connections (struts as load transmission paths) between the sole horizontal impact load in the bottom middle area and the remaining vertical distribution on the top right corner; and those two loading points with the fixed left wall withstanding them. This results in thinner horizontal contour struts, the impact load making the bottom one thicker. Also, volume is more evenly spread, with various intermediate twigs as opposed to the thick branches in other examples shown in Figures 3.27 and 3.28.

Despite all these variations in boundary conditions, the overall contour remains virtually unchanged. In Figure 3.28, different material layouts fill up the space inside the outer "shell" (contour) depending on loading conditions. Of course, what constitutes a convenient solution is up to the designer's requirements (material, volume fraction, type of loading, etc.).

Remarkably, the splattered strut layout in Figure 3.28 right is similar to that of cancellous bone tissue, as they both seek to be optimized for the most varied eventual loads in all directions and moduli, i.e. generating inner isotropy inside the contour. In a Machine Learning scenario, this would be tantamount to a validation step: the topology which has been optimized for a known set of testing loads can now withstand previously unseen loading with minor structural changes.

Since damage penalization (Equation 2.50) comes with each iteration, applying forces gradually should affect the topology progressively as well, which could be more representative of some scenarios in the service life of a prototype, e.g. loading and unloading. Two cantilever examples are examined in Figure 3.29. In both cases, loading starts with a 10% of the original value, increasing by a 10% in each iteration until it reaches 100 %. Then, it follows the same process in descending order, back to the starting point. This loading-unloading cycle is continuously repeated until convergence.

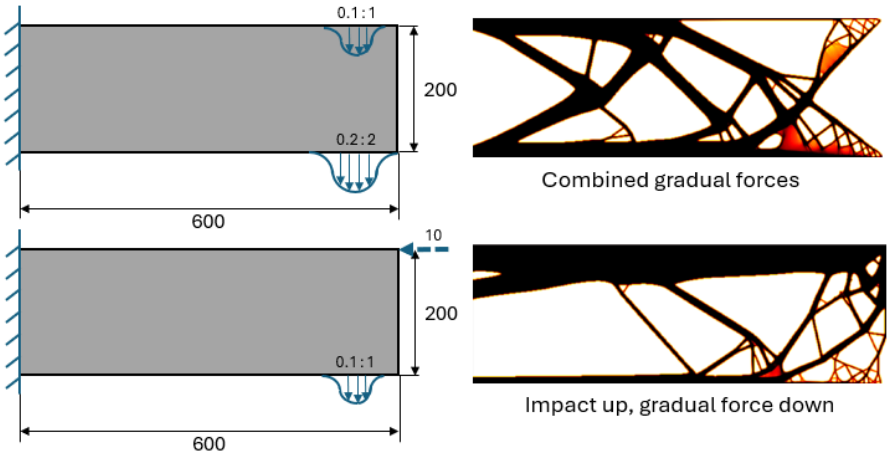

Figure 3.29: Variations on Figures 3.27 and 3.28 (with configuration 1), applying gradual forces on both corners (top row) or one in the bottom and an impact on top (bottom row). Iteration 500.

Figure 3.29 top row combines gradual distributed vertical forces with different modulus and positions: $|F| = \mathcal{N}(1, 0.1), |x| = \mathcal{N}(575, 25)$ on the top right corner and $|F| = \mathcal{N}(2, 0.2), |x| = \mathcal{N}(550, 50)$ on the bottom one. They are always present (simultaneous), albeit under different iterative moduli and positions. The generated branches are thicker and broader in the bottom right corner than in the top one, since the top load is twice as big in modulus and twice as spread in position. Its deeply ramified ending and multiple inner struts again resemble trabecular bone (as Figure 3.27 right).

Figure 3.29 bottom row features an occasional horizontal impact load ($|F| = 10, |y| = 200$) - applied every 10 iterations - on this gradual loading ($|F| = \mathcal{N}(1, 0.1), |x| = \mathcal{N}(575, 25)$ on the bottom right corner). Heavy ramification is present too, but truncated due to the bigger impact load. When the impact comes for the first time, it displaces a fair share of material to withstand it, neglecting the bottom distributed load whose scattered needs are only partially met. This imbalance shows the importance of eventual non-service loads (e.g. impacts), ignored by common deterministic TO.

This gradual introduction of (un)loading leads to strut ramifications: as the algorithm progresses, it distributes material where it is first needed. As the force is increased in modulus and varied in position, such branches become thicker in order to withstand the ever-growing load while accounting for its spatial dispersion. The inverse is true for unloading: tweaks become thinner, but not excessively, since they still have to cover a wide range of loading points. This way, the algorithm implicitly ensures a minimum threshold thickness for all generated struts.

3.2.2.1.4 Manufacturability Considerations Thinking in manufacturing terms, all of the aforementioned case studies could be improved by filtering techniques, in the hopes of easing problems arising from thin, feeble twigs and intermediate density clusters. Let the probabilistic simultaneous case in Figure 3.19 be subjected to the proposed filter with minimum threshold thickness $r = 5$, explained in Section 2.2, each 10 iterations. The results can be found in Figure 3.30.

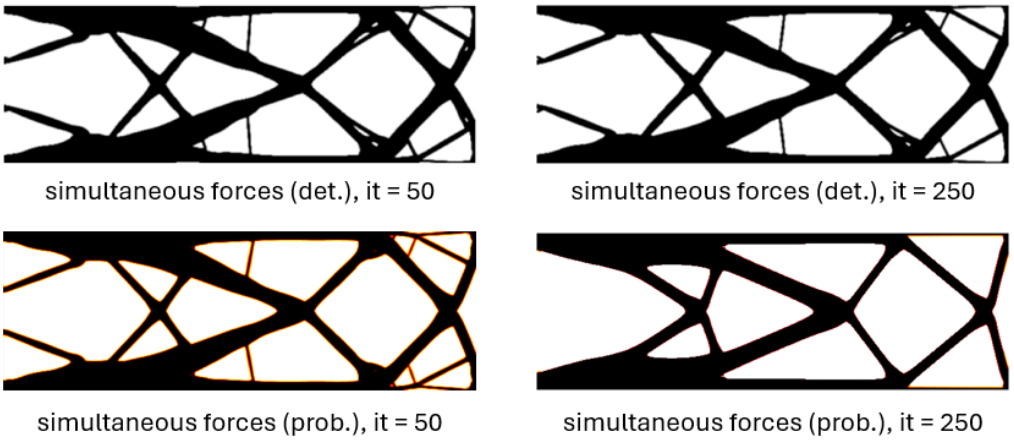

Figure 3.30: Filtered ($r_f = 5$) versions (bottom row) of topologies presented in Figure 3.19 (top row).

The filtered topologies (Figure 3.30 bottom row) are symmetric, simpler (genus is lower, i.e. less holes) and more robust: the volume is more concentrated in junctions and along certain "master struts", more directly connecting loads to supports. With the same volume fraction (0.4) for all cases, it is best leveraged when probabilistic, which is closer to the combined form (Figure 3.30 bottom row), although in a more robust format. It must be noted that this filtering technique is thickness-based, focusing on the struts thinner than the prescribed threshold; and so it produces simpler topologies with equally sharp material-void contrast, unlike the density filter proposed in [205].

Another filtering-free option (and thus computationally cheaper) to leverage intermediate density areas is to interpret those material-void interphases as a thickness gradient in 3-dimensional, real manufactured parts, as in Figure 3.31. By doing that, several benefits are directly obtained. Firstly, accepting intermediate densities instead of a sharp material-void layout speeds up the optimization process, since convergence is now reliant on a design criterion rather than just minimization.

This is further enhanced by the aforementioned savings in computational costs by avoiding demanding post-processing filtering techniques. Secondly, breaking the SIMP method's assumed isotropy by defining density gradients (and thus, stiffness gradients) holds great potentiality for functionally graded behavior, as in composites and metamaterials.

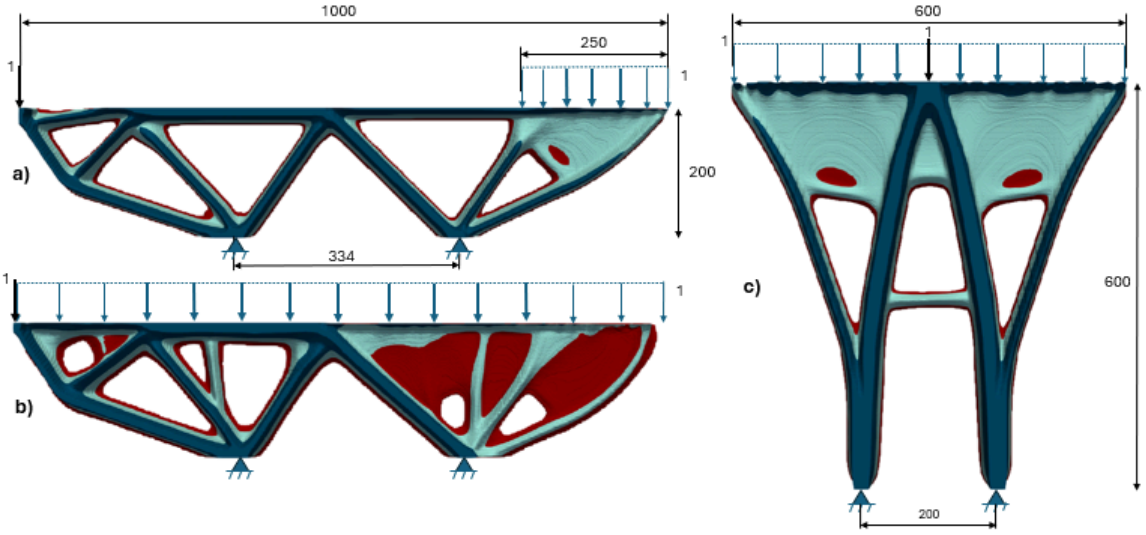

Figure 3.31: Different combination of punctual (black arrows) and randomly-distributed (blue arrows) constant loads on several supported beams with volume fraction $v_f = 0.2$. Dark blue represents maximum thickness, light blue 50% of the maximum and red its 10%.

Figure 3.31 shows several non-binary topologies where material is distributed by layers, imitating level-set optimization techniques [210]. The effects of deterministic loading (constant in modulus, position and frequency) and randomly-spaced loads can be clearly seen. In all three examples, the "master struts" with maximum stiffness (dark blue) are given by the constant loads (black arrows), while random spatial distributions dictate the intermediate density areas (light blue, red).

As expected, symmetric loading implies mostly symmetric topologies, although not exactly due to randomness in loading position (Figure 3.31c top left). Remarkably, the smaller the randomly-distributed loading is, the more closely it resembles punctual loading, due to momentum balance.

That explains why Figure 3.31a, featuring a reduced distributed loading on one end balancing the sole punctual load in the other, is more symmetric than the fully randomly-loaded case (Figure 3.31b). This also applies to Figure 3.26.

3.2.2.2 Multi-Objective Topological Optimization

The damage penalization introduced in Section 2.1 and tested in previous examples can now be leveraged for more practical purposes on an element basis, such as fatigue, mechanical response, manufacturing concerns and distortion - see article **Probabilistic combination of loads in topology optimization designs via cumulative damage criteria** [486]. Again, the *top*88.*m* code [205] will be the base for 2D examples.

3.2.2.2.1 Individual Criteria Picture a 3-point bending test beam (see Figure 3.32 top left) subjected to a central downward load with modulus given by $\mathcal{N}(1, 0.3)$. Strong supports (10-element wide) are placed for more feasible boundary conditions in experimental test settings. As a result, global isostaticity is locally compromised. Upon isolated application of each individual criterion, some optimized topologies can be found in Figure 3.32.

The isotropic criterion (Figure 3.32 top right) is virtually equivalent to the vanilla *top*88.*m* case, except for a few reinforcements on strut junctions and near the supports. It can be considered a reference for comparison with all other criteria.

As expected, the printing criterion reinforces struts along the chosen direction, whether horizontally (0°, Figure 3.32 second row left), obliquely (45°, Figure 3.32 second row right) or vertically (90°, Figure 3.32 third row left), following the layer's direction, i.e. the most resistant, respectively, or the closest they can get for a feasible solution while withstanding the applied loads. Note how, for fully horizontal (0°) or fully vertical (90°) printing directions, some symmetry with respect to the vertical loading axis is expected. For sideways angles (30°, 45°, 60°, etc.), this symmetry has to be explicitly enforced by mirrored optimization with respect to the loading axis.

Compression (Figure 3.32 third row right) and traction (Figure 3.32 bottom left) penalties act analogously for mechanical responses. They favor compression or traction responses, respectively, by distributing material along the directions in which those responses are expected, with the necessary topological complexity to maximize the number of "struts" undergoing the desired response type.

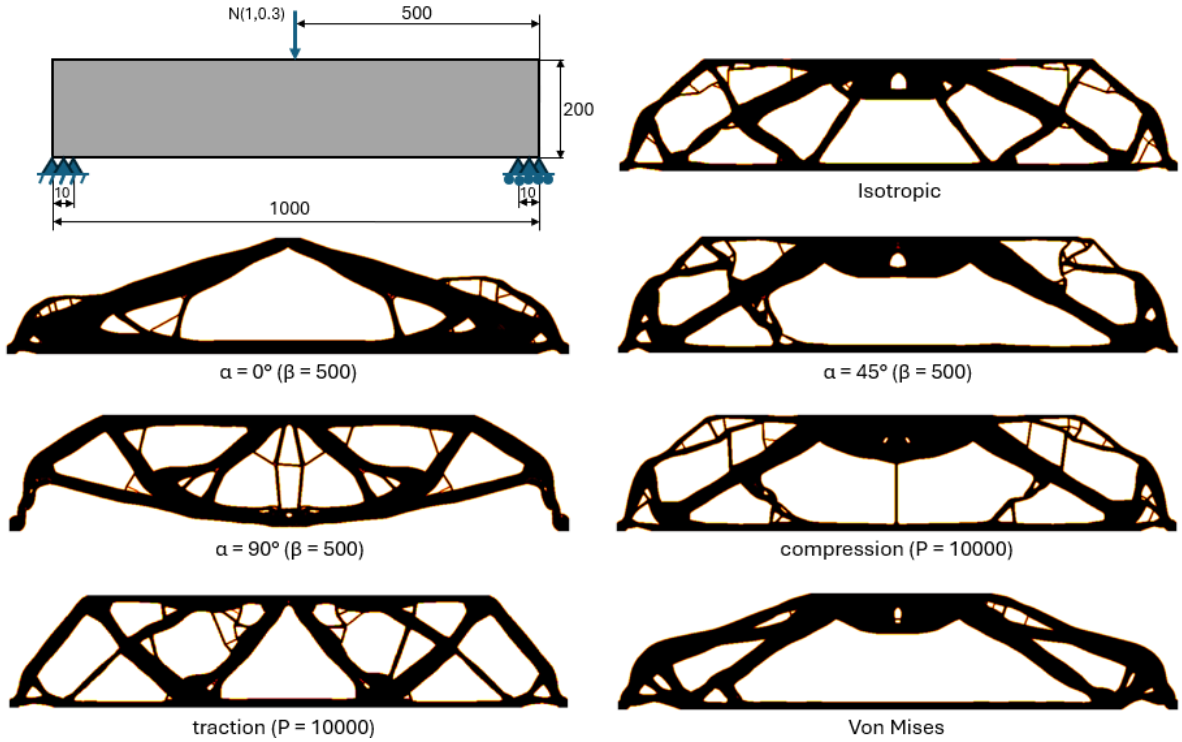

Figure 3.32: Iteration 200, 3-point bending beam (size 1000x200, $v_f = 0.4$). Row-wise, left to right: boundary conditions, isotropic (configuration 3 with $\kappa_f = 5 \cdot 10^{-7}$, $\sigma_f = 5 \cdot 10^{-3}$ and $\alpha = -9 \cdot 10^{-5}$), printing angles of 0°, 45° and 90° (all three with $\beta = 500$), compression, traction (both with $P = 10000$) and von Mises equivalent stress criteria.

The distortion criterion (von Mises, Figure 3.32 bottom right) reduces elastic deformation (and thus, compliance) by rearranging the material mostly along the two diagonals connecting the load application point in the top middle to the supports on the bottom left and right corners, hence minimizing distortion energy. Von Mises stress-penalized compliance minimization is not equivalent to stress-based TO where von Mises stress itself is the minimized objective, yielding smoother contours and very different overall topologies - see Figure 3.33. Perhaps this stress-penalized approach can be interpreted as weighted compliance-stress optimization [268].

Figure 3.33: Stress-based optimization (KS, von Mises) for Figure 3.32 top left with code from [4]. Iteration 200, $v_f = 0.4$

Interestingly, von Mises penalization is able to eliminate layer orientation dependency, thus changing the topology's failure mode - see Figure 3.34. On top of the most inefficient volume distribution ($v_f = 1$ in a vs $v_f = 0.4$ in b), stress is globally higher in the bulk design (c) than in the optimized version (d). Despite both being additively printed in horizontal layers, the failure mode is different: layer separation - printing-derived - (e) and plasticity (f) - material-given -, respectively.

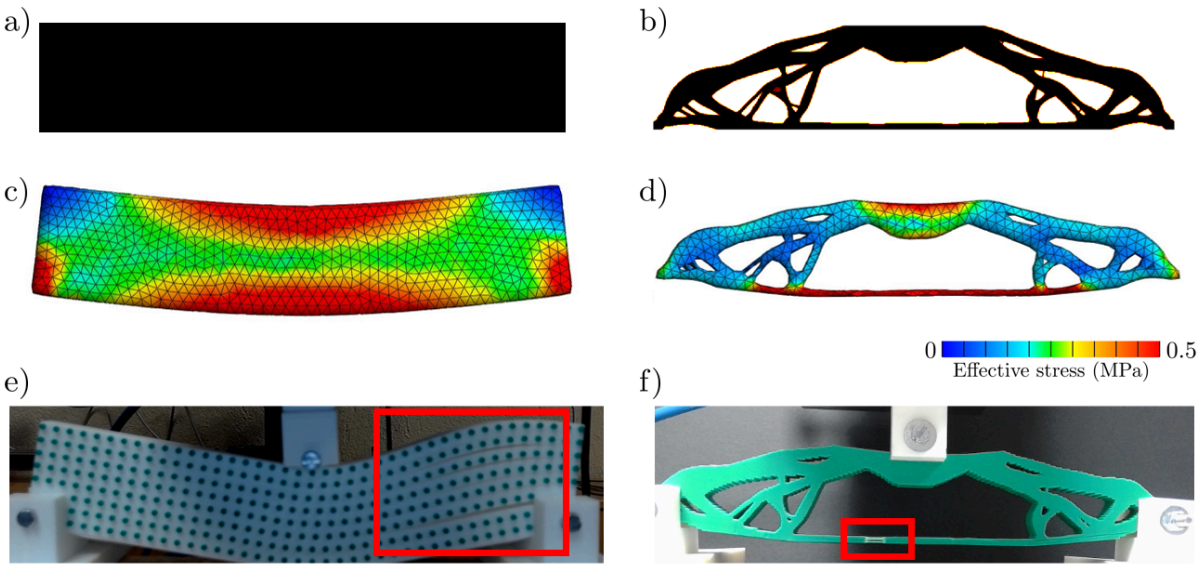

Figure 3.34: 3-point bending beam (Figure 3.32 top left) as a bulk (left column) and compliance-minimized (SIMP) with von Mises stress penalization (right column): material layout (first row), FEM-simulated (middle row) and experimental testing (bottom row). Failure in red squares.

Some patterns can be observed in Figure 3.32. Isotropic (top right), 90° printing (third row left) and traction cases (bottom left) share a master layout, resembling an X-truss. Two main diagonals emerge from the loading point (top middle) dividing the bottom into three parts, then diverging outwards until reaching the top again, and finally closing the contour with parallel struts. Similarities can also be spotted for 0° (second row left) and von Mises (bottom right); and the isotropic (top right) and 45° (second row right) cases: a big triangle joining loading and supports and some inner struts with varying thicknesses.

For instance, the vertically printed topology (90°, Figure 3.32 third row left) must avoid horizontal struts because the orthogonal direction to the printed layers is the weakest, and so it leaves out the horizontal bottom line present in all other cases. Reinforcing the outer contour is more important under milder anisotropy, e.g. 45° printing direction and compression.

A slight topological asymmetry is also observed in Figure 3.32, due to asymmetric boundary conditions required to ease experimental testing: the supports on the bottom corners are not exactly equal (the left end is more constricted than the right, to keep global isostatic conditions). The fixed support on the left creates local hyperstaticity, despite the structure being globally isostatic.

Figure 3.32 shows how auxiliary thin tweaks are generated to reinforce thicker and stronger struts. Unfortunately, although mathematically optimal, such tweaks are not structurally meaningful, in turn provoking unnecessary deformation (thus increasing compliance) and being difficult to manufacture and fragile. Two possible solutions exist to alleviate this problem: either decreasing the target volume fraction v_f or applying filters (like the density-based one in [205]), be it during TO or as an extra post-processing step.

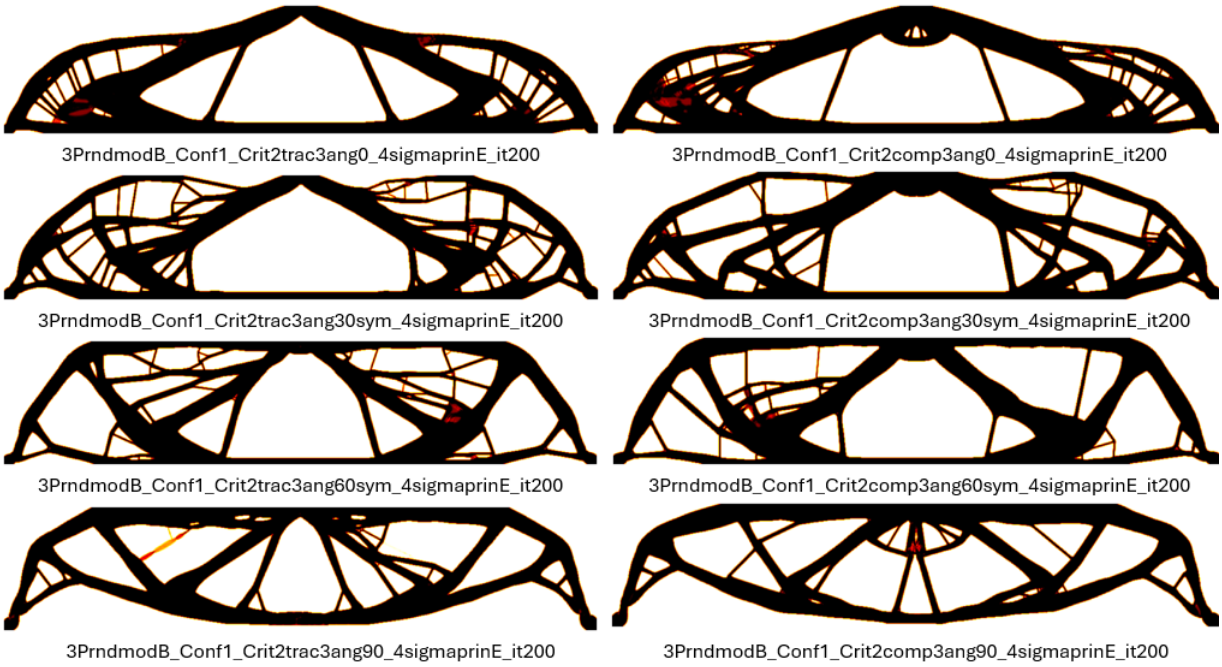

Figure 3.35: Iteration 200,$v_f = 0.4$, 3-point bending test with 10-element wide supports (Figure 3.32 top left). Simultaneous criteria: von Mises stress, traction (left column) or compression (right column) and printing angles 0° (first row), 30° (second row), 60° (third row) and 90° (fourth row).

3.2.2.2.2 Combined Criteria While the proposed criteria can in fact be combined (mostly without mutual canceling effects), some of them are prevalent over others, which must be accounted for when facing multiple design requirements.

In Figure 3.35, several criteria were applied simultaneously to a 3-point bending beam with a load whose modulus is given by $\mathcal{N}(1, 0.3)$ N (same boundary conditions as Figure 3.32 top left). A naming convention of the form $Load.ConfA.CritXYZ.itIII$ has been adopted to distinguish the numerous examples, denoting: loading conditions, isotropic parameter configuration (Equation 2.49), applied criteria with their respective specifications and iteration number.

All examples in Figure 3.35 obey the von Mises criterion, minimizing distortion by avoiding unnecessary ramifications. However, the topologies only resemble the isolated canon (Figure 3.32 bottom right) when combined with a 0° printing direction (first row) - also similar in its purest form (Figure 3.32 top right). Designs penalized for traction (Figure 3.35 left column) mimic their canonical shape (Figure 3.32 bottom left) when the printing angle is high, i.e. 60° (Figure 3.35 third row left) and 90° (Figure 3.35 fourth row left), already similar to the 90° simple criterion (Figure 3.32 third row left).

The opposite can be said for the compression examples (Figure 3.35 right column): the closer the printing angle is to 0°, the more features the topologies share with the pure compression canon (Figure 3.32 third row right). Therefore, although different criteria do not directly contradict each other, some combinations are synergic while others dilute some of their effects.

The combined effects of various criteria at once exacerbates the presence of thin tweaks inbetween thicker struts. The 30° and 60° cases present axial symmetry with respect to the loading vertical line. Interestingly, applying multiple criteria partially balances out the slight asymmetry seen in Figure 3.32.

3.2.2.2.3 Mechanical Response Out of all possible results obtainable through post-processing from the TO-defined displacements $\mathbf{u}$, shear strain and von Mises equivalent stress are deemed the most relevant to ponder the criteria's consequences on mechanical response, displaying the most complex gradients with stress concentration in loading points and supports. For a meaningful comparison, results coming from different examples are normalized ($\mathbf{x}_{norm} = (\mathbf{x} - \bar{x})/\sigma_x$).

In Figure 3.36's top row, the plain isotropic topology (Figure 3.32 top right) exhibits strain and stress concentrations around loading and support points, most strut junctions and along the center bottom strut. For the printing criterion with 0° (middle row, Figure 3.32 top right), stress and strain concentrations lessen in the bottom strut in exchange for a slightly more stressed area around the loading point. For 60° under traction penalty (bottom row, Figure 3.35 third row left column), the situation is close to the isotropic case, with smaller stress and strain concentrations in junctions.

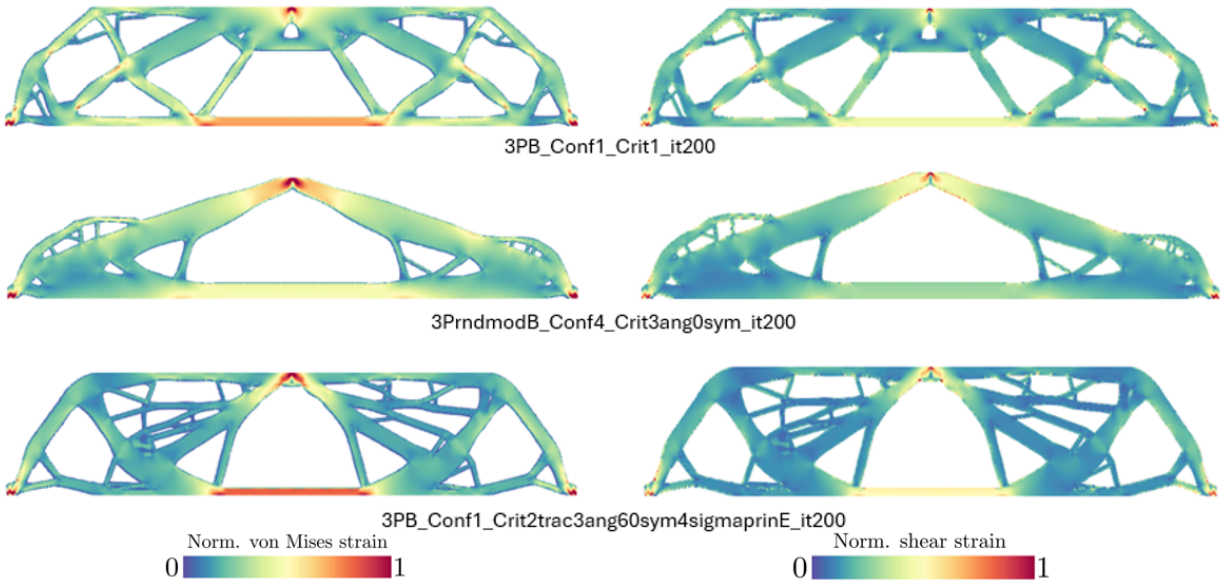

Figure 3.36: Iteration 200,$v_f = 0.4$, Figure 3.32 top left. Normalized mechanical response (left: von Mises equivalent stress, right: shear strain) under isotropic damage (first row), printing angle 0° and von Mises (second row) and traction, printing angle 60° and von Mises (third row).

Which combination is preferable depends greatly on the material's mechanical properties, loading conditions and, of course, the designer's goals and choices (e.g. reinforcing highly stressed areas with thicker layers and/or a more resistant material). The middle and bottom topologies have been slightly filtered to reduce their topological complexity.

3.2.2.2.4 Asymmetric and Restrictive Boundary Conditions Should loading conditions be asymmetric, the topologies will be too. Consider shifting the load in Figure 3.32 rightwards to two thirds of the beam's total length, as in Figure 3.37 top left. The same isolated criteria are applied to such scenario.

The most loaded half of the structures (right) in Figure 3.37 is obviously more reinforced (thicker struts, more volume concentration), while the left half is dominated by thinner, longer struts connecting the distant load to the corresponding support. This leaves room for functional grading, (tailored anisotropy), although some mechanical issues could arise (e.g. buckling on the left side).

The optimized topologies will not be as diverse when the boundary conditions are too restraining (hyperstaticity). This gives less freedom for topological evolution, resulting in most criteria being either slight variations of a constrained optimum or ill-defined density maps. See Figure 3.38 for an example.

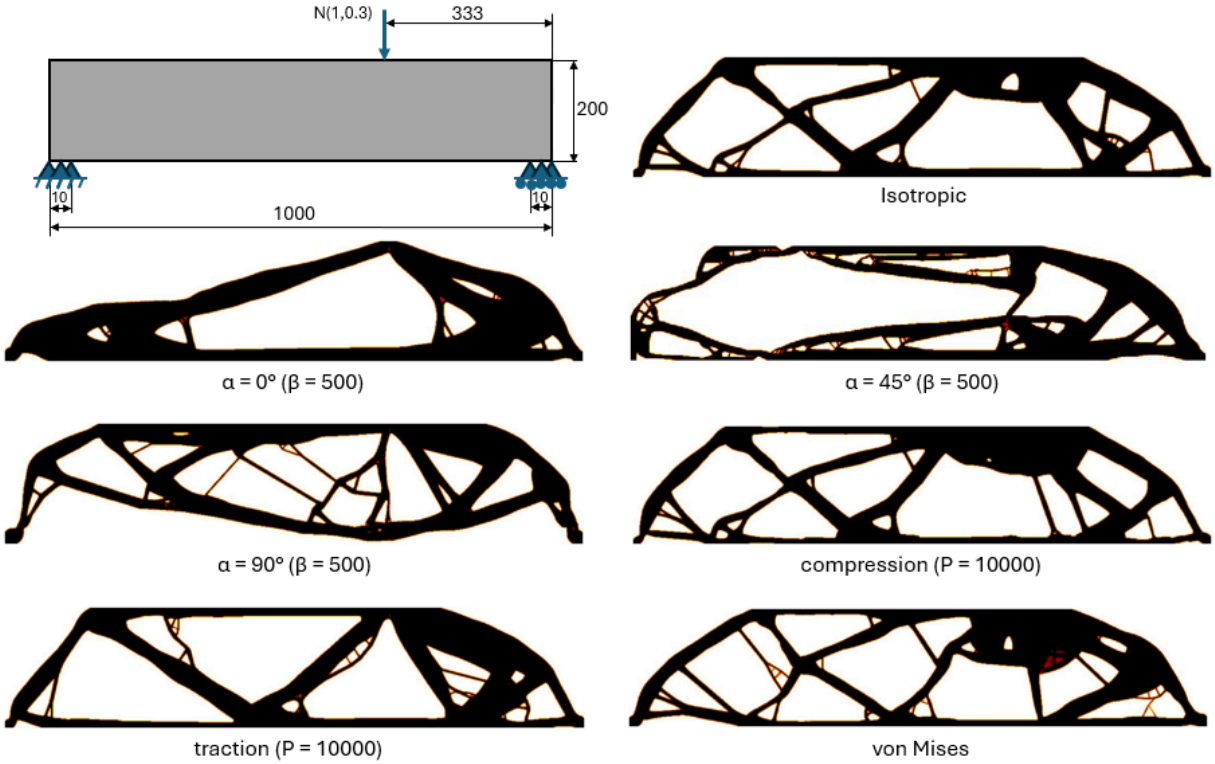

Figure 3.37: Examples from Figure 3.32 with rightwards-skewed loading at two thirds of their length.

The almost identical topologies for all proposed criteria in Figure 3.38 demonstrates how certain boundary conditions are too restrictive, rendering damage penalization somewhat useless. Similarity between the isotropic (top right) and compression cases (third row right) still applies. The von Mises stress criterion (bottom right) yields an irregular material distribution, compromising convergence.

3.2.2.2.5 Damage Criteria under Undeterministic Loading Previous cases in this section have assumed static loading, always locked in position and sometimes in modulus and frequency as well. Consider Figure 3.39, where the distributed loads' position are given by $\mathcal{N}(550, 50)$ on the top right corner and $\mathcal{N}(300, 50)$ in the bottom middle. Again, criteria reinforce their target mechanical responses (traction/compression) or printing directions ($0°$/ $45°$/$90°$), although not as clearly due to randomness introduced by non-static loading.

If the modulating scalar parameters P, β are increased (see Figure 3.40), their effects become sharper. Since the load distribution is probabilistic, slight differences can be noted on the contour of some topologies, despite nominally being under the same loading conditions.

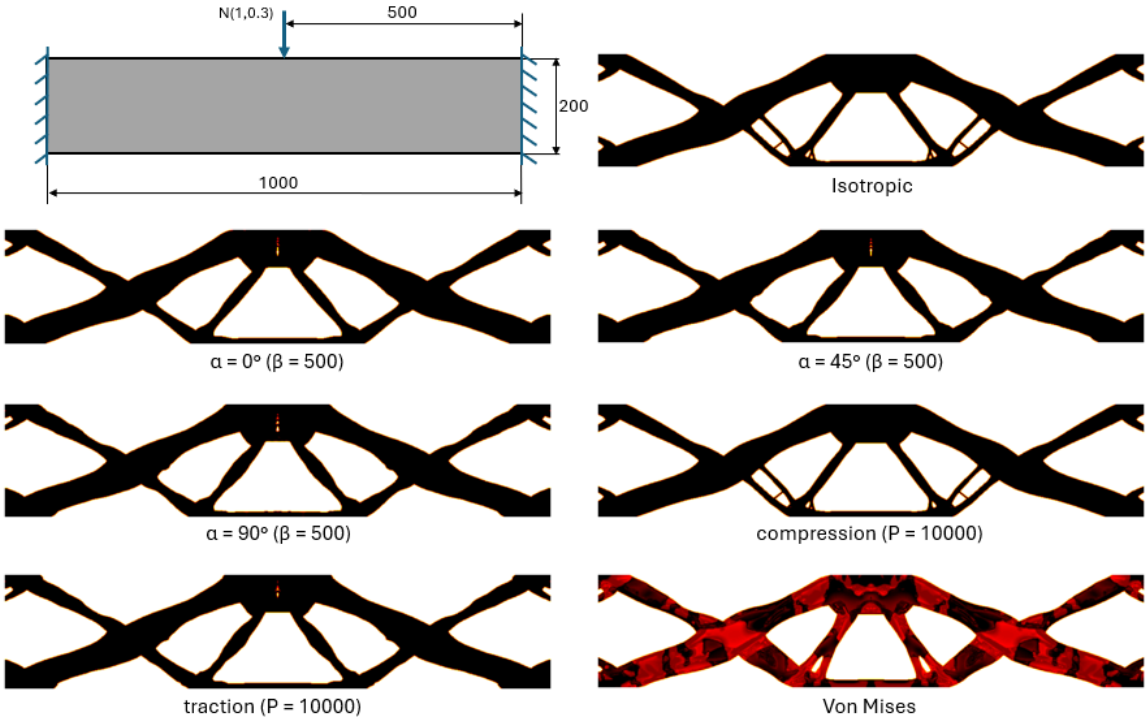

Figure 3.38: Fixed beam examples for single isolated criteria.

All cases in Figures 3.39 and 3.40 share two features: pockets of intermediate density and convoluted topologies with many feeble twigs among the principal, load-bearing struts. Both are a direct result of uncertainty in load position forcing continuous gradient changes during the TO process and thus making the algorithm withdraw and restore volume alternatively in the same region. It also induces heavy ramification to support every individual load. These facts make convergence difficult and time-consuming, but their consequences can be corrected via filtering.

3.2.2.3 Filtering-Assisted Logarithmic Interpolation

To alleviate all mechanical and manufacturing issues coming from ill-defined and/or ramified topologies seen before, novel filtering techniques will be embedded into the TO process, saving computational expenses by avoiding extra post-processing steps. Additionally, the interpolation methodology proposed in Section 2.2 offering a design space with two degrees of freedom (volume fraction, compliance) will be extended through filtering to add its third optimization variable (minimum strut thickness). This is all contained in the article **Mechanostat-type effective density correction for the Carter-Hayes growth applied to topology optimization and its efficient interpolation** [488].

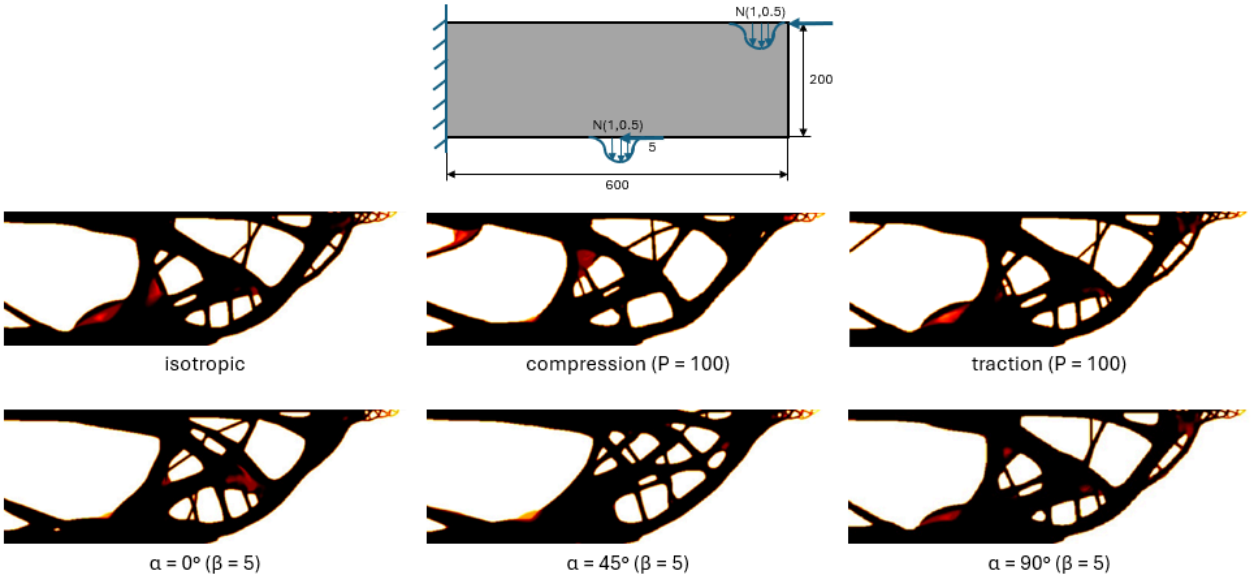

Figure 3.39: Cantilever beam (600x200) with uncertain loading conditions (top row). Row-wise, from left to right: isotropic (configuration 2 with $\kappa_f = 5 \cdot 10^{-5}$, $\sigma_f = 5 \cdot 10^{-2}$ and $\alpha = 9 \cdot 10^{-3}$), compression and traction (both with $P = 100$) and printing angles of 0°, 45° and 90° (with $\beta = 5$). Iteration 100.

3.2.2.3.1 Filtering Effects on Mechanical behavior As an example, consider the topology in 3.20 middle right: a 1000x200 cantilever beam loaded on both ends with equally frequent unitary loads.

Filtering with threshold radius $r = 5$ is applied as a post-processing step in Figure 3.41, effectively tackling most of those structurally superfluous yet difficult to manufacture twigs, which is among the main objectives. Alas, if such a trimming were to be directly introduced, it would not be structurally optimal either: many junctions would be left unsupported, discontinuities would further complicate manufacturing (needing supports if 3D-printed) and the target volume fraction would not be met after getting rid of those elements. Also, some junction points (joints) would be left with undesirable stumps unreachable by the filter as the distance to the main structure is greater than the prescribed radius r.

Therefore, the filter must be embedded and applied not once at the end (post-processing) but periodically during the iterative optimization, to allow for restructuring. This cannot be done for the first iterations as the optimized structure is in its early growth stages, and so densities x_{Phys} have not yet reached values close to 1 (full) or 0 (void), rather presenting an ill-defined intermediate density distribution. Early filtering would create incompatibilities with the already embedded density filters in $top88, m$ [205] or even force full annihilation (void).

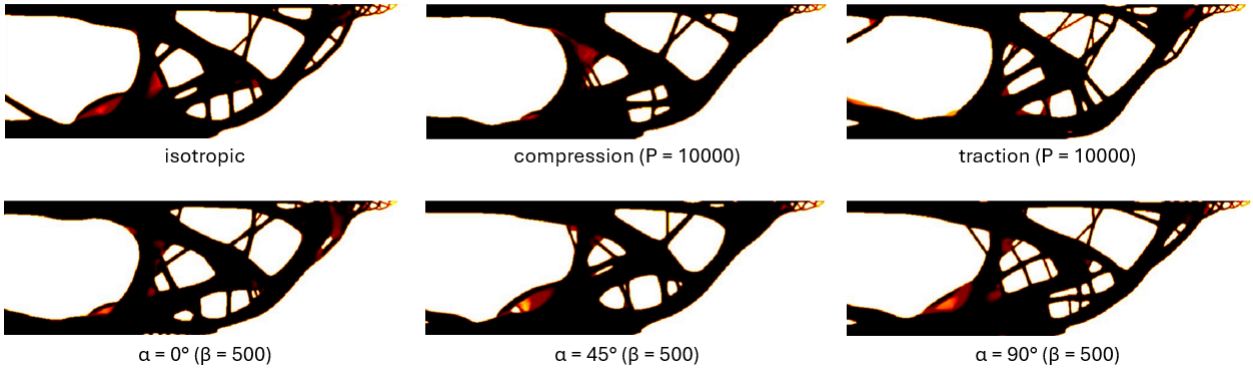

Figure 3.40: Cantilever beam (600x200) with mixed nondeterministic loading conditions (Figure 3.39 top row). Row-wise, from left to right: isotropic (configuration 2 with $\kappa_f = 5 \cdot 10^{-5}$, $\sigma_f = 5 \cdot 10^{-2}$ and $\alpha = 9 \cdot 10^{-3}$), compression and traction (both with $P = 10000$) and printing angles of 0°, 45° and 90° (with $\beta = 500$). Iteration 100.

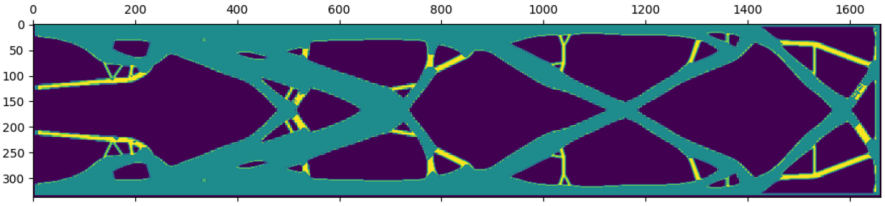

Figure 3.41: Filter of radius $r = 5$ applied to the double cantilever structure at iteration 200 (Figure 3.42a). Dark blue colors represent void, yellow the erased (filtered) twigs and light blue stands for the remaining structure.

Decreased volume fraction comes as a side effect under the proposed filtering strategy. Since the trimming operation takes an unforeseen amount of volume each time, the algorithm needs time to replenish the lost fraction to attain the target. However, if the iteration interval is too short, it might not have the chance to reach the desired volume fraction until no more twigs under the filtering radius are forming, which could very well take hundreds of iterations. Thus, the timing of the filter is also a tuneable parameter. Otherwise, the naturally occurring results can be leveraged as savings in material. After some brute-force tuning, 10 iterations is chosen as an appropriate interval.

The obtained topologies are showcased in Figure 3.42, with their respective normalized shear strain and equivalent von Mises stress (b and c for the unfiltered version (a), e and f for the filtered one (d)). Focusing on the left side (Figures 3.42a, b and c), it is clear how the thinnest struts are not actually performing any strain or stress transfer worth of mention in the vanilla topology - especially regarding shear strains since loading is vertically applied -, rendering them obsolete.

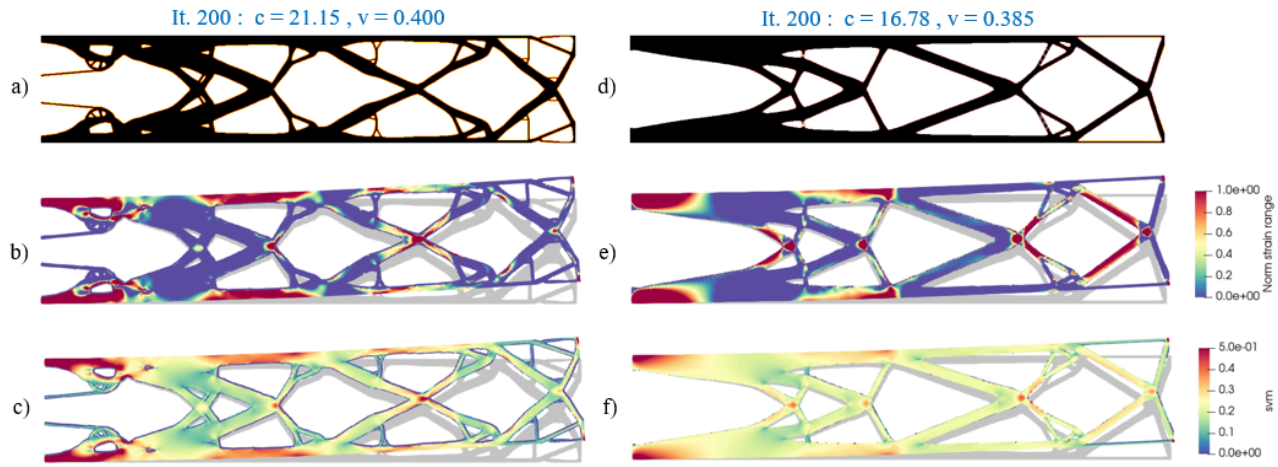

Figure 3.42: Vanilla (left) and filtered (right) topologies for Figure 3.20 middle left. Designs (a, b), their shear strain (b, e) and von Mises equivalent stress distributions (c, f). Iteration 200.

As a result of that, both shear and strain are highly concentrated in some joints and near loading points and supports, whereas the remainder of the structure is idle, bearing a fraction of the load. This means load distribution will be quite heterogeneous: both the normalized shear strain (Figure 3.42b) and the von Mises equivalent stress (Figure 3.42c) are highly concentrated in junctions, cross-section changes and notches, which puts the structure at risk of cracks and fatigue failure (fracture).

There are still some unnecessarily convoluted topological features in the filtered version (Figure 3.42d), but the structure is mostly cleared - the genus, i.e. "number of holes", decreased greatly - and the majority of those inconvenient twigs have disappeared giving way to thicker, more robust ones with a meaningful contribution to load bearing - namely between joints and support points. Additionally, the stumps seen in Figure 3.41 have been completely erased as a result of the iterative process. Extending the TO processes to iteration 1000 yields the results in Figure 3.43.

An optimized design could benefit from thicker joints and structurally meaningful struts for the same volume fraction, plus the already mentioned manufacturing handicap makes such preliminary results impractical. However, extending the vanilla iterative process (up to 1000 iterations, see Figure 3.43a) does not improve neither shear (Figure 3.43b) nor stress distribution (Figure 3.43c), which stay virtually unchanged, except for some minor simplifications (e.g. erasing one of the handles on the left). This ultimately incurs in a slight volume relocation (constant 0.4 fraction) to reduce compliance (21.15 to 4.08, that is, more than 80%). Most of the useless twigs remain nonetheless.

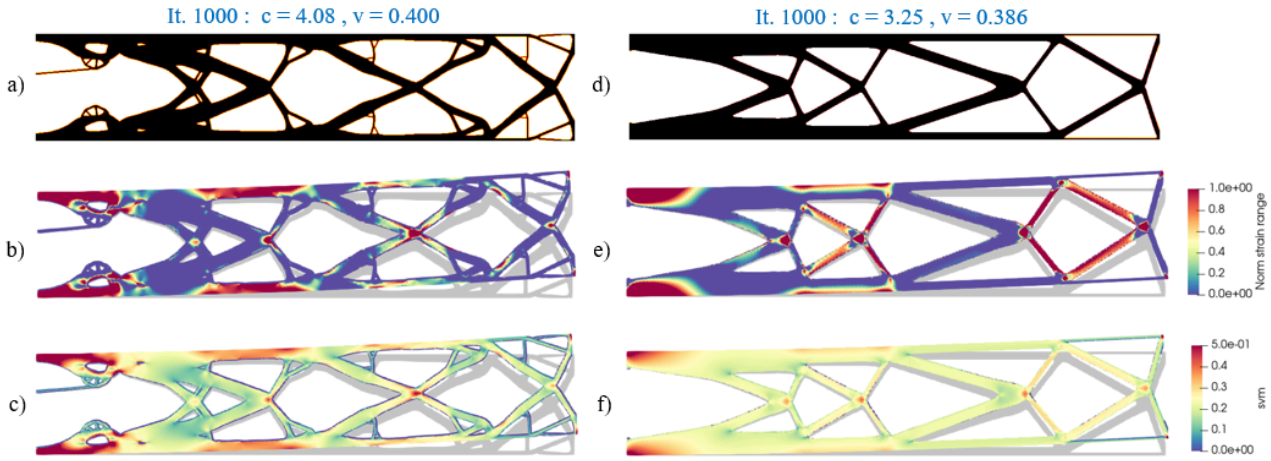

Figure 3.43: Vanilla (left) and filtered (right) topology optimization of Figure 3.20 middle left. The resulting optimized structures (a, b) are shown along their shear strain (b, e) and von Mises equivalent stress distributions (c, f). Iteration 1000.

Iterations do matter when the filter is applied: a great topological simplification can be observed for iteration 1000 (Figure 3.43d) compared to iteration 200 (Figure 3.42d). Conversely, change is minimal in the unfiltered versions (Figure 3.42a versus 3.43a). This has noticeable effects on their shear strain (Figure 3.43, second row) and von Mises equivalent stress (Figure 3.43, third row): fewer struts guarantee more consistent and homogeneous load distribution, so less ribs are enough, instead of unevenly loaded sections of struts creating dangerous stress concentrations. This option is preferable both from the mechanical and practical perspectives (manufacturability), since reinforcing those individual struts entirely (e.g. making it thicker or choosing a sturdier material) is easier than doing so for multiple local points.

Overall, load distribution is better in Figure 3.43's right side: while strain is higher in modulus, its distribution is more homogeneous, making struts contribute roughly equally; except for the two horizontal struts at the right end, connecting the diagonals supporting the loads to the main structure. Thus, not only is the resulting filtered topology (Figure 3.43d) smoother, but also more efficient in load distribution, as the remaining ribs are robuster and structurally significant.

All of that comes with a slightly smaller volume fraction (material savings) and compliance (stiffer structures). Interestingly, zero-shear areas (in blue, second row in Figures 3.42 and 3.43) imply equal principal stresses ($\varepsilon_1 = \varepsilon_2$), which could be further leveraged for manufacturing purposes, e.g. by printing filaments along those principal directions so axial strength is maximized.

The filter is suitable for any applied loads and boundary conditions. For instance, the hyperstatic beam in Figure 3.38 top left can be filtered under various threshold radii - see Figure 3.44.

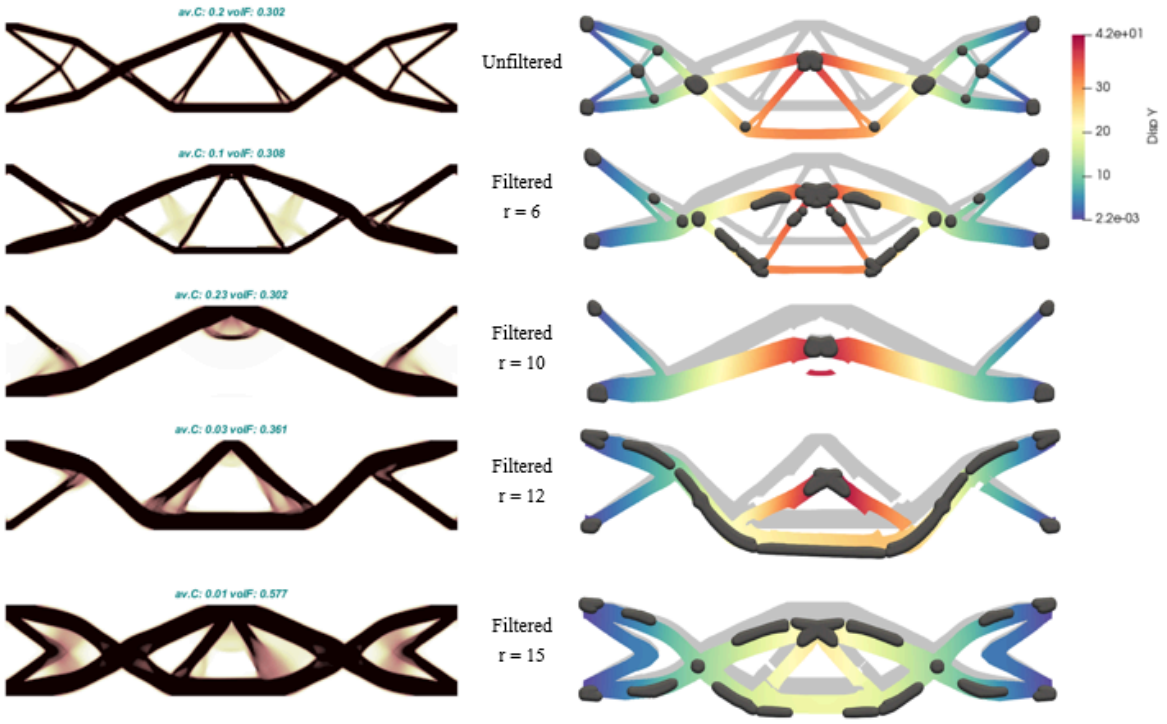

Figure 3.44: Optimized topologies (left side) for Figure 3.38 top left along their vertical displacement (color map) and von Mises (gray for > 0.05 MPa) equivalent stress (right): unfiltered (1^{st} row), $r = 6$ (2^{nd} row), $r = 10$ (3^{rd} row), $r = 12$ (4^{th} row), $r = 15$ (5^{th} row).

As expected, topologies in Figure 3.44 are simpler when filtered, although boundary conditions and loading may be prevalent. As the radius grows, two mutually linked effects are noticeable (see Figure 3.44 left, on top of each topology): volume fraction grows and compliance decreases (i.e., stiffness increases). Structurally important ribs are thickened to comply with filtering requirements, thus accelerating compliance descent: topologies become simpler (fewer deformable parts) and stiffer (less deformation overall) - see vertical displacement color maps in Figure 3.44 right.

Filtering can also be partial, i.e. exclusively along some search directions. See Figure 3.45 for a cantilever example with a downward force on its top left corner. While there's virtually no difference for low radii (e.g. compare $Unfiltered$ to $Alldirections, r = 2$), heavier filtering creates simpler topologies with more homogeneous displacement (color map) and stress (gray areas), while stiffer (smallest tip displacement for $r = 8$).

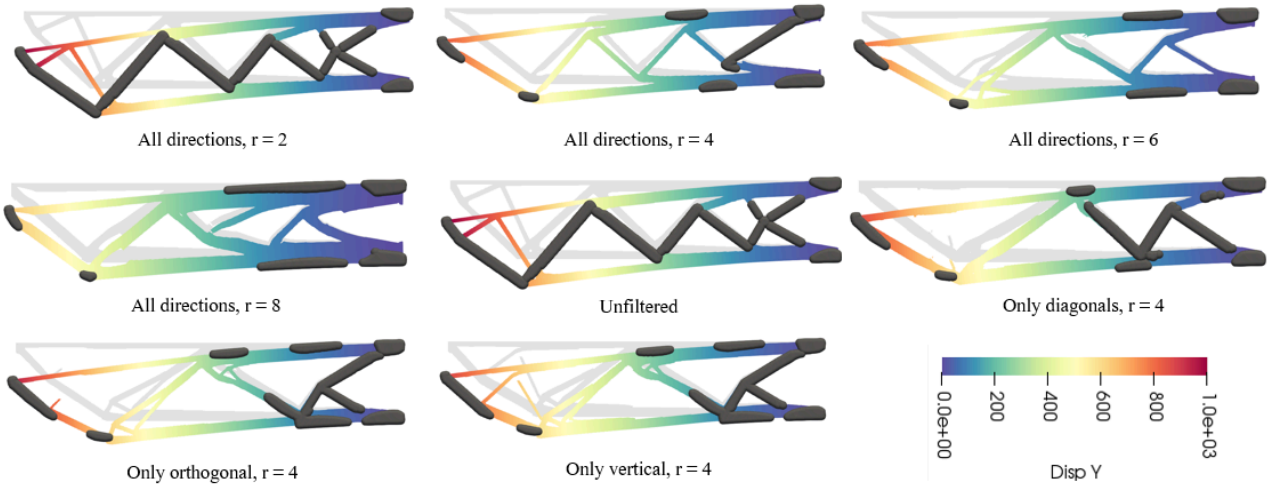

Figure 3.45: Displacements (colors) and stresses (von Mises > 0.05 MPa in gray) for optimized cantilever beams with various filtering strategies.

When the filter is applied in all directions equally (axial and radial symmetry), results are coherent with observations for Figure 3.44. However, that is not the case when filtering is asymmetric. Diagonally applied filters favor diagonal struts, longer in the center section and mostly stressed near the support and loading point - see 3.44 center right for $r = 4$ and directions 135° and 315°, that is, l_2 and l_6 in Figure 2.12. Orthogonal filtering (directions l_1, l_3, l_5 and l_7 in Figure 2.12) yields further ramification in the remaining unfiltered directions (diagonals) and more localized stresses. After filtering vertically (directions l_3 and l_7 in Figure 2.12), horizontal capillarity remains and so some ribs are closed.

This partial filtering could prove useful to induce tailored anisotropy for mechanical reasons (e.g. printing directions), thus tuning and/or preventing the incidence of buckling, compression, traction, etc. to meet the designer's requirements (material, boundary conditions, reliability, manufacturing method). This is particularly interesting for the design of functionally graded structures and metamaterials.

3.2.2.3.2 Logarithmic Volume-Compliance Interpolation Following the methodology described in Section 2.2, Figure 3.46 can be plotted. The red curves (solid for $v_0 = 0.01$, dashed for $v_0 = 0.99$) are asymptotic limits for the most extreme cases: starting from void and full material (almost vertical line), respectively. Within the area contained by them, any curve can be drawn to describe topological families evolving according to Equation 2.71, each of them describing a different optimization process.

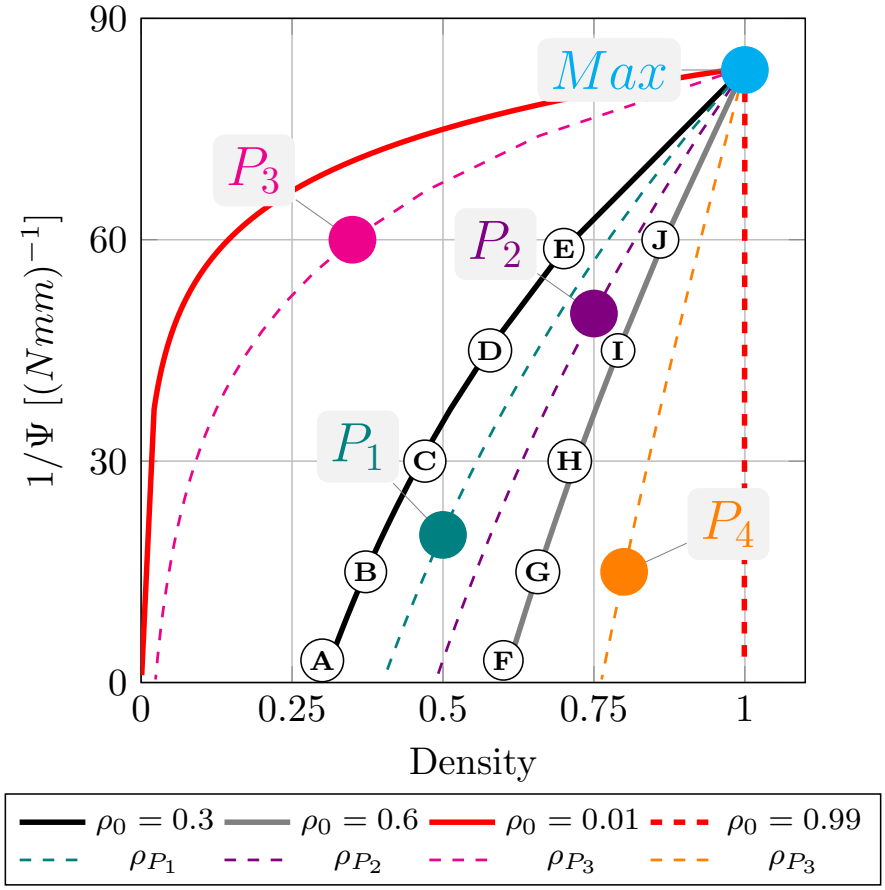

Figure 3.46: Evolution of inverse strain energy $1/\Psi$ over density ρ given by Equation 2.69 for several starting volume fractions v_0.

For instance, points A-E in Figure 3.46 mark different steps in the topology described by the black curve starting with $\rho_0 = 0.3$, and so do F-J for the gray one starting with $\rho_0 = 0.6$. Pair-wise (A and F, B and G, C and H, D and I, E and J), they have the same strain energy density (and thus, identical compliance and stiffness), but their designs will differ as much as their initial conditions, furthermore when evolved separately. Regarding density, the same conclusions apply: while some points (B and P_3, C and P_3, I and P_2 and P_4) are close, their topologies will be as diverse as the curves they are on.

A practical example of logarithmic optimization for Figure 3.32 top left can be seen in Figure 3.47. Several independent optimization processes starting with different minimum volume fractions $v_0 = 0.1$, $v_0 = 0.3$, $v_0 = 0.5$ and $v_0 = 0.7$ have been carried out, yielding different stiffnesses (inverse of compliance, 1/c). For the same material, this $v - c$ layout is equivalent to Figure 3.46. See more details in Table 3.7.

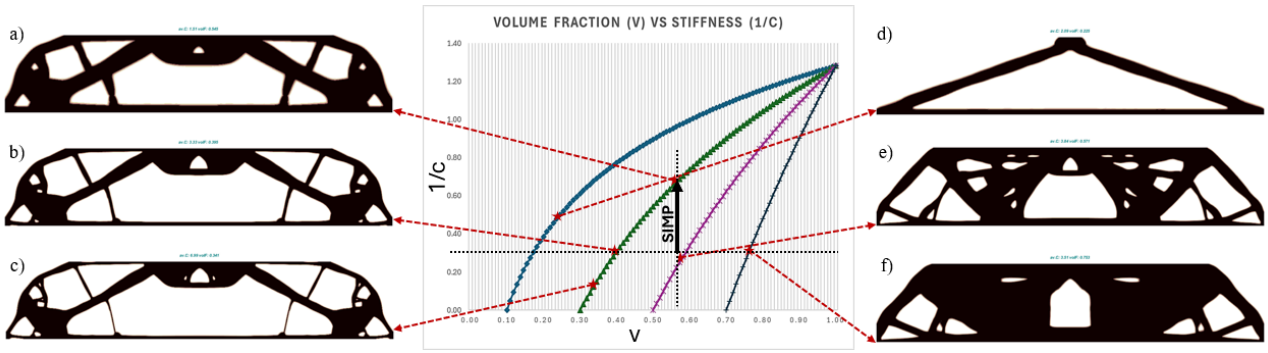

Figure 3.47: Unfiltered evolving topologies according to Equation 2.70 for Figure 3.32 for several initial volume fractions: 0.1 (light blue), 0.3 (green), 0.5 (purple) and 0.7 (dark blue).

Figure 3.47	**a**	**b**	**c**	**d**	**e**	**f**
v_0	0.3	0.3	0.3	0.1	0.5	0.7
v_i	0.545	0.395	0.341	0.225	0.571	0.753
c_i	1.51	3.33	6.99	2.09	3.84	3.51
i	65	45	25	125	20	15

Table 3.7: Information describing the topologies shown in Figure 3.47: the curve's initial v_0 and current volume fraction v_i and compliance c_i for iteration i.

Focusing on Figure 3.47's left side, the development of a topological family with $v_0 = 0.3$ can be seen at different iterations: 25 (c), 45 (b) and 65 (a). Since the filter has not yet been applied, the only possible way to grow in volume is widening the already existing ribs, which in turn decreases compliance (structures get stiffer). This process somewhat resembles shape optimization, where topology remains practically invariant (aside from little holes being engulfed by strut thickening alone).

If the designer is aiming at lower volume fractions, the optimized topologies get much simpler (bare triangles linking loading points and supports directly) and relatively stiff, although they take longer to converge since the initial volume $v_0 = 0.1$ is too low and such compliant structures need time to evolve. See Figure 3.47d for an example with $v_i = 0.225$ and $c_i = 2.09$ at iteration $i = 125$ (Table 3.7).

Should the modeler prefer sturdier options, starting with higher volume fractions could help speed up convergence to a desired compliance (e.g. Figure 3.47f with $v_0 = 0.7$). Consider labels b, e and f in Figure 3.47 and their respective data in Table 3.7: while all three topologies have approximately the same compliance c_i, their respective volume fractions v_i are very different (f's being almost twice as big as b's), as well as the steps needed (b takes three times as many iterations i as f does).

Thus, v_0 becomes a key user-defined hyper-parameter controlling both computation time (number of iteration steps) and final volume fraction v_i for a given compliance c_i. The needs of each topology will be determined by the material, loading and boundary conditions. Interestingly, isochoric (vertical) lines (e.g. a to e) represent processes with various compliance values for identical volume fractions, i.e. different stiffness for the same amount of material.

In Figure 3.47, going up (vertically) means lowering compliance while maintaining volume fraction, that is, the regular SIMP method (black upward arrow in Figure 3.47). Observing the greatly different layouts for topologies a and e proves how this methodology is not tantamount to SIMP - which would have produced much more similar results. Heading downwards vertically (same volume, less stiff) is also possible in case a more compliant structure is sought, e.g. mechanisms.

This way, design interpolation can be performed by jumping between different logarithmic curves (with their respective v_0). The transition between curves can be horizontal (fixing a compliance target c_t and varying the volume fraction v_i till intersection) or vertical (fixing a volume v_t and adjusting the compliance c_i). See Figure 3.48 for some practical examples (filtered/unfiltered, horizontal/vertical) for the same 3-point bending case (Figure 3.32 top left).

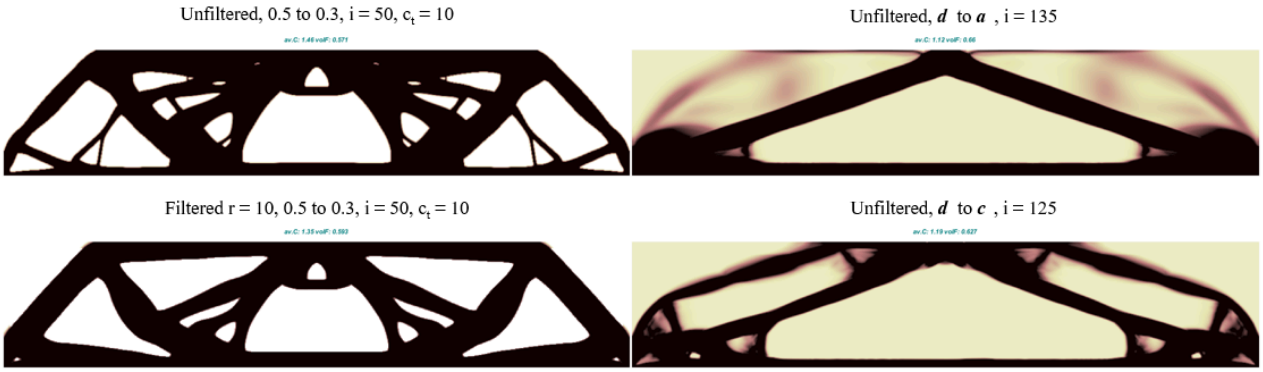

Figure 3.48: Hybrid topologies generated by interpolation. Left column: horizontal from $v_f = 0.3$ to $v_f = 0.5$ with compliance threshold $c_t = 10$ at $i = 50$, under $r = 10$ filter (top) and unfiltered (bottom). Right column: vertical with volume threshold $v_t = 0.3$, d to a (top) and d to c (bottom).

Figure 3.48's left column displays horizontal interpolation with a compliance threshold $c_t = 10$. Both topologies closely resemble the initial curve's ($v_0 = 0.5$) family (e.g. Figure 3.47e). For the same iteration ($i = 50$), the filtered ($r = 10$, bottom left) one's layout is simpler than the unfiltered case (top left), with equivalent compliance (up 1.46 vs down 1.35) and volume fraction (up 0.571 vs down 0.593).

Figure 3.48 right displays vertical interpolation with different volume thresholds v_t. It showcases importance of both the initial curve (determined by its initial volume fraction v_0) and the amount of iterations traversed on each curve. While the results do reflect aspects of both curves, prevalence of the initial one ($v_0 = 0.1$) is clear, visible by the absence of central vertical ribs (present in both a and c) under the load-supports triangle (coming from d). These intermediate solutions are close in compliance (up 1.12 vs down 1.19) and volume (up 0.660 vs down 0.627). An exact match could be found if needed.

Thus, path-dependence applies to this kind of interpolation schemes, which must be taken into account accordingly. Reaching the exact targets (Figures 3.47a and 3.47c, respectively) becomes inefficient due to the many factors involved (initial volume, interpolation, threshold, boundary conditions, filters, etc.). Ideally, volume fraction should only be fixed or increased ($v_{i+1} \geq v_i$), since a decrease would contradict Equation 2.71 and lead to trivial void solutions.

The obvious differences between horizontal (c_t) and vertical (v_t) interpolation boil down to the chosen iterative scheme. According to Equation 2.71, volume fraction in the next iteration v^{i+1} depends on the (averaged) compliance for the current iteration c^i - SIMP optimization -. This means that constant compliance interpolation (horizontal, Figure 3.48 left) does not incur in any meaningful volume changes (unless a filter is applied, see Figure 3.48 bottom left). Hence, topologies in Figure 3.48's left side remain true to their initial curve's ($v_0 = 0.5$) canonical shape (represented by Figure 3.47e).

Conversely, vertical interpolation (constant volume v_t, Figure 3.48 right) does not prevent the free evolution of compliance between curves, so an intermediate trade-off solution is found between the beginning and ending curves' "canonical topologies", with a greater influence of the latter for already disclosed reasons. In these cases, convergence is slow and ill-defined. Interpolation between more than two curves would also be possible, although complex, and needing enough iterations in between.

3.2.2.3.3 Combined Effects Leveraging both the filter and the logarithmic approach, very diverse topologies can be obtained for the same design requirements (compliance, volume fraction). Let the 3-point bending beam in Figure 3.32 top left be considered again. Several initial volumes v_0 and filtering radii r are enforced to produce a plethora of design points with similar compliance c_i and volume fraction v_i but very different topologies. Multiple alternative layouts are given for iterations $i = 25$ (Figure 3.49 and Table 3.8) and $i = 50$ (Figure 3.50 and Table 3.9).

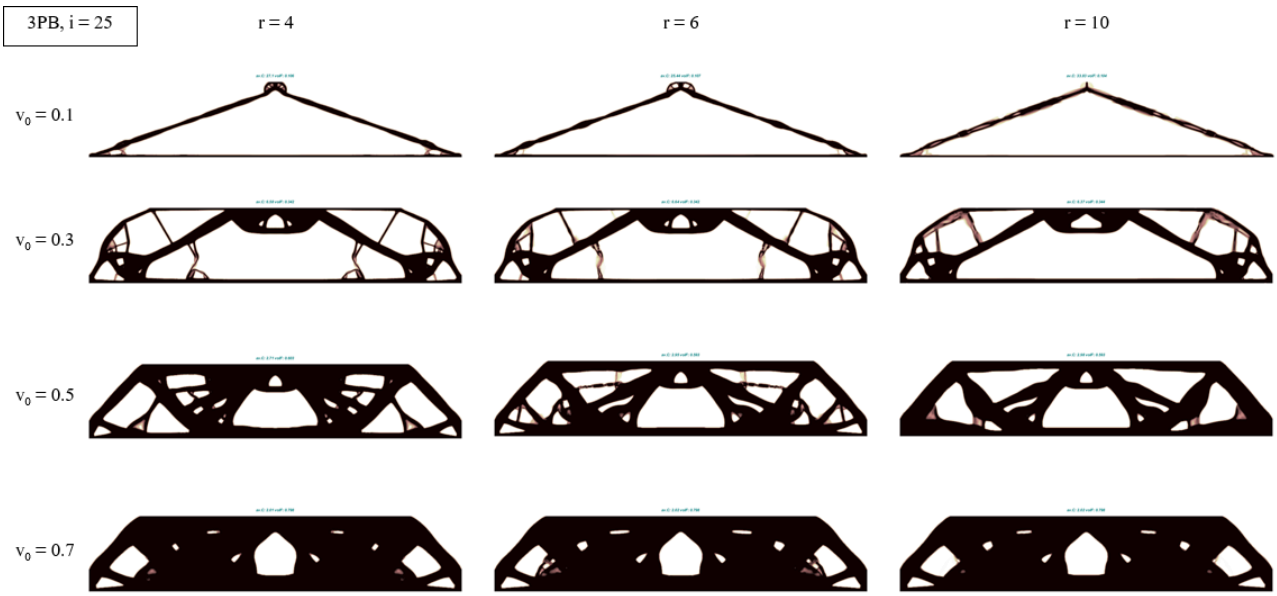

Figure 3.49: Filtered versions of Figure 3.32 top left with different filtering radii r (4, 6 and 10) and starting volume fractions v_0 (0.1, 0.3, 0.5 and 0.7). Iteration 25.

$c_i \vert v_i$ **(i = 25)**	**r = 4**	**r = 6**	**r = 10**
$v_0 = 0.1$	27.1 | 0.106	25.44 | 0.107	33.83 | 0.104
$v_0 = 0.3$	6.58 | 0.342	6.64 | 3.42	6.37 | 0.344
$v_0 = 0.5$	2.71 | 0.603	2.95 | 0.593	2.98 | 0.593
$v_0 = 0.7$	2.01 | 0.798	2.02 | 0.798	2.02 | 0.798

Table 3.8: Compliances c_i and volume fractions v_i for topologies shown in Figure 3.49.

Figure 3.49 and Table 3.8 show an array of topologies for iteration $i = 25$ and various starting volumes v_0 (0.1, 0.3, 0.5, 0.7) and filtering radii r (4, 6, 10), with their respective compliance c_i and volume fraction v_i. Row-wise, greater filtering radii (rightwards) "simplify" the topologies, reducing their *genus* ("number of holes"), as observed in previous examples. Column-wise, bigger initial volume fractions v_0 (downwards) densify the structures, not only performing a sort of shape optimization (as in Figure 3.47*c* to *a*) but also significantly altering their genus.

According to Table 3.8, topologies in the same row (same v_0, different r) present very similar volume fractions v_i. This is expected, being contained in the same v_0 curve after the same number of steps i. Their compliances (c_i) are similar too, thus representing different topologies for virtually the same data point (v_i, c_i) in Figure 3.47. This row-wise equivalence is truer the closer r's are to each other and the greater the v_0's are, becoming slight variations of a restrained optimum - as in Figure 3.38.

For very low starting volumes (e.g. $v_0 = 0.1$), their simpler topology is far less limited and so noticeably different features for each filtering radius provoke relatively important fluctuations (see middle top on the topologies shown in Figure 3.49 first row) in volume and compliance - see Table 3.8. Nevertheless, these trivial discrepancies can be solved by varying iteration steps, since convergence follows different paces depending on the chosen logarithmic curve and filtering strategy.

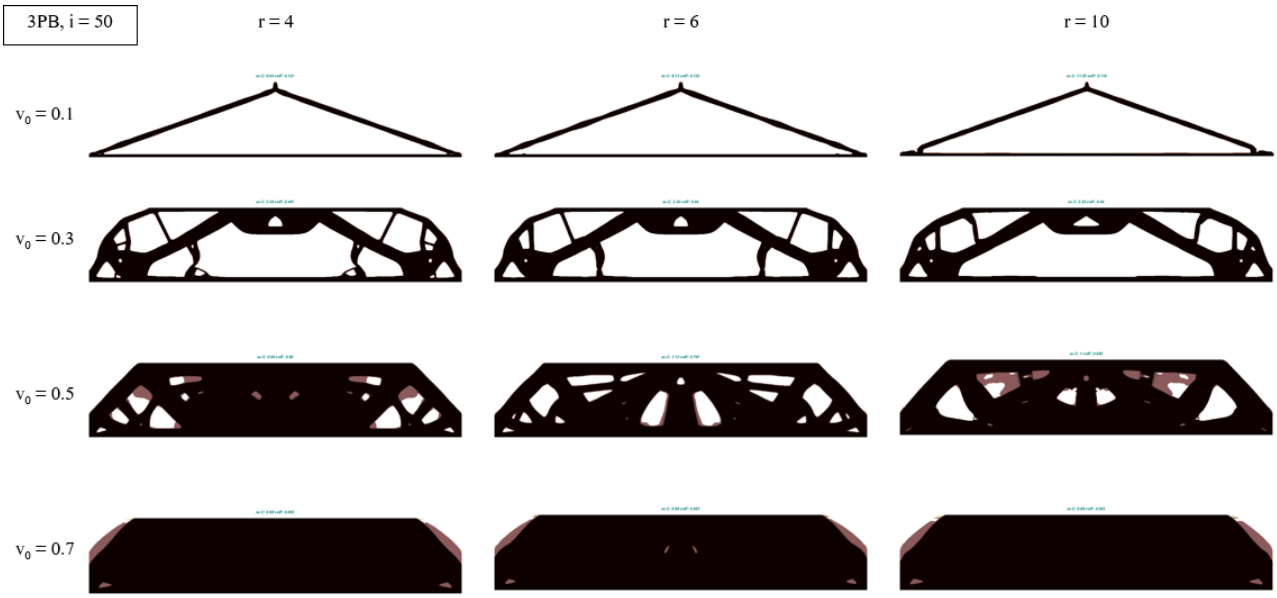

Figure 3.50: Filtered versions of Figure 3.32 top left with different filtering radii r (4, 6 and 10) and starting volume fractions v_0 (0.1, 0.3, 0.5 and 0.7). Iteration 50.

$c_i \vert v_i$ **(i = 50)**	**r = 4**	**r = 6**	**r = 10**
$v_0 = 0.1$	8.94 | 0.121	8.73 | 0.122	11.55 | 0.116
$v_0 = 0.3$	2.38 | 0.441	2.38 | 0.440	2.38 | 0.440
$v_0 = 0.5$	0.96 | 0.86	1.12 | 0.797	1.00 | 0.838
$v_0 = 0.7$	0.88 | 0.953	0.88 | 0.953	0.88 | 0.953

Table 3.9: Compliances c_i and volume fractions v_i for topologies shown in Figure 3.50.

Figure 3.50 and Table 3.50 show the evolution of the topologies seen in Figure 3.49. While middle volumes greatly changed (namely $v_0 = 0.3$ and $v_0 = 0.5$), others remain practically unaltered (lower volume, $v_0 = 0.1$). Higher volumes ($v_0 = 0.7$) have almost reached the maximum possible stiffness, i.e. a full material block. With respect to Table 3.8, Table 3.9 reflects closer compliance and volume values for the same row, virtually identical for $v_0 = 0.3$ and $v_0 = 0.7$. Whereas no meaningful differences can be noticed for $v_0 = 0.7$, $v_0 = 0.3$ offers diverse alternatives for the same data point (c_i, v_i).

All the remarks and observations applied for this case of study remain true for different loads, boundary conditions, radii and starting volumes, as soon as linear elasticity is verified. The combination of filtering and logarithmic interpolation provides a powerful and versatile inverse design methodology with three degrees of freedom: compliance c_i, volume fraction v_i and filtering radius r (somewhat equivalent to minimum thickness).

3.2.2.3.4 3D Generalization The proposed filtering technique is easy to generalize for 3-dimensional settings. With [206] as a SIMP 3D base code for compliance optimization, the extra needed out-of-plane search directions are added: those analogous to the ones in Figure 2.12 in the YZ and XZ planes, plus the ones corresponding to the cube's four vertices.

To ponder its performance, let a 3D periodic lattice be considered. Should an isotropic metamaterial be sought for, the elementary cell to be repeatedly placed along all three directions must be symmetric in all three of them. To achieve that, boundary conditions and loading for TO must be such that they keep connectivity among cells in all axes. One option would be fixing the cube's vertices in all three directions and loading its face centers along their respective orthogonal directions, facing outwards. See Figure 3.51d for an explanatory diagram and a, b, c, e and f for several examples with $F = 1$.

Axial symmetry can be found in 4 out of 5 examples in Figure 3.51, which is expected since loading and boundary conditions are symmetric - considering all extra unseen faces an vertices in Figure 3.51d. However, Figures 3.51b and 3.51f are not axially symmetric, since their top front face is unlike the other five: three out of four of their top vertices is directly joined to its center. In this case, the filter has been applied asymmetricly: those particular three search directions have been excluded from filtering and so thinner-than-prescribed ($r < 4$) struts have been allowed to grow between the face center and those three corners. Although this distorts the isotropic assumption, it can be of interest to suit other eventual requirements, e.g. custom functional grading.

The proposed filter's effect is analogous to the 2D case, as expected. The finer the mesh, the clearer (and simpler) the contour is, but it is kept coarse to reduce computational cost. Note the resolution gain for the same global constraints ($v_f = 0.3$, $r = 2$) when increasing the cube's side from 20 (Figure 3.51a) to 24 elements (Figure 3.51e). These two examples have been optimized with a filtering radius $r = 2$, preventing the formation of occluded inner holes in the cube's center. Otherwise, with a high enough radius (e.g. $r = 5$ in Figure 3.51b), inner hollow parts could appear - see Figure 3.52.

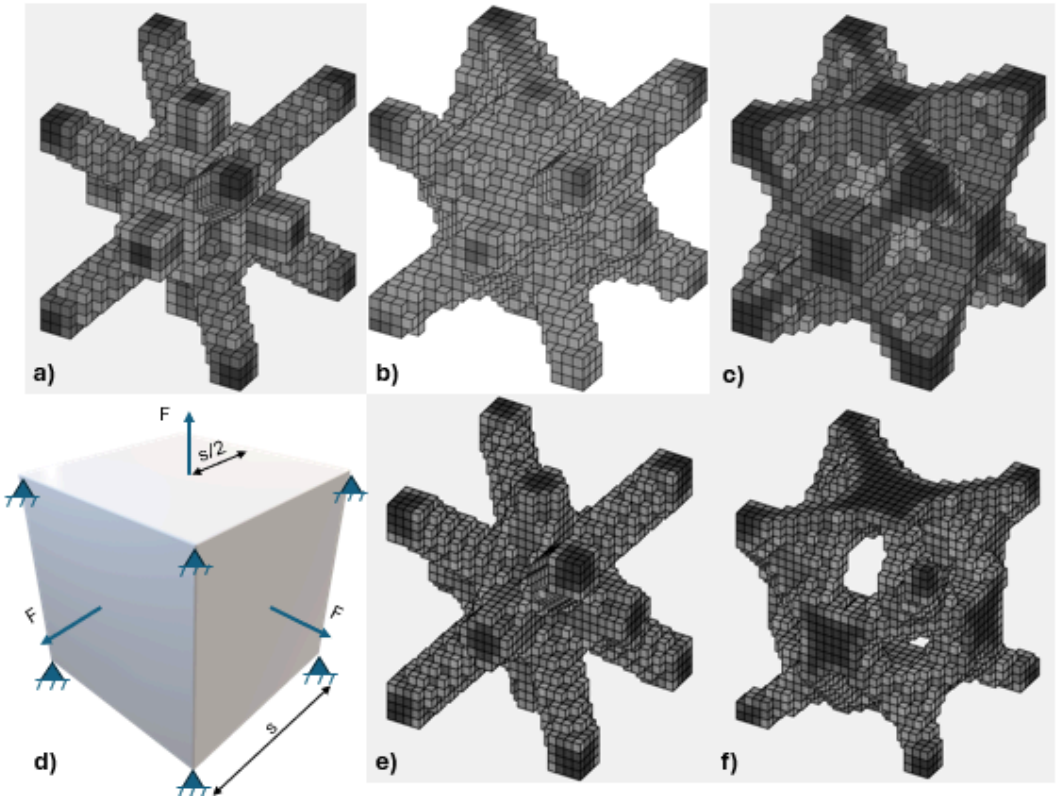

Figure 3.51: 3D compliance minimization (SIMP) for a face-loaded (F) and vertex-fixed cube (d) with side s, volume fractions v_f and filtering radii r: (a) $s = 20$, $v_f = 0.3$, $r = 2$; (b) $s = 20$, $v_f = 0.3$, $r = 5$; (c) $s = 20$, $v_f = 0.5$, $r = 2$; (e) $s = 24$, $v_f = 0.3$, $r = 2$ and (f) $s = 24$, $v_f = 0.3$, $r = 4^*$. Color represents null (white void), low ($0.2 <$ gray < 0.8) and high density (black > 0.8). Iteration 200.

Proceeding with caution, the opposite solution can avoid hollow encapsulated areas, i.e. setting a large enough radius and/or a fine enough mesh to purposefully create a central spherical hole reaching the external void contour - see Figure 3.51f for an example with $s = 24$ and $r = 4$ (partial filtering).

Hollow inner volumes constitute a great hindrance for two main reasons. Regarding the optimization process itself, the compliance-minimization scheme is stress-agnostic and so it can create very sharp stress-concentrating edges - see Figure 3.52's inner contour - interfering with filtering techniques. Visibility maps [230] and stress-based TO [268, 269, 270] could help in this regard.

The second one is related to manufacturing constraints. In many metamaterial cell designs, the cube's side is $1mm$ or less [27], close to the feasible manufacturing precision in many additive settings. Thus, manufacturing resolutions would probably fail short if a hollow cell like Figure 3.52 were to be printed, especially when using Laser Powder Bed Fusion (LPBF) [489].

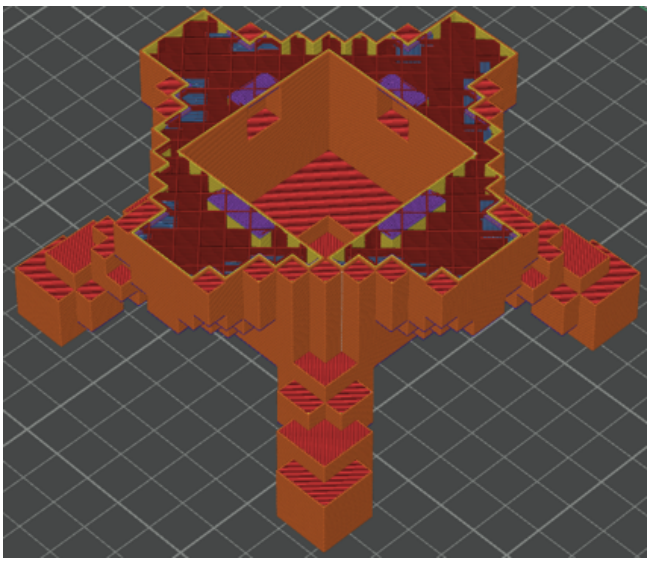

Figure 3.52: Hollow area captured in Figure 3.51b visualized through a cross-section by the mid-horizontal plane. Printing environment (*.stl* file).

The strut-like topologies in Figures 3.51a and 3.51e also ease manufacturing, additive or not, as well as conceptual representations and numerical simulations. However, these "struts" must be thick and/or short enough to avoid buckling and so keep the linear elasticity assumption.

Using the same data processing procedure in Figures 3.36 and 3.42 (among others), mechanical properties can be easily visualized with Paraview©. Examples for Figure 3.51b can be found in Figure 3.53, where lower values define its contour and higher shear and stress concentrations in the center give useful hints for its inner cubic hole (see Figure 3.52) - a sort of visualization map in itself.

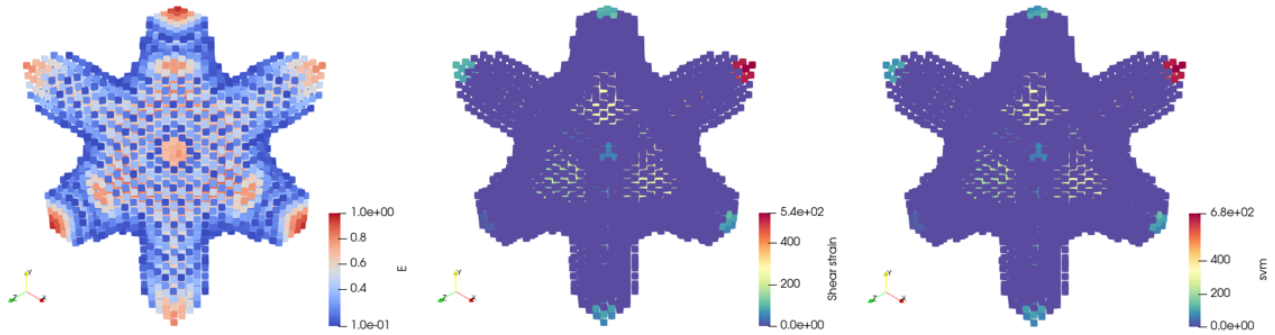

Figure 3.53: Mechanical performance for Figure 3.51b: normalized Young's modulus E (left), shear strain γ (middle) and von Mises equivalent stress σ_{vM} (right).

If material (and thus, weight and money) savings are prioritized, the minimum volume fraction v_f and maximum density ρ can be selected as objectives, yielding minimal strut topologies like in Figure 3.54.

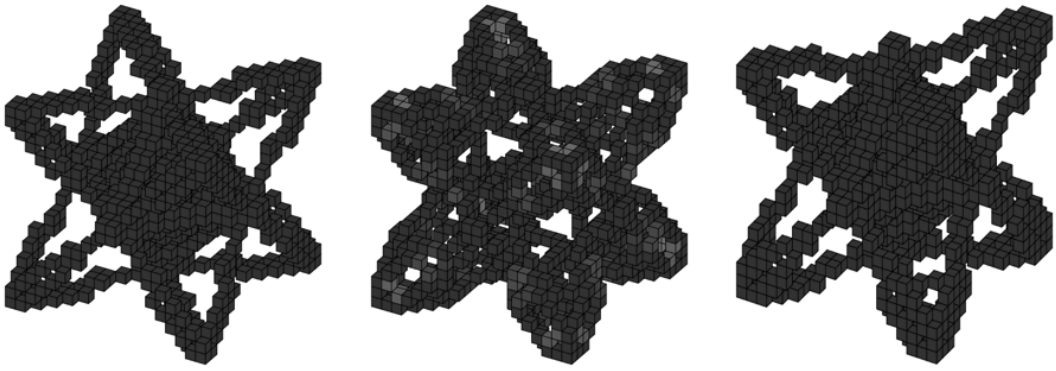

Figure 3.54: Several minimum-volume ($v_f = 0.1$) and maximum-density ($\rho > 0.8$) alternatives for Figure 3.51d under varied filtering conditions. From left to right: unfiltered, $r = 4$ and $r = 6$.

Figure 3.54 displays different ways to dramatically reduce volume while keeping the most structurally significant struts linking load-bearing nodes to supported ones. However, if the volume and/or filtering constraints are too harsh, symmetry could be compromised: note the absence of the back left top corner in Figure 3.54 right when compared to Figure 3.54 left.

Filtering constriction bifurcates possible minimum-volume solutions: either concentrate material at the cell's center (avoiding hidden inner holes) as in Figures 3.54 left and 3.54 right, or completely empty the center in favor of reinforced supports (Figure 3.54 center). The desired option will depend on further design aspects neglected in those examples (e.g. buckling, plasticity).

A 3D extension for 3-point bending beams (same boundary conditions as Figure 3.32 top left except single-node supports and a 3D 17x12x4 dominion) can be seen in Figure 3.55. Strict density thresholds ($\rho > 0.8$) have been applied in all cases but one (middle right, $v_f = 0.5$). Whereas this particular case presents wide loosely-defined middle-density contours, all others prove more efficient in material distribution (e.g. lateral notches instead of inner contours, support miniaturization).

Some other contributions of this thesis, such as probabilistic loading, damage criteria and logarithmic interpolation, are also implemented and fully functional in 3D. Unfortunately, there has been no time yet to properly explore their possibilities.

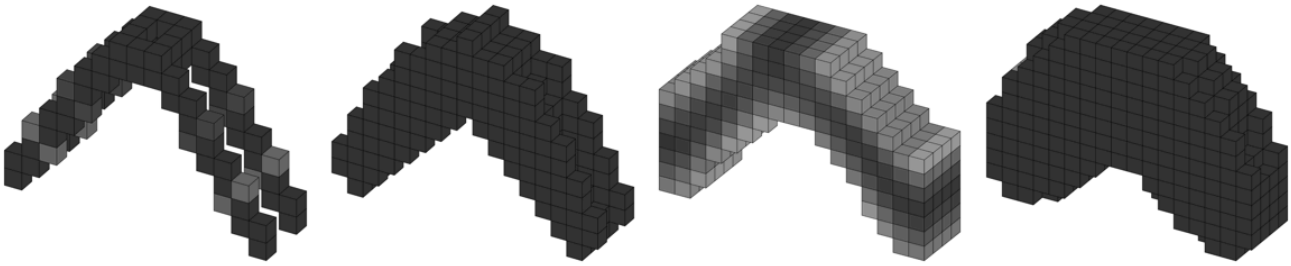

Figure 3.55: Unfiltered 3D TO for a 3-point bending beam with $F = 1$ and several volume fractions. From left to right: $v_f = 0.1$, $v_f = 0.3$, $v_f = 0.5$, $v_f = 0.7$. Color palette from Figure 3.51. Iteration 10.

3.2.2.3.5 MLP-Powered Convergence Boost A MLP-driven surrogate is devised to accelerate TO convergence, featuring alternating linear (3) and ReLU layers (2) and a final sigmoid pooling. It is trained for 500 epochs to predict compliance and volume values from topologies as image files.

These images depict interpolation points A-J in Figure 3.46, serving as database to obtain intermediate topologies P_1-P_4 via Equation 2.71, MLP or both - see Figure 3.56. The physical loss in the MLP scheme is given by the distance (in compliance and volume) between the interpolation point's and the target's respective curves.

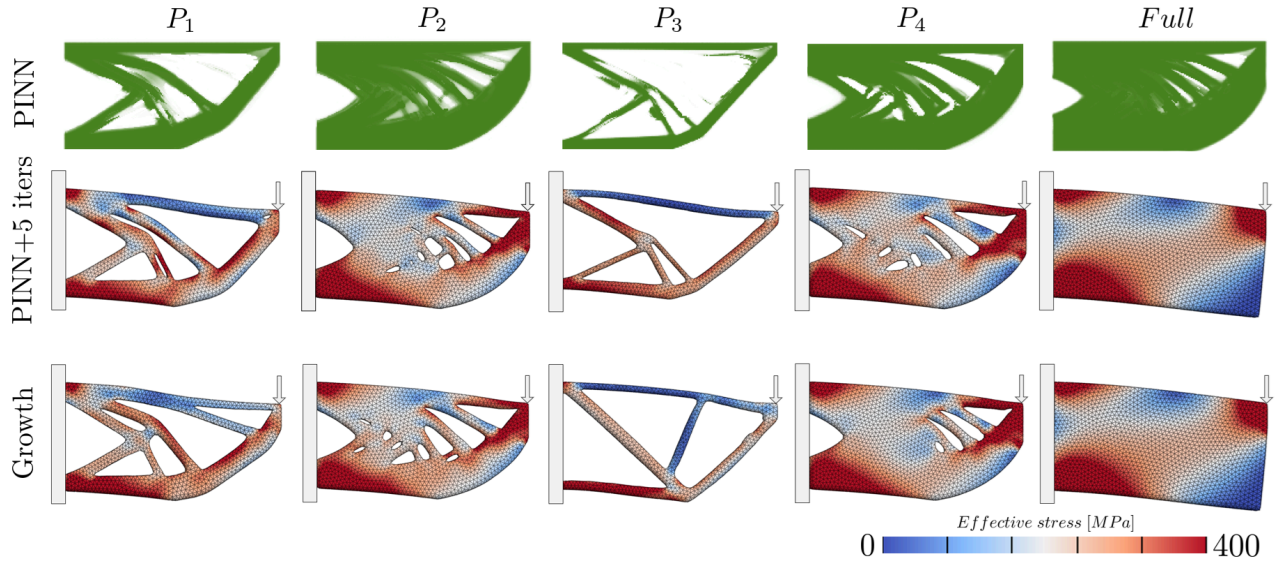

Figure 3.56: Topology optimization of a cantilever beam for points P_1-P_4 in Figure 3.46 and the full material block (columns), via MLP exclusively (top row), MLP after 5 initial iterations of Equation 2.71 (middle row) and 2,000 iterations (bottom row). Blue-red scale indicates stress values (MPa). Filtering radius $r = 4$

Figure 3.56 exhibits great column-wise similarities, meaning the MLP-based surrogate (500 training epochs, top row) reaches very close results to the vanilla scheme (2,000 iterations, bottom row), saving a lot of computation time since, once trained, the MLP-driven option is about 25 times faster. If, instead of running the MLP from the initial curve's volume v_0, the scheme is run for only the 5 first iterations (middle row), the results are even closer to the ground truth, with almost exactly matching stress distributions - especially in the full configuration.

Of course, this resemblance is never exact, since the dataset (A-J) is made up from points in different curves than the targets P_1-P_4 - see Figures 3.57 and 3.58 for examples with filtering radii $r = 1$ and $r = 4$, respectively. Thus, this methodology could be interpreted as a quick way to obtain mechanically equivalent designs to the target - in terms of compliance, volume and minimum thickness - without actually having to compute all the needed iterations along their unexplored curves.

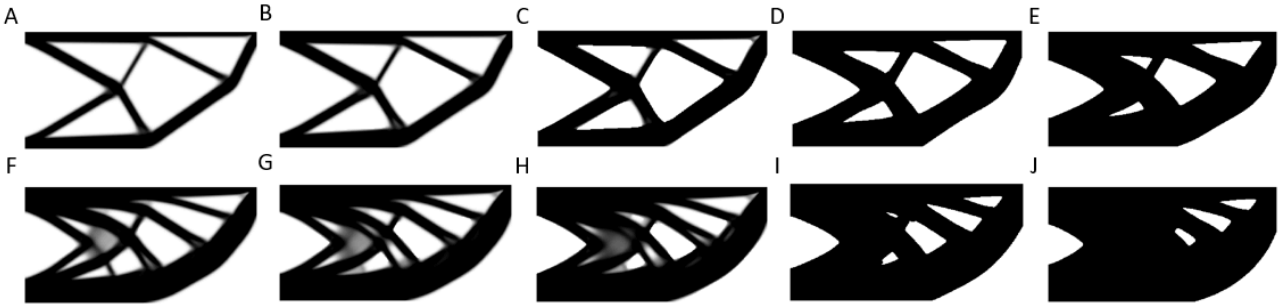

Figure 3.57: Training set: points A-J in Figure 3.46 for the ML surrogate with filtering radius $r = 1$.

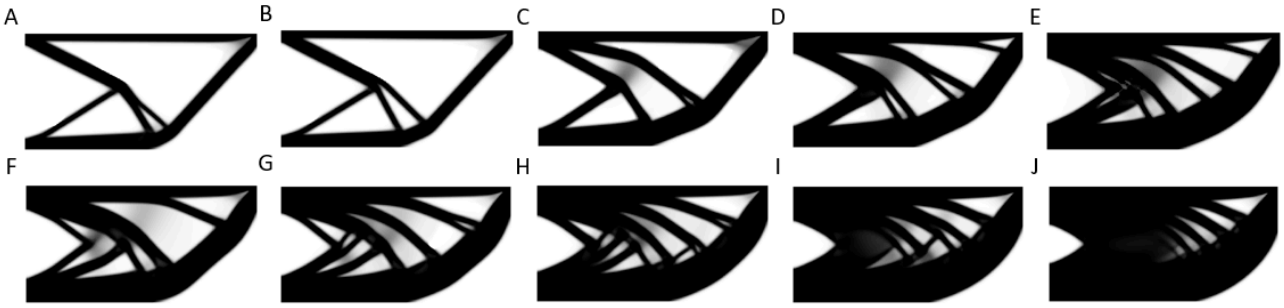

Figure 3.58: Training set: points A-J in Figure 3.46 for the ML surrogate with filtering radius $r = 4$.

This tool can also be employed to predict points along the same A-E and F-J curves, quickening dataset generation for training and so further accelerating the whole TO approximation process. See Figure 3.59 for some examples. The predictions are now much closer, as interpolation is done along the same curve for datasets and targets.

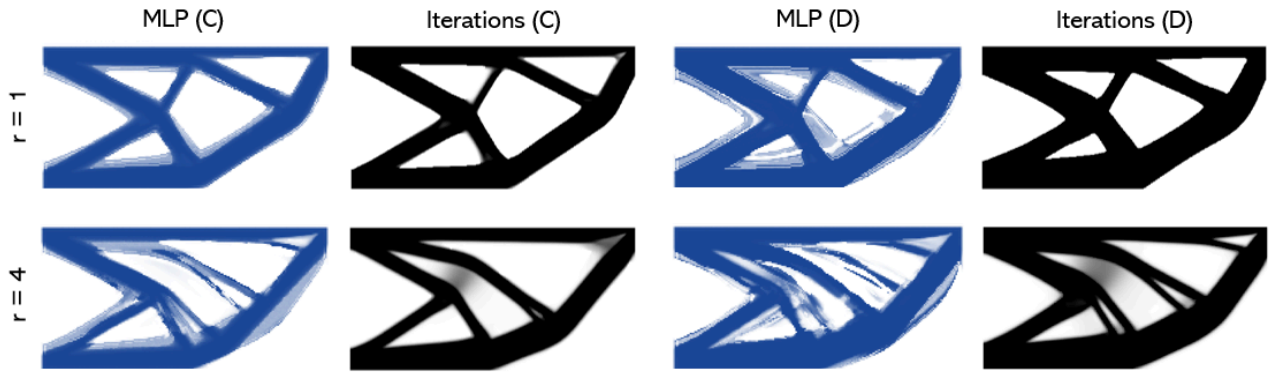

Figure 3.59: Prediction along the training dataset curve A-E in Figure 3.46 (points C and D) for filtering radii $r = 1$ (top row) and $r = 4$ (bottom row).

This technique disrupts SIMP's initial homogeneous assumption, accelerating convergence.

3.3 Digital Twins for Biomedical Applications

This section shows some results of the implemented biomedical surrogate model. The adaptation process is two-fold: logical (inhibition and excitation yielding plastic remodeling) and biophysical (neuron migration). A biologically-plausible and computationally-affordable Digital Twin for the connectome is created, featuring fully-functional synapse propagation, neuronal migration and neuroplasticty - see Section 2.3. The results show the *in silico* biological network's capability to adapt the delay of a signal when subjected to change, i.e. pulse-width modulation for a given target latency.

3.3.1 Biologically-Plausible Synapse Propagation

This is an initial proof of concept for the developed biomedical brain mock-up, see the author's pre-print "**Numerical reproduction of the Sherrington-Adrian observations through a community of McCulloch-Pitts neurons with plastic remodeling**" [490]. Sherrington and Adrian [491, 492] received the Nobel prize in Physiology and Medicine in 1932 for "discovering that the explosive waves of impulses discharged along the nerve are always the same size, regardless of how strong the stimulus is" [493].

The brain's impedance was also proven independent of the stimuli's frequency [494]. Neuronal circuits stabilize different input signals [495] - with implications for diseases such as Parkinson or Glioblastoma multiforme [496] (see [125] for an overview). This can be modeled by introducing noise into the neuronal circuit [497, 498]. Experimental results [499] confirm this case of metastability [307].

A network based on McCulloch-Pitts neurons [87] is proposed, using plastic remodeling to adapt to a required signal delay [124]. A spheric domain ($r = 2mm$) is filled with 40,000 neurons, *circa* the real brain's density (40,000 $neurons/mm^3$ [472]). The top 1,000 neurons are excitatory, whereas the bottom 1,000 ones register neuroplasticity [124].

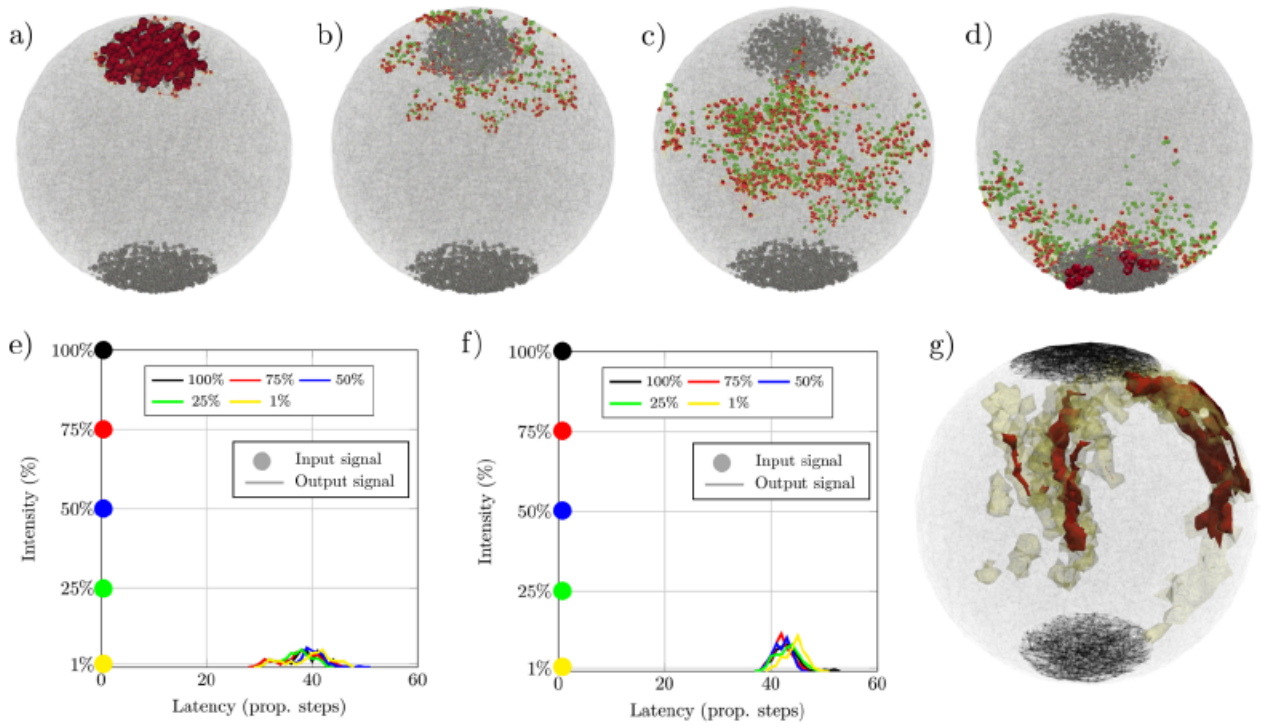

Figure 3.60: Stages in signal propagation (a-d), with "input" and "output" neurons in red, pre-synaptic neurons in green and inner firing neurons in orange. Intensity (fraction of output lit neurons) in (e-f), with inhibitory backpropagation in red (g).

Figure 3.60 shows how different signals within an intensity range excite the neuronal network: 100% of initial stimulation is considered for propagation steps 0 (a), 5 (b), 15 (c) and 35 (d). Red dots are neurons firing at this step and green dots their corresponding pre-synaptic neurons. The signal's peak occurs after 45 propagation steps. Figure 3.60e shows the original network signal outputs under different stimuli, and f its remodeled outputs - meant to have the same amplitude after 45 steps.

Those output curves represent the density of output neurons excited at each step. Figure 3.60g displays the regions with active remodeled neurons. Red regions denote more intense neuroplasticity, while greenish color presents milder events. If a signal propagation step takes 10 ms, its average speed reaches 5 μs - coherent with experimental findings [303].

The preliminary results of Figure 3.60 demonstrate the network's capability to modulate signals and so produce the same output excitation regardless of the intensity of the stimuli, ranging from 1% (i.e. 10 neurons) to 100% of the neurons excited (i.e. 1,000) - see Figure 3.60a-d for the 100% case. In all cases, the output pulse is equal in size and latency under different stimuli.

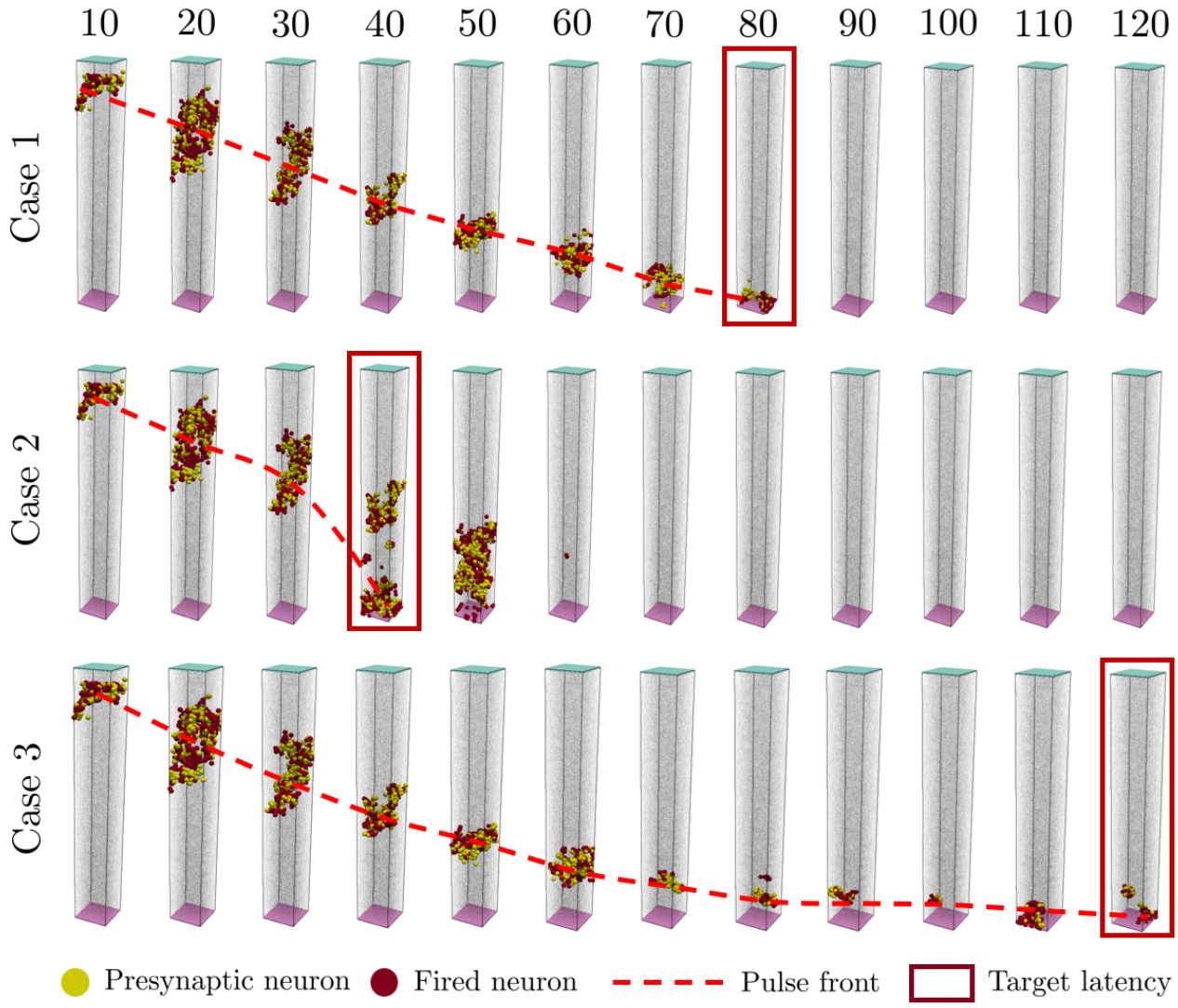

Figure 3.61: Signal progression in different scenarios: reference (Case 1), reduced delay (Case 2) and increased delay (Case 3). Note the reference case's steady propagation rate, unlike the other two.

3.3.2 Adjustable Pulse Latency

Consider a 4x0.5x0.5 mm prism, containing a neural network traversed by a synaptic signal with a reference latency of 80 propagation steps, i.e. an average 0.05mm per propagation step. The speed of the signal in the brain can range from 0.5 to 100m/s. Considering, for example, 10m/s as the reference velocity, each propagation step will be equal to 5 μs, as in the previous study.

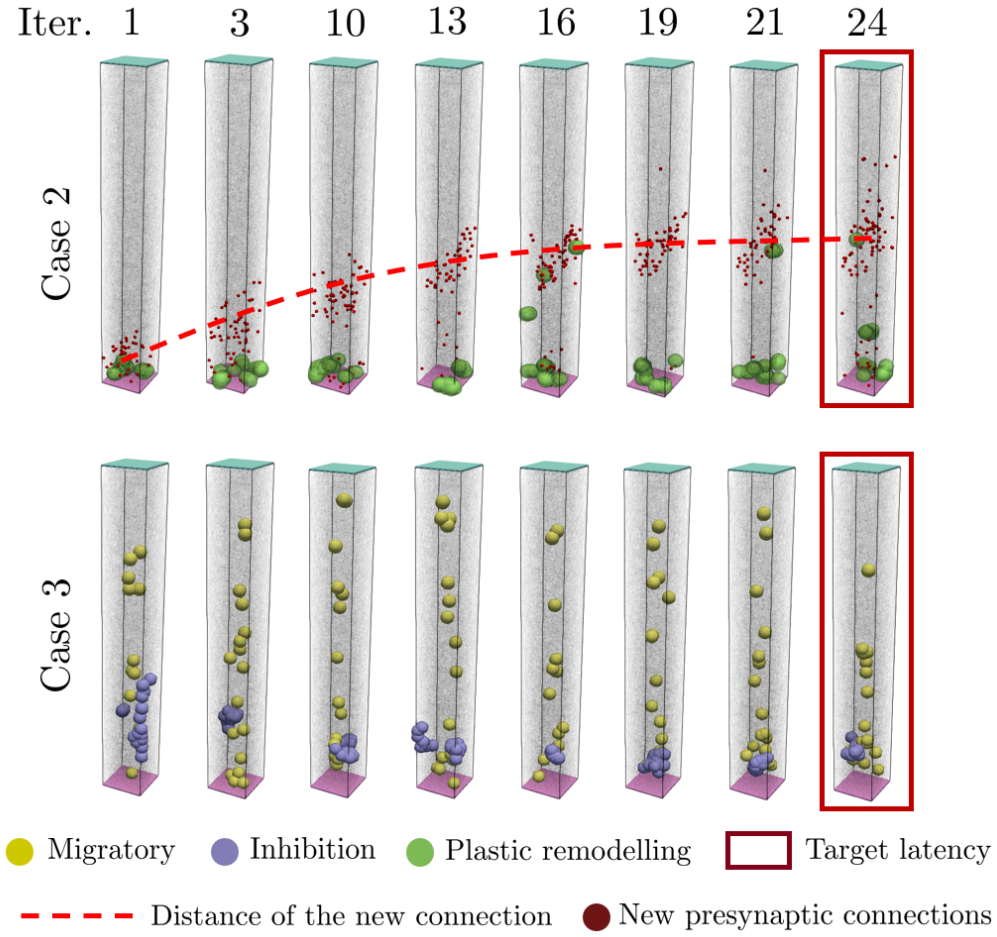

Figure 3.62: Remodeling strategies adopted by the neurons for cases 2 and 3 during progressive iterations to achieve the target latency.

Neuroplasticity shortens the reference pulse delay (Case 1, Figure 3.61 top row) to 40 steps (Case 2, Figure 3.61 middle row) or extends it to 120 (Case 3, Figure 3.61 bottom row). Top squares (light blue) contain neurons excited by the input signal, while bottom ones (light purple) show supervising neurons. After forward-propagation (top to bottom), supervising neurons send backpropagation signals.

The red dashed line in Figure 3.62 denoting the signal's propagation front shows how speed is not uniform, due to migration and neuroplasticity: in Case 2 it is accelerated, whereas Case 3 ends with a reduced pace. In Case 1, this velocity is roughly constant as a consequence of neuron scattering. At propagation step 50, Case 2 shows how the main signal front goes backwards and intercepts other signal fronts, i.e. spurious signals naturally dampened before reaching the output.

The results in Figure 3.61 have been obtained after remodeling. Figure 3.62 shows the changes involved in the inhibition and excitation needed to change the signal's delay in Cases 2 and 3. In Case 2, changes are mainly due to plastic remodeling (variations in synaptic and/or new pre-synaptic connections), increasing the average distance of neighboring neurons and accelerating signal propagation. The neural structure eventually converges to its target latency.

In Case 3, synaptic plastic remodeling does not seem to be sufficient or adequate, so neurons engage in inhibitory or migratory activity to achieve the target latency mandated by supervisor neurons. Some neurons are inhibited to extend the signal's path while others migrate and rewire with their new neighborhood to ensure its continuity (preventing signal blackout).

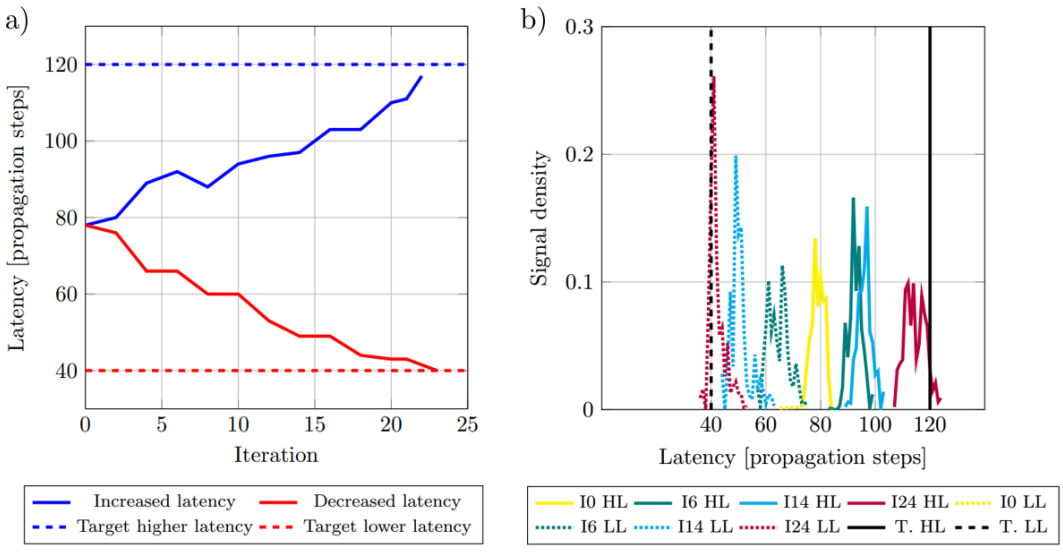

Figure 3.63: Signal output evolution after neuroplasticity. **Left**: Latency of the signal towards the target. **Right**: Received signal density. H (continuous) and L (dashed) stand for higher and lower latency, respectively, T for target and I for iteration.

In quantitative terms, Figure 3.63a shows the evolution of the signal's delay for different remodeling iterations. Figure 3.63b displays the output signal for both the increased and decreased delays. Faster convergence to the decreased latency can be observed because of neuronal migration.

Note how the signal generally tends to showcase higher amplitudes (spikes) for lower latencies, due to the high number (and thus, density) of neurons (migrating or not) involved in shortening the path. This proves that, for two of those prisms in parallel, different uncoordinated stimuli originated in different parts can result in a coordinated pair of signals - i.e. brain metastability - capable of performing logic calculations.

Chapter 4

DISCUSSION

This section aims to ponder results in terms of generalization capability, accuracy/fidelity and computational cost. Again, three subsections will be clearly differentiated: structural description, structural design and optimization and biomedical models; each with their own particularities.

Contenu

In general terms, computational expenses have been low enough to run relatively extensive simulations on a single Intel® Core™ i7-8550U CPU @ 1.80GHz with 16 GB RAM, never taking more than 2h until (user-defined) convergence, or 1 minute per iteration.

The generalization capability of the present surrogates must be evaluated within their respective areas, since standards vary vastly between mechanical and biomedical simulations. Nevertheless, a wide variety of cases have been considered for each study, yielding reasonable solutions. Detailed research strategies have been laid out for more complex implementations that time constraints have unfortunately not allowed to fully develop.

The fidelity of results is satisfactory when compared to state-of-the-art experimental and simulated ground data. Since the whole point of this thesis work has been to recreate real-life phenomena (physical, chemical, biological, etc.) with surrogate models, high accuracy is a crucial feature. All these aspects will now be evaluated in detail, along the models' weaknesses and opportunities.

4.1 Structural Description

Several Machine Learning approaches have been applied to describe the a given structure's mechanical behavior (direct problem). To predict an aperiodic lattice's equivalent Young's modulus $\overline{E_z^{\text{eq}}}$, $\sim 10^5$ parameters were needed to train and test a surrogate model with ($R^2_{\text{test}} = 0.965$). A GNN-based alternative can yield better results (($R^2_{\text{test}} = 0.987$ for pin-jointed trusses) with only $\sim 10^3$ parameters. The model is agnostic to the lattice's number of nodes and elements, increasing versatility [190].

Performance is similar or even better than similar studies [500, 501, 444, 502, 503] presented in Section 3.1, considering this proposal covers aperiodic 3D architectures. Some other comparable options are variational autoencoders [444] ($R^2_{\text{test}} = 0.982$) and CNNs [502] ($R^2_{\text{test}} = 0.971$). A much simpler ML architecture (Random Forest) yielded particularly accurate results when training 6 598 periodic Euler-Bernoulli beams, yielding $R^2_{\text{test}} = 0.9991$ in [504].

Regarding partial observability, it has been proven that, for time-independent models, a model relating only observable outputs to their inputs exists, whose hidden variables are condensed into the observed ones. As soon as the loading in the internal unresolved degrees of freedom does not change, the computed model can be re-used for any other prediction in the observed region.

In the transient case, the model involves the variables' recent history (present and recent past). Applying the Fourier transform in the linear case (far away from the transient regime), such a model remains valid, given the forces applied on the hidden part have the same Fourier transforms.

When operating in the time domain, rNN and LSTM are demonstrably the most natural choices for learning tasks, able to address nonlinear dynamical systems. Regarding time integration, the performances of both neural networks, rNN and LSTM, remain similar and prove that, as expected, the model relating observable inputs and outputs can be learned as soon as history is included in the model construction.

4.2 Structural Design and Optimization

Various inverse problem examples, i.e. trying to define the particular structure(s) yielding a desired behavior or property, have been addressed in Section 3.2. As explained throughout the manuscript, these problems are famously ill-posed and thus computationally complex.

Concerning discrete lattice inverse designs, two different methodologies have been followed to yield (1) a given global equivalent property or (2) a tailored external mechanical response. For the first case, similar inverse problem approaches have been explored via Variational Graph Auto-encoders, yielding $R^2 > 0.999$ [444] albeit with more geometric restrictions and a quite sizable dataset containing 965 736 points, i.e. 10 times larger than the biggest dataset used in the present work.

Aperiodic 2D structures were defined by a Conditional Generative Adversarial Network (CGAN) [500] with MSE under $1 \cdot 10^{-2}$ after 100 epochs, using an equally big data set (100 000 samples). An improved version of that CGAN generalized for 3D structures results in the same MSE after half the epochs (50), considering only 10% of the dataset [503]. Other GAN-powered lightweight optimization inverse processes show greater deviations i.e. RMSE > 0.2 [501].

Regarding continuous inverse design domains, Topology Optimization (mainly SIMP) has been the tool of choice, yielding similarly satisfactory results to state-of-the-art approaches [204, 236, 457, 215], while keeping computational cost minimal (usually around 1 second per iteration). This probabilistic damage-induced compliance penalization (Section 2.2) has reinforced the optimized topologies in several aspects: fatigue, mechanical response, manufacturing technique and von Mises yield criterion. On top of that, manufacturability-oriented filtering and logarithmic interpolation approaches are presented.

This constrained optimization is particularly convenient for the design and improvement of functionally graded materials, e.g. architectured materials - see Section 0.1.2 for further insight. Multiple data-driven methodologies are available for metamaterial design, starting from the continuum [505, 506, 507, 444] or discrete lattices [501, 141]. Their performance is similarly good, but they generally lack the additional flexibility and variability given by the suggested probabilistic framework.

Mechanical metamaterials share some design constraints with macroscopic structures, given by their geometry and loading conditions, namely fatigue [508, 509] - thoroughly examined in additive manufacturing [510, 511, 512, 513, 514], buckling [515, 516] and creep [517, 518]. Since metamaterials already largely consist of void, the TO process should be simpler and faster, guaranteeing light weight. Thus, TO would mostly focus on re-organizing the material layout so as to yield the desired observable macroscopical properties (e.g. auxeticity), guiding their design [519, 520, 236, 432, 521] as a form of inverse homogenization [522, 523].

4.3 Digital Twins for Biomedical Applications

The proposed biomedical digital twin's results reflect a simplified yet sufficiently realistic representation of the brain's information flow considering the low computational cost: it imitates metastability by coordinating one or multiple diverse and out-of-phase input signals into a single output target signal, while enforcing biologically-plausible backpropagation with separate inhibitory and excitatory paths. This is further enhanced by the introduced migration and neuroplasticity functions. Remarkably, this model reaches the target by organically adjusting functional and structural paths, without any explicit optimization parameters nor loss functions.

All needed data is produced by self-made serial code in Python© considering some limitations such as size: the real amount of neurons is estimated to be around 100 billion [338], yet only around 300,000 are modeled to keep an affordable computational cost. Regarding computational times, single-core runs for a full simulation of synpase propagation took approximately 43 seconds. For every adaptation step, 24 iterations were needed.

Some other biological and chemical shortcomings must be noted, having a tangible influence on the brain's functioning - including information flow, around which this proposal revolves. This model is but an attempt to replicate complex brain phenomena - metastability, backpropagation, neuroplasticity and migration - from a mathematical perspective with some simple biological considerations.

Focusing solely on information flow through the network, some limitations become apparent, namely the shortest/longest path problem. On the one hand, moving the target "backwards" in time (fewer propagation steps) is equivalent to organically shortening paths to arrive to the same output. For a negatively-weighted, undirected partially connected graph like this, it can be solved by algorithms like Bellman–Ford's [524], Johnson's [525] or Floyd–Warshall's ([526], with worst-case complexity $\mathbb{O}(V^3)$, being $V = n_0 + n_1 + n_2$ the total number of connected vertices). Obviously, it is unlikely that this network heuristically solves such a problem in a limited amount of steps, although it can be helped through neural migration to a certain extent.

On the other hand, should the target move "forward" in time (more steps), the model would have to artificially extend paths to synchronize the signals, searching for the longest path, i.e. a NP-hard problem, NP-complete for a given target length. Some solutions exist for directed, acyclic graphs [527, 528] (even with perturbations - adding and eliminating edges - [529]), but checking whether a Delaunay-generated graph contains cycles is a NP-complete problem in itself [530, 531].

As a clarifying note, NP-hard problems are those that offering a binary answer (yes/no) whose individual cases - but not general solutions, which may well not exist - can be checked within a polynomial - i.e. finite - time. NP-complete is a subset of NP-hard problems concerning the "translation" of one NP-hard problem into another one in polynomial time - which is still more difficult to prove. Understandably, the emergence of such problems within a model poses severe practical issues, e.g. long computing times.

Migration mitigates these issues to some degree by relocating neurons - albeit a tiny fraction of them (0.05%) for computation time savings - throughout the network and thus organically shortening some paths and enlarging others. To further address this issue, some global (clustering, small-world coefficients) and node-dependent (vulnerability, shortest path) graph parameters could be leveraged to choose the most convenient path - short or long, on demand.

Such indicators would deliver useful information on the topological characteristics of the connectome, so clustered areas - known as "hubs" [532] - could be avoided (shorter paths) or crossed (longer paths). Vulnerability-related indicators can help ponder which alternative paths to follow when certain connections (structural or functional) are damaged or severed; i.e. neuroplasticity. Most of these parameters have already been studied on a brain regional level [438, 441, 442, 440], but not on a neuron level like suggested here.

Chapter 5

CONCLUSIONS

This closing section sums up this manuscript's contributions, the lessons learned and some suggestions for future research.

Contenu

Along this manuscript, two main different fields, i.e. architected materials (including structural description and design) and biomedical modeling, have been addressed under the common umbrella of their dire necessity for surrogate models, considering the expenses of ground-truth experimental data. Such models must capture their characteristics with enough accuracy and generalization capability while keeping the model's complexity (and thus, its computational cost) as low as possible.

Often times, an analytical expression of the phenomena's behavior is too complex or outright impossible to manage due to the observer's bias (choosing an incomplete and/or unmeasurable set of variables) and their complex nature (perhaps not fully captured by the model). To overcome such limitations, some surrogate alternatives have been developed for several practical case studies with various characteristics and needs. In doing so, the effectiveness of these "shortcuts" has been tested.

The variety of numerical examples presented in this manuscript makes global conclusions challenging, since many observations may be only applicable to that specific research field. However, a set of general learned lessons can be drawn:

- Surrogate models must be robust alternatives to recreate complex physical phenomena, especially in the event of costly, scarce and/or incomplete data.
- Data-driven techniques can power these models, yielding high accuracy while incurring in reduced computational cost.
- Particularly, Machine Learning offers a wide range of modeling possibilities with tailored architectures for each data type (temporal/spatial sequences, regression, etc.).
- Many engineering problems can be represented in simple yet conceptually significant formats, such as time sequences, spikes, layered structures or graphs. The latter can convey both topological (relationships with neighboring elements) and physical information (state evolution through message-passing updates).
- A change of paradigm is taking place in many fields of Science where fast, reliable solutions are needed, e.g Engineering. To bypass their inherent challenges, data-driven modeling techniques are clearly taking a forefront position.

Keeping the previous list of general conclusions in mind, they will be disclosed and analyzed for the three main themes addressed throughout this document, the first two of them (structural description and design) revolving around material architectures and the third on biomedical approaches.

5.1 Structural Description

Several non FE-based surrogate models for mechanical characterization of structures were developed for this thesis. One of them aims to fast compute effective mechanical properties in pin-jointed truss or Euler-Bernoulli beam (aperiodic) lattices with varied topologies. Just by scanning a given lattice in three directions to compute its effective areas, and weighing the specimen to obtain its volume, the equivalent Young's modulus can be accurately predicted. The energetically equivalent effective behavior of Young's modulus is computed with the direct stiffness method (DSM), yielding the high-fidelity ground-truth solutions used to fit the ML model.

This study improves previous research [533, 502, 504, 534, 535] by dealing with different mesh/lattice sizes. Two non-intrusive, NN architectures are proposed to predict the equivalent mechanical property: a DNN approach fed with "engineered" features and a GNN model using the structure's geometry and material as inputs. This may be straightforwardly generalized to other mechanical properties such as Poisson's ratio [504] or the homogenized components of the stiffness tensor [189].

The DNN-powered surrogate model slices the structure into n_s portions in the three directions, considering the effective area $A_{i,s}^{\text{eff}}$ per slice s and direction i. It is hypothesized that it similarly to a spring-in-series system, hence the slicing and computation of effective areas.

The GNN-based model leverages the physical meaning of the lattices' adjacencies, represented as graphs in the learning process. Features are embedded in the nodes (coordinates) and edges (coordinates of endpoints and length). The graph updates consist of message-passing layers and posterior convolution, mimicking their nodal force equilibrium. These messages are sent through the elements (trusses, beams), accounting for geometrical (length, cross-sectional area) and material properties (Young's modulus).

Lastly, the pooling layer considers the resultant reaction forces in the nodes required to compute the effective behavior E_z^{eq}. These steps are simple matrix operations - linear except for the activation functions - thus bypassing the classical FE analysis requiring the assembly and inversion (or factorization) of the stiffness matrix to compute the displacements and reaction forces.

These procedures constitute a novel bottom-up methodology i.e. particular to general, from the design of the metamaterial's architecture to the *offline* data-driven description of its properties. It can tackle both periodic and aperiodic layouts by means of several ML techniques, from which GNNs are the most efficient.

Whereas other approaches have opted to directly incorporate mechanical and geometrical variables into their ML model (e.g. angle-bending forces [23]), this method yields accurate mechanical behavior predictions even when just provided with very basic geometrical information, regardless of the topological complexity or the chosen mechanical framework (pin-jointed lattices or beams). Hence, the need for a periodic cell [535] or any hierarchical orthotropic underlinings - e.g. composite fibers [536] - is overcome.

Getting rid of the design limitations derived from the choice of a parametric, symmetric unit cell - complex as it may be [444] -, this study aims to encompass the whole design space, whose variability implies two main advantages. Firstly, the aforementioned localization of mechanical issues - buckling, fatigue, etc, - by ensuring the variability of struts and their respective loading conditions. This reproduces irregular designs found in nature, e.g. biological designs and heterogeneous micro-structures in porous media, addressed by ML techniques for periodic MM cells [502, 537].

Secondly, the possibility to imitate continuous media's (bulk materials) most convenient features (resistance, strength) while limiting their inconveniences (e.g. weight) by fine-tuning aperiodic architectures to make them as dense as possible. This is done without risk of intersection, thanks to Delaunay's tetrahedralisation - while localising void spaces on demand, thus controlling "porosity" and diminishing the infinite contrast phenomenon [35].

Although the whole study is restricted to linear elastic lattice structures of the same material, non-linear and/or inelastic effects can be considered. For instance, path-independent non-linear settings, e.g. hyperelasticity, would require to implement the material's strain energy curve as extra edge features of the graph. Likewise, an approach for path-dependent behavior e.g. plasticity, would require quantifying the loading history, using the internal variables to this end.

An extension for multi-material and/or multi-scale structures is possible, since this architecture can address heterogeneous lattices, i.e. with each member being made of (potentially different) materials. This is of great practical relevance to address the data-driven description of deformable solids, with consequent valuable computational time savings.

As a second surrogate model for behavior prediction, the numerical example for behavior prediction in partial observability settings proved that, for time-independent models, a model linking inputs to outputs exists, in which hidden variables are condensed into the observed ones, valid if the internal loading does not change.

RNN and LSTM are chosen for the learning task, allowing to address non-linear dynamical systems. Their performance is similar to state-of-the-art solutions and prove that, as expected, the model relating observable inputs and outputs can be learned when some of their past values are considered in the model's construction. Future applications include inelastic and path-dependent behaviors where mechanical history needs to be kept.

5.2 Structural Design and Optimization

Once accurate surrogate models for discrete lattice design are obtained, inverse analysis (obtaining structures for a target mechanical behavior) might be performed by evaluating a large number of already generated samples, thus bypassing the computationally expensive step of solving the equilibrium equation. Although simple, it may prove a more convenient and versatile method than existing ones - mostly restricted to either periodic [538, 539] and/or 2D designs [500].

Furthermore, the problem's non-bijectivity allows for multiple lattices behaving similarly, thus leaving room to optimize a second variable, e.g. weight, in the subsequent multi-objective optimization problem - which can be tackled via Pareto optimality [453]. This addresses the multi-scale optimization issue posed in [540] by replacing the macro-to-micro step dependent on empirical laws with the forward-evaluation of the proposed surrogate model.

Regarding TO for continuous inverse designs, some of its most common weaknesses have been addressed: vulnerability to damage, oversizing, unrealistic material layouts due to a poor grasp of uncertainty, etc. An easily-implementable solution based on statistics has been proposed, addressing both uncertainty and damage concerns - via an isotropic stress-based fatigue approach.

The examples shown as results prove the robustness of the presented method when compared to the vanilla configuration [204, 205], providing damage-proof alternatives to traditional deterministic designs. At the same time, the proposed methodology can be combined with multi-objective optimization (multi-axial, uncertain load in modulus, frequency and position). This upgrade greatly eases the inverse design of flexible and damage-ready topologies, without incurring in an excessive computational cost.

By progressively penalizing compliance for each cycle and load, the algorithm can effectively "learn" to expect and react to randomly distributed loads, impacts, vibrations, alternating loads and other eventualities by statistically conveying their structural implications onto the optimization process.

This "learning process" has been proven capable of optimizing topologies under a statistically-predictable set of multi-axial loads, as well as adapting its results for important loading changes and/or previously unseen loads, which can be construed as a "validation" phase. These implications, while partial and perhaps reductionist in some aspects, entail interesting implications to be explored in subsequent settings with varied loading, boundary conditions, materials, etc.

Concerning the optimized design's vulnerability to different material conditions commonly ignored by the traditional TO framework (fatigue, mechanical response, manufacturing techniques, elastic/plastic regions, etc.), several criteria have been proposed to reinforce TO designs by penalizing compliance accordingly. This effectively shapes material distribution according to the desired response without incurring in excessive additional computation power either. The proposed criteria's versatility is tested under several boundary conditions, in an individual and combined manner, evaluating its purposes computationally and experimentally with satisfactory results.

Other shape and mechanical issues affect most common topological optimization schemes, namely capillary struts which, although mathematically correct (following the minimization process), do not efficiently distribute neither material nor mechanical loading (strain/stress). This makes them prone to stress concentration and thus vulnerable to fracture, among other problems; besides being difficult to manufacture depending on the chosen technique. Two approaches have been offered as ways to alleviate such drawbacks.

The first one consists of a simple filter which effectively eliminates useless thin ribs while redistributing an equal or even smaller volume more wisely, thus improving mechanical performance. In contrast to most common high-pass density filters smearing out material contours [522], this method creates the opposite effect, defining clear void-material limits.

The second proposal consists of an analytical expression linking the two main design variables in the SIMP method (compliance and volume fraction) in an experimentally-consistent manner which in turn yields different "families" evolving in shape and topology. Importantly, these two ingredients can be combined and allow for interpolation (even ML-assisted), as seen in various examples.

These tools create a versatile design space with adjustable compliance c, volume v and minimum thickness r - i.e., multi-objective optimization for 3 target variables within reasonable computational cost. This allows for simultaneous shape-topological optimization with tuneable rib width.

Future developments include a full 3D generalization (already partially implemented, see Section 3.2) and the amalgamation of probabilistic, damage-based approaches and filter-enhanced interpolation (not only between compliance and volume but also considering stress constraints). Stress-based optimization schemes, along with heuristic approaches such as Evolutionary Structural Optimization (ESO) can be explored. Other damage criteria can be considered, e.g. anti-buckling/creep/fracture, as well as more elaborate finite element frameworks, including non-linear phenomena (contact, viscoelasticity, viscoplasticity, hyperelasticity), tackled by the Method of Moving Asymptotes (MMA) [541].

5.3 Digital Twins for Biomedical Applications

In this work, some aspects of modeling brain plasticity have been addressed. Neuroplasticity implies both logical (pre-synaptic connections and signal processing strengths) and biophysical considerations (cell migration, community behavior, inhibition and excitation, among others). Synapses are considered an instantaneous, purely electrical process.

The present model is also capable of reproducing the Boolean logic behavior of neuronal communities. This is achieved through the biological rules for interaction, considering neurons as cells able to perform synaptic connections in order to transfer information through signaling. This is validated by the two given examples where the latency of a signal through a neuronal community is delayed or increased.

The results are promising since they illustrate how computationally affordable simulations can somewhat convey complex brain phenomena - albeit with vast simplifications - and motivate further research to better understand changes in brain processing, like those related to aging, illness and/or injuries - soon to be explored in future updates of this work.

Quantitative verification, for the time being, remains difficult due to the scarcity and opaqueness of such experimental tests, although agent-based modeling of functional brain connectivity appears to be a hot research topic [411, 410], also in combination with Machine Learning techniques [542].

This model's flexibility and fidelity for the low incurred computational cost is relevant to one of computational neuroscience's biggest issues, besides the already mentioned reproducibility problem. Computationally affordable simulations like this are vital for the spread of medical monitoring of the brain to every corner of the world, especially in low-income countries where cheap alternatives to costly and unavailable equipment are most needed.

This proposition is in its initial stages and so it is relatively simple, but its limited computational cost can prove an advantage when means are scarce - i.e. emergency situations and/or unavailability of instrumentation. New upcoming developments will strive for a more precise portrayal of the brain in multiple scales, both in time and space, incorporating brain damage so it can be used by physicians for preventive diagnosis, follow-up and personalized treatment of brain illnesses and injuries. An emphasis on preventive monitoring and more accurate diagnoses is ubiquitous in engineering, materialized by so-called digital/hybrid twins [12].

This is an ambitious and complex objective, which may take time to fully develop. For now, the improvement of existing methodologies through these modern tools and the completeness of the theoretical neuroscientific framework - perhaps with these very tools - constitutes a reachable and valued mission for patients.

Rules to shorten or enlarge neural pathways could be introduced, although biological evidence for such a behavior remains elusive. Time constraints, such as refractory periods [317] replicating membrane functioning, could substitute propagation steps (quasi-static). For this model, axon/dendrite lengths are ignored (instantaneous signal transmission), so the only meaningful way to shorten (or extend) neural paths is artificially skipping (or adding) synapses along the way.

A graph-based approach would entail two self-evident ramifications for brain networks: multi-scalarity - in both time [543] and space [294] - and the involvement of Graph Neural Networks [61, 63, 43, 66, 65] or similar ML techniques [64, 67] - notwithstanding the aforementioned simplifications and caveats.

The next significant step is the development of a bio-mechanical model of the brain capturing the interaction between information transmission and external loads or accelerations (leading to Traumatic Brain Injury), loss or damage of axons (neurodegenerative diseases) or even areas with distinct properties (tumor growth, brain stiffening caused by Alzheimer's).

There is a plethora of bibliography proposing bio-mechanical models [372, 370, 544, 390, 545, 369, 546, 547, 393, 383], but the correlation between physical damage and information flow leaves room for research. Also, the model itself could be enriched by including and emphasizing the role of other parts of the neuron (like the myelin sheath) or another components of the CNS, such as glial cells [548].

Bibliography

[1] V. Champaney *et al.*, "Modeling systems from partial observations," *Frontiers in Materials*, vol. 9, 2022. [Online]. Available: https://doi.org/10.3389/fmats.2022.970970

[2] H. Gray, *Anatomy: Descriptive and Surgical, Anatomy of the Human Body*. John William Parker, 1858.

[3] M. Glickstein, "Golgi and cajal: The neuron doctrine and the 100th anniversary of the 1906 nobel prize," *Current Biology*, vol. 16, no. 5, p. R147–R151, Mar. 2006. [Online]. Available: http://dx.doi.org/10.1016/j.cub.2006.02.053

[4] G. Capasso *et al.*, "Stress-based topology optimization of compliant mechanisms using nonlinear mechanics," *Mechanics and Industry*, vol. 21, no. 3, p. 304, 2020. [Online]. Available: http://dx.doi.org/10.1051/meca/2020011

[5] C. Khosla and B. S. Saini, "Enhancing performance of deep learning models with different data augmentation techniques: A survey," in *2020 International Conference on Intelligent Engineering and Management (ICIEM)*. IEEE, Jun. 2020. [Online]. Available: http://dx.doi.org/10.1109/ICIEM48762.2020.9160048

[6] C. Guilhaumon *et al.*, "Data augmentation for regression machine learning problems in high dimensions," *Computation*, vol. 12, no. 2, p. 24, Feb. 2024. [Online]. Available: http://dx.doi.org/10.3390/computation12020024

[7] F. Chinesta, P. Ladeveze, and E. Cueto, "A short review on model order reduction based on proper generalized decomposition," *Archives of Computational Methods in Engineering*, vol. 18, no. 4, pp. 395–404, Oct. 2011. [Online]. Available: https://doi.org/10.1007/s11831-011-9064-7

[8] F. Chinesta, R. Keunings, and A. Leygue, *The Proper Generalized Decomposition for Advanced Numerical Simulations: A Primer*. Springer International Publishing, 2014. [Online]. Available: http://dx.doi.org/10.1007/978-3-319-02865-1

[9] E. J. Tuegel *et al.*, "Reengineering aircraft structural life prediction using a digital twin," *International Journal of Aerospace Engineering*, vol. 2011, pp. 1–14, 2011. [Online]. Available: https://doi.org/10.1155/2011/154798

[10] B. Moya *et al.*, "Digital twins that learn and correct themselves," *International Journal for Numerical Methods in Engineering*, vol. 123, no. 13, pp. 3034–3044, Sep. 2020. [Online]. Available: https://doi.org/10.1002/nme.6535

[11] A. Sancarlos *et al.*, "Learning stable reduced-order models for hybrid twins," *Data-Centric Engineering*, vol. 2, 2021. [Online]. Available: https://doi.org/10.1017/dce.2021.16

[12] F. Chinesta *et al.*, "Virtual, digital and hybrid twins: A new paradigm in data-based engineering and engineered data," *Archives of Computational Methods in Engineering*, vol. 27, no. 1, pp. 105–134, Nov. 2018. [Online]. Available: https://doi.org/10.1007/s11831-018-9301-4

[13] ——, "PGD-based computational vademecum for efficient design, optimization and control," *Archives of Computational Methods in Engineering*, vol. 20, no. 1, pp. 31–59, Jan. 2013. [Online]. Available: https://doi.org/10.1007/s11831-013-9080-x

[14] R. Ibáñez *et al.*, "A multidimensional data-driven sparse identification technique: The sparse proper generalized decomposition," *Complexity*, vol. 2018, pp. 1–11, Nov. 2018. [Online]. Available: https://doi.org/10.1155/2018/5608286

[15] Y. Lecun *et al.*, "Gradient-based learning applied to document recognition," *Proceedings of the IEEE*, vol. 86, no. 11, p. 2278–2324, 1998. [Online]. Available: http://dx.doi.org/10.1109/5.726791

[16] F. Scarselli *et al.*, "The graph neural network model," *IEEE Transactions on Neural Networks*, vol. 20, no. 1, pp. 61–80, Jan. 2009. [Online]. Available: https://doi.org/10.1109/tnn.2008.2005605

[17] G.-B. Zhou *et al.*, "Minimal gated unit for recurrent neural networks," *International Journal of Automation and Computing*, vol. 13, no. 3, pp. 226–234, Jun. 2016. [Online]. Available: https://doi.org/10.1007/s11633-016-1006-2

[18] A. Sherstinsky, "Fundamentals of recurrent neural network (rnn) and long short-term memory (lstm) network," *Physica D: Nonlinear Phenomena*, vol. 404, p. 132306, Mar. 2020. [Online]. Available: http://dx.doi.org/10.1016/j.physd.2019.132306

[19] S. Hochreiter and J. Schmidhuber, "Long short-term memory," *Neural Computation*, vol. 9, no. 8, p. 1735–1780, Nov. 1997. [Online]. Available: http://dx.doi.org/10.1162/neco.1997.9.8.1735

[20] M. M. Bronstein *et al.*, "Geometric deep learning: Grids, groups, graphs, geodesics, and gauges," 2021. [Online]. Available: https://arxiv.org/abs/2104.13478

[21] V. G. Veselago, "The electrodynamics of substances with simultaneously negative values of ϵ and μ," *Soviet Physics Uspekhi*, vol. 10, no. 4, p. 509–514, Apr. 1968. [Online]. Available: http://dx.doi.org/10.1070/PU1968v010n04ABEH003699

[22] R. Lakes, "Foam structures with a negative poisson's ratio," *Science*, vol. 235, no. 4792, p. 1038–1040, Feb. 1987. [Online]. Available: http://dx.doi.org/10.1126/science.235.4792.1038

[23] D. R. Reid *et al.*, "Auxetic metamaterials from disordered networks," *Proceedings of the National Academy of Sciences*, vol. 115, no. 7, Jan. 2018. [Online]. Available: http://dx.doi.org/10.1073/pnas.1717442115

[24] H. Wang, S. Xiao, and J. Wang, "Disordered auxetic metamaterials architected by random peanut-shaped perturbations," *Materials and Design*, vol. 212, p. 110291, Dec. 2021. [Online]. Available: http://dx.doi.org/10.1016/j.matdes.2021.110291

[25] J. Pendry *et al.*, "Magnetism from conductors and enhanced nonlinear phenomena," *IEEE Transactions on Microwave Theory and Techniques*, vol. 47, no. 11, p. 2075–2084, 1999. [Online]. Available: http://dx.doi.org/10.1109/22.798002

[26] D. R. Smith *et al.*, "Composite medium with simultaneously negative permeability and permittivity," *Physical Review Letters*, vol. 84, no. 18, p. 4184–4187, May 2000. [Online]. Available: http://dx.doi.org/10.1103/PhysRevLett.84.4184

[27] J. Fan *et al.*, "A review of additive manufacturing of metamaterials and developing trends," *Materials Today*, vol. 50, p. 303–328, Nov. 2021. [Online]. Available: http://dx.doi.org/10.1016/j.mattod.2021.04.019

[28] W. Prager and G. Rozvany, *OPTIMIZATION OF STRUCTURAL GEOMETRY*. Elsevier, 1977, p. 265–293. [Online]. Available: http://dx.doi.org/10.1016/B978-0-12-083750-2.50023-0

[29] M. P. Bendsøe and N. Kikuchi, "Generating optimal topologies in structural design using a homogenization method," *Computer Methods in Applied Mechanics and Engineering*, vol. 71, no. 2, pp. 197–224, Nov. 1988. [Online]. Available: https://doi.org/10.1016/0045-7825(88)90086-2

[30] M. Naebe and K. Shirvanimoghaddam, "Functionally graded materials: A review of fabrication and properties," *Applied Materials Today*, vol. 5, p. 223–245, Dec. 2016. [Online]. Available: http://dx.doi.org/10.1016/j.apmt.2016.10.001

[31] Y. Li *et al.*, "A review on functionally graded materials and structures via additive manufacturing: From multi-scale design to versatile functional properties," *Advanced Materials Technologies*, vol. 5, no. 6, Apr. 2020. [Online]. Available: http://dx.doi.org/10.1002/admt.201900981

[32] X. Zheng *et al.*, "Multiscale metallic metamaterials," *Nature Materials*, vol. 15, no. 10, p. 1100–1106, Jul. 2016. [Online]. Available: http://dx.doi.org/10.1038/nmat4694

[33] B. Hassani and E. Hinton, "A review of homogenization and topology optimization i—homogenization theory for media with periodic structure," *Computers and Structures*, vol. 69, no. 6, p. 707–717, Dec. 1998. [Online]. Available: http://dx.doi.org/10.1016/S0045-7949(98)00131-X

[34] ——, "A review of homogenization and topology opimization ii—analytical and numerical solution of homogenization equations," *Computers and Structures*, vol. 69, no. 6, p. 719–738, Dec. 1998. [Online]. Available: http://dx.doi.org/10.1016/S0045-7949(98)00132-1

[35] H. Danesh, T. Brepols, and S. Reese, "Challenges in two-scale computational homogenization of mechanical metamaterials," *PAMM*, vol. 23, no. 1, p. e202200139, 2023.

[36] Z. Padamsey and N. L. Rochefort, "Paying the brain's energy bill," *Current Opinion in Neurobiology*, vol. 78, p. 102668, Feb. 2023. [Online]. Available: https://doi.org/10.1016/j.conb.2022.102668

[37] H. Ritchie, F. Spooner, and M. Roser, "Causes of death," *Our World in Data*, 2018, https://ourworldindata.org/causes-of-death.

[38] P. A. McKinney, "Brain tumours: incidence, survival, and aetiology," *Journal of Neurology, Neurosurgery and Psychiatry*, vol. 75, no. suppl_2, pp. ii12–ii17, Jun. 2004. [Online]. Available: https://doi.org/10.1136/jnnp.2004.040741

[39] K. D. Miller *et al.*, "Brain and other central nervous system tumor statistics, 2021," *CA: A Cancer Journal for Clinicians*, vol. 71, no. 5, pp. 381–406, Aug. 2021. [Online]. Available: https://doi.org/10.3322/caac.21693

[40] C. Mattiuzzi and G. Lippi, "Current cancer epidemiology," *Journal of Epidemiology and Global Health*, vol. 9, no. 4, p. 217, 2019. [Online]. Available: https://doi.org/10.2991/jegh.k.191008.001

[41] V. L. Feigin and multiple collaborators, "Global, regional, and national burden of neurological disorders, 1990-2016: a systematic analysis for the global burden of disease study 2016," *The Lancet Neurology*, vol. 18, no. 5, pp. 459–480, May 2019. [Online]. Available: https://doi.org/10.1016/s1474-4422(18)30499-x

[42] R. L. Pfeiffer *et al.*, "A pathoconnectome of early neurodegeneration: Network changes in retinal degeneration," *Experimental Eye Research*, vol. 199, p. 108196, Oct. 2020. [Online]. Available: https://doi.org/10.1016/j.exer.2020.108196

[43] W. Liu *et al.*, "Exploring oscillatory dysconnectivity networks in major depression during resting state using coupled tensor decomposition," *IEEE Transactions on Biomedical Engineering*, vol. 69, no. 8, pp. 2691–2700, Aug. 2022. [Online]. Available: https://doi.org/10.1109/tbme.2022.3152413

[44] M. Rubinov and E. Bullmore, "Fledgling pathoconnectomics of psychiatric disorders," *Trends in Cognitive Sciences*, vol. 17, no. 12, pp. 641–647, Dec. 2013. [Online]. Available: https://doi.org/10.1016/j.tics.2013.10.007

[45] J. Chojdak-Łukasiewicz *et al.*, "Cerebral small vessel disease: A review," *Advances in Clinical and Experimental Medicine*, vol. 30, no. 3, pp. 349–356, Mar. 2021. [Online]. Available: http://dx.doi.org/10.17219/acem/131216

[46] A. K. Dey *et al.*, "Pathoconnectomics of cognitive impairment in small vessel disease: A systematic review," *Alzheimer's and Dementia*, vol. 12, no. 7, pp. 831–845, Feb. 2016. [Online]. Available: https://doi.org/10.1016/j.jalz.2016.01.007

[47] J. Olesen *et al.*, "The economic cost of brain disorders in europe," *European Journal of Neurology*, vol. 19, no. 1, pp. 155–162, Dec. 2011. [Online]. Available: https://doi.org/10.1111/j.1468-1331.2011.03590.x

[48] M. DiLuca and J. Olesen, "The cost of brain diseases: A burden or a challenge?" *Neuron*, vol. 82, no. 6, pp. 1205–1208, Jun. 2014. [Online]. Available: https://doi.org/10.1016/j.neuron.2014.05.044

[49] O. Parés-Badell *et al.*, "Cost of disorders of the brain in spain," *PLoS ONE*, vol. 9, no. 8, p. e105471, Aug. 2014. [Online]. Available: https://doi.org/10.1371/journal.pone.0105471

[50] R. D. Pino *et al.*, "Costs and effects of telerehabilitation in neurological and cardiological diseases: A systematic review," *Frontiers in Medicine*, vol. 9, Nov. 2022. [Online]. Available: https://doi.org/10.3389/fmed.2022.832229

[51] S. J. Faruqi *et al.*, "Cost of investigating neurological disease: Experience of a tertiary care center in karachi, pakistan," *Cureus*, Jul. 2020. [Online]. Available: https://doi.org/10.7759/cureus.9291

[52] V. L. Feigin and multiple collaborators, "Global, regional, and national burden of neurological disorders during 1990-2015: a systematic analysis for the global burden of disease study 2015," *The Lancet Neurology*, vol. 16, no. 11, pp. 877–897, Nov. 2017. [Online]. Available: https://doi.org/10.1016/s1474-4422(17)30299-5

[53] E. B. Falk *et al.*, "What is a representative brain? neuroscience meets population science," *Proceedings of the National Academy of Sciences*, vol. 110, no. 44, pp. 17 615–17 622, Oct. 2013. [Online]. Available: https://doi.org/10.1073/pnas.1310134110

[54] V. M. Dotson and A. Duarte, "The importance of diversity in cognitive neuroscience," *Annals of the New York Academy of Sciences*, vol. 1464, no. 1, pp. 181–191, Oct. 2019. [Online]. Available: https://doi.org/10.1111/nyas.14268

[55] K. H. Green *et al.*, "A perspective on enhancing representative samples in developmental human neuroscience: Connecting science to society," *Frontiers in Integrative Neuroscience*, vol. 16, Sep. 2022. [Online]. Available: https://doi.org/10.3389/fnint.2022.981657

[56] S. Siuly and Y. Zhang, "Medical big data: Neurological diseases diagnosis through medical data analysis," *Data Science and Engineering*, vol. 1, no. 2, pp. 54–64, Jun. 2016. [Online]. Available: https://doi.org/10.1007/s41019-016-0011-3

[57] S. G. Alonso *et al.*, "Data mining algorithms and techniques in mental health: A systematic review," *Journal of Medical Systems*, vol. 42, no. 9, Jul. 2018. [Online]. Available: https://doi.org/10.1007/s10916-018-1018-2

[58] L. Dipietro *et al.*, "The evolution of big data in neuroscience and neurology," *Journal of Big Data*, vol. 10, no. 1, Jul. 2023. [Online]. Available: https://doi.org/10.1186/s40537-023-00751-2

[59] R. Li, "Data mining and machine learning methods for dementia research," in *Biomarkers for Alzheimer's Disease Drug Development*. Springer New York, 2018, pp. 363–370. [Online]. Available: https://doi.org/10.1007/978-1-4939-7704-8_25

[60] B. Baniya *et al.*, "Neurodegenerative alzheimer's disease disorders and deep learning approaches," in *Data Analysis for Neurodegenerative Disorders*. Springer Nature Singapore, 2023, pp. 49–66. [Online]. Available: https://doi.org/10.1007/978-981-99-2154-6_3

[61] K. M. Eschenburg, T. J. Grabowski, and D. R. Haynor, "Learning cortical parcellations using graph neural networks," *Frontiers in Neuroscience*, vol. 15, Dec. 2021. [Online]. Available: https://doi.org/10.3389/fnins.2021.797500

[62] F. Liu *et al.*, "Editorial: Graph learning for brain imaging," *Frontiers in Neuroscience*, vol. 16, Aug. 2022. [Online]. Available: https://doi.org/10.3389/fnins.2022.1001818

[63] W. Qiu *et al.*, "Unrevealing reliable cortical parcellation of individual brains using resting-state functional magnetic resonance imaging and masked graph convolutions," *Frontiers in Neuroscience*, vol. 16, Mar. 2022. [Online]. Available: https://doi.org/10.3389/fnins.2022.838347

[64] X. Y. Zhang *et al.*, "A novel auxetic metamaterial with enhanced mechanical properties and tunable auxeticity," *Thin-Walled Structures*, vol. 174, p. 109162, May 2022. [Online]. Available: https://doi.org/10.1016/j.tws.2022.109162

[65] M. C. Kurucu and I. Rekik, "Graph neural network based unsupervised influential sample selection for brain multigraph population fusion," *Computerized Medical Imaging and Graphics*, vol. 108, p. 102274, Sep. 2023. [Online]. Available: https://doi.org/10.1016/j.compmedimag.2023.102274

[66] A. Bessadok, M. A. Mahjoub, and I. Rekik, "Graph neural networks in network neuroscience," *IEEE Transactions on Pattern Analysis and Machine Intelligence*, vol. 45, no. 5, pp. 5833–5848, May 2023. [Online]. Available: https://doi.org/10.1109/tpami.2022.3209686

[67] E. Najarro, S. Sudhakaran, and S. Risi, "Towards self-assembling artificial neural networks through neural developmental programs," 2023. [Online]. Available: https://arxiv.org/abs/2307.08197

[68] H. Makram, "Seven challenges for neuroscience," *Functional Neurology*, vol. 28, pp. 145–151, Jul. 2013. [Online]. Available: https://www.ncbi.nlm.nih.gov/pmc/articles/PMC3812747/

[69] H. Akil, M. E. Martone, and D. C. Van Essen, "Challenges and opportunities in mining neuroscience data," *Science*, vol. 331, no. 6018, pp. 708–712, Feb. 2011. [Online]. Available: http://dx.doi.org/10.1126/science.1199305

[70] R. Alizadeh, J. K. Allen, and F. Mistree, "Managing computational complexity using surrogate models: a critical review," *Research in Engineering Design*, vol. 31, no. 3, p. 275–298, Apr. 2020. [Online]. Available: http://dx.doi.org/10.1007/s00163-020-00336-7

[71] F. Chinesta *et al.*, "Model reduction methods," p. 1–36, Dec. 2017. [Online]. Available: http://dx.doi.org/10.1002/9781119176817.ecm2110

[72] J. L. Lumley, "The structure of inhomogeneous turbulent flows," *Atmospheric Turbulence and Radio Wave Propagation*, pp. 166–178, 1967.

[73] J. Weiss, "A tutorial on the proper orthogonal decomposition," in *AIAA Aviation 2019 Forum*. American Institute of Aeronautics and Astronautics, Jun. 2019. [Online]. Available: http://dx.doi.org/10.2514/6.2019-3333

[74] K. Pearson, "Liii. on lines and planes of closest fit to systems of points in space," *The London, Edinburgh, and Dublin Philosophical Magazine and Journal of Science*, vol. 2, no. 11, p. 559–572, Nov. 1901. [Online]. Available: http://dx.doi.org/10.1080/14786440109462720

[75] H. Hotelling, "Analysis of a complex of statistical variables into principal components." *Journal of Educational Psychology*, vol. 24, no. 6, p. 417–441, Sep. 1933. [Online]. Available: http://dx.doi.org/10.1037/h0071325

[76] I. T. Jolliffe and J. Cadima, "Principal component analysis: a review and recent developments," *Philosophical Transactions of the Royal Society A: Mathematical, Physical and Engineering Sciences*, vol. 374, no. 2065, p. 20150202, Apr. 2016. [Online]. Available: http://dx.doi.org/10.1098/rsta.2015.0202

[77] B. Schölkopf, A. Smola, and K.-R. Müller, *Kernel principal component analysis*. Springer Berlin Heidelberg, 1997, p. 583–588. [Online]. Available: http://dx.doi.org/10.1007/BFb0020217

[78] ——, "Nonlinear component analysis as a kernel eigenvalue problem," *Neural Computation*, vol. 10, no. 5, p. 1299–1319, Jul. 1998. [Online]. Available: http://dx.doi.org/10.1162/089976698300017467

[79] S. T. Roweis and L. K. Saul, "Nonlinear dimensionality reduction by locally linear embedding," *Science*, vol. 290, no. 5500, p. 2323–2326, Dec. 2000. [Online]. Available: http://dx.doi.org/10.1126/science.290.5500.2323

[80] E. Fix and J. L. Hodges, "Discriminatory analysis. nonparametric discrimination: Consistency properties," *International Statistical Review / Revue Internationale de Statistique*, vol. 57, no. 3, p. 238, Dec. 1989. [Online]. Available: http://dx.doi.org/10.2307/1403797

[81] F. J. Montáns, E. Cueto, and K.-J. Bathe, *Machine Learning in Computer Aided Engineering.* Springer International Publishing, 2023, p. 1–83. [Online]. Available: http://dx.doi.org/10.1007/978-3-031-36644-4_1

[82] R. Ibañez *et al.*, "A manifold learning approach to data-driven computational elasticity and inelasticity," *Archives of Computational Methods in Engineering*, vol. 25, no. 1, p. 47–57, Oct. 2016. [Online]. Available: http://dx.doi.org/10.1007/s11831-016-9197-9

[83] J. V. Aguado *et al.*, "New trends in computational mechanics: Model order reduction, manifold learning and data-driven," p. 239–266, Nov. 2017. [Online]. Available: http://dx.doi.org/10.1002/9781119476757.ch9

[84] S. L. Brunton and J. N. Kutz, *Data-Driven Science and Engineering: Machine Learning, Dynamical Systems, and Control.* Cambridge University Press, 2019.

[85] Z. Liu and M. Tegmark, "Machine learning conservation laws from trajectories," *Phys. Rev. Lett.*, vol. 126, p. 180604, May 2021. [Online]. Available: https://link.aps.org/doi/10.1103/PhysRevLett.126.180604

[86] K. Lee and K. T. Carlberg, "Model reduction of dynamical systems on nonlinear manifolds using deep convolutional autoencoders," *Journal of Computational Physics*, vol. 404, p. 108973, 2020. [Online]. Available: https://www.sciencedirect.com/science/article/pii/S0021999119306783

[87] W. S. McCulloch and W. Pitts, "A logical calculus of the ideas immanent in nervous activity," *The Bulletin of Mathematical Biophysics*, vol. 5, no. 4, p. 115–133, Dec. 1943. [Online]. Available: http://dx.doi.org/10.1007/BF02478259

[88] J. McCarthy *et al.*, "A proposal for the dartmouth summer research project on artificial intelligence," in *AI Magazine*, 1956. [Online]. Available: https://ojs.aaai.org/aimagazine/index.php/aimagazine/article/view/1904

[89] D. E. Rumelhart, G. E. Hinton, and R. J. Williams, "Learning representations by back-propagating errors," *Nature*, vol. 323, no. 6088, p. 533–536, Oct. 1986. [Online]. Available: http://dx.doi.org/10.1038/323533a0

[90] K. Hornik, M. Stinchcombe, and H. White, "Multilayer feedforward networks are universal approximators," *Neural Networks*, vol. 2, no. 5, p. 359–366, Jan. 1989. [Online]. Available: http://dx.doi.org/10.1016/0893-6080(89)90020-8

[91] H. Robbins and S. Monro, "A stochastic approximation method," *The Annals of Mathematical Statistics*, vol. 22, no. 3, p. 400–407, Sep. 1951. [Online]. Available: http://dx.doi.org/10.1214/aoms/1177729586

[92] T. Dozat, "Incorporating nesterov momentum into adam," in *Proceedings of the 4th International Conference on Learning Representations, Workshop Track, San Juan, Puerto Rico, 2-4 May 2016, 1-4*, May 2016, pp. 1–4.

[93] R. J. Williams and D. Zipser, *Back-propagation: Theory, Architectures and Applications.* Hillsdale, NJ: Erlbaum, 1992, ch. 13: Gradient-based learning algorithms for recurrent networks and their computational complexity.

[94] G.-B. Zhou *et al.*, "Minimal gated unit for recurrent neural networks," *International Journal of Automation and Computing*, vol. 13, no. 3, pp. 226–234, Jun 2016. [Online]. Available: https://doi.org/10.1007/s11633-016-1006-2

[95] L. Benabou, "Development of lstm networks for predicting viscoplasticity with effects of deformation, strain rate, and temperature history," *Journal of Applied Mechanics*, vol. 88, no. 7, p. 071008, 2021.

[96] H. Luo, M. Huang, and Z. Zhou, "Integration of multi-gaussian fitting and lstm neural networks for health monitoring of an automotive suspension component," *Journal of Sound and Vibration*, vol. 428, pp. 87–103, 2018.

[97] P. Pillai *et al.*, "Leveraging long short-term memory (lstm)-based neural networks for modeling structure–property relationships of metamaterials from electromagnetic responses," *Scientific Reports*, vol. 11, no. 1, Sep. 2021. [Online]. Available: http://dx.doi.org/10.1038/s41598-021-97999-6

[98] C. Goller and A. Kuchler, "Learning task-dependent distributed representations by backpropagation through structure," in *Proceedings of International Conference on Neural Networks (ICNN'96)*, ser. ICNN-96, vol. 1. IEEE, 1996, p. 347–352. [Online]. Available: http://dx.doi.org/10.1109/ICNN.1996.548916

[99] J. Gilmer *et al.*, "Neural message passing for quantum chemistry," in *Proceedings of the 34th International Conference on Machine Learning*, ser. Proceedings of Machine Learning Research, D. Precup and Y. W. Teh, Eds., vol. 70. PMLR, 06–11 Aug 2017, pp. 1263–1272. [Online]. Available: https://proceedings.mlr.press/v70/gilmer17a.html

[100] Q. Hernández *et al.*, "Thermodynamics-informed graph neural networks," *IEEE Transactions on Artificial Intelligence*, vol. 5, no. 3, p. 967–976, Mar. 2024. [Online]. Available: http://dx.doi.org/10.1109/TAI.2022.3179681

[101] T. N. Kipf and M. Welling, "Semi-supervised classification with graph convolutional networks," 2016. [Online]. Available: https://arxiv.org/abs/1609.02907

[102] P. Veličković *et al.*, "Graph attention networks," 2018. [Online]. Available: https://www.repository.cam.ac.uk/handle/1810/301348

[103] I. Ben-Yelun *et al.*, "On the data-driven description of lattice materials mechanics," *Results in Engineering*, vol. 22, p. 102235, Jun. 2024. [Online]. Available: http://dx.doi.org/10.1016/j.rineng.2024.102235

[104] Z. Ye *et al.*, "A comprehensive survey of graph neural networks for knowledge graphs," *IEEE Access*, vol. 10, p. 75729–75741, 2022. [Online]. Available: http://dx.doi.org/10.1109/ACCESS.2022.3191784

[105] W. Fan *et al.*, "Graph neural networks for social recommendation," in *The World Wide Web Conference*, ser. WWW '19. ACM, May 2019. [Online]. Available: http://dx.doi.org/10.1145/3308558.3313488

[106] S. Wein *et al.*, "A graph neural network framework for causal inference in brain networks," *Scientific Reports*, vol. 11, no. 1, Apr. 2021. [Online]. Available: http://dx.doi.org/10.1038/s41598-021-87411-8

[107] F. Parisi *et al.*, "On the use of mechanics-informed models to structural engineering systems: Application of graph neural networks for structural analysis," *Structures*, vol. 59, p. 105712, Jan. 2024. [Online]. Available: http://dx.doi.org/10.1016/j.istruc.2023.105712

[108] Z. Wu *et al.*, "A comprehensive survey on graph neural networks," *IEEE Transactions on Neural Networks and Learning Systems*, vol. 32, no. 1, p. 4–24, Jan. 2021. [Online]. Available: http://dx.doi.org/10.1109/TNNLS.2020.2978386

[109] J. Zhou *et al.*, "Graph neural networks: A review of methods and applications," *AI Open*, vol. 1, p. 57–81, 2020. [Online]. Available: http://dx.doi.org/10.1016/j.aiopen.2021.01.001

[110] B. P. Chamberlain *et al.*, "Grand: Graph neural diffusion," 2021. [Online]. Available: https://arxiv.org/abs/2106.10934

[111] M. Raissi, P. Perdikaris, and G. Karniadakis, "Physics-informed neural networks: A deep learning framework for solving forward and inverse problems involving nonlinear partial differential equations," *Journal of Computational Physics*, vol. 378, p. 686–707, Feb. 2019. [Online]. Available: http://dx.doi.org/10.1016/j.jcp.2018.10.045

[112] G. E. Karniadakis *et al.*, "Physics-informed machine learning," *Nature Reviews Physics*, vol. 3, no. 6, p. 422–440, May 2021. [Online]. Available: http://dx.doi.org/10.1038/s42254-021-00314-5

[113] Q. Hernández *et al.*, "Structure-preserving neural networks," *Journal of Computational Physics*, vol. 426, p. 109950, Feb. 2021. [Online]. Available: http://dx.doi.org/10.1016/j.jcp.2020.109950

[114] G. E. Hinton and R. S. Zemel, "Autoencoders, minimum description length and helmholtz free energy," in *Proceedings of the 6th International Conference on Neural Information Processing Systems*, ser. NIPS'93. San Francisco, CA, USA: Morgan Kaufmann Publishers Inc., 1993, p. 3–10.

[115] A. Vaswani *et al.*, "Attention is all you need," 2017. [Online]. Available: https://arxiv.org/abs/1706.03762

[116] C. Cortes and V. Vapnik, "Support-vector networks," *Machine Learning*, vol. 20, no. 3, p. 273–297, Sep. 1995. [Online]. Available: http://dx.doi.org/10.1007/BF00994018

[117] W. Maass, "Networks of spiking neurons: The third generation of neural network models," *Neural Networks*, vol. 10, no. 9, p. 1659–1671, Dec. 1997. [Online]. Available: http://dx.doi.org/10.1016/S0893-6080(97)00011-7

[118] I. Goodfellow *et al.*, "Generative adversarial networks," *Communications of the ACM*, vol. 63, no. 11, p. 139–144, Oct. 2020. [Online]. Available: http://dx.doi.org/10.1145/3422622

[119] B. Settles, "Active learning literature survey," in *Computer Sciences Department Technical Report*, 2009. [Online]. Available: https://api.semanticscholar.org/CorpusID:324600

[120] C. M. Macal and M. J. North, "Tutorial on agent-based modelling and simulation," *Journal of Simulation*, vol. 4, no. 3, p. 151–162, Sep. 2010. [Online]. Available: http://dx.doi.org/10.1057/jos.2010.3

[121] E. Bonabeau, "Agent-based modeling: Methods and techniques for simulating human systems," *Proceedings of the National Academy of Sciences*, vol. 99, no. 3, p. 7280–7287, May 2002. [Online]. Available: http://dx.doi.org/10.1073/pnas.082080899

[122] G. An *et al.*, "Agent-based models in translational systems biology," *WIREs Systems Biology and Medicine*, vol. 1, no. 2, p. 159–171, Sep. 2009. [Online]. Available: http://dx.doi.org/10.1002/wsbm.45

[123] M. Pogson *et al.*, "Formal agent-based modelling of intracellular chemical interactions," *Biosystems*, vol. 85, no. 1, p. 37–45, Jul. 2006. [Online]. Available: http://dx.doi.org/10.1016/j.biosystems.2006.02.004

[124] L. Irastorza-Valera *et al.*, "An agent-based model to reproduce the boolean logic behaviour of neuronal self-organised communities through pulse delay modulation and generation of logic gates," *Biomimetics*, vol. 9, no. 2, p. 101, Feb. 2024. [Online]. Available: http://dx.doi.org/10.3390/biomimetics9020101

[125] ——, "Review of the brain's behaviour after injury and disease for its application in an agent-based model (abm)," *Biomimetics*, vol. 9, no. 6, p. 362, Jun. 2024. [Online]. Available: http://dx.doi.org/10.3390/biomimetics9060362

[126] K. Man, K. Tang, and S. Kwong, "Genetic algorithms: concepts and applications [in engineering design]," *IEEE Transactions on Industrial Electronics*, vol. 43, no. 5, p. 519–534, 1996. [Online]. Available: http://dx.doi.org/10.1109/41.538609

[127] J. McCall, "Genetic algorithms for modelling and optimisation," *Journal of Computational and Applied Mathematics*, vol. 184, no. 1, p. 205–222, Dec. 2005. [Online]. Available: http://dx.doi.org/10.1016/j.cam.2004.07.034

[128] C. Ortmann and A. Schumacher, "Graph and heuristic based topology optimization of crash loaded structures," *Structural and Multidisciplinary Optimization*, vol. 47, no. 6, p. 839–854, Jan. 2013. [Online]. Available: http://dx.doi.org/10.1007/s00158-012-0872-7

[129] J.-A. Mejía-de Dios and E. Mezura-Montes, "A surrogate-assisted metaheuristic for bilevel optimization," in *Proceedings of the 2020 Genetic and Evolutionary Computation Conference*, ser. GECCO '20, vol. 6. ACM, Jun. 2020, p. 629–635. [Online]. Available: http://dx.doi.org/10.1145/3377930.3390236

[130] N. Yang, "Novel structural design method inspired by dna and origami," *Results in Engineering*, vol. 4, p. 100069, 2019.

[131] M. Ashby, "Overview no. 92: Materials and shape," *Acta metallurgica et materialia*, vol. 39, no. 6, pp. 1025–1039, 1991.

[132] M. F. Ashby and D. Cebon, "Materials selection in mechanical design," *Le Journal de Physique IV*, vol. 3, no. C7, pp. C7–1, 1993.

[133] A. R. Diaz and O. Sigmund, "A topology optimization method for design of negative permeability metamaterials," *Structural and Multidisciplinary Optimization*, vol. 41, pp. 163–177, 2010.

[134] B. Ozbey *et al.*, "Wireless displacement sensing enabled by metamaterial probes for remote structural health monitoring," *Sensors*, vol. 14, no. 1, pp. 1691–1704, 2014.

[135] S. Rodriguez *et al.*, "Single atom convolutional matching pursuit: Theoretical framework and application to lamb waves based structural health monitoring," 2024. [Online]. Available: https://arxiv.org/abs/2408.08929

[136] D. Di Lorenzo *et al.*, "Damage identification technique by model enrichment for structural elastodynamic problems," *Results in Engineering*, vol. 23, p. 102389, Sep. 2024. [Online]. Available: http://dx.doi.org/10.1016/j.rineng.2024.102389

[137] S. Choukir and C. Singh, "Role of topology in dictating the fracture toughness of mechanical metamaterials," *International Journal of Mechanical Sciences*, vol. 241, p. 107945, 2023.

[138] Y. Liu *et al.*, "Enhanced vibration suppression using diatomic acoustic metamaterial with negative stiffness mechanism," *Engineering Structures*, vol. 271, p. 114939, 2022.

[139] Q. Yang *et al.*, "Aperiodic-metamaterial-based absorber," *APL Materials*, vol. 5, no. 9, Sep. 2017. [Online]. Available: https://doi.org/10.1063/1.4996112

[140] L. D'Alessandro *et al.*, "A design strategy to match the band gap of periodic and aperiodic metamaterials," *Scientific Reports*, vol. 10, no. 1, Oct. 2020. [Online]. Available: https://doi.org/10.1038/s41598-020-73299-3

[141] J.-H. Bastek *et al.*, "Inverting the structure-property map of truss metamaterials by deep learning," *Proceedings of the National Academy of Sciences*, vol. 119, no. 1, Dec. 2021. [Online]. Available: https://doi.org/10.1073/pnas.2111505119

[142] F. W. Zok, R. M. Latture, and M. R. Begley, "Periodic truss structures," *Journal of the Mechanics and Physics of Solids*, vol. 96, pp. 184–203, Nov. 2016. [Online]. Available: https://doi.org/10.1016/j.jmps.2016.07.007

[143] M. C. Messner, "Optimal lattice-structured materials," *Journal of the Mechanics and Physics of Solids*, vol. 96, pp. 162–183, Nov. 2016. [Online]. Available: https://doi.org/10.1016/j.jmps.2016.07.010

[144] L. R. Meza *et al.*, "Reexamining the mechanical property space of three-dimensional lattice architectures," *Acta Materialia*, vol. 140, pp. 424–432, Nov. 2017. [Online]. Available: https://doi.org/10.1016/j.actamat.2017.08.052

[145] M. Zhang *et al.*, "Effective elastic properties and initial yield surfaces of two 3d lattice structures," *International Journal of Mechanical Sciences*, vol. 138-139, pp. 146–158, Apr. 2018. [Online]. Available: https://doi.org/10.1016/j.ijmecsci.2018.02.008

[146] A. Wei *et al.*, "Deep learning-assisted elastic isotropy identification for architected materials," *Extreme Mechanics Letters*, vol. 43, p. 101173, Feb. 2021. [Online]. Available: https://doi.org/10.1016/j.eml.2021.101173

[147] S. Torquato, "Statistical description of microstructures," *Annual Review of Materials Research*, vol. 32, no. 1, pp. 77–111, Aug. 2002. [Online]. Available: https://doi.org/10.1146/annurev.matsci.32.110101.155324

[148] S. Cui *et al.*, "The correlation between statistical descriptors of heterogeneous materials," *Computer Methods in Applied Mechanics and Engineering*, vol. 384, p. 113948, Oct. 2021. [Online]. Available: https://doi.org/10.1016/j.cma.2021.113948

[149] E. Munch, "A user's guide to topological data analysis," *Journal of Learning Analytics*, vol. 4, no. 2, Jul. 2017. [Online]. Available: https://doi.org/10.18608/jla.2017.42.6

[150] F. Chazal and B. Michel, "An introduction to topological data analysis: Fundamental and practical aspects for data scientists," *Frontiers in Artificial Intelligence*, vol. 4, Sep. 2021. [Online]. Available: https://doi.org/10.3389/frai.2021.667963

[151] A. Runacher *et al.*, "Describing and modeling rough composites surfaces by using topological data analysis and fractional brownian motion," *Polymers*, vol. 15, no. 6, p. 1449, Mar. 2023. [Online]. Available: https://doi.org/10.3390/polym15061449

[152] A. Vigliotti, V. S. Deshpande, and D. Pasini, "Non linear constitutive models for lattice materials," *Journal of the Mechanics and Physics of Solids*, vol. 64, pp. 44–60, Mar. 2014. [Online]. Available: https://doi.org/10.1016/j.jmps.2013.10.015

[153] M. J. Mirzaali *et al.*, "Non-affinity in multi-material mechanical metamaterials," *Scientific Reports*, vol. 10, no. 1, Jul. 2020. [Online]. Available: https://doi.org/10.1038/s41598-020-67984-6

[154] T. Xue, S. Adriaenssens, and S. Mao, "Learning the nonlinear dynamics of mechanical metamaterials with graph networks," *International Journal of Mechanical Sciences*, vol. 238, p. 107835, Jan. 2023. [Online]. Available: https://doi.org/10.1016/j.ijmecsci.2022.107835

[155] J. Somnic and B. W. Jo, "Homogenization methods of lattice materials," *Encyclopedia*, vol. 2, no. 2, pp. 1091–1102, 2022.

[156] J. Schröder, "A numerical two-scale homogenization scheme: the fe2-method," in *Plasticity and beyond: microstructures, crystal-plasticity and phase transitions*. Springer, 2014, pp. 1–64.

[157] B. Hassani and E. Hinton, "A review of homogenization and topology optimization i—homogenization theory for media with periodic structure," *Computers & Structures*, vol. 69, no. 6, pp. 707–717, Dec. 1998. [Online]. Available: https://doi.org/10.1016/s0045-7949(98)00131-x

[158] ——, "A review of homogenization and topology opimization II—analytical and numerical solution of homogenization equations," *Computers & Structures*, vol. 69, no. 6, pp. 719–738, Dec. 1998. [Online]. Available: https://doi.org/10.1016/s0045-7949(98)00132-1

[159] ——, "A review of homogenization and topology optimization III—topology optimization using optimality criteria," *Computers & Structures*, vol. 69, no. 6, pp. 739–756, Dec. 1998. [Online]. Available: https://doi.org/10.1016/s0045-7949(98)00133-3

[160] N. Coutris, L. L. Thompson, and S. Kosaraju, "Asymptotic homogenization models for pantographic lattices with variable order rotational resistance at pivots," *Journal of the Mechanics and Physics of Solids*, vol. 134, p. 103718, Jan. 2020. [Online]. Available: https://doi.org/10.1016/j.jmps.2019.103718

[161] A. Braides and L. D'Elia, "Homogenization of discrete thin structures," *Nonlinear Analysis*, vol. 231, p. 112951, Jun. 2023. [Online]. Available: https://doi.org/10.1016/j.na.2022.112951

[162] L. Xu and Z. Qian, "Topology optimization and de-homogenization of graded lattice structures based on asymptotic homogenization," *Composite Structures*, vol. 277, p. 114633, Dec. 2021. [Online]. Available: https://doi.org/10.1016/j.compstruct.2021.114633

[163] F. Vladulescu and D. M. Constantinescu, "Lattice topology homogenization and crack propagation through finite element analyses," *Procedia Structural Integrity*, vol. 28, pp. 637–647, 2020. [Online]. Available: https://doi.org/10.1016/j.prostr.2020.10.074

[164] O. K. Johnson, J. M. Lund, and T. R. Critchfield, "Spectral graph theory for characterization and homogenization of grain boundary networks," *Acta Materialia*, vol. 146, pp. 42–54, Mar. 2018. [Online]. Available: https://doi.org/10.1016/j.actamat.2017.11.054

[165] U. D. Ambroggio, F. Polito, and L. Sacerdote, "On dynamic random graphs with degree homogenization via anti-preferential attachment probabilities," *Physica D: Nonlinear Phenomena*, vol. 414, p. 132689, Dec. 2020. [Online]. Available: https://doi.org/10.1016/j.physd.2020.132689

[166] C. Yang *et al.*, "A meta-path graph-based graph homogenization framework for machine fault diagnosis," *Engineering Applications of Artificial Intelligence*, vol. 121, p. 105960, May 2023. [Online]. Available: https://doi.org/10.1016/j.engappai.2023.105960

[167] D. Dold and D. A. van Egmond, "Differentiable graph-structured models for inverse design of lattice materials," *Cell Reports Physical Science*, p. 101586, Sep. 2023. [Online]. Available: https://doi.org/10.1016/j.xcrp.2023.101586

[168] A. Tessarin *et al.*, "A multiscale numerical homogenization-based method for the prediction of elastic properties of components produced with the fused deposition modelling process," *Results in Engineering*, vol. 14, p. 100409, 2022.

[169] H. Moulinec and P. Suquet, "A fast numerical method for computing the linear and nonlinear mechanical properties of composites," *Comptes Rendus de l'Académie des sciences. Série II. Mécanique, physique, chimie, astronomie*, 1994.

[170] M. Schneider, "A review of nonlinear fft-based computational homogenization methods," *Acta Mechanica*, vol. 232, no. 6, pp. 2051–2100, 2021.

[171] F. J. Montáns *et al.*, "Data-driven modeling and learning in science and engineering," *Comptes Rendus Mécanique*, vol. 347, no. 11, pp. 845–855, 2019.

[172] S. L. Brunton, J. L. Proctor, and J. N. Kutz, "Discovering governing equations from data by sparse identification of nonlinear dynamical systems," *Proceedings of the national academy of sciences*, vol. 113, no. 15, pp. 3932–3937, 2016.

[173] Q. Hernandez *et al.*, "Deep learning of thermodynamics-aware reduced-order models from data," *Computer Methods in Applied Mechanics and Engineering*, vol. 379, p. 113763, 2021.

[174] R. Vinuesa, "High-fidelity simulations in complex geometries: Towards better flow understanding and development of turbulence models," *Results in Engineering*, vol. 11, p. 100254, 2021.

[175] Z. Ji *et al.*, "AI-aided design of multiscale lattice metastructures for controllable anisotropy," *Materials & Design*, vol. 223, p. 111254, Nov. 2022. [Online]. Available: https://doi.org/10.1016/j.matdes.2022.111254

[176] M. Seo and S. Min, "Graph neural networks and implicit neural representation for near-optimal topology prediction over irregular design domains," *Engineering Applications of Artificial Intelligence*, vol. 123, p. 106284, Aug. 2023. [Online]. Available: https://doi.org/10.1016/j.engappai.2023.106284

[177] C. Jiang and N.-Z. Chen, "Graph neural networks (GNNs) based accelerated numerical simulation," *Engineering Applications of Artificial Intelligence*, vol. 123, p. 106370, Aug. 2023. [Online]. Available: https://doi.org/10.1016/j.engappai.2023.106370

[178] P. Prachaseree and E. Lejeune, "Learning mechanically driven emergent behavior with message passing neural networks," *Computers & Structures*, vol. 270, p. 106825, Oct. 2022. [Online]. Available: https://doi.org/10.1016/j.compstruc.2022.106825

[179] K. Karapiperis and D. M. Kochmann, "Prediction and control of fracture paths in disordered architected materials using graph neural networks," *Communications Engineering*, vol. 2, no. 1, Jun. 2023. [Online]. Available: https://doi.org/10.1038/s44172-023-00085-0

[180] R. Perera and V. Agrawal, "Dynamic and adaptive mesh-based graph neural network framework for simulating displacement and crack fields in phase field models," *Mechanics of Materials*, vol. 186, p. 104789, Nov. 2023. [Online]. Available: https://doi.org/10.1016/j.mechmat.2023.104789

[181] A. Thomas *et al.*, "Materials fatigue prediction using graph neural networks on microstructure representations," *Scientific Reports*, vol. 13, no. 1, Aug. 2023. [Online]. Available: https://doi.org/10.1038/s41598-023-39400-2

[182] M. Maurizi, C. Gao, and F. Berto, "Predicting stress, strain and deformation fields in materials and structures with graph neural networks," *Scientific Reports*, vol. 12, no. 1, Dec. 2022. [Online]. Available: https://doi.org/10.1038/s41598-022-26424-3

[183] E. J. Hall *et al.*, "GINNs: Graph-informed neural networks for multiscale physics," *Journal of Computational Physics*, vol. 433, p. 110192, May 2021. [Online]. Available: https://doi.org/10.1016/j.jcp.2021.110192

[184] H. Gao, M. J. Zahr, and J.-X. Wang, "Physics-informed graph neural galerkin networks: A unified framework for solving pde-governed forward and inverse problems," *Computer Methods in Applied Mechanics and Engineering*, vol. 390, p. 114502, 2022.

[185] D. Dalton, D. Husmeier, and H. Gao, "Physics-informed graph neural network emulation of soft-tissue mechanics," *Computer Methods in Applied Mechanics and Engineering*, vol. 417, p. 116351, Dec. 2023. [Online]. Available: https://doi.org/10.1016/j.cma.2023.116351

[186] D. Di Lorenzo *et al.*, "Physics informed and data-based augmented learning in structural health diagnosis," *Computer Methods in Applied Mechanics and Engineering*, vol. 414, p. 116186, 2023.

[187] M. M. Lavrentiev, V. G. Romanov, and S. P. Shishatskii, *Ill-posed problems of mathematical physics and analysis*. American Mathematical Soc., 1986, vol. 64.

[188] J. Kaipio and E. Somersalo, *Statistical and computational inverse problems*. Springer Science & Business Media, 2006, vol. 160.

[189] H. T. Kollmann *et al.*, "Deep learning for topology optimization of 2d metamaterials," *Materials & Design*, vol. 196, p. 109098, 2020.

[190] B. Sanchez-Lengeling *et al.*, "A gentle introduction to graph neural networks," *Distill*, vol. 6, no. 9, p. e33, 2021.

[191] F. Pichi, B. Moya, and J. S. Hesthaven, "A graph convolutional autoencoder approach to model order reduction for parametrized pdes," *Journal of Computational Physics*, p. 112762, 2024.

[192] R. Das and A. Soulaimani, "Non-deterministic methods and surrogates in the design of rockfill dams," *Applied Sciences*, vol. 11, no. 8, p. 3699, Apr. 2021. [Online]. Available: https://doi.org/10.3390/app11083699

[193] H. Jordan, "A non-deterministic deep learning based surrogate for ice sheet modelling," Master of Science (MS) Thesis, Department of Computer Science, University of Montana, 2022. [Online]. Available: https://scholarworks.umt.edu/etd/11991/

[194] N. Luethen, S. Marelli, and B. Sudret, "A spectral surrogate model for stochastic simulators computed from trajectory samples," *Computer Methods in Applied Mechanics and Engineering*, vol. 406, p. 115875, Mar. 2023. [Online]. Available: https://doi.org/10.1016/j.cma.2022.115875

[195] Y. Feng *et al.*, "Past, current and future trends and challenges in non-deterministic fracture mechanics: A review," *Computer Methods in Applied Mechanics and Engineering*, vol. 412, p. 116102, Jul. 2023. [Online]. Available: https://doi.org/10.1016/j.cma.2023.116102

[196] M. A. Hariri-Ardebili and G. Mahdavi, "Generalized uncertainty in surrogate models for concrete strength prediction," *Engineering Applications of Artificial Intelligence*, vol. 122, p. 106155, Jun. 2023. [Online]. Available: https://doi.org/10.1016/j.engappai.2023.106155

[197] X. Wang, H. Chen, and F. Xuan, "Neural network-assisted probabilistic creep-fatigue assessment of hydrogenation reactor with physics-based surrogate model," *International Journal of Pressure Vessels and Piping*, vol. 206, p. 105051, Dec. 2023. [Online]. Available: https://doi.org/10.1016/j.ijpvp.2023.105051

[198] S. Cheng *et al.*, "Surrogate modeling and global sensitivity analysis for the simultaneous growth of multiple hydraulic fractures," *Computers and Geotechnics*, vol. 162, p. 105709, Oct. 2023. [Online]. Available: https://doi.org/10.1016/j.compgeo.2023.105709

[199] S. Huzni *et al.*, "Physics-based surrogate model for reinforced concrete corrosion simulation," *Results in Engineering*, vol. 16, p. 100659, 2022.

[200] A. Michell, "The limits of economy of materials in frame-structures," *Phil Mag*, vol. 8, pp. 589–597, 1904. [Online]. Available: http://habitat.aq.upm.es/gi/mve/dt/Michell-1904.pdf

[201] G. Rozvany, "Grillages of maximum strength and maximum stiffness," *International Journal of Mechanical Sciences*, vol. 14, no. 10, pp. 651–666, Oct. 1972. [Online]. Available: https://doi.org/10.1016/0020-7403(72)90023-9

[202] M. P. Bendsøe, "Optimal shape design as a material distribution problem," *Structural Optimization*, vol. 1, no. 4, pp. 193–202, Dec. 1989. [Online]. Available: https://doi.org/10.1007/bf01650949

[203] G. I. N. Rozvany, "A critical review of established methods of structural topology optimization," *Structural and Multidisciplinary Optimization*, vol. 37, no. 3, pp. 217–237, Feb. 2008. [Online]. Available: https://doi.org/10.1007/s00158-007-0217-0

[204] O. Sigmund, "A 99 line topology optimization code written in matlab," *Structural and Multidisciplinary Optimization*, vol. 21, no. 2, p. 120–127, Apr. 2001. [Online]. Available: http://dx.doi.org/10.1007/s001580050176

[205] E. Andreassen *et al.*, "Efficient topology optimization in matlab using 88 lines of code," *Structural and Multidisciplinary Optimization*, vol. 43, no. 1, p. 1–16, Nov. 2010. [Online]. Available: http://dx.doi.org/10.1007/s00158-010-0594-7

[206] K. Liu and A. Tovar, "An efficient 3d topology optimization code written in matlab," *Structural and Multidisciplinary Optimization*, vol. 50, no. 6, p. 1175–1196, Jun. 2014. [Online]. Available: http://dx.doi.org/10.1007/s00158-014-1107-x

[207] P. Hajela and E. Lee, "Genetic algorithms in truss topological optimization," *International Journal of Solids and Structures*, vol. 32, no. 22, pp. 3341–3357, Nov. 1995. [Online]. Available: https://doi.org/10.1016/0020-7683(94)00306-h

[208] Y. Xie and G. Steven, "Evolutionary structural optimization for dynamic problems," *Computers and Structures*, vol. 58, no. 6, p. 1067–1073, Mar. 1996. [Online]. Available: http://dx.doi.org/10.1016/0045-7949(95)00235-9

[209] G. Allaire and R. V. Kohn, "Topology optimization and optimal shape design using homogenization," in *Topology Design of Structures*. Springer Netherlands, 1993, pp. 207–218. [Online]. Available: https://doi.org/10.1007/978-94-011-1804-0_14

[210] M. Y. Wang, X. Wang, and D. Guo, "A level set method for structural topology optimization," *Computer Methods in Applied Mechanics and Engineering*, vol. 192, no. 1–2, p. 227–246, Jan. 2003. [Online]. Available: http://dx.doi.org/10.1016/S0045-7825(02)00559-5

[211] N. P. van Dijk *et al.*, "Level-set methods for structural topology optimization: a review," *Structural and Multidisciplinary Optimization*, vol. 48, no. 3, p. 437–472, Mar. 2013. [Online]. Available: http://dx.doi.org/10.1007/s00158-013-0912-y

[212] P. D. Dunning, H. A. Kim, and G. Mullineux, "Introducing loading uncertainty in topology optimization," *AIAA Journal*, vol. 49, no. 4, p. 760–768, Apr. 2011. [Online]. Available: http://dx.doi.org/10.2514/1.J050670

[213] J. Zhao and C. Wang, "Robust topology optimization under loading uncertainty based on linear elastic theory and orthogonal diagonalization of symmetric matrices," *Computer Methods in Applied Mechanics and Engineering*, vol. 273, p. 204–218, May 2014. [Online]. Available: http://dx.doi.org/10.1016/j.cma.2014.01.018

[214] A. P. Torres *et al.*, "Robust topology optimization under loading uncertainties via stochastic reduced order models," *International Journal for Numerical Methods in Engineering*, vol. 122, no. 20, p. 5718–5743, Aug. 2021. [Online]. Available: http://dx.doi.org/10.1002/nme.6770

[215] G. Kharmanda, I. R. Antypas, and A. G. Dyachenko, "Inverse optimum safety factor method for reliability-based topology optimization applied to free vibrated structures," *Engineering Technologies and Systems*, no. 1, p. 8–19, Mar. 2019. [Online]. Available: http://dx.doi.org/10.15507/2658-4123.029.201901.008-019

[216] G. Kharmanda, S. Gowid, and A. Shokry, "Reliability-based topology optimization using inverse optimum safety factor approaches," *Alexandria Engineering Journal*, vol. 59, no. 6, p. 4577–4592, Dec. 2020. [Online]. Available: http://dx.doi.org/10.1016/j.aej.2020.08.013

[217] M. Karamooz Ravari *et al.*, "Numerical investigation on mechanical properties of cellular lattice structures fabricated by fused deposition modeling," *International Journal of Mechanical Sciences*, vol. 88, p. 154–161, Nov. 2014. [Online]. Available: http://dx.doi.org/10.1016/j.ijmecsci.2014.08.009

[218] G. I. N. Rozvany, T. Sokół, and V. Pomezanski, "Fundamentals of exact multi-load topology optimization – stress-based least-volume trusses (generalized michell structures) – part i: Plastic design," *Structural and Multidisciplinary Optimization*, vol. 50, no. 6, p. 1051–1078, Aug. 2014. [Online]. Available: http://dx.doi.org/10.1007/s00158-014-1118-7

[219] H. Cui and K. Zhou, "Topology optimization of truss-like structure with stress constraints under multiple-load cases," *Acta Mechanica Solida Sinica*, vol. 33, no. 2, p. 226–238, Aug. 2019. [Online]. Available: http://dx.doi.org/10.1007/s10338-019-00125-3

[220] S. Shi and K. Zhou, "Topology optimization of truss-like structures with bidirectional non-orthogonal materials based on mathematical programming," *Optimization and Engineering*, vol. 25, no. 2, p. 871–910, Jul. 2023. [Online]. Available: http://dx.doi.org/10.1007/s11081-023-09828-6

[221] B. Bourdin and A. Chambolle, "Design-dependent loads in topology optimization," *ESAIM: Control, Optimisation and Calculus of Variations*, vol. 9, p. 19–48, Jan. 2003. [Online]. Available: http://dx.doi.org/10.1051/cocv:2002070

[222] A. Díaz and O. Sigmund, "Checkerboard patterns in layout optimization," *Structural Optimization*, vol. 10, no. 1, p. 40–45, Aug. 1995. [Online]. Available: http://dx.doi.org/10.1007/BF01743693

[223] B. Bourdin, "Filters in topology optimization," *International Journal for Numerical Methods in Engineering*, vol. 50, no. 9, p. 2143–2158, Feb. 2001. [Online]. Available: http://dx.doi.org/10.1002/nme.116

[224] O. Sigmund, "Morphology-based black and white filters for topology optimization," *Structural and Multidisciplinary Optimization*, vol. 33, no. 4–5, p. 401–424, Jan. 2007. [Online]. Available: http://dx.doi.org/10.1007/s00158-006-0087-x

[225] B. S. Lazarov and O. Sigmund, "Filters in topology optimization based on helmholtz-type differential equations," *International Journal for Numerical Methods in Engineering*, vol. 86, no. 6, p. 765–781, Dec. 2010. [Online]. Available: http://dx.doi.org/10.1002/nme.3072

[226] J. Liu and Y. Ma, "A survey of manufacturing oriented topology optimization methods," *Advances in Engineering Software*, vol. 100, p. 161–175, Oct. 2016. [Online]. Available: http://dx.doi.org/10.1016/j.advengsoft.2016.07.017

[227] I. Ostanin, A. Safonov, and I. Oseledets, "Natural erosion of sandstone as shape optimisation," *Scientific Reports*, vol. 7, no. 1, Dec. 2017. [Online]. Available: http://dx.doi.org/10.1038/s41598-017-17777-1

[228] B. S. Lazarov, F. Wang, and O. Sigmund, "Length scale and manufacturability in density-based topology optimization," *Archive of Applied Mechanics*, vol. 86, no. 1–2, p. 189–218, Jan. 2016. [Online]. Available: http://dx.doi.org/10.1007/s00419-015-1106-4

[229] J. Zhu *et al.*, "A review of topology optimization for additive manufacturing: Status and challenges," *Chinese Journal of Aeronautics*, vol. 34, no. 1, p. 91–110, Jan. 2021. [Online]. Available: http://dx.doi.org/10.1016/j.cja.2020.09.020

[230] Y. Chen, J. Lu, and Y. Wei, "Topology optimization for manufacturability based on the visibility map," *Computer-Aided Design and Applicati*, vol. 13, no. 1, p. 86–94, Aug. 2015. [Online]. Available: http://dx.doi.org/10.1080/16864360.2015.1059199

[231] M. Langelaar, "Topology optimization of 3d self-supporting structures for additive manufacturing," *Additive Manufacturing*, vol. 12, p. 60–70, Oct. 2016. [Online]. Available: http://dx.doi.org/10.1016/j.addma.2016.06.010

[232] Y.-D. Seo, H.-J. Kim, and S.-K. Youn, "Isogeometric topology optimization using trimmed spline surfaces," *Computer Methods in Applied Mechanics and Engineering*, vol. 199, no. 49–52, p. 3270–3296, Dec. 2010. [Online]. Available: http://dx.doi.org/10.1016/j.cma.2010.06.033

[233] X. Qian, "Topology optimization in b-spline space," *Computer Methods in Applied Mechanics and Engineering*, vol. 265, p. 15–35, Oct. 2013. [Online]. Available: http://dx.doi.org/10.1016/j.cma.2013.06.001

[234] M. Langelaar, "An additive manufacturing filter for topology optimization of print-ready designs," *Structural and Multidisciplinary Optimization*, vol. 55, no. 3, p. 871–883, Jul. 2016. [Online]. Available: http://dx.doi.org/10.1007/s00158-016-1522-2

[235] S. C. Subedi, C. S. Verma, and K. Suresh, "A review of methods for the geometric post-processing of topology optimized models," *Journal of Computing and Information Science in Engineering*, vol. 20, no. 6, Jun. 2020. [Online]. Available: http://dx.doi.org/10.1115/1.4047429

[236] E. Andreassen, B. S. Lazarov, and O. Sigmund, "Design of manufacturable 3d extremal elastic microstructure," *Mechanics of Materials*, vol. 69, no. 1, p. 1–10, Feb. 2014. [Online]. Available: http://dx.doi.org/10.1016/j.mechmat.2013.09.018

[237] M. Abdelhamid and A. Czekanski, "Revisiting non-convexity in topology optimization of compliance minimization problems," *Engineering Computations*, vol. 39, no. 3, p. 893–915, Aug. 2021. [Online]. Available: http://dx.doi.org/10.1108/EC-01-2021-0052

[238] Z. Liao *et al.*, "A triple acceleration method for topology optimization," *Structural and Multidisciplinary Optimization*, vol. 60, no. 2, p. 727–744, Mar. 2019. [Online]. Available: http://dx.doi.org/10.1007/s00158-019-02234-6

[239] O. Sigmund and J. Petersson, "Numerical instabilities in topology optimization: A survey on procedures dealing with checkerboards, mesh-dependencies and local minima," *Structural Optimization*, vol. 16, no. 1, p. 68–75, Aug. 1998. [Online]. Available: http://dx.doi.org/10.1007/BF01214002

[240] M. Yano, T. Huang, and M. J. Zahr, "A globally convergent method to accelerate topology optimization using on-the-fly model reduction," *Computer Methods in Applied Mechanics and Engineering*, vol. 375, p. 113635, Mar. 2021. [Online]. Available: http://dx.doi.org/10.1016/j.cma.2020.113635

[241] E. Holmberg, B. Torstenfelt, and A. Klarbring, "Stress constrained topology optimization," *Structural and Multidisciplinary Optimization*, vol. 48, no. 1, p. 33–47, Feb. 2013. [Online]. Available: http://dx.doi.org/10.1007/s00158-012-0880-7

[242] D. M. De Leon *et al.*, "Stress-constrained topology optimization for compliant mechanism design," *Structural and Multidisciplinary Optimization*, vol. 52, no. 5, p. 929–943, Jul. 2015. [Online]. Available: http://dx.doi.org/10.1007/s00158-015-1279-z

[243] D. Yang *et al.*, "Stress-constrained topology optimization based on maximum stress measures," *Computers and Structures*, vol. 198, p. 23–39, Mar. 2018. [Online]. Available: http://dx.doi.org/10.1016/j.compstruc.2018.01.008

[244] E. Holmberg, B. Torstenfelt, and A. Klarbring, "Fatigue constrained topology optimization," *Structural and Multidisciplinary Optimization*, vol. 50, no. 2, p. 207–219, Feb. 2014. [Online]. Available: http://dx.doi.org/10.1007/s00158-014-1054-6

[245] J. Oest and E. Lund, "Topology optimization with finite-life fatigue constraints," *Structural and Multidisciplinary Optimization*, vol. 56, no. 5, p. 1045–1059, Jun. 2017. [Online]. Available: http://dx.doi.org/10.1007/s00158-017-1701-9

[246] S. Suresh *et al.*, "Topology optimization using a continuous-time high-cycle fatigue model," *Structural and Multidisciplinary Optimization*, vol. 61, no. 3, p. 1011–1025, Nov. 2019. [Online]. Available: http://dx.doi.org/10.1007/s00158-019-02400-w

[247] A. M. Mirzendehdel and K. Suresh, "Support structure constrained topology optimization for additive manufacturing," *Computer-Aided Design*, vol. 81, p. 1–13, Dec. 2016. [Online]. Available: http://dx.doi.org/10.1016/j.cad.2016.08.006

[248] Y. Chen *et al.*, "Physics-informed neural networks for inverse problems in nano-optics and metamaterials," *Optics Express*, vol. 28, no. 8, p. 11618, Apr. 2020. [Online]. Available: https://doi.org/10.1364/oe.384875

[249] S.-P. Zhu *et al.*, "Probabilistic low cycle fatigue life prediction using an energy-based damage parameter and accounting for model uncertainty," *International Journal of Damage Mechanics*, vol. 21, no. 8, p. 1128–1153, Dec. 2011. [Online]. Available: http://dx.doi.org/10.1177/1056789511429836

[250] J. París *et al.*, "Topology optimization of continuum structures with local and global stress constraints," *Structural and Multidisciplinary Optimization*, vol. 39, no. 4, p. 419–437, Nov. 2008. [Online]. Available: http://dx.doi.org/10.1007/s00158-008-0336-2

[251] L. Xia and P. Breitkopf, "Multiscale structural topology optimization with an approximate constitutive model for local material microstructure," *Computer Methods in Applied Mechanics and Engineering*, vol. 286, p. 147–167, Apr. 2015. [Online]. Available: http://dx.doi.org/10.1016/j.cma.2014.12.018

[252] S. Chu *et al.*, "Topology optimization of multi-material structures with graded interfaces," *Computer Methods in Applied Mechanics and Engineering*, vol. 346, p. 1096–1117, Apr. 2019. [Online]. Available: http://dx.doi.org/10.1016/j.cma.2018.09.040

[253] K. Golos and F. Ellyin, "A total strain energy density theory for cumulative fatigue damage," *Journal of Pressure Vessel Technology*, vol. 110, no. 1, p. 36–41, Feb. 1988. [Online]. Available: http://dx.doi.org/10.1115/1.3265565

[254] ——, *Total Strain Energy Density as a Fatigue Damage Parameter*. Springer Netherlands, 1989, p. 849–858. [Online]. Available: http://dx.doi.org/10.1007/978-94-009-2277-8_42

[255] J. B. Russ and H. Waisman, "A novel elastoplastic topology optimization formulation for enhanced failure resistance via local ductile failure constraints and linear buckling analysis," *Computer Methods in Applied Mechanics and Engineering*, vol. 373, p. 113478, Jan. 2021. [Online]. Available: http://dx.doi.org/10.1016/j.cma.2020.113478

[256] Z. Kang, P. Liu, and M. Li, "Topology optimization considering fracture mechanics behaviors at specified locations," *Structural and Multidisciplinary Optimization*, vol. 55, no. 5, p. 1847–1864, Dec. 2016. [Online]. Available: http://dx.doi.org/10.1007/s00158-016-1623-y

[257] J. B. Russ and H. Waisman, "Topology optimization for brittle fracture resistance," *Computer Methods in Applied Mechanics and Engineering*, vol. 347, p. 238–263, Apr. 2019. [Online]. Available: http://dx.doi.org/10.1016/j.cma.2018.12.031

[258] Y. Wu *et al.*, "Topology optimization for enhanced dynamic fracture resistance of structures," *Computer Methods in Applied Mechanics and Engineering*, vol. 394, p. 114846, May 2022. [Online]. Available: http://dx.doi.org/10.1016/j.cma.2022.114846

[259] Y. Cha and O. Buyukozturk, "Structural damage detection using modal strain energy and hybrid multiobjective optimization," *Computer-Aided Civil and Infrastructure Engineering*, vol. 30, no. 5, p. 347–358, Feb. 2015. [Online]. Available: http://dx.doi.org/10.1111/mice.12122

[260] L. Saucedo-Mora *et al.*, "The updated properties model (upm): A topology optimization algorithm for the creation of macro–micro optimized structures with variable stiffness," *Finite Elements in Analysis and Design*, vol. 223, p. 103970, Oct. 2023. [Online]. Available: http://dx.doi.org/10.1016/j.finel.2023.103970

[261] J. Gao *et al.*, "Topology optimization for multiscale design of porous composites with multi-domain microstructures," *Computer Methods in Applied Mechanics and Engineering*, vol. 344, p. 451–476, Feb. 2019. [Online]. Available: http://dx.doi.org/10.1016/j.cma.2018.10.017

[262] S. Das and A. Sutradhar, "Multi-physics topology optimization of functionally graded controllable porous structures: Application to heat dissipating problems," *Materials and Design*, vol. 193, p. 108775, Aug. 2020. [Online]. Available: http://dx.doi.org/10.1016/j.matdes.2020.108775

[263] Q. Liu *et al.*, "Metamaterials mapped lightweight structures by principal stress lines and topology optimization: Methodology, additive manufacturing, ductile failure and tests," *Materials and Design*, vol. 212, p. 110192, Dec. 2021. [Online]. Available: http://dx.doi.org/10.1016/j.matdes.2021.110192

[264] J. Chen *et al.*, "3d-printed anisotropic polymer materials for functional applications," *Advanced Materials*, vol. 34, no. 5, Dec. 2021. [Online]. Available: http://dx.doi.org/10.1002/adma.202102877

[265] Y. Han *et al.*, "Topology optimization of material nonlinear continuum structures under stress constraints," *Computer Methods in Applied Mechanics and Engineering*, vol. 378, p. 113731, May 2021. [Online]. Available: http://dx.doi.org/10.1016/j.cma.2021.113731

[266] T. Buhl, C. Pedersen, and O. Sigmund, "Stiffness design of geometrically nonlinear structures using topology optimization," *Structural and Multidisciplinary Optimization*, vol. 19, no. 2, p. 93–104, Apr. 2000. [Online]. Available: http://dx.doi.org/10.1007/s001580050089

[267] D. Jung and H. C. Gea, "Topology optimization of nonlinear structures," *Finite Elements in Analysis and Design*, vol. 40, no. 11, p. 1417–1427, Jul. 2004. [Online]. Available: http://dx.doi.org/10.1016/j.finel.2003.08.011

[268] R. J. Yang and C. J. Chen, "Stress-based topology optimization," *Structural Optimization*, vol. 12, no. 2–3, p. 98–105, Oct. 1996. [Online]. Available: http://dx.doi.org/10.1007/BF01196941

[269] C. Le *et al.*, "Stress-based topology optimization for continua," *Structural and Multidisciplinary Optimization*, vol. 41, no. 4, p. 605–620, Oct. 2009. [Online]. Available: http://dx.doi.org/10.1007/s00158-009-0440-y

[270] H. Deng, P. S. Vulimiri, and A. C. To, "An efficient 146-line 3d sensitivity analysis code of stress-based topology optimization written in matlab," *Optimization and Engineering*, vol. 23, no. 3, p. 1733–1757, Aug. 2021. [Online]. Available: http://dx.doi.org/10.1007/s11081-021-09675-3

[271] J. Gu *et al.*, "Nonlinear fatigue damage constrained topology optimization," *Computer Methods in Applied Mechanics and Engineering*, vol. 429, p. 117136, Sep. 2024. [Online]. Available: http://dx.doi.org/10.1016/j.cma.2024.117136

[272] L. Xia and P. Breitkopf, "Recent advances on topology optimization of multiscale nonlinear structures," *Archives of Computational Methods in Engineering*, vol. 24, no. 2, p. 227–249, Jan. 2016. [Online]. Available: http://dx.doi.org/10.1007/s11831-016-9170-7

[273] P. Srivastava *et al.*, "Models of communication and control for brain networks: distinctions, convergence, and future outlook," *Network Neuroscience*, vol. 4, no. 4, pp. 1122–1159, Jan. 2020. [Online]. Available: https://doi.org/10.1162/netn_a_00158

[274] K. Shibata *et al.*, "Differential activation patterns in the same brain region led to opposite emotional states," *PLOS Biology*, vol. 14, no. 9, p. e1002546, Sep. 2016. [Online]. Available: https://doi.org/10.1371/journal.pbio.1002546

[275] J. Nakuci *et al.*, "Multiple brain activation patterns for the same task," *bioRxiv*, Apr. 2023. [Online]. Available: https://doi.org/10.1101/2023.04.08.536107

[276] C. Y. Baek *et al.*, "Change in activity patterns in the prefrontal cortex in different phases during the dual-task walking in older adults," *Journal of NeuroEngineering and Rehabilitation*, vol. 20, no. 1, Jul. 2023. [Online]. Available: https://doi.org/10.1186/s12984-023-01211-x

[277] M. E. Raichle, "The brain's default mode network," *Annual Review of Neuroscience*, vol. 38, no. 1, p. 433–447, Jul. 2015. [Online]. Available: http://dx.doi.org/10.1146/annurev-neuro-071013-014030

[278] R. L. Buckner and L. M. DiNicola, "The brain's default network: updated anatomy, physiology and evolving insights," *Nature Reviews Neuroscience*, vol. 20, no. 10, pp. 593–608, Sep. 2019. [Online]. Available: https://doi.org/10.1038/s41583-019-0212-7

[279] J. Smallwood *et al.*, "The default mode network in cognition: a topographical perspective," *Nature Reviews Neuroscience*, vol. 22, no. 8, pp. 503–513, Jul. 2021. [Online]. Available: https://doi.org/10.1038/s41583-021-00474-4

[280] R. L. Buckner, "The brain's default network: origins and implications for the study of psychosis," *Dialogues in Clinical Neuroscience*, vol. 15, no. 3, pp. 351–358, Sep. 2013. [Online]. Available: https://doi.org/10.31887/dcns.2013.15.3/rbuckner

[281] S. H. Siddiqi *et al.*, "Causal mapping of human brain function," *Nature Reviews Neuroscience*, vol. 23, no. 6, pp. 361–375, Apr. 2022. [Online]. Available: https://doi.org/10.1038/s41583-022-00583-8

[282] D. C. Van Essen, "Cartography and connectomes," *Neuron*, vol. 80, no. 3, pp. 775–790, Oct. 2013. [Online]. Available: http://dx.doi.org/10.1016/j.neuron.2013.10.027

[283] K. Amunts *et al.*, "Julich-brain: A 3d probabilistic atlas of the human brain's cytoarchitecture," *Science*, vol. 369, no. 6506, pp. 988–992, Jul. 2020. [Online]. Available: https://doi.org/10.1126/science.abb4588

[284] Y. Alemán-Gómez *et al.*, "A multi-scale probabilistic atlas of the human connectome," *Scientific Data*, vol. 9, no. 1, Aug. 2022. [Online]. Available: http://dx.doi.org/10.1038/s41597-022-01624-8

[285] H. Shibasaki, "Human brain mapping: Hemodynamic response and electrophysiology," *Clinical Neurophysiology*, vol. 119, no. 4, pp. 731–743, Apr. 2008. [Online]. Available: http://dx.doi.org/10.1016/j.clinph.2007.10.026

[286] K. Milligan, A. Balwani, and E. Dyer, "Brain mapping at high resolutions: Challenges and opportunities," *Current Opinion in Biomedical Engineering*, vol. 12, pp. 126–131, Dec. 2019. [Online]. Available: https://doi.org/10.1016/j.cobme.2019.10.009

[287] O. Sporns, G. Tononi, and R. Kötter, "The human connectome: A structural description of the human brain," *PLoS Computational Biology*, vol. 1, no. 4, p. e42, 2005. [Online]. Available: http://dx.doi.org/10.1371/journal.pcbi.0010042

[288] S. Finger and C. Almli, "Brain damage and neuroplasticity: Mechanisms of recovery or development?" *Brain Research Reviews*, vol. 10, no. 3, pp. 177–186, Dec. 1985. [Online]. Available: https://doi.org/10.1016/0165-0173(85)90023-2

[289] J. Grafman, "Conceptualizing functional neuroplasticity," *Journal of Communication Disorders*, vol. 33, no. 4, pp. 345–356, Jul. 2000. [Online]. Available: https://doi.org/10.1016/s0021-9924(00)00030-7

[290] E. Fuchs and G. Flügge, "Adult neuroplasticity: More than 40 years of research," *Neural Plasticity*, vol. 2014, pp. 1–10, 2014. [Online]. Available: https://doi.org/10.1155/2014/541870

[291] B. Kolb and R. Gibb, "Brain plasticity and behaviour in the developing brain," *Journal of the Canadian Academy of Child and Adolescent Psychiatry*, 2011. [Online]. Available: https://www.ncbi.nlm.nih.gov/pmc/articles/PMC3222570/

[292] D. C. Park and G. N. Bischof, "The aging mind: neuroplasticity in response to cognitive training," *Dialogues in Clinical Neuroscience*, vol. 15, no. 1, pp. 109–119, Mar. 2013. [Online]. Available: https://doi.org/10.31887/dcns.2013.15.1/dpark

[293] T. A. Viel *et al.*, "Mechanisms of neuroplasticity and brain degeneration: strategies for protection during the aging process," *Neural Regeneration Research*, vol. 16, no. 1, p. 58, 2021. [Online]. Available: https://doi.org/10.4103/1673-5374.286952

[294] S. H. Bennett, A. J. Kirby, and G. T. Finnerty, "Rewiring the connectome: Evidence and effects," *Neuroscience and Biobehavioral Reviews*, vol. 88, pp. 51–62, May 2018. [Online]. Available: https://doi.org/10.1016/j.neubiorev.2018.03.001

[295] Y. B. Seven and G. S. Mitchell, "Mechanisms of compensatory plasticity for respiratory motor neuron death," *Respiratory Physiology and Neurobiology*, vol. 265, pp. 32–39, Jul. 2019. [Online]. Available: https://doi.org/10.1016/j.resp.2019.01.001

[296] N. L. Hill, A. M. Kolanowski, and D. J. Gill, "Plasticity in early alzheimer disease," *Topics in Geriatric Rehabilitation*, vol. 27, no. 4, pp. 257–267, Oct. 2011. [Online]. Available: https://doi.org/10.1097/tgr.0b013e31821e588e

[297] J. S. Meyer, K. Obara, and K. Muramatsu, "Diaschisis," *Neurological Research*, vol. 15, no. 6, pp. 362–366, Dec. 1993. [Online]. Available: https://doi.org/10.1080/01616412.1993.11740164

[298] I. T. Irastorza, "Glial localization of the cannabinoid cb1 and cb2 receptors in a mouse model of alzheimer's disease," Ph.D. dissertation, Neuroscience Department, Faculty of Medicine and Nursery, Universidad del País Vasco / Euskal Herriko Unibersitatea (UPV/EHU), 2021. [Online]. Available: https://addi.ehu.es/handle/10810/54056

[299] Y. Hatanaka *et al.*, "From migration to settlement: the pathways, migration modes and dynamics of neurons in the developing brain," *Proceedings of the Japan Academy, Series B*, vol. 92, no. 1, pp. 1–19, 2016. [Online]. Available: http://dx.doi.org/10.2183/pjab.92.1

[300] H. T. Ghashghaei, C. Lai, and E. S. Anton, "Neuronal migration in the adult brain: are we there yet?" *Nature Reviews Neuroscience*, vol. 8, no. 2, pp. 141–151, Feb. 2007. [Online]. Available: http://dx.doi.org/10.1038/nrn2074

[301] B. Nadarajah and J. G. Parnavelas, "Modes of neuronal migration in the developing cerebral cortex," *Nature Reviews Neuroscience*, vol. 3, no. 6, pp. 423–432, Jun. 2002. [Online]. Available: http://dx.doi.org/10.1038/nrn845

[302] N. A. Crossley, *Connectome analysis and psychiatric disorders*. Elsevier, 2023, pp. 423–432. [Online]. Available: http://dx.doi.org/10.1016/B978-0-323-85280-7.00001-4

[303] F. Crick, "The recent excitement about neural networks," *Nature*, vol. 337, no. 6203, pp. 129–132, Jan. 1989. [Online]. Available: http://dx.doi.org/10.1038/337129a0

[304] J. C. Whittington and R. Bogacz, "Theories of error back-propagation in the brain," *Trends in Cognitive Sciences*, vol. 23, no. 3, pp. 235–250, Mar. 2019. [Online]. Available: https://doi.org/10.1016/j.tics.2018.12.005

[305] F. Pulvermüller *et al.*, "Biological constraints on neural network models of cognitive function," *Nature Reviews Neuroscience*, vol. 22, no. 8, pp. 488–502, Jun. 2021. [Online]. Available: https://doi.org/10.1038/s41583-021-00473-5

[306] N. Schaworonkow, "Overcoming harmonic hurdles: Genuine beta-band rhythms vs. contributions of alpha-band waveform shape," *Imaging Neuroscience*, vol. 1, pp. 1–8, Sep. 2023. [Online]. Available: https://doi.org/10.1162/imag_a_00018

[307] E. Tognoli and J. A. S. Kelso, "The metastable brain," *Neuron*, vol. 81, no. 1, pp. 35–48, Jan. 2014. [Online]. Available: https://doi.org/10.1016/j.neuron.2013.12.022

[308] J. A. Roberts *et al.*, "Metastable brain waves," *Nature Communications*, vol. 10, no. 1, Mar. 2019. [Online]. Available: https://doi.org/10.1038/s41467-019-08999-0

[309] A. Demertzi *et al.*, "Human consciousness is supported by dynamic complex patterns of brain signal coordination," *Science Advances*, vol. 5, no. 2, Feb. 2019. [Online]. Available: https://doi.org/10.1126/sciadv.aat7603

[310] P. G. Nagappan, H. Chen, and D.-Y. Wang, "Neuroregeneration and plasticity: a review of the physiological mechanisms for achieving functional recovery postinjury," *Military Medical Research*, vol. 7, no. 1, Jun. 2020. [Online]. Available: https://doi.org/10.1186/s40779-020-00259-3

[311] F. E. Garcea and L. J. Buxbaum, "Mechanisms and neuroanatomy of response selection in tool and non-tool action tasks: Evidence from left-hemisphere stroke," *Cortex*, vol. 167, pp. 335–350, Oct. 2023. [Online]. Available: https://doi.org/10.1016/j.cortex.2023.06.012

[312] C. F. Ferris *et al.*, "Life without a brain: Neuroradiological and behavioral evidence of neuroplasticity necessary to sustain brain function in the face of severe hydrocephalus," *Scientific Reports*, vol. 9, no. 1, Nov. 2019. [Online]. Available: https://doi.org/10.1038/s41598-019-53042-3

[313] D. J. Hodkinson, S. R. Jackson, and J. Jung, "Task-dependent plasticity in distributed neural circuits after transcranial direct current stimulation of the human motor cortex: A proof-of-concept study," *Frontiers in Pain Research*, Nov. 2022. [Online]. Available: https://doi.org/10.3389%2Ffpain.2022.1005634

[314] S. N. Burke and C. A. Barnes, "Neural plasticity in the ageing brain," *Nature Reviews Neuroscience*, vol. 7, no. 1, pp. 30–40, Jan. 2006. [Online]. Available: https://doi.org/10.1038/nrn1809

[315] L. Pauwels, S. Chalavi, and S. P. Swinnen, "Neural plasticity in the ageing brain," *Aging (Albany NY)*, vol. 10, no. 8, pp. 1789–1790, Aug. 2018. [Online]. Available: 10.18632%2Faging.101514

[316] B. M. D. Vik, G. O. Skeie, and K. Specht, "Neuroplastic effects in patients with traumatic brain injury after music-supported therapy," *Frontiers in Human Neuroscience*, vol. 13, Jun. 2019. [Online]. Available: https://doi.org/10.3389/fnhum.2019.00177

[317] S. Sakuma *et al.*, "Learning times required to identify the stimulated position and shortening of propagation path by hebb's rule in neural network," *AIMS Neuroscience*, vol. 4, no. 4, pp. 238–253, 2017. [Online]. Available: https://doi.org/10.3934/neuroscience.2017.4.238

[318] Y. Bengio *et al.*, "STDP-compatible approximation of backpropagation in an energy-based model," *Neural Computation*, vol. 29, no. 3, pp. 555–577, Mar. 2017. [Online]. Available: https://doi.org/10.1162/neco_a_00934

[319] J. Guerguiev, T. P. Lillicrap, and B. A. Richards, "Towards deep learning with segregated dendrites," *eLife*, vol. 6, Dec. 2017. [Online]. Available: https://doi.org/10.7554/elife.22901

[320] J. a. Sacramento *et al.*, "Dendritic cortical microcircuits approximate the backpropagation algorithm," *Proceedings of the 32nd International Conference on Neural Information Processing Systems*, p. 8735–8746, 2018. [Online]. Available: https://dl.acm.org/doi/10.5555/3327546.3327550

[321] T. P. Lillicrap *et al.*, "Backpropagation and the brain," *Nature Reviews Neuroscience*, vol. 21, no. 6, pp. 335–346, Apr. 2020. [Online]. Available: https://doi.org/10.1038/s41583-020-0277-3

[322] Y. Song *et al.*, "Can the brain do backpropagation? —exact implementation of backpropagation in predictive coding networks," *Advances in Neural Information Processing Systems*, vol. 2020, no. 33, p. 22566–22579, Apr. 2020. [Online]. Available: https://www.ncbi.nlm.nih.gov/pmc/articles/PMC7610561/

[323] M. Hausser, N. Spruston, and G. J. Stuart, "Diversity and dynamics of dendritic signaling," *Science*, vol. 290, no. 5492, pp. 739–744, Oct. 2000. [Online]. Available: https://doi.org/10.1126/science.290.5492.739

[324] K. Staley, "Epileptic neurons go wireless," *Science*, vol. 305, no. 5683, pp. 482–483, Jul. 2004. [Online]. Available: https://doi.org/10.1126/science.1101133

[325] M. Rapp, Y. Yarom, and I. Segev, "Modeling back propagating action potential in weakly excitable dendrites of neocortical pyramidal cells," *Proceedings of the National Academy of Sciences (PNAS)*, vol. 93, no. 21, pp. 11 985—-11 990, Oct. 1996. [Online]. Available: https://www.ncbi.nlm.nih.gov/pmc/articles/PMC38170/

[326] H.-R. Lüscher and M. E. Larkum, "Modeling action potential initiation and back-propagation in dendrites of cultured rat motoneurons," *Journal of Neurophysiology*, vol. 80, no. 2, pp. 715–729, Aug. 1998. [Online]. Available: https://doi.org/10.1152/jn.1998.80.2.715

[327] J. Waters and F. Helmchen, "Boosting of action potential backpropagation by neocortical network activity in vivo," *The Journal of Neuroscience*, vol. 24, no. 49, pp. 11 127–11 136, Dec. 2004. [Online]. Available: https://doi.org/10.1523/jneurosci.2933-04.2004

[328] M. Bartholomew-Biggs *et al.*, "Automatic differentiation of algorithms," *Journal of Computational and Applied Mathematics*, vol. 124, no. 1-2, pp. 171–190, Dec. 2000. [Online]. Available: https://doi.org/10.1016/s0377-0427(00)00422-2

[329] A. Paszke *et al.*, "Automatic differentiation in pytorch," in *NIPS 2017 Workshop on Autodiff*, 2017. [Online]. Available: https://openreview.net/forum?id=BJJsrmfCZ

[330] ——, *PyTorch: an imperative style, high-performance deep learning library*. Red Hook, NY, USA: Curran Associates Inc., 2019. [Online]. Available: https://dl.acm.org/doi/10.5555/3454287.3455008

[331] M. Abadi *et al.*, "Tensorflow: a system for large-scale machine learning," in *Proceedings of the 12th USENIX Conference on Operating Systems Design and Implementation*, ser. OSDI'16. USENIX Association, 2016, p. 265–283. [Online]. Available: https://dl.acm.org/doi/10.5555/3026877.3026899

[332] B. Shah and H. Bhavsar, "Time complexity in deep learning models," *Procedia Computer Science*, vol. 215, pp. 202–210, 2022. [Online]. Available: https://doi.org/10.1016/j.procs.2022.12.023

[333] P. R. Roelfsema, V. A. F. Lamme, and H. Spekreijse, "Object-based attention in the primary visual cortex of the macaque monkey," *Nature*, vol. 395, no. 6700, pp. 376–381, Sep. 1998. [Online]. Available: https://doi.org/10.1038/26475

[334] C. N. Olivers and P. R. Roelfsema, "Attention for action in visual working memory," *Cortex*, vol. 131, pp. 179–194, Oct. 2020. [Online]. Available: https://doi.org/10.1016/j.cortex.2020.07.011

[335] P. R. Roelfsema and A. van Ooyen, "Attention-gated reinforcement learning of internal representations for classification," *Neural Computation*, vol. 17, no. 10, pp. 2176–2214, Oct. 2005. [Online]. Available: https://doi.org/10.1162/0899766054615699

[336] J. Vohryzek *et al.*, "Understanding brain states across spacetime informed by whole-brain modelling," *Philosophical Transactions of the Royal Society A: Mathematical, Physical and Engineering Sciences*, vol. 380, no. 2227, May 2022. [Online]. Available: http://dx.doi.org/10.1098/rsta.2021.0247

[337] A. Pathak, D. Roy, and A. Banerjee, "Whole-brain network models: From physics to bedside," *Frontiers in Computational Neuroscience*, vol. 16, May 2022. [Online]. Available: http://dx.doi.org/10.3389/fncom.2022.866517

[338] S. Herculano-Houzel, "The human brain in numbers: a linearly scaled-up primate brain," *Frontiers in Human Neuroscience*, vol. 3, 2009. [Online]. Available: http://dx.doi.org/10.3389/neuro.09.031.2009

[339] T. Nguyen, "Total number of synapses in the adult human neocortex," *Undergraduate Journal of Mathematical Modeling: One + Two*, vol. 3, no. 1, May 2013. [Online]. Available: http://dx.doi.org/10.5038/2326-3652.3.1.26

[340] E. D' Angelo and V. Jirsa, "The quest for multiscale brain modeling," *Trends in Neurosciences*, vol. 45, no. 10, pp. 777–790, Oct. 2022. [Online]. Available: http://dx.doi.org/10.1016/j.tins.2022.06.007

[341] Z. Xu *et al.*, "Meta-connectomic analysis maps consistent, reproducible, and transcriptionally relevant functional connectome hubs in the human brain," *Communications Biology*, vol. 5, no. 1, Oct. 2022. [Online]. Available: http://dx.doi.org/10.1038/s42003-022-04028-x

[342] S. C. de Lange *et al.*, "Shared vulnerability for connectome alterations across psychiatric and neurological brain disorders," *Nature Human Behaviour*, vol. 3, no. 9, pp. 988–998, Aug. 2019. [Online]. Available: http://dx.doi.org/10.1038/s41562-019-0659-6

[343] B.-y. Park *et al.*, "Multiscale neural gradients reflect transdiagnostic effects of major psychiatric conditions on cortical morphology," *Communications Biology*, vol. 5, no. 1, Sep. 2022. [Online]. Available: http://dx.doi.org/10.1038/s42003-022-03963-z

[344] G. Deco *et al.*, "Rethinking segregation and integration: contributions of whole-brain modelling," *Nature Reviews Neuroscience*, vol. 16, no. 7, pp. 430–439, Jun. 2015. [Online]. Available: http://dx.doi.org/10.1038/nrn3963

[345] ——, "The most relevant human brain regions for functional connectivity: Evidence for a dynamical workspace of binding nodes from whole-brain computational modelling," *NeuroImage*, vol. 146, pp. 197–210, Feb. 2017. [Online]. Available: http://dx.doi.org/10.1016/j.neuroimage.2016.10.047

[346] H. Jiang *et al.*, "Structural-functional decoupling predicts suicide attempts in bipolar disorder patients with a current major depressive episode," *Neuropsychopharmacology*, vol. 45, no. 10, pp. 1735–1742, Jun. 2020. [Online]. Available: http://dx.doi.org/10.1038/s41386-020-0753-5

[347] J. J. Crofts *et al.*, "Structure-function clustering in weighted brain networks," *Scientific Reports*, vol. 12, no. 1, Oct. 2022. [Online]. Available: http://dx.doi.org/10.1038/s41598-022-19994-9

[348] V. Bazinet, J. Y. Hansen, and B. Misic, "Towards a biologically annotated brain connectome," *Nature Reviews Neuroscience*, vol. 24, no. 12, pp. 747–760, Oct. 2023. [Online]. Available: http://dx.doi.org/10.1038/s41583-023-00752-3

[349] J. Y. Hansen *et al.*, "Local molecular and global connectomic contributions to cross-disorder cortical abnormalities," *Nature Communications*, vol. 13, no. 1, Aug. 2022. [Online]. Available: http://dx.doi.org/10.1038/s41467-022-32420-y

[350] A. L. Hodgkin and A. F. Huxley, "A quantitative description of membrane current and its application to conduction and excitation in nerve," *The Journal of Physiology*, vol. 117, no. 4, pp. 500–544, Aug. 1952. [Online]. Available: http://dx.doi.org/10.1113/jphysiol.1952.sp004764

[351] P. A. Robinson *et al.*, "Multiscale brain modelling," *Philosophical Transactions of the Royal Society B: Biological Sciences*, vol. 360, no. 1457, pp. 1043–1050, May 2005. [Online]. Available: http://dx.doi.org/10.1098/rstb.2005.1638

[352] M. Martín-Loeches *et al.*, "Electrophysiology and intelligence: the electrophysiology of intellectual functions in intellectual disability," *Journal of Intellectual Disability Research*, vol. 45, no. 1, pp. 63–75, Feb. 2001. [Online]. Available: http://dx.doi.org/10.1046/j.1365-2788.2001.00292.x

[353] M. Vincent *et al.*, "Electrophysiological brain mapping: Basics of recording evoked potentials induced by electrical stimulation and its physiological spreading in the human brain," *Clinical Neurophysiology*, vol. 128, no. 10, pp. 1886–1890, Oct. 2017. [Online]. Available: http://dx.doi.org/10.1016/j.clinph.2017.07.402

[354] ——, "The difference between electrical microstimulation and direct electrical stimulation - towards new opportunities for innovative functional brain mapping?" *Reviews in the Neurosciences*, vol. 27, no. 3, pp. 231–258, Apr. 2016. [Online]. Available: http://dx.doi.org/10.1515/revneuro-2015-0029

[355] C. Chang and J. E. Chen, "Multimodal eeg-fmri: Advancing insight into large-scale human brain dynamics," *Current Opinion in Biomedical Engineering*, vol. 18, p. 100279, Jun. 2021. [Online]. Available: http://dx.doi.org/10.1016/j.cobme.2021.100279

[356] M. K. van Vugt, P. B. Sederberg, and M. J. Kahana, "Comparison of spectral analysis methods for characterizing brain oscillations," *Journal of Neuroscience Methods*, vol. 162, no. 1–2, pp. 49–63, May 2007. [Online]. Available: http://dx.doi.org/10.1016/j.jneumeth.2006.12.004

[357] V. A. Kalatsky, *Fourier Approach for Functional Imaging*. Boca Raton (FL): CRC Press/Taylor & Francis, 2009. [Online]. Available: https://www.ncbi.nlm.nih.gov/books/NBK20236/

[358] H. A. Mallot, *Fourier Analysis for Neuroscientists*. Springer International Publishing, 2013, pp. 57–81. [Online]. Available: http://dx.doi.org/10.1007/978-3-319-00861-5_3

[359] N. Graham, "Does the brain perform a fourier analysis of the visual scene?" *Trends in Neurosciences*, vol. 2, pp. 207–208, Jan. 1979. [Online]. Available: http://dx.doi.org/10.1016/0166-2236(79)90082-1

[360] A. L. Ochs, "Is fourier analysis performed by the visual system or by the visual investigator," *Journal of the Optical Society of America*, vol. 69, no. 1, p. 95, Jan. 1979. [Online]. Available: http://dx.doi.org/10.1364/JOSA.69.000095

[361] P. Chavoshnejad *et al.*, "Mechanical hierarchy in the formation and modulation of cortical folding patterns," *Scientific Reports*, vol. 13, no. 1, Aug. 2023. [Online]. Available: http://dx.doi.org/10.1038/s41598-023-40086-9

[362] M. Destrade *et al.*, "Extreme softness of brain matter in simple shear," *International Journal of Non-Linear Mechanics*, vol. 75, pp. 54–58, Oct. 2015. [Online]. Available: http://dx.doi.org/10.1016/j.ijnonlinmec.2015.02.014

[363] A. Goriely *et al.*, "Mechanics of the brain: perspectives, challenges, and opportunities," *Biomechanics and Modeling in Mechanobiology*, vol. 14, no. 5, pp. 931–965, Feb. 2015. [Online]. Available: http://dx.doi.org/10.1007/s10237-015-0662-4

[364] B. Rashid, M. Destrade, and M. D. Gilchrist, "Mechanical characterization of brain tissue in simple shear at dynamic strain rates," *Journal of the Mechanical Behavior of Biomedical Materials*, vol. 28, pp. 71–85, Dec. 2013. [Online]. Available: http://dx.doi.org/10.1016/j.jmbbm.2013.07.017

[365] M. Gilchrist *et al.*, "Quasi-static deformations of biological soft tissue," *Mathematics and Mechanics of Solids*, vol. 18, no. 6, pp. 622–633, May 2013. [Online]. Available: http://dx.doi.org/10.1177/1081286513485770

[366] N. Reiter, F. Paulsen, and S. Budday, "Mechanisms of mechanical load transfer through brain tissue," *Scientific Reports*, vol. 13, no. 1, May 2023. [Online]. Available: http://dx.doi.org/10.1038/s41598-023-35768-3

[367] S. Budday *et al.*, "Fifty shades of brain: A review on the mechanical testing and modeling of brain tissue," *Archives of Computational Methods in Engineering*, vol. 27, no. 4, pp. 1187–1230, Jul. 2019. [Online]. Available: http://dx.doi.org/10.1007/s11831-019-09352-w

[368] Y. Lanir, "Mechanistic micro-structural theory of soft tissues growth and remodeling: tissues with unidirectional fibers," *Biomechanics and Modeling in Mechanobiology*, vol. 14, no. 2, pp. 245–266, Jun. 2014. [Online]. Available: http://dx.doi.org/10.1007/s10237-014-0600-x

[369] F. A. Braeu *et al.*, "Homogenized constrained mixture models for anisotropic volumetric growth and remodeling," *Biomechanics and Modeling in Mechanobiology*, vol. 16, no. 3, pp. 889–906, Dec. 2016. [Online]. Available: http://dx.doi.org/10.1007/s10237-016-0859-1

[370] B. Rashid, M. Destrade, and M. D. Gilchrist, "Influence of preservation temperature on the measured mechanical properties of brain tissue," *Journal of Biomechanics*, vol. 46, no. 7, pp. 1276–1281, Apr. 2013. [Online]. Available: http://dx.doi.org/10.1016/j.jbiomech.2013.02.014

[371] J. Zhang and H. Xiong, *Brain Tissue Preparation, Sectioning, and Staining*. Springer New York, Sep. 2013, pp. 3–30. [Online]. Available: http://dx.doi.org/10.1007/978-1-4614-8794-4_1

[372] B. Rashid, M. Destrade, and M. D. Gilchrist, "Temperature effects on brain tissue in compression," *Journal of the Mechanical Behavior of Biomedical Materials*, vol. 14, pp. 113–118, Oct. 2012. [Online]. Available: http://dx.doi.org/10.1016/j.jmbbm.2012.04.005

[373] A. P. Sarvazyan, M. W. Urban, and J. F. Greenleaf, "Acoustic waves in medical imaging and diagnostics," *Ultrasound in Medicine and Biology*, vol. 39, no. 7, pp. 1133–1146, Jul. 2013. [Online]. Available: http://dx.doi.org/10.1016/j.ultrasmedbio.2013.02.006

[374] Y. Jiang *et al.*, "Measuring the linear and nonlinear elastic properties of brain tissue with shear waves and inverse analysis," *Biomechanics and Modeling in Mechanobiology*, vol. 14, no. 5, pp. 1119–1128, Feb. 2015. [Online]. Available: http://dx.doi.org/10.1007/s10237-015-0658-0

[375] N. Antonovaite *et al.*, "Regional variations in stiffness in live mouse brain tissue determined by depth-controlled indentation mapping," *Scientific Reports*, vol. 8, no. 1, Aug. 2018. [Online]. Available: http://dx.doi.org/10.1038/s41598-018-31035-y

[376] D. R. Walsh *et al.*, "Mechanical and structural characterisation of the dural venous sinuses," *Scientific Reports*, vol. 10, no. 1, Dec. 2020. [Online]. Available: http://dx.doi.org/10.1038/s41598-020-78694-4

[377] J. Weickenmeier *et al.*, "Brain stiffness increases with myelin content," *Acta Biomaterialia*, vol. 42, pp. 265–272, Sep. 2016. [Online]. Available: http://dx.doi.org/10.1016/j.actbio.2016.07.040

[378] K. Holtzmann *et al.*, "Brain tissue stiffness is a sensitive marker for acidosis," *Journal of Neuroscience Methods*, vol. 271, pp. 50–54, Sep. 2016. [Online]. Available: http://dx.doi.org/10.1016/j.jneumeth.2016.07.002

[379] B. Rashid, M. Destrade, and M. D. Gilchrist, "Inhomogeneous deformation of brain tissue during tension tests," *Computational Materials Science*, vol. 64, pp. 295–300, Nov. 2012. [Online]. Available: http://dx.doi.org/10.1016/j.commatsci.2012.05.030

[380] ——, "Determination of friction coefficient in unconfined compression of brain tissue," *Journal of the Mechanical Behavior of Biomedical Materials*, vol. 14, pp. 163–171, Oct. 2012. [Online]. Available: http://dx.doi.org/10.1016/j.jmbbm.2012.05.001

[381] N. Reiter *et al.*, "Insights into the microstructural origin of brain viscoelasticity: Prospects for microstructure-informed constitutive modeling," *Journal of Elasticity*, vol. 145, no. 1-2, pp. 99–116, Jan. 2021. [Online]. Available: http://dx.doi.org/10.1007/s10659-021-09814-y

[382] W. Li, D. E. T. Shepherd, and D. M. Espino, "Investigation of the compressive viscoelastic properties of brain tissue under time and frequency dependent loading conditions," *Annals of Biomedical Engineering*, vol. 49, no. 12, pp. 3737–3747, Oct. 2021. [Online]. Available: http://dx.doi.org/10.1007/s10439-021-02866-0

[383] Z. Zhu, C. Jiang, and H. Jiang, "A visco-hyperelastic model of brain tissue incorporating both tension/compression asymmetry and volume compressibility," *Acta Mechanica*, vol. 230, no. 6, pp. 2125–2135, Mar. 2019. [Online]. Available: http://dx.doi.org/10.1007/s00707-019-02383-1

[384] B. Rashid, "Mechanical characterization of brain tissue in compression, tension and shear under dynamic conditions," Ph.D. dissertation, School of Mechanical and Materials Engineering, University College Dublin, 2012.

[385] B. Rashid, M. Destrade, and M. D. Gilchrist, "Hyperelastic and viscoelastic properties of brain tissue in tension," in *Volume 2: Biomedical and Biotechnology*, ser. IMECE2012. American Society of Mechanical Engineers, Nov. 2012. [Online]. Available: http://dx.doi.org/10.1115/IMECE2012-85675

[386] B. Mokri, "The monro-kellie hypothesis: Applications in CSF volume depletion," *Neurology*, vol. 56, no. 12, pp. 1746–1748, Jun. 2001. [Online]. Available: https://doi.org/10.1212/wnl.56.12.1746

[387] C. J. Cyron, R. C. Aydin, and J. D. Humphrey, "A homogenized constrained mixture (and mechanical analog) model for growth and remodeling of soft tissue," *Biomechanics and Modeling in Mechanobiology*, vol. 15, no. 6, pp. 1389–1403, Mar. 2016. [Online]. Available: http://dx.doi.org/10.1007/s10237-016-0770-9

[388] A. C. J. Kalisvaart *et al.*, "An update to the monro-kellie doctrine to reflect tissue compliance after severe ischemic and hemorrhagic stroke," *Scientific Reports*, vol. 10, no. 1, Dec. 2020. [Online]. Available: https://doi.org/10.1038/s41598-020-78880-4

[389] J. M. Barnes, L. Przybyla, and V. M. Weaver, "Tissue mechanics regulate brain development, homeostasis and disease," *Journal of Cell Science*, vol. 130, no. 1, pp. 71–82, Jan. 2017. [Online]. Available: http://dx.doi.org/10.1242/jcs.191742

[390] C. J. Cyron and J. D. Humphrey, "Growth and remodeling of load-bearing biological soft tissues," *Meccanica*, vol. 52, no. 3, pp. 645–664, Jun. 2016. [Online]. Available: http://dx.doi.org/10.1007/s11012-016-0472-5

[391] J. D. Humphrey, "Constrained mixture models of soft tissue growth and remodeling - twenty years after," *Journal of Elasticity*, vol. 145, no. 1-2, pp. 49–75, Jan. 2021. [Online]. Available: http://dx.doi.org/10.1007/s10659-020-09809-1

[392] S. Budday *et al.*, "Mechanical characterization of human brain tissue," *Acta Biomaterialia*, vol. 48, pp. 319–340, Jan. 2017. [Online]. Available: http://dx.doi.org/10.1016/j.actbio.2016.10.036

[393] G. A. Holzapfel and B. Fereidoonnezhad, *Modeling of Damage in Soft Biological Tissues*. Elsevier, 2017, pp. 101–123. [Online]. Available: http://dx.doi.org/10.1016/B978-0-12-804009-6.00005-5

[394] L. Saucedo-Mora *et al.*, "A two-parameter strain energy function for brain matter: An extension of the hencky model to incorporate locking," *Brain Multiphysics*, vol. 2, p. 100036, 2021. [Online]. Available: http://dx.doi.org/10.1016/j.brain.2021.100036

[395] F. Davenport *et al.*, "Neurodegenerative disease of the brain: a survey of interdisciplinary approaches," *Journal of The Royal Society Interface*, vol. 20, no. 198, Jan. 2023. [Online]. Available: https://doi.org/10.1098/rsif.2022.0406

[396] J. W. Vogel *et al.*, "Connectome-based modelling of neurodegenerative diseases: towards precision medicine and mechanistic insight," *Nature Reviews Neuroscience*, vol. 24, no. 10, pp. 620–639, Aug. 2023. [Online]. Available: http://dx.doi.org/10.1038/s41583-023-00731-8

[397] J. Zwirner *et al.*, "Mechanical properties of human dura mater in tension - an analysis at an age range of 2 to 94 years," *Scientific Reports*, vol. 9, no. 1, Nov. 2019. [Online]. Available: http://dx.doi.org/10.1038/s41598-019-52836-9

[398] A. E. Forte, S. M. Gentleman, and D. Dini, "On the characterization of the heterogeneous mechanical response of human brain tissue," *Biomechanics and Modeling in Mechanobiology*, vol. 16, no. 3, pp. 907–920, Dec. 2016. [Online]. Available: http://dx.doi.org/10.1007/s10237-016-0860-8

[399] R. R. Wilcox and G. A. Rousselet, "An updated guide to robust statistical methods in neuroscience," *Current Protocols*, vol. 3, no. 3, Mar. 2023. [Online]. Available: http://dx.doi.org/10.1002/cpz1.719

[400] D. D. Garrett *et al.*, "The importance of being variable," *The Journal of Neuroscience*, vol. 31, no. 12, pp. 4496–4503, Mar. 2011. [Online]. Available: http://dx.doi.org/10.1523/JNEUROSCI.5641-10.2011

[401] R. L. T. Goris, J. A. Movshon, and E. P. Simoncelli, "Partitioning neuronal variability," *Nature Neuroscience*, vol. 17, no. 6, pp. 858–865, Apr. 2014. [Online]. Available: http://dx.doi.org/10.1038/nn.3711

[402] R. Mizutani *et al.*, "Structural diverseness of neurons between brain areas and between cases," *Translational Psychiatry*, vol. 11, no. 1, Jan. 2021. [Online]. Available: http://dx.doi.org/10.1038/s41398-020-01173-x

[403] L. Waschke *et al.*, "Behavior needs neural variability," *Neuron*, vol. 109, no. 5, pp. 751–766, Mar. 2021. [Online]. Available: http://dx.doi.org/10.1016/j.neuron.2021.01.023

[404] P. M. Thompson *et al.*, "Three-dimensional statistical analysis of sulcal variability in the human brain," *The Journal of Neuroscience*, vol. 16, no. 13, pp. 4261–4274, Jul. 1996. [Online]. Available: http://dx.doi.org/10.1523/JNEUROSCI.16-13-04261.1996

[405] D. Bzdok, "Classical statistics and statistical learning in imaging neuroscience," *Frontiers in Neuroscience*, vol. 11, Oct. 2017. [Online]. Available: http://dx.doi.org/10.3389/fnins.2017.00543

[406] F. Bertacchini *et al.*, "Modelling brain dynamics by boolean networks," *Scientific Reports*, vol. 12, no. 1, Oct. 2022. [Online]. Available: http://dx.doi.org/10.1038/s41598-022-20979-x

[407] M. W. Macy and R. Willer, "From factors to actors: Computational sociology and agent-based modeling," *Annual Review of Sociology*, vol. 28, no. 1, pp. 143–166, Aug. 2002. [Online]. Available: http://dx.doi.org/10.1146/annurev.soc.28.110601.141117

[408] S. de Marchi and S. E. Page, "Agent-based models," *Annual Review of Political Science*, vol. 17, no. 1, pp. 1–20, May 2014. [Online]. Available: http://dx.doi.org/10.1146/annurev-polisci-080812-191558

[409] D. L. DeAngelis and S. G. Diaz, "Decision-making in agent-based modeling: A current review and future prospectus," *Frontiers in Ecology and Evolution*, vol. 6, Jan. 2019. [Online]. Available: http://dx.doi.org/10.3389/fevo.2018.00237

[410] R. Miller Neilan *et al.*, "Agent-based modeling of the central amygdala and pain using cell-type specific physiological parameters," *PLOS Computational Biology*, vol. 17, no. 6, p. e1009097, Jun. 2021. [Online]. Available: http://dx.doi.org/10.1371/journal.pcbi.1009097

[411] S. Avin, A. Currie, and S. H. Montgomery, "An agent-based model clarifies the importance of functional and developmental integration in shaping brain evolution," *BMC Biology*, vol. 19, no. 1, May 2021. [Online]. Available: http://dx.doi.org/10.1186/s12915-021-01024-1

[412] M. Tracy, M. Cerdá, and K. M. Keyes, "Agent-based modeling in public health: Current applications and future directions," *Annual Review of Public Health*, vol. 39, no. 1, pp. 77–94, Apr. 2018. [Online]. Available: http://dx.doi.org/10.1146/annurev-publhealth-040617-014317

[413] J. M. Benítez *et al.*, "A simple agent-based model to simulate 3d tumor-induced angiogenesis considering the evolution of the hypoxic conditions of the cells," *Engineering with Computers*, vol. 38, no. 5, pp. 4115–4133, Mar. 2022. [Online]. Available: https://doi.org/10.1007/s00366-022-01625-6

[414] L. Saucedo-Mora *et al.*, "A simple agent-based hybrid model to simulate the biophysics of glioblastoma multiforme cells and the concomitant evolution of the oxygen field," *Computer Methods and Programs in Biomedicine*, vol. 246, p. 108046, Apr. 2024. [Online]. Available: http://dx.doi.org/10.1016/j.cmpb.2024.108046

[415] N. Nagarajan and C. F. Stevens, "How does the speed of thought compare for brains and digital computers?" *Current Biology*, vol. 18, no. 17, pp. R756–R758, Sep. 2008. [Online]. Available: http://dx.doi.org/10.1016/j.cub.2008.06.043

[416] A. Rocha, E. Massad, and F. Coutinho, "Can the human brain do quantum computing?" *Medical Hypotheses*, vol. 63, no. 5, pp. 895–899, Jan. 2004. [Online]. Available: http://dx.doi.org/10.1016/j.mehy.2004.03.044

[417] S. R. Hameroff, "The brain is both neurocomputer and quantum computer," *Cognitive Science*, vol. 31, no. 6, pp. 1035–1045, Nov. 2007. [Online]. Available: http://dx.doi.org/10.1080/03640210701704004

[418] C. D. Schuman *et al.*, "Opportunities for neuromorphic computing algorithms and applications," *Nature Computational Science*, vol. 2, no. 1, pp. 10–19, Jan. 2022. [Online]. Available: http://dx.doi.org/10.1038/s43588-021-00184-y

[419] B. Rajendran *et al.*, "Low-power neuromorphic hardware for signal processing applications: A review of architectural and system-level design approaches," *IEEE Signal Processing Magazine*, vol. 36, no. 6, pp. 97–110, Nov. 2019. [Online]. Available: http://dx.doi.org/10.1109/MSP.2019.2933719

[420] D. Marković and J. Grollier, "Quantum neuromorphic computing," *Applied Physics Letters*, vol. 117, no. 15, Oct. 2020. [Online]. Available: http://dx.doi.org/10.1063/5.0020014

[421] J. S. Montijn *et al.*, "A parameter-free statistical test for neuronal responsiveness," *eLife*, vol. 10, Sep. 2021. [Online]. Available: http://dx.doi.org/10.7554/eLife.71969

[422] R. Yamashita *et al.*, "Convolutional neural networks: an overview and application in radiology," *Insights into Imaging*, vol. 9, no. 4, pp. 611–629, Jun. 2018. [Online]. Available: http://dx.doi.org/10.1007/s13244-018-0639-9

[423] J. Bernal *et al.*, "Deep convolutional neural networks for brain image analysis on magnetic resonance imaging: a review," *Artificial Intelligence in Medicine*, vol. 95, pp. 64–81, Apr. 2019. [Online]. Available: http://dx.doi.org/10.1016/j.artmed.2018.08.008

[424] A. Çinar and M. Yildirim, "Detection of tumors on brain mri images using the hybrid convolutional neural network architecture," *Medical Hypotheses*, vol. 139, p. 109684, Jun. 2020. [Online]. Available: http://dx.doi.org/10.1016/j.mehy.2020.109684

[425] A. Chattopadhyay and M. Maitra, "Mri-based brain tumour image detection using cnn based deep learning method," *Neuroscience Informatics*, vol. 2, no. 4, p. 100060, Dec. 2022. [Online]. Available: http://dx.doi.org/10.1016/j.neuri.2022.100060

[426] M. M. Badža and M. v. Barjaktarović, "Classification of brain tumors from mri images using a convolutional neural network," *Applied Sciences*, vol. 10, no. 6, p. 1999, Mar. 2020. [Online]. Available: http://dx.doi.org/10.3390/app10061999

[427] W. Lin *et al.*, "Convolutional neural networks-based mri image analysis for the alzheimer's disease prediction from mild cognitive impairment," *Frontiers in Neuroscience*, vol. 12, Nov. 2018. [Online]. Available: http://dx.doi.org/10.3389/fnins.2018.00777

[428] J. Vreeken, "Spiking neural networks, an introduction," 2003. [Online]. Available: https://www.semanticscholar.org/paper/Spiking-neural-networks%2C-an-introduction-Vreeken/4ced5f507d2ca65c35580bcd1709969650171a55#citing-papers

[429] S. Ghosh-Dastidar and H. Adeli, "Spiking neural networks," *International Journal of Neural Systems*, vol. 19, no. 04, pp. 295–308, Aug. 2009. [Online]. Available: http://dx.doi.org/10.1142/S0129065709002002

[430] K. Yamazaki *et al.*, "Spiking neural networks and their applications: A review," *Brain Sciences*, vol. 12, no. 7, p. 863, Jun. 2022. [Online]. Available: http://dx.doi.org/10.3390/brainsci12070863

[431] N. Kasabov and E. Capecci, "Spiking neural network methodology for modelling, classification and understanding of eeg spatio-temporal data measuring cognitive processes," *Information Sciences*, vol. 294, pp. 565–575, Feb. 2015. [Online]. Available: http://dx.doi.org/10.1016/j.ins.2014.06.028

[432] F. Wang, O. Sigmund, and J. Jensen, "Design of materials with prescribed nonlinear properties," *Journal of the Mechanics and Physics of Solids*, vol. 69, p. 156–174, Sep. 2014. [Online]. Available: http://dx.doi.org/10.1016/j.jmps.2014.05.003

[433] A. Tavanaei and A. Maida, "Bp-stdp: Approximating backpropagation using spike timing dependent plasticity," *Neurocomputing*, vol. 330, pp. 39–47, Feb. 2019. [Online]. Available: http://dx.doi.org/10.1016/j.neucom.2018.11.014

[434] Y. Gong *et al.*, "Lightweight spiking neural network training based on spike timing dependent backpropagation," *Neurocomputing*, p. 127059, Nov. 2023. [Online]. Available: http://dx.doi.org/10.1016/j.neucom.2023.127059

[435] A. R. Young *et al.*, "A review of spiking neuromorphic hardware communication systems," *IEEE Access*, vol. 7, pp. 135 606–135 620, 2019. [Online]. Available: http://dx.doi.org/10.1109/ACCESS.2019.2941772

[436] P. K. Huynh *et al.*, "Implementing spiking neural networks on neuromorphic architectures: A review," 2022. [Online]. Available: https://arxiv.org/abs/2202.08897

[437] A. Crimi *et al.*, "Multilink analysis: Brain network comparison via sparse connectivity analysis," *Scientific Reports*, vol. 9, no. 1, Jan. 2019. [Online]. Available: http://dx.doi.org/10.1038/s41598-018-37300-4

[438] Y. Iturria-Medina *et al.*, "Studying the human brain anatomical network via diffusion-weighted mri and graph theory," *NeuroImage*, vol. 40, no. 3, pp. 1064–1076, Apr. 2008. [Online]. Available: http://dx.doi.org/10.1016/j.neuroimage.2007.10.060

[439] A. Fornito, A. Zalesky, and M. Breakspear, "Graph analysis of the human connectome: Promise, progress, and pitfalls," *NeuroImage*, vol. 80, pp. 426–444, Oct. 2013. [Online]. Available: http://dx.doi.org/10.1016/j.neuroimage.2013.04.087

[440] G. Martensson *et al.*, "Stability of graph theoretical measures in structural brain networks in alzheimer's disease," *Scientific Reports*, vol. 8, no. 1, Aug. 2018. [Online]. Available: https://doi.org/10.1038/s41598-018-29927-0

[441] F. V. Farahani, W. Karwowski, and N. R. Lighthall, "Application of graph theory for identifying connectivity patterns in human brain networks: A systematic review," *Frontiers in Neuroscience*, vol. 13, Jun. 2019. [Online]. Available: http://dx.doi.org/10.3389/fnins.2019.00585

[442] A. Sankar *et al.*, "Graph theory analysis of whole brain functional connectivity to assess disturbances associated with suicide attempts in bipolar disorder," *Translational Psychiatry*, vol. 12, no. 1, Jan. 2022. [Online]. Available: http://dx.doi.org/10.1038/s41398-021-01767-z

[443] J. H. Smith *et al.*, "How neurons exploit fractal geometry to optimize their network connectivity," *Scientific Reports*, vol. 11, no. 1, Jan. 2021. [Online]. Available: http://dx.doi.org/10.1038/s41598-021-81421-2

[444] L. Zheng *et al.*, "Unifying the design space and optimizing linear and nonlinear truss metamaterials by generative modeling," *Nature Communications*, vol. 14, no. 1, Nov. 2023. [Online]. Available: http://dx.doi.org/10.1038/s41467-023-42068-x

[445] A. Bowyer, "Computing dirichlet tessellations," *The Computer Journal*, vol. 24, no. 2, pp. 162–166, Feb. 1981. [Online]. Available: https://doi.org/10.1093/comjnl/24.2.162

[446] D. F. Watson, "Computing the n-dimensional delaunay tessellation with application to voronoi polytopes," *The Computer Journal*, vol. 24, no. 2, pp. 167–172, Feb. 1981. [Online]. Available: https://doi.org/10.1093/comjnl/24.2.167

[447] J. S. Przemieniecki, *Theory of matrix structural analysis*. Courier Corporation, 1985.

[448] K. Hornik, M. Stinchcombe, and H. White, "Multilayer feedforward networks are universal approximators," *Neural networks*, vol. 2, no. 5, pp. 359–366, 1989.

[449] G. Klambauer *et al.*, "Self-normalizing neural networks," *Advances in neural information processing systems*, vol. 30, 2017.

[450] D. González, F. Chinesta, and E. Cueto, "Learning non-markovian physics from data," *Journal of Computational Physics*, vol. 428, p. 109982, 2021. [Online]. Available: https://www.sciencedirect.com/science/article/pii/S0021999120307567

[451] J. L. Proctor, S. L. Brunton, and J. N. Kutz, "Dynamic mode decomposition with control," *SIAM Journal on Applied Dynamical Systems*, vol. 15, no. 1, p. 142–161, Jan. 2016. [Online]. Available: http://dx.doi.org/10.1137/15M1013857

[452] A. G. Baydin *et al.*, "Automatic differentiation in machine learning: a survey," *Journal of Marchine Learning Research*, vol. 18, pp. 1–43, 2018.

[453] S. P. Boyd and L. Vandenberghe, *Convex optimization*. Cambridge university press, 2004.

[454] C. R. Farrar and K. Worden, "An introduction to structural health monitoring," *Philosophical Transactions of the Royal Society A: Mathematical, Physical and Engineering Sciences*, vol. 365, no. 1851, p. 303–315, Dec. 2006. [Online]. Available: http://dx.doi.org/10.1098/rsta.2006.1928

[455] J. Mueller and K. Shea, "Buckling, build orientation, and scaling effects in 3d printed lattices," *Materials Today Communications*, vol. 17, p. 69–75, Dec. 2018. [Online]. Available: http://dx.doi.org/10.1016/j.mtcomm.2018.08.013

[456] Y. Zhao, Y. Chen, and Y. Zhou, "Novel mechanical models of tensile strength and elastic property of fdm am pla materials: Experimental and theoretical analyses," *Materials and Design*, vol. 181, p. 108089, Nov. 2019. [Online]. Available: http://dx.doi.org/10.1016/j.matdes.2019.108089

[457] O. Sigmund, "Manufacturing tolerant topology optimization," *Acta Mechanica Sinica*, vol. 25, no. 2, p. 227–239, Mar. 2009. [Online]. Available: http://dx.doi.org/10.1007/s10409-009-0240-z

[458] M. Bruggi and P. Duysinx, "Topology optimization for minimum weight with compliance and stress constraints," *Structural and Multidisciplinary Optimization*, vol. 46, no. 3, p. 369–384, Jan. 2012. [Online]. Available: http://dx.doi.org/10.1007/s00158-012-0759-7

[459] B. Zhu *et al.*, "Design of compliant mechanisms using continuum topology optimization: A review," *Mechanism and Machine Theory*, vol. 143, p. 103622, Jan. 2020. [Online]. Available: http://dx.doi.org/10.1016/j.mechmachtheory.2019.103622

[460] P. D. Dunning and H. A. Kim, "Robust topology optimization: Minimization of expected and variance of compliance," *AIAA Journal*, vol. 51, no. 11, p. 2656–2664, Nov. 2013. [Online]. Available: http://dx.doi.org/10.2514/1.J052183

[461] M. Arredondo-Soto, E. Cuan-Urquizo, and A. Gómez-Espinosa, "A review on tailoring stiffness in compliant systems, via removing material: Cellular materials and topology optimization," *Applied Sciences*, vol. 11, no. 8, p. 3538, Apr. 2021. [Online]. Available: http://dx.doi.org/10.3390/app11083538

[462] S. Koppen, "Topology optimization of compliant mechanisms with multiple degrees of freedom," Ph.D. dissertation, Computational Design and Mechanics, 2022. [Online]. Available: http://resolver.tudelft.nl/uuid:21994a92-e365-4679-b6ac-11a2b70572b7

[463] M. P. Bendsøe and O. Sigmund, "Material interpolation schemes in topology optimization," *Archive of Applied Mechanics (Ingenieur Archiv)*, vol. 69, no. 9–10, p. 635–654, Nov. 1999. [Online]. Available: http://dx.doi.org/10.1007/s004190050248

[464] M. Stolpe and K. Svanberg, "An alternative interpolation scheme for minimum compliance topology optimization," *Structural and Multidisciplinary Optimization*, vol. 22, no. 2, p. 116–124, Sep. 2001. [Online]. Available: http://dx.doi.org/10.1007/s001580100129

[465] W. Zuo and K. Saitou, "Multi-material topology optimization using ordered simp interpolation," *Structural and Multidisciplinary Optimization*, vol. 55, no. 2, p. 477–491, Jun. 2016. [Online]. Available: http://dx.doi.org/10.1007/s00158-016-1513-3

[466] J. M. Hughes and M. A. Petit, "Biological underpinnings of frost's mechanostat thresholds: the important role of osteocytes," *Journal of Musculoskeletal and Neuronal Interactions (JMNI)*, vol. 2, no. 10, pp. 128–135, 2010. [Online]. Available: https://pubmed.ncbi.nlm.nih.gov/20516629/

[467] J. Wolff, *The Law of Bone Remodelling*. Springer Berlin Heidelberg, 1986. [Online]. Available: http://dx.doi.org/10.1007/978-3-642-71031-5

[468] H. M. Frost, "Bone "mass" and the "mechanostat": A proposal," *The Anatomical Record*, vol. 219, no. 1, p. 1–9, Sep. 1987. [Online]. Available: http://dx.doi.org/10.1002/ar.1092190104

[469] R. Huiskes *et al.*, "Adaptive bone-remodeling theory applied to prosthetic-design analysis," *Journal of Biomechanics*, vol. 20, no. 11–12, p. 1135–1150, Jan. 1987. [Online]. Available: http://dx.doi.org/10.1016/0021-9290(87)90030-3

[470] R. Huiskes, "If bone is the answer, then what is the question?" *Journal of Anatomy*, vol. 197, no. 2, p. 145–156, Aug. 2000. [Online]. Available: http://dx.doi.org/10.1046/j.1469-7580.2000.19720145.x

[471] H. Weinans, R. Huiskes, and H. Grootenboer, "The behavior of adaptive bone-remodeling simulation models," *Journal of Biomechanics*, vol. 25, no. 12, p. 1425–1441, Dec. 1992. [Online]. Available: http://dx.doi.org/10.1016/0021-9290(92)90056-7

[472] G. Leuba and L. Garey, "Comparison of neuronal and glial numerical density in primary and secondary visual cortex of man," *Experimental Brain Research*, vol. 77, no. 1, 1989. [Online]. Available: https://doi.org/10.1007/bf00250564

[473] S. Rebay, "Efficient unstructured mesh generation by means of delaunay triangulation and bowyer-watson algorithm," *Journal of Computational Physics*, vol. 106, no. 1, pp. 125–138, May 1993. [Online]. Available: https://doi.org/10.1006/jcph.1993.1097

[474] S. Abar *et al.*, "Agent based modelling and simulation tools: A review of the state-of-art software," *Computer Science Review*, vol. 24, p. 13–33, May 2017. [Online]. Available: http://dx.doi.org/10.1016/j.cosrev.2017.03.001

[475] S. Sahara *et al.*, "The fraction of cortical gabaergic neurons is constant from near the start of cortical neurogenesis to adulthood," *The Journal of Neuroscience*, vol. 32, no. 14, p. 4755–4761, Apr. 2012. [Online]. Available: http://dx.doi.org/10.1523/JNEUROSCI.6412-11.2012

[476] L. Luo and D. D. O'Leary, "Axon retraction and degeneration in development and disease," *Annual Review of Neuroscience*, vol. 28, no. 1, pp. 127–156, Jul. 2005. [Online]. Available: https://doi.org/10.1146/annurev.neuro.28.061604.135632

[477] A. Citri and R. C. Malenka, "Synaptic plasticity: Multiple forms, functions, and mechanisms," *Neuropsychopharmacology*, vol. 33, no. 1, pp. 18–41, Aug. 2007. [Online]. Available: https://doi.org/10.1038/sj.npp.1301559

[478] X. Glorot and Y. Bengio, "Understanding the difficulty of training deep feedforward neural networks," in *Proceedings of the Thirteenth International Conference on Artificial Intelligence and Statistics*, ser. Proceedings of Machine Learning Research, Y. W. Teh and M. Titterington, Eds., vol. 9. Chia Laguna Resort, Sardinia, Italy: PMLR, 13–15 May 2010, pp. 249–256. [Online]. Available: https://proceedings.mlr.press/v9/glorot10a.html

[479] M. Zaiser and S. Zapperi, "Disordered mechanical metamaterials," *Nature Reviews Physics*, vol. 5, no. 11, p. 679–688, Sep. 2023. [Online]. Available: http://dx.doi.org/10.1038/s42254-023-00639-3

[480] M. Bagge, "A model of bone adaptation as an optimization process," *Journal of Biomechanics*, vol. 33, no. 11, p. 1349–1357, Nov. 2000. [Online]. Available: http://dx.doi.org/10.1016/s0021-9290(00)00124-x

[481] A. Andrade-Campos, A. Ramos, and J. A. Simões, "A model of bone adaptation as a topology optimization process with contact," *Journal of Biomedical Science and Engineering*, vol. 05, no. 05, p. 229–244, 2012. [Online]. Available: http://dx.doi.org/10.4236/jbise.2012.55030

[482] N. Pashine, "Local rules for fabricating allosteric networks," *Physical Review Materials*, vol. 5, no. 6, Jun. 2021. [Online]. Available: http://dx.doi.org/10.1103/PhysRevMaterials.5.065607

[483] L. Yan *et al.*, "Architecture and coevolution of allosteric materials," *Proceedings of the National Academy of Sciences*, vol. 114, no. 10, p. 2526–2531, Feb. 2017. [Online]. Available: http://dx.doi.org/10.1073/pnas.1615536114

[484] ——, "Principles for optimal cooperativity in allosteric materials," *Biophysical Journal*, vol. 114, no. 12, p. 2787–2798, Jun. 2018. [Online]. Available: http://dx.doi.org/10.1016/j.bpj.2018.05.015

[485] R. Valle *et al.*, "Design and characterization of asymmetric cell structure of auxetic material for predictable directional mechanical response," *Materials*, vol. 15, no. 5, p. 1841, Mar. 2022. [Online]. Available: http://dx.doi.org/10.3390/ma15051841

[486] L. Irastorza-Valera and L. Saucedo-Mora, "Probabilistic combination of loads in topology optimization designs via cumulative damage criteria," 2025. [Online]. Available: https://arxiv.org/abs/2503.19807

[487] O. Sigmund, "Morphology-based black and white filters for topology optimization," *Structural and Multidisciplinary Optimization*, vol. 33, no. 4–5, p. 401–424, Jan. 2007. [Online]. Available: http://dx.doi.org/10.1007/s00158-006-0087-x

[488] L. Irastorza-Valera *et al.*, "Mechanostat-type effective density correction for carter-hayes growth applied to topology optimization and its efficient interpolation for a target strain energy and volume fraction," 2025. [Online]. Available: https://arxiv.org/abs/2503.21456

[489] S. Chowdhury *et al.*, "Laser powder bed fusion: a state-of-the-art review of the technology, materials, properties and defects, and numerical modelling," *Journal of Materials Research and Technology*, vol. 20, p. 2109–2172, Sep. 2022. [Online]. Available: http://dx.doi.org/10.1016/j.jmrt.2022.07.121

[490] L. Irastorza-Valera *et al.*, "Numerical reproduction of the sherrington-adrian observations through a community of mcculloch-pitts neurons with plastic remodelling," *bioRxiv*, Dec. 2023. [Online]. Available: http://dx.doi.org/10.1101/2023.12.05.570084

[491] E. D. Adrian, "The spread of activity in the cerebral cortex," *The Journal of Physiology*, vol. 88, no. 2, p. 127–161, Nov. 1936. [Online]. Available: http://dx.doi.org/10.1113/jphysiol.1936.sp003427

[492] D. N. Levine, "Sherrington's "the integrative action of the nervous system": A centennial appraisal," *Journal of the Neurological Sciences*, vol. 253, no. 1–2, p. 1–6, Feb. 2007. [Online]. Available: http://dx.doi.org/10.1016/j.jns.2006.12.002

[493] C. Sherrington, "The integrative action of the nervous system," *Nature*, vol. 76, no. 1962, p. 122–122, Jun. 1907. [Online]. Available: http://dx.doi.org/10.1038/076122a0

[494] N. K. Logothetis, C. Kayser, and A. Oeltermann, "In vivo measurement of cortical impedance spectrum in monkeys: Implications for signal propagation," *Neuron*, vol. 55, no. 5, p. 809–823, Sep. 2007. [Online]. Available: http://dx.doi.org/10.1016/j.neuron.2007.07.027

[495] C. G. McNamara, M. Rothwell, and A. Sharott, "Stable, interactive modulation of neuronal oscillations produced through brain-machine equilibrium," *Cell Reports*, vol. 41, no. 6, p. 111616, Nov. 2022. [Online]. Available: http://dx.doi.org/10.1016/j.celrep.2022.111616

[496] R. Ganji *et al.*, "A mathematical model and numerical solution for brain tumor derived using fractional operator," *Results in Physics*, vol. 28, p. 104671, Sep. 2021. [Online]. Available: http://dx.doi.org/10.1016/j.rinp.2021.104671

[497] M. Nolte *et al.*, "Cortical reliability amid noise and chaos," *Nature Communications*, vol. 10, no. 1, Aug. 2019. [Online]. Available: http://dx.doi.org/10.1038/s41467-019-11633-8

[498] G. Bouallegue, R. Djemal, and K. Belwafi, "Artificial eeg signal generated by a network of neurons with one and two dendrites," *Results in Physics*, vol. 20, p. 103699, Jan. 2021. [Online]. Available: http://dx.doi.org/10.1016/j.rinp.2020.103699

[499] G. Fuhrmann, H. Markram, and M. Tsodyks, "Spike frequency adaptation and neocortical rhythms," *Journal of Neurophysiology*, vol. 88, no. 2, p. 761–770, Aug. 2002. [Online]. Available: http://dx.doi.org/10.1152/jn.2002.88.2.761

[500] X. Zheng *et al.*, "Controllable inverse design of auxetic metamaterials using deep learning," *Materials & Design*, vol. 211, p. 110178, Dec. 2021. [Online]. Available: https://doi.org/10.1016/j.matdes.2021.110178

[501] A. Challapalli, D. Patel, and G. Li, "Inverse machine learning framework for optimizing lightweight metamaterials," *Materials and Design*, vol. 208, p. 109937, Oct. 2021. [Online]. Available: http://dx.doi.org/10.1016/j.matdes.2021.109937

[502] S. C.-y. Shen and M. J. Buehler, "Nature-inspired architected materials using unsupervised deep learning," *Communications Engineering*, vol. 1, no. 1, Nov. 2022. [Online]. Available: http://dx.doi.org/10.1038/s44172-022-00037-0

[503] X. Zheng *et al.*, "Deep-learning-based inverse design of three-dimensional architected cellular materials with the target porosity and stiffness using voxelized voronoi lattices," *Science and Technology of Advanced Materials*, vol. 24, no. 1, Jan. 2023. [Online]. Available: http://dx.doi.org/10.1080/14686996.2022.2157682

[504] I. Ben-Yelun *et al.*, "Gam: General auxetic metamaterial with tunable 3d auxetic behavior using the same unit cell boundary connectivity," *Materials*, vol. 16, no. 9, p. 3473, 2023.

[505] S. Kumar *et al.*, "Inverse-designed spinodoid metamaterials," *npj Computational Materials*, vol. 6, no. 1, Jun. 2020. [Online]. Available: http://dx.doi.org/10.1038/s41524-020-0341-6

[506] H. T. Kollmann *et al.*, "Deep learning for topology optimization of 2d metamaterials," *Materials and Design*, vol. 196, p. 109098, Nov. 2020. [Online]. Available: http://dx.doi.org/10.1016/j.matdes.2020.109098

[507] C. Qiu, S. Du, and J. Yang, "A deep learning approach for efficient topology optimization based on the element removal strategy," *Materials and Design*, vol. 212, p. 110179, Dec. 2021. [Online]. Available: http://dx.doi.org/10.1016/j.matdes.2021.110179

[508] L. Francesconi *et al.*, "An investigation of the enhanced fatigue performance of low-porosity auxetic metamaterials," *Experimental Mechanics*, vol. 60, no. 1, pp. 93–107, Sep. 2019. [Online]. Available: https://doi.org/10.1007/s11340-019-00539-7

[509] V. Lvov *et al.*, "Low-cycle fatigue behavior of 3d-printed metallic auxetic structure," *Materials Today: Proceedings*, vol. 33, pp. 1979–1983, 2020. [Online]. Available: https://doi.org/10.1016/j.matpr.2020.06.130

[510] R. Hedayati *et al.*, "Computational prediction of the fatigue behavior of additively manufactured porous metallic biomaterials," *International Journal of Fatigue*, vol. 84, pp. 67–79, Mar. 2016. [Online]. Available: https://doi.org/10.1016/j.ijfatigue.2015.11.017

[511] B. V. Hooreweder *et al.*, "Improving the fatigue performance of porous metallic biomaterials produced by selective laser melting," *Acta Biomaterialia*, vol. 47, pp. 193–202, Jan. 2017. [Online]. Available: https://doi.org/10.1016/j.actbio.2016.10.005

[512] S. Ahmadi *et al.*, "Fatigue performance of additively manufactured meta-biomaterials: The effects of topology and material type," *Acta Biomaterialia*, vol. 65, pp. 292–304, Jan. 2018. [Online]. Available: https://doi.org/10.1016/j.actbio.2017.11.014

[513] H. Kolken *et al.*, "Fatigue performance of auxetic meta-biomaterials," *Acta Biomaterialia*, vol. 126, pp. 511–523, May 2021. [Online]. Available: https://doi.org/10.1016/j.actbio.2021.03.015

[514] D. Barba *et al.*, "On the fatigue performance of additively manufactured metamaterials: A combined experimental and simulation study," in *The Minerals, Metals & Materials Series*. Springer Nature Switzerland, 2023, pp. 91–101. [Online]. Available: https://doi.org/10.1007/978-3-031-22524-6_10

[515] Z. Vangelatos, G. X. Gu, and C. P. Grigoropoulos, "Architected metamaterials with tailored 3d buckling mechanisms at the microscale," *Extreme Mechanics Letters*, vol. 33, p. 100580, Nov. 2019. [Online]. Available: https://doi.org/10.1016/j.eml.2019.100580

[516] V. A. Eremeyev and E. Turco, "Enriched buckling for beam-lattice metamaterials," *Mechanics Research Communications*, vol. 103, p. 103458, Jan. 2020. [Online]. Available: https://doi.org/10.1016/j.mechrescom.2019.103458

[517] J. B. Pascual-Francisco *et al.*, "Additive manufacturing and viscoelasticity evaluation of bézier metamaterials fabricated via vat photopolymerization," *Additive Manufacturing*, vol. 60, p. 103281, Dec. 2022. [Online]. Available: https://doi.org/10.1016/j.addma.2022.103281

[518] K. M. Fitzgerald *et al.*, "Compressive creep buckling of single cell metamaterial at elevated temperatures," *Fatigue & Fracture of Engineering Materials & Structures*, vol. 46, no. 2, pp. 366–378, Oct. 2022. [Online]. Available: https://doi.org/10.1111/ffe.13871

[519] O. Sigmund and J. Søndergaard Jensen, "Systematic design of phononic band–gap materials and structures by topology optimization," *Philosophical Transactions of the Royal Society of London. Series A: Mathematical, Physical and Engineering Sciences*, vol. 361, no. 1806, p. 1001–1019, Mar. 2003. [Online]. Available: http://dx.doi.org/10.1098/rsta.2003.1177

[520] A. R. Diaz and O. Sigmund, "A topology optimization method for design of negative permeability metamaterials," *Structural and Multidisciplinary Optimization*, vol. 41, no. 2, p. 163–177, Jul. 2009. [Online]. Available: http://dx.doi.org/10.1007/s00158-009-0416-y

[521] Y. Wang, F. Chen, and M. Y. Wang, "Concurrent design with connectable graded microstructures," *Computer Methods in Applied Mechanics and Engineering*, vol. 317, p. 84–101, Apr. 2017. [Online]. Available: http://dx.doi.org/10.1016/j.cma.2016.12.007

[522] O. Sigmund, *Systematic Design of Metamaterials by Topology Optimization*. Springer Netherlands, 2009, p. 151–159. [Online]. Available: http://dx.doi.org/10.1007/978-1-4020-9557-3_16

[523] G. Nika and A. Constantinescu, "Design of multi-layer materials using inverse homogenization and a level set method," *Computer Methods in Applied Mechanics and Engineering*, vol. 346, p. 388–409, Apr. 2019. [Online]. Available: http://dx.doi.org/10.1016/j.cma.2018.11.029

[524] R. Bellman, "On a routing problem," *Quarterly of Applied Mathematics*, vol. 16, no. 1, pp. 87–90, 1958. [Online]. Available: https://doi.org/10.1090/qam/102435

[525] D. B. Johnson, "Efficient algorithms for shortest paths in sparse networks," *Journal of the ACM*, vol. 24, no. 1, pp. 1–13, Jan. 1977. [Online]. Available: https://doi.org/10.1145/321992.321993

[526] R. W. Floyd, "Algorithm 97: Shortest path," *Communications of the ACM*, vol. 5, no. 6, p. 345, Jun. 1962. [Online]. Available: https://doi.org/10.1145/367766.368168

[527] N. Broutin and O. Fawzi, "Longest path distance in random circuits," *Combinatorics, Probability and Computing*, vol. 21, no. 6, pp. 856–881, Jul. 2012. [Online]. Available: https://doi.org/10.1017/s0963548312000260

[528] E. Ando, "The distribution function of the longest path length in constant treewidth dags with random edge length," 2019. [Online]. Available: https://arxiv.org/abs/1910.09791

[529] G. Madraki and R. P. Judd, "Recalculating the length of the longest path in perturbed directed acyclic graph," *IFAC-PapersOnLine*, vol. 52, no. 13, pp. 1560–1565, 2019. [Online]. Available: https://doi.org/10.1016/j.ifacol.2019.11.422

[530] M. B. Dillencourt, "Finding hamiltonian cycles in delaunay triangulations is NP-complete," *Discrete Applied Mathematics*, vol. 64, no. 3, pp. 207–217, Feb. 1996. [Online]. Available: https://doi.org/10.1016/0166-218x(94)00125-w

[531] M. B. Dillencourt and W. D. Smith, "Graph-theoretical conditions for inscribability and delaunay realizability," *Discrete Mathematics*, vol. 161, no. 1-3, pp. 63–77, Dec. 1996. [Online]. Available: https://doi.org/10.1016/0012-365x(95)00276-3

[532] S. Oldham and A. Fornito, "The development of brain network hubs," *Developmental Cognitive Neuroscience*, vol. 36, p. 100607, Apr. 2019. [Online]. Available: https://doi.org/10.1016/j.dcn.2018.12.005

[533] Y. Kim *et al.*, "Deep learning framework for material design space exploration using active transfer learning and data augmentation," *npj Computational Materials*, vol. 7, no. 1, Sep. 2021. [Online]. Available: http://dx.doi.org/10.1038/s41524-021-00609-2

[534] A. J. Lew, K. Jin, and M. J. Buehler, "Designing architected materials for mechanical compression via simulation, deep learning, and experimentation," *npj Computational Materials*, vol. 9, no. 1, May 2023. [Online]. Available: http://dx.doi.org/10.1038/s41524-023-01036-1

[535] T. Meier *et al.*, "Obtaining auxetic and isotropic metamaterials in counterintuitive design spaces: an automated optimization approach and experimental characterization," *npj Computational Materials*, vol. 10, no. 1, Jan. 2024. [Online]. Available: http://dx.doi.org/10.1038/s41524-023-01186-2

[536] S. Zhu *et al.*, "Bioinspired structural hydrogels with highly ordered hierarchical orientations by flow-induced alignment of nanofibrils," *Nature Communications*, vol. 15, no. 1, Jan. 2024. [Online]. Available: http://dx.doi.org/10.1038/s41467-023-44481-8

[537] P. C. H. Nguyen *et al.*, "Synthesizing controlled microstructures of porous media using generative adversarial networks and reinforcement learning," *Scientific Reports*, vol. 12, no. 1, May 2022. [Online]. Available: http://dx.doi.org/10.1038/s41598-022-12845-7

[538] H. Qin, D. Yang, and C. Ren, "Design method of lightweight metamaterials with arbitrary poisson's ratio," *Materials*, vol. 11, no. 9, p. 1574, Sep. 2018. [Online]. Available: http://dx.doi.org/10.3390/ma11091574

[539] X. Zheng *et al.*, "Minimal-surface-based multiphase metamaterials with highly variable stiffness," *Materials and Design*, vol. 237, p. 112548, Jan. 2024. [Online]. Available: http://dx.doi.org/10.1016/j.matdes.2023.112548

[540] I. Ben-Yelun *et al.*, "Topology optimization approach for functionally graded metamaterial components based on homogenization of mechanical variables," *Computers & Structures*, vol. 289, p. 107151, 2023.

[541] K. Svanberg, "The method of moving asymptotes—a new method for structural optimization," *International Journal for Numerical Methods in Engineering*, vol. 24, no. 2, p. 359–373, Feb. 1987. [Online]. Available: http://dx.doi.org/10.1002/nme.1620240207

[542] K. E. Joyce, S. Hayasaka, and P. J. Laurienti, "A genetic algorithm for controlling an agent-based model of the functional human brain," *Biomedical Sciences Instrumentation*, no. 48, pp. 210–217, Apr. 2013.

[543] R. F. Betzel and D. S. Bassett, "Multi-scale brain networks," *NeuroImage*, vol. 160, pp. 73–83, Oct. 2017. [Online]. Available: https://doi.org/10.1016/j.neuroimage.2016.11.006

[544] B. Rashid, M. Destrade, and M. D. Gilchrist, "Mechanical characterization of brain tissue in tension at dynamic strain rates," *Journal of the Mechanical Behavior of Biomedical Materials*, vol. 33, pp. 43–54, May 2014. [Online]. Available: https://doi.org/10.1016/j.jmbbm.2012.07.015

[545] C. J. Cyron and J. D. Humphrey, "Growth and remodeling of load-bearing biological soft tissues," *Meccanica*, vol. 52, no. 3, pp. 645–664, Jun. 2016. [Online]. Available: https://doi.org/10.1007/s11012-016-0472-5

[546] F. Morin *et al.*, "Biomechanical modeling of brain soft tissues for medical applications," in *Biomechanics of Living Organs*. Elsevier, 2017, pp. 127–146. [Online]. Available: https://doi.org/10.1016/b978-0-12-804009-6.00006-7

[547] L. A. Mihai *et al.*, "A family of hyperelastic models for human brain tissue," *Journal of the Mechanics and Physics of Solids*, vol. 106, pp. 60–79, Sep. 2017. [Online]. Available: https://doi.org/10.1016/j.jmps.2017.05.015

[548] R. D. Fields, D. H. Woo, and P. J. Basser, "Glial regulation of the neuronal connectome through local and long-distant communication," *Neuron*, vol. 86, no. 2, pp. 374–386, Apr. 2015. [Online]. Available: https://doi.org/10.1016/j.neuron.2015.01.014

Luis IRASTORZA VALERA
Learning Techniques for Optimization in Engineering: Data-driven tools for Mechanical and Biomedical Settings

Résumé : Dans les industries automotive et aéronautique, les structures doivent s'adapter aux besoins les plus exigeants. En même temps, des raisons mécaniques et économiques privilégient des options plus légères. Dans certains cas, le comportement des matériaux structurels doit être graduel, comme chez les composites ou les matériaux architecturés, dits métamatériaux. Les géométries de ces designs dans l'échelle micro offrent des propriétés macro introuvables dans les milieux continus, dans le moindre volume. En revanche, leur versatilité pose des problèmes pour les modéliser (problème direct) et concevoir (problème inverse).

Le problème direct, c'est-à-dire, décrire la performance d'un matériau architecturé de géométrie prédéfinie, devient parfois intraitable par les méthodes traditionnelles de calcul structurel à cause de la non-linéarité et complexité générale de son comportement. Ainsi, la définition d'un modèle purement analytique (comme la loi d'Hooke chez les matériaux isotropes) n'est pas pratique car les variables nécessaires sont trop nombreuses et/ou partiellement inconnues (dits internes ou non observables).

Pourtant, la seule solution est parfois de créer des modèles substitutifs qui puissent capturer les caractéristiques principales de la réponse mécanique de la structure en réduisant le coût de calcul, comme la réduction de l'ordre des modèles (MOR) et l'apprentissage automatique (ML).

Le problème inverse s'occupe d'une tâche beaucoup plus difficile, celle de trouver la structure (géométrie, matériau, etc.) qui donne les propriétés souhaitées. C'est un enjeu car il n'y a pas de solution unique et souvent la formulation mathématique du problème est mal conditionnée pour en trouver une (non-convexité). Des méthodes d'optimisation topologique sont employés, notamment en pénalisant les solides isotropes (SIMP) en enlevant du matériau jusqu'au minimum nécessaire pour supporter la charge appliquée avec la moindre énergie de déformation. Cette approche doit considérer les propriétés réelles du matériau (anisotropie, fatigue) ainsi que les conditions pratiques de fabrication et usage ; introduits comme des pénalisations, filtres d'image ou même nouvelles algorithmes. Tout cela permet de construire un modèle d'apprentissage automatique pour simplifier et, pourtant, accélérer le processus d'optimisation.

En tant qu'objet mathématique, les graphes offrent de multiples possibilités pour la représentation compacte de données avec des états comme vertex et leurs interrelations comme segments. Cette analogie s'applique directement aux deux principaux cas d'étude qui concernent ce travail, à savoir les structures mécaniques (centrées sur les métamatériaux) et les réseaux neuronaux biologiques, pouvant dans les deux cas assimiler des nœuds/neurones comme vertex et des poutres/axons comme segments d'un graphe. De cette façon, on profite des méthodologies développées pour créer un jumeau numérique basique du cerveau humain pour améliorer les diagnoses médicales.

Mots clés : Modèles réduits, Apprentissage automatique, Métamatériaux, Neuroscience, Jumeaux digitaux

Abstract: In the automotive and aeronautical industries, structures must adapt to the most demanding needs. At the same time, mechanical and economic reasons favor lighter options. In some cases, the behavior of structural materials must be gradual, as in composites or architectural materials, the so-called metamaterials. The geometries of these designs in the micro scale offer macro properties not found in continuous media, within the smallest volume. Conversely, their versatility poses problems for modeling ("direct" problem) and designing ("inverse" problem).

The direct problem, i.e. describing the performance of an architectural material with a predefined geometry, becomes sometimes intractable by traditional structural calculation methods because of the general complexity and non-linearity of its behavior. Thus, the definition of a purely analytical model (such as Hooke's law for isotropic materials) is impractical because the necessary variables are too numerous and/or partially unknown (internal or non-observable).

Sometimes, the only solution is to create surrogate models that can capture key features of the structure's mechanical response, thus reducing computation cost of calculation, via Model Order Reduction (MOR) or Machine Learning (ML).

The inverse problem deals with a much more difficult task, that of finding the structure (geometry, material, etc.) which gives the desired properties. This is a challenge since there is no unique solution and the mathematical formulation of the problem is ill-posed (non-convexity). Topology optimization methods are used, e.g. penalizing the isotropic solids (SIMP) by removing material to the minimum necessary to support the applied load with the least energy of deformation. This approach must consider the real properties of the material (anisotropy, fatigue) as well as the practical conditions of manufacture and use; introduced as further penalization, image filters or even new algorithms. All this allows to build a machine learning model to simplify and, thus, accelerate the optimization process.

As a mathematical object, graphs offer multiple possibilities for the compact representation of data with states as vertex and their relationships as segments. This analogy applies directly to the two main case studies that are relevant to this work, namely mechanical structures (centered on metamaterials) and biological neural networks, assimilating nodes/neurons as vertex and beams/axons as segments of a graph. This way, we take advantage of the methodologies developed to create a basic Digital Twin of the human brain to improve medical diagnoses.

Keywords : Reduced Models, Machine Learning, Metamaterials, Neuroscience, Digital Twins